UNIVERSITÀ DEGLI STUDI DI PADOVA

UNIVERSITÀ DEGLI STUDI DI PADOVA
Dipartimento di Fisica e Astronomia “Galileo Galilei”

CORSO DI DOTTORATO DI RICERCA IN ASTRONOMIA
CICLO XXIX

Chemical ejecta and final fates of intermediate-mass and massive stars

Tesi redatta con il contributo finanziario della fondazione Cariparo

Direttore della scuola: Prof. Giampaolo Piotto
Supervisore: Prof.ssa Paola Marigo
Co-supervisore: Prof. Alessandro Bressan

Dottoranda: Alessandra Slemer

Abstract

In my PhD work I carried out a detailed investigation on the final fates and chemical ejecta produced by intermediate-mass and massive stars.

The first part of the thesis is focused on massive and very massive stars. We derive the ejecta for a large number of elemental species (H, He, C, N, O, F, Ne, Na, Mg, Al, Si, S,, Ar, K, Ca, Sc, Ti, Cr, Mn, Fe, Ni, Zn) during the pre-supernova evolution and after the explosion or collapse event. We use a set of stellar tracks computed with PAdova and TRieste Stellar Evolution Code (PARSEC), with initial masses in the range between $8\,M_{\odot}$ to $350\,M_{\odot}$, for thirteen different initial metallicities from Z = 0.0001 to Z = 0.02. Adopting suitable explodability criteria available in the recent literature, for each stellar model we derive the final fate and remnant mass, which critically depend on the initial mass and metallicity. Three main classes of explosion events are considered. *Massive stars* with initial masses from $\sim 8\,M_{\odot}$ to $\sim 100\,M_{\odot}$, build a degenerate iron core which eventually collapses either generating a successful explosion and a neutron star, or experiencing an inexorable infall with consequent black hole formation (failed supernovae). Very massive objects (VMOs), with initial mass $\sim 100\,M_{\odot}$, can end their life either as pulsation pair instability supernovae (PPISN), pair instability supernovae (PISN), or directly collapsing to black hole (DBH). For these objects, the fate is mainly determined by the mass of helium-core.

From our analysis we derive a general scenario on the fate of massive and very massive stars emerges. It is evident that both the pre-SN evolution and the subsequent SN channel are significantly affected by the initial metallicity, as a consequence of its impact on the efficiency of mass loss and the growth of the stellar core. In particular, we find that suitable conditions for the occurrence of PPISN and PISN events are not limited to extremely low metallicities, as invoked in early studies. Rather, such energetic events may take place already at $Z > Z_{\odot}/3$, hence in the local Universe, in agreement with recent findings in the literature.

Once final fates and remnant masses are known, we compute the elemental ejecta for all stars in the grid, accounting for both wind and explosion contributions. The wind ejecta are directly derived from PARSEC stellar evolution models, for all isotopes from ^{1}H to ^{28}Si and heavier elements up to Zn. The explosion ejecta are obtained from supernova nucleosynthesis calculations available in the literature, for the three classes here considered(CCSN, PISN or PPISN). Suitable parameters (masses of the CO and He cores) are adopted to link the explosion models to our PARSEC tracks. We also calculate the integrated yields – ejected by a simple stellar population with a specified initial mass function – in view of comparing the chemical contributions of both winds and explosions from the three classes of stars (CCSNe, PISNe and PPISNe).

As a final result of this work, we will provide the community with a large database of chemical ejecta and compact remnants produced by massive and very massive stars over a wide range of initial masses and metallicites. These may be fruitfully used as ingredients in models of galaxy chemical evolution.

In the second part of the thesis we investigate the chemical ejecta of intermediate-mass stars, with particular focus on the thermally-pulsing asymptotic giant branch (TP-AGB) stars that experience both the third dredge-up and hot-bottom burning. This study was performed in the context of the LUNA (Laboratory Underground Nuclear Astrophysics) collaboration. Nucleosynthesis calculations were carried out adopting the new rate for the key reaction ^{22}Ne(p,γ)^{23}Na, which plays a major role in determining the abundance of sodium. To this aim we used the `PARSEC` and `COLIBRI` codes to compute the complete evolution, from the pre-main sequence up to the termination of the TP-AGB phase, of a set of stellar models with initial masses in the range $3.0\,M_{\odot} - 6.0\,M_{\odot}$, and metallicities Z=0.0005, Z=0.006, and Z = 0.014. We find that the new LUNA measurements have much reduced the nuclear uncertainties of the ^{22}Ne and ^{23}Na AGB ejecta, which drop from factors of $\simeq$ 10 to only a factor of few for the lowest metallicity models. Relying on the most recent estimations for the destruction rate of ^{23}Na, the uncertainties that still affect the ^{22}Ne and ^{23}Na AGB ejecta are mainly dominated by evolutionary aspects (efficiency of mass-loss, third dredge-up, convection). Finally, we discuss how the LUNA results impact on the hypothesis that invokes massive AGB stars as the main agents of the observed O-Na anti-correlation in Galactic globular clusters. We derive quantitative indications on the efficiencies of key physical processes (mass loss, third dredge-up, sodium destruction) in order to simultaneously reproduce both the Na-rich, O-poor extreme of the anti-correlation, and the observational constraints on the CNO abundance. While best-fitting AGB models can be singled out, the AGB hypothesis still needs to be validated, as various issues still remain.

Sommario

Il mio lavoro si occupa dell'analisi degli ejecta chimici espulsi dalle stelle di massa intermadia e massiccia. È strutturato in due macro-argomenti relativi, rispettivamente, alle stelle massicce e alle stelle di massa intermedia.

Nella prima parte, questo lavoro si concentra sullo studio dei *final fates* e degli *ejecta chimici* prodotti da stelle massicce e molto massicce. Abbiamo calcolato il materiale espulso per un gran numero di elementi (H, He, C, N, O, F, Ne, Na, Mg, Al, Si, S,, Ar, K, Ca, Sc, Ti, Cr, Mn, Fe, Ni, Zn) sia durante l'evoluzione pre-supernova che durante l'esplosione o il collasso. A questo scopo abbiamo usato un set di tracce evolutive calcolate con il codice di evoluzione stellare Padova and Trieste stellar Evolution Code (PARSEC), con masse iniziali nel range tra $8\,M_\odot$ a $350\,M_\odot$, per tredici diverse metallicità iniziali da Z = 0.0001 a Z = 0.02. Abbiamo ottenuto il final fate e il resto di supernova per ciascuna delle tracce PARSEC. Abbiamo quindi considerato separatamente due sottoclassi: le *stelle massicce*, che vanno da $\sim 8\,M_\odot$ a $\sim 100\,M_\odot$ e si evolvono come core-collapse supernovae; i *very massive objects* (VMOS), che sono in generale più massicci di $\sim 100\,M_\odot$ e, a seconda della massa del core di helio, possono evolvere come *pair instability supernovae* (PISN), *pulsation instability supernovae* (PPISN) o collassare direttamente al buco nero (DBH).

Dalla nostra analisi si ricava un quadro generale sui *final fates* di stelle massicce e molto massicce. È evidente che l'evoluzione pre-supernova e il verificarsi dell'esplosione sono significativamente influenzati dalla metallicità iniziale, conseguentemente al suo impatto sull'efficienza della perdita di massa e sulla crescita del nucleo stellare. In particolare, troviamo che le condizioni nelle quali si verificano eventi di PPISN e PISN non sono limitati a bassissime metallicità, come invocato nei primi studi. Piuttosto, tali eventi energetici possono aver luogo già a $Z > Z_\odot/3$, quindi nell'universo locale, in accordo con le recenti risultati presenti in letteratura.

Una volta noti i *final fates* e i resti di supernova, abbiamo calcolato la quantità di materiale espulso per diversi elementi chimici, dividendoli in contributi di vento e di esplosione. Gli elementi espulsi nel vento stellare sono derivati direttamente dai modelli di evoluzione stellare PARSEC, per tutti gli isotopi dall' ^{1}H al ^{28}Si e gli elementi più pesanti fino a Zn. Il materiale espulso è stato ottenuto da calcoli di nucleosintesi di supernova disponibili in letteratura, per le tre classi qui considerate (CCSN, PISN o PPISN). Sono stati adottati alcuni parametri chiave (come la massa del core di CO e di He) per assegnare gli ejecta di altri modelli di esplosione alle nostre tracce PARSEC. Abbiamo calcolato gli ejecta integrati - ottenuti da una semplice popolazione stellare e da una funzione di massa iniziale specificata - per confrontare il contributo all'arricchimento chimico da parte di CCSNe, PISNe e PPISNe in termini di vento ed ejecta esplosivi.

Come risultato finale di questo lavoro, ci proponiamo di fornire alla comunità scientifica un ampio database di ejecta chimici e di resti compatti prodotti da stelle massicce e molto massicce in un ampio intervallo di masse iniziali e metallicità. Questi potranno essere utilizzati quali ingredienti di base nei modelli di evoluzione chimica delle galassie.

La seconda parte di questo lavoro si occupa dell'analisi del materiale espulso da stelle di massa intermedia, con particolare attenzione alle stelle nella fase di "thermally-pulsing asymptotic giant branch" (TP-AGB), in cui ha luogo il processo di "hot-bottom burning". Questo lavoro è stato svolto in collaborazione con LUNA (Linear Underground National Laboratory), che ha fornito una nuova misura della sezione d'urto per la reazione ^{22}Ne$(p,\gamma)^{23}$Na. A questo scopo sono stati utlilizzati i codici di evoluzione stellare `PARSEC` e `COLIBRI` per completare l'evoluzione stellare dalla pre-main sequence alla fine della fase TP-AGB, per un set di modelli con massa iniziale nell'intervallo $3.0\,M_{\odot} - 6.0\,M_{\odot}$ e metallicità iniziali Z = 0.0005, Z = 0.006, and Z = 0.014. Grazie alla misura di sezione d'urto fornita dalla collaborazione LUNA abbiamo ridotto l'incertezza sugli ejecta di ^{22}Ne e ^{23}Na, abbassandola da un fattore $\simeq 10$ a poche unità per le metellicità più basse. Basandosi sulle più recenti stime della sezone d'urto della reazione ^{22}Ne$(\mathrm{p},\gamma)^{23}$Na, possiamo affermare che le incertezze sulle quantità di ^{22}Ne e ^{23}Na espulse sono perlopiù dominate da aspetti evolutivi (come l'efficienza della mass loss, il terzo dredge-up e la convezione). Infine, abbiamo discusso il modo in cui i risultati di LUNA impattano sull'impotesi che pone le stelle AGB come principali responsabili dell'anticorrelazione O-Na osservata negli ammassi globulari Galattici. Abbiamo derivato i vincoli quantitativi all'efficienza dei processi fisici principali (mass loss, terzo dredge-up, distruzione del Na) al fine di riprodurre l'estremo ricco di Na e povero di O, e i vincoli dati dalle osservazioni sull'abbondanza deli elementi C,N e O. Nonostante siano stati individuati prescrizioni fisiche ragionevoli che consentono di soddisfare tali vincoli, l'ipotesi che attribuisce alle stelle AGB la causa dell'anticorrelazione O-Na deve essere ancora convalidata, a causa di problematiche non ancora risolte.

Contents

List of Figures

List of Tables

Chapter 1

Context and thesis outline

Following a standard terminology we define *massive stars* those stars that are able to ignite all core nuclear burnings in absence of complete degeneracy (Heger & Woosley 2002). Massive stars play a key role in the chemical evolution of galaxies, despite their absolute number at birth and lifetimes are lower with respect to those of low mass stars. Massive stars contribute to the chemical enrichment of the interstellar medium (ISM) during both the quiescent hydrostatic phases of their evolution and, later, through powerful supernova (SN) explosions (Prantzos 2000; Hirschi & et al. 2006; Bromm 2005). These stars are usually born in dense clusters and have a complex circumstellar material, which results from strong stellar winds. With modern telescopes it is now possible to observe and resolve individual massive stars in such environments. The most massive stars observed so far have masses above $150\,M_{\odot}$. The first observation of such massive stars is due to Davidson (1999), who estimated the mass of η-Carina-A as $\simeq 160\,M_{\odot}$. More recently, Schnurr et al. (2008) estimated the mass of NGC 3603-B as $132\,M_{\odot}$, and Martins et al. (2008) observes the Arches-F9, attributing a mass of $\simeq 120\,M_{\odot}$. These two objects are located in our Galaxy. Furthermore, Crowther et al. (2010) estimated the mass of a stellar cluster in Large Magellanic Cloud, which is composed of R136a1 ($265\,M_{\odot}$), R136a2 ($195\,M_{\odot}$) and R136c ($M = 175\,M_{\odot}$). A recent study of Schneider (2014) confirms these results.

The evolution of massive stars, with initial mass above $8-10\,M_{\odot}$, is characterized by a rich nucleosynthesis, following a sequence of nuclear burnings that eventually ends with the synthesis of the iron-group elements. Differently from stars of lower initial mass, after the exhaustion of hydrogen and helium in the central regions, the resulting CO-core of a massive star does not encounter the condition of electron degeneracy so that carbon is ignited and burnt quiescently as the central temperatures reach $\sim 8\times10^{8}$ K. This phase is quite short, lasting only few 100 years. The nuclear burnings continue with neon and oxygen, burnt on timescales of the order of few

years. The last exothermic nuclear fusion involves silicon burning that lasts only a few hours. The final product is a degenerate iron core which soon enters a dramatic dynamical instability followed by gravitational collapse, triggered by electron captures and photodisintegration processes. The violent bounce of the infalling material onto the rigid proto-neutron star (neutrons also degenerate and the equation of state becomes stiff) produces an outward shock wave that may be able to produce an explosion, expelling the overlying layers. This event is named *Supernova*.

The evolution of massive stars has a paramount importance for the study of galaxy chemical evolution. The elements ejected by massive stars are produced during different evolution phases. The light elements C,N,O, Ne and Mg are produced during hydrostatic burning phases and are not effected by explosive processes. Heavier elements, from Al to Ca, are produced not only by hydrostatic burning, but are also affected by the passage of the shock wave. The iron group nuclei are formed during the advanced nuclearly stages involved in the supernova explosion, when it occurs (Thielemann & Arnett 1985; Woosley & Weaver 1995; Prantzos 2000; Pignatari et al. 2016; Limongi & Chieffi 2003). Massive stars are also the site of weak s-processes (Heger & Woosley 2002), which take place during core He-burning and convective shell C-burning (Heger & Woosley 2002; The et al. 2007; Pignatari et al. 2010) producing elements with mass number up to A $\sim$ 88 (Heger & Woosley 2002). The other source of trans iron elements is due to the r-processes, which are associated with the neutrino driven winds during core collapse SN (CCSN) events (Janka et al. 2007; Thielemann et al. 2011; Perego et al. 2014). In the framework of CCSNe a presently debated aspect is the effective occurrence of the explosion. In the recent years detailed numerical simulations have shown that not all stars that build an iron core will be able to explode as supernovae leaving a neutron star as a compact remnant. A failed explosion followed by the collapse into a black hole is the alternative channel. The definition of suitable physical criteria (linked to the pre-SN evolution, the structure of the degenerate core, and the efficiency of neutrino energy deposition) to establish the effective explodability are subject of major efforts from several authors (Fryer 1999; Fryer et al. 2006; Fryer & Kalogera 2001; Heger & Woosley 2002; Heger et al. 2003; Frayer & Taylor 2012; Janka 2012; Ugliano et al. 2012; Ertl et al. 2016)

Another source of ISM enrichment is due to the explosion of stars more massive than $\sim 100\,M_{\odot}$. These stars, named *Very massive objects* (VMOs), may not experience the whole chain of nuclear burnings due to the occurrence of dynamical instability conditions. After the end of the core He-burning, these stars encounter the electron-positron instability during carbon and oxygen burning, which can result in violent pulsations. Depending on the mass of the He-core and the strength of pulsations, the star may explode either as pair instability supernova (PISN) or experience a series of violent pulsations, evolving as pulsation-pair instability supernova (PPISN). In the case of

PPISN, the pulsations continue until the star has lost so much mass to recover a condition of dynamical stability, resuming the sequence of quiescent nuclear burning until an iron core is formed (Heger & Woosley 2002; Langer et al. 2007; Kozyreva et al. 2014b; Woosley & Heger 2015)). Until recently, the occurrence of VMO and their final fate were thought to apply only to primordial Pop III stars (Bond et al. 1982, 1984; Heger & Woosley 2002; Nomoto et al. 2013). More recently Langer et al. (2007) and Kozyreva et al. (2014b) investigate also the possible existence of pair instability events for higher metallicities. The main elements produced by these violent explosions are mostly oxygen, helium and hydrogen (Kozyreva et al. 2014b; Woosley & Heger 2015; Woosley 2016).

The calculation of the chemical ejecta from massive stars has been the focus of several studies in the literature. The stellar wind ejecta are provided by Portinari et al. (1998); Lamers & Cassinelli (1999); Crowther (2001); Hirschi et al. (2005b) and Pignatari et al. (2016), who used different stellar evolution models with different inputs for stellar micro-physics (e.g. opacities and nuclear reaction rates), and stellar macro-physics (e.g. mass loss). The ejecta of CCSNe are provided by Woosley & Weaver (1995); Portinari et al. (1998); Chieffi & Limongi (2004); Limongi & Chieffi (2006); Nomoto et al. (2006); Pignatari et al. (2016). The contribution of very massive stars is computed by Heger & Woosley (2002) Umeda & Nomoto (2002), Woosley & Heger (2015) and Woosley (2016) for stars at zero metallicity, and by Kozyreva et al. (2014b) for pair instability supernova at Z=0.001.

In this work we focus on massive and very massive stars. We obtain tables of chemical ejecta for a wide range of initial masses (from $M_{\rm i} = 8 M_{\odot}$ to $M_{\rm i} = 350\,M_{\odot}$) and initial metallicity (from $Z_{\rm i} = 0.0001$ to $Z_{\rm i} = 0.02$). These tables include a large number of elemental species (H, He, C, N, O, F, Ne, Na, Mg, Al, Si, P, S, Cl, Ar, K, Ca, Sc, Ti, Cr, Mn, Fe, Co, Ni, Zn) produced both during the pre-supernova evolution and after explosion or collapse event. The stellar tracks are computed with the PAdova and TRieste Stellar Evolution Code (`PARSEC`).

Adopting the suitable explodability criteria available in the recent literature, for each stellar model we derive the final fate and remnant mass for each `PARSEC` track, which critically depend on the initial mass and metallicity. We consider two main classes of explosion events:

- *Massive stars*, with with initial masses from $\sim 8\,\mathrm{M}_{\odot}$ to $\sim 100\,\mathrm{M}_{\odot}$. These stars build a degenerate iron core which eventually collapses either generating a successful explosion and a neutron star, or experiencing an inexorable infall with consequent black hole formation (failed supernovae).

- *Very massive objects* (VMOs), with initial mass higher than $\sim 100\,\mathrm{M}_{\odot}$. VMOs can end their life either as pulsation pair instability supernovae (PPISN), pair instability supernovae

(PISN), or directly collapse to black hole (DBH). For these objects, the fate is mainly determined by the mass of helium-core.

We built a final fate scenario for massive and very massive stars. From this analysis we derived a series of considerations:

- Both the pre-SN evolution and the subsequent SN channel are significantly affected by the initial metallicity, as a consequence of its impact on the efficiency of mass loss and the growth of the stellar core. Furthermore, concerning the CCSNe channel, the contribution of dark remnants depends on the adopted explosion criterion. The final fate scenarios obtained using the mono-parametric model of Frayer & Taylor (2012) show that black holes are generated both by successful and failed SNe, while following the bi-parametric explodability models of Ertl et al. (2016) the fall-back of material after the explosion is minor so that only failed CCSNe can leave behind a black hole.

- The predicted window of failed supernovae and the corresponding compact remnants is particularly relevant in the context of the recent discovery of gravitational waves originated from the from binary black hole merger GW150914 (Abbott et al. 2016). According to our calculations, black holes of masses comparable to the estimated ones ($29\,M_\odot$ and $36\,M_\odot$) may be produced by massive stars with initial masses in the range $30\,M_\odot \lesssim M_i \lesssim 100\,M_\odot$ and metallicity $0.004 \lesssim Z \lesssim 0.006$.

- The suitable conditions for the occurrence of PPISN and PISN events are not limited to extremely low metallicities, as invoked in early studies (Bond et al. 1982, 1984; Heger & Woosley 2002; Umeda & Nomoto 2002; Nomoto et al. 2006). Rather, such energetic events may take place already at $Z \gtrsim Z_\odot/3$, hence in the local Universe, in agreement with recent findings in the literature (Langer et al. 2007; Kozyreva et al. 2014c).

- From the analysis of the progenitors of supernova events, we find that at low metallicity ($Z \lesssim 0.0001$) the pre-supernova scenario is dominated by red supergiant (RSG) stars, up to $M_i \sim 100\,M_\odot$, while more massive stars usually evolve as luminous blue variables (LBV). This behavior is related to the efficiency of mass loss driven by radiative pressure. We conclude that for $Z \lesssim 10^{-3}$ the quasi totality of the stars reach the pre-SN stage as RSG. For higher metallicities ($10^{-3} \lesssim Z \lesssim 0.006$) and initial masses higher than $100\,M_\odot$, SN progenitors belong to the Wolf Rayet stars rich in N and C (WN and WO classes, respectively). The progenitors of failed SNe could be stars in LBV, WN and WO phases. Finally, at increasing metallicity the critical mass window of SN region favors the Wolf Rayet class rather than

the LBV channel. Thus, for $Z \gtrsim Z_{\odot}/4$ the progenitors of CCSNe and PISNe are mostly WC stars and WO stars, respectively.

Once the remnant masses are known, we compute the elemental ejecta for all stars in the grid, accounting for both wind and explosion contributions. The wind ejecta are directly derived from PARSEC stellar evolution models, for all isotopes from ^{1}H to ^{28}Si and heavier elements up to Zn. The explosion ejecta are obtained from supernova nucleosynthesis calculations available in the literature, for the CCSNe, PISNe and PPISNe. Suitable parameters (masses of the CO and He cores) are adopted to link the explosion models to our PARSEC tracks. We also calculate the integrated yields and the production factors– ejected by a simple stellar population with a specified initial mass function – in view of comparing the chemical contributions of both winds and explosions from the three classes of stars (CCSNe, PISNe and PPISNe).

The main results are summarized as follows:

- We provide tables of chemical ejecta for stars spanning a wide range of initial masses and metallicities. We separated the contributions of stellar winds and explosion ejecta. While the wind contributions are derived directly from our PARSEC stellar evolution models, the explosion ejecta are obtained from available databases of explosive nucleosynthesis. The result is a large grid of chemical ejecta which can be fruitfully employed studies of galaxy chemical evolution.

- We observe that the amount of element ejected as stellar winds increases with initial mass and initial metallicity, as expected. This trend is inverted for in the case of carbon and oxygen. We found that, for $Z \lesssim 0.004$ the wind ejecta from stars more massive than $\sim 100\,M_{\odot}$ are higher by up to one order of magnitude for C and two orders of magnitude for O, compared to those contributed at near solar metallicities. This result is explained considering the stage at which the stars of different mass and Z enter in the Wolf Rayet phases characterized by strong winds enriched in carbon and oxygen (named WC and WO, respectively). Furthermore, since the strong winds of WR stars exhibit the nucleosynthesis products on the surface, a fraction of such high ejecta may be formed by primary carbon and oxygen.

- As already shown extensively in the literature (Woosley & Weaver 1995; Limongi et al. 2000; Prantzos 2000; Kozyreva et al. 2014c; Pignatari et al. 2016), the production factors of explosive nucleosynthesis exhibit the so-called "odd-even effect", that is the production of elements with even mass number is favoured with respect to the elements with odd mass number. This property is particularly evident at low metallicity, while it tends to decrease at near solar metallicity. The odd-even effect is characteristic of both massive and very

massive stars, and it is most evident for light and α-elements, since the production of the heavier ones is critically determined by the neutronization during the explosive burning and therefore less affected by initial metallicity.

As to the production factors of wind ejecta, we may conclude that the contribution due to winds is higher for lighter elements and higher metallicities. In particular, the contribution of carbon and nitrogen ejected in the winds with respect to the total ejecta vary from $\sim 5\%$ at low Z, to $\sim 20\%$ at near solar Z, and from $\sim 15\%$ to $\sim 35\%$, respectively.

- Comparing the contribution in the α-elements production by PISNe at low metallicities ($\sim 10^{-3}$) to those of pop III stars, we confirm the results obtained by Kozyreva et al. (2014c), who found that both classes of stars contribute in comparable way to the ISM enrichment. Furthermore, at low metallicities the PISNe give a large contribution also to the production of light elements. This fact is explained by considering that these stars experience violent mass loss episodes during the pulsations that occurred at the onset of the pair instability.

We also include the analysis of the chemical ejecta of intermediate-mass stars, with particular focus on the thermally-pulsing asymptotic giant branch (TP-AGB) stars that experience both the third dredge-up and hot-bottom burning. This work has been published in the paper Slemer et al. (2017). The study was performed in the context of the LUNA (Laboratory Underground Nuclear Astrophysics) collaboration. We carried out nucleosynthesis calculations adopting the new rate for the key reaction ^{22}Ne(p,γ)^{23}Na, which critically affects the abundance of sodium. We used the stellar evolution codes `PARSEC` (Bressan et al. 2012) and `COLIBRI` (Marigo et al. 2013) to compute the complete evolution, from the pre-main sequence up to the termination of the TP-AGB phase. The set of stellar models considered has initial masses from $3.0\,M_\odot$ to $6.0\,M_\odot$, and metallicities Z=0.0005, Z=0.006, and Z = 0.014. We find that the new LUNA measurements have much reduced the nuclear uncertainties of the ^{22}Ne and ^{23}Na AGB ejecta, which drop from factors of $\simeq 10$ to only a factor of few for the lowest metallicity models. Relying on the most recent estimations for the destruction rate of ^{23}Na, we find that the uncertainties that affect the ^{22}Ne and ^{23}Na AGB ejecta are mainly dominated by evolutionary aspects (efficiency of mass-loss, third dredge-up, convection). Finally, we discuss how the LUNA results impact on the hypothesis that invokes massive AGB stars as the main agents of the observed O-Na anti-correlation in Galactic globular clusters. We derive quantitative indications on the efficiencies of key physical processes (mass loss, third dredge-up, sodium destruction) in order to simultaneously reproduce both the Na-rich, O-poor extreme of the anti-correlation, and the observational constraints on the CNO abundance. While best-fitting AGB models can be singled out, the AGB hypothesis still needs to

be validated, as various issues still remain.

The structure of the thesis is as follow. Chapter 2 briefly describes the stellar evolution and pathways of massive and very massive stars, including the main nuclear reactions processes and their products. In chapter 3 we describe the main feature of the PARSEC stellar evolution code, used in this work. Chapter 4 is dedicated to the analysis of the final fate of massive and very massive stars and the derivation of chemical ejecta. Finally, chapter 5 is devoted to the analysis of the chemical ejecta of neon and sodium produced by intermediate-mass stars, in the light of recent nuclear measurements of the proton-capture reaction $^{22}\mathrm{Ne}(\mathrm{p},\gamma)^{23}\mathrm{Na}$.

Chapter 2

Evolution and nucleosynthesis

In this chapter I briefly describe the evolution and the main nuclear burning stages experienced by massive and very massive stars during the pre-supernova evolution, including also the explosion mechanism that permit the supernova event.

Depending on its initial mass, a star may experience several nuclear burnings in the central core. These are the sequential phases of core burning of hydrogen, helium, carbon, neon, oxygen, and silicon (Fowler & Hoyle 1964; Wallerstein et al. 1997). If all nuclear burnings occur without degenerate conditions, the thermonuclear reactions that take place in the centre of the star cease with the formation of the iron core, since no exothermic fusion reaction can occur beyond this point. This pathway is experienced by stars less massive than $\sim 100\,M_{\odot}$. According to the criterion of Heger & Woosley (2002) this mass interval corresponds to stars that develop an helium core less massive than $40\,M_{\odot}$.

If the pre-supernova stars develop a more massive helium core, a new kind of explosion mechanism becomes accessible. This is the domain of *very massive objects* (VMO), which are the progenitors of *pair instability supernovae* (PISNe) and *pulsation-pair instability supernovae* (PPISNe). For this kind of stars, the mass of helium core is the driver of the explosion, because it determines the depth at which the bounce forms and its temperature.

2.1 Massive stars

The evolution of *massive stars* is characterized by two important features:

- The massive stars proceed through all nuclear stages in steady state up to silicon burning, with consequent formation of iron core. This implies that carbon burning must be ignited in non-degenerate conditions in the centre and that oxygen-neon core is built up with a mass larger than $\sim 1.37\,M_\odot$, as indicated by detailed stellar models (Nomoto 1984). The correspondent minimum mass of the massive stars is named M_{mas}.

  Recent stellar evolution calculations (Siess 2007; Hurley et al. 2000, e.g) indicate that M_{mas} corresponds to a threshold value of CO-core (M_{CO}) formed at the end of core He-burning, with relatively small dependence on the initial metallicity. Following the detailed analysis of Siess (2007) this critical value is $M_{CO} \simeq 1.179 \pm 0.001\,M_\odot$ and $M_{CO} \simeq 1.246 \pm 0.015\,M_\odot$ for stellar models without and with convective overshoot, respectively.

  The effect of overshooting on the M_{mas} value is a reduction of $\sim 2\,M_\odot$, from $10.93\,M_\odot$ without overshooting to $8.83\,M_\odot$ with overshooting effect. For more detailes see table 3 of Siess (2007).

  As our PARSEC tracks include overshoot from the class of massive stars, we adopt the latter criterion to define the class of massive stars, i.e. all models of $M_{CO} > 1.246\,M_\odot$. We find that M_{mas} is a weakly increasing function of the metallicity, ranging from $M_{mas} \simeq 7\,M_\odot$ at $Z = 0.0001$ to $M_{mas} \simeq 8\,M_\odot$ at $Z = 0.02$.

  The upper mass limit of the massive stars is decided by the He-core mass. The stars that develop the He-core less massive than $\sim 40\,M_\odot$ are thought to be the progenitors of core collapse supernovae (CCSNe) (Heger & Woosley 2002; Nomoto et al. 2013; Kozyreva et al. 2014b), while more massive stars, named *very massive object* (VMOs), experience a different evolution, which can end with a thermonuclear explosion. We describe in detail the VMOs in section 4.0.2.

- For masses $M \gtrsim 14\,M_\odot$ the *mass loss by stellar winds* becomes important during all evolution phases, including the main sequence. For masses above $\sim 30\,M_\odot$ the mass-loss rates $\dot{M}$ are so large that the timescale of mass loss, $\tau_{ml} = M/\dot{M}$ becomes smaller than the nuclear timescale τ_{nuc}. Therefore mass loss has a very significant effect on their evolution. The stellar wind mechanism involved are in many cases not well understood, so that $\dot{M}$ is often quite uncertain. This introduces substantial uncertainties in massive star evolution. The effect of mass loss on massive star evolution is discussed in section 2.1.1.

2.1.1 Mass-loss in massive stars

Massive stars experience episodes of mass loss throughout the pre-supernova evolution, both through continuous winds and bursts, loosing large amounts of mass in the immediate surrounding. The study of mass loss in stellar evolution has greatly improved the understanding of massive stars properties, and several major consequences have been found to result from evolution with mass loss (Chiosi & Maeder 1986). First, the inclusion of mass loss in stellar evolution models changed significantly the tracks in HR diagram. In particular, the relation between OB star, Hubble-Sandage variables, blue and red supergiants, and Wolf-Rayet (WR) stars has been clarified. Another effect of mass loss is the removal of stellar envelope, which leads the products of core nucleosynthesis to appear at the stellar surface. These products are spectroscopically observable and thus offer a new test of stellar evolution. The wind ejecta also contribute to the galactic chemical enrichment. Depending on internal structure, massive stars can lose up to 90% of their initial mass through stellar winds. The last main effect of mass loss in massive stars is the influence on the nature of supernovae precursor and their chemical yields, as well as general stellar stability throughout evolution.

The material ejected just before the explosion of a supernova also impacts on the nature of the supernova itself. Indeed, depending on the density of the medium into which the supernova expands, its spectrum may be very different. For instance, type IIn supernova are though to have a spectrum dominated by nebular emission. Furthermore, the formation of different types of core-collapse supernovae depends on the physical properties of the progenitor, which are determined also by the mass loss history.

In this section, I describe the wind properties of massive stars in different evolutionary phase: O and B phases, red supergiants (RGB), luminous blue variables (LBV) and Wolf-Rayet phase (WR).

The phase O and B corresponds to the first stages of massive stars evolution. During this phase the effective temperature (T_{eff}) is higher than 15000 K, and it corresponds to the main sequence and slightly beyond for blue supergiants stars. During the main sequence, massive stars eject material in the interstellar medium at a rate between $10^{-9}\,M_{\odot}/yr$ and $10^{-5}\,M_{\odot}/yr$ depending on the initial mass and initial metallicity. Winds of OB stars are explained by the radiatively driven wind theory, which is first developed by Lucy & Solomon (1970) and Castor et al. (1975) and later by Vink et al. (2001). The efficiency of mass loss is determined by the radiative line acceleration, which is expressed in units of Thomson acceleration and it is parametrized as

$$M[t(r)] = kt^{-\alpha}n^{\delta} \tag{2.1}$$

where $t(r)$ is the Thomson optical parameter. The parameter k represents the normalization integral over the contribution of all photons that absorb the spectral lines with different line strength, and n is the ratio of the local number density of electrons to the local geometrical dilution factor of radiation field, and finally α and δ describe the optical depth and density dependence of radiative line force (Castor et al. 1975; Abbott 1982; Kudritzki et al. 1988).

Computations of Vink et al. (2001) show quantitatively that the main elements that generate the wind acceleration are iron and the CNO ions. The last ones become dominant wind drivers at low metallicity. The role of radiation pressure on the resonance lines of metallic ions like CIII, NeII and OII, in driving mass loss from massive stars has been a result of theoretical astrophysics studies since the pioneer works of Lucy & Solomon (1970) and Castor et al. (1975). The radiation driven wind theory affirms that the mass loss scales with the power of the luminosity. Since the acceleration depends on metallic lines, stars with low initial metallicity should have lower mass loss rates. This is confirmed empirically by Mokiem et al. (2007), who finds the scaling relation $\dot{M} \propto Z^{0.83}$ from the winds of OB stars in Galaxy and Magellanic Clouds. The dependence of radiative wind efficiency on metallicity (in the range from $Z_\odot$ to $0.01Z_\odot$) has been investigated also by Abbott et al. (1982); Leitherer et al. (1992); Kudritzki & Puls (2000); Vink et al. (2000). Even though radiatively driven winds are continuous, they are not homogeneous, because of the intrinsic instability of driving mechanism. Since the radiative acceleration is proportional to the velocity gradient, any change in the later will lead to a high change in the former. Consequently, regions of higher-than-average velocities follow regions with lower-than-average velocities. Due to mass conservation, this translates into inhomogeneities in the density distribution.

After the main sequence, at solar metallicity, the stars with initial mass between $\sim 8\,M_\odot$ and M_{VMO} cross the HR diagram to become red supergiants (RSG). The upper limit M_{VMO} depends on initial metallicity and it ranges from $\sim 100\,M_\odot$ for $Z = 1 \cdot 10^{-4}$ to $\sim$ 40-50 $M_\odot$ for $Z_\odot$. The RSG phase strongly impacts on the neighbouring environments. Stars are affected by mass loss rates from 10^{-7} to $10^{-4}\,M_\odot$/yr and the winds velocities are typically of 10-40 km/s. Hence the wind density is about a thousand times larger than in the OB phase. The main characteristics of stellar winds in this phase are two. First, the mass loss is directly proportioned to luminosity. Second, at a given luminosity, the dispersion in mas loss rates is about a factor of ten (Mauron & Josselin 2011). Stars with $M_i \lesssim 40\,M_\odot$ spend a large fraction of thei core-he-burning phase as RSG. During this phase a large part part or even the entire envelope can be evaporated by the wind, exposing helium core of the star as a Wolf-Rayet (WR) star.

Wolf-Rayet stars are hot, very luminous stars with bright emission lines in their spectra. The emission indicates very strong, optically thick stellar winds, with mass-loss rates of $\dot{M} \sim 10^{-5}$-

$10^{-4}\,M_\odot/yr$. They are often surrounded by circumstellar nebulae of ejected material. The winds are probably driven by radiation pressure as for O stars, but multiple photon scattering in the optically thick outflow can increase the mass-loss rate to well above the single-scattering limit.

The spectra of WR stars show increased CNO abundances, indicating that they are the exposed H- or He-burning core of massive stars. On the basis of the surface abundances they are classified into several sub-types:

- **WNL stars**. These stars have H present on their surfaces ($X_H <= .4$), and increased he and N abundances, consistent with equilibrium values from CNO-cycles
- **WNE stars** are similar to WNL in their He and N abundances, but they lack hydrogen.
- **WC stars** have no hydrogen, little or no N, and increased He, C and O abundances (consistent with partial He-burning)
- **WO stars** are similar to WC stars with strongly increased O abundances.

For stars more massive than M_{VMO}, the red-wards evolution at high luminosity implies that the star reaches the Humphreys-Davidson limit (Humphreys & Davidson 1979) above which it is not bound anymore. The stars that reach this part of HR diagram are classified as luminous blue variables (LBV). During the LBV phase, the effective temperature T_{eff} is greater than 10000 K, the maximum luminosity increases to $L \sim 10^7 L_\odot$ at 40000 K (O stars) and the star experience mass loss episodes with $\dot{M} > 10^{-3}\,M_\odot/yr$ (Stahl et al. 2001; Vink & de Koter 2002). The luminosity of the star exceeds the classical Eddington limit

$$L_{Edd} = \frac{4\pi cGM}{k_e} \tag{2.2}$$

where k_e is the electron scattering opacity. Examples of LBV stars in our Galaxy are η-Carinae and P-Cygni. After the vigorous mass loss episodes the circumstellar nebulae can be seen. The nebula is considerably enriched in nitrogen, showing that the layers processed by CNO-cycling are being ejected. Stars losing mass due to LBV outbursts are destined to become WR stars. The strong LBV mass loss prevent them from ever becoming RSG.

2.1.2 The effects of overshooting

The stellar evolution of massive stars is affected mainly by mass loss and convection. Since the time scale of stellar winds for massive stars is comparable to the life-time of stars, it is necessary to take into account the mass loss in the stellar tracks. For stars more massive than $30\,M_\odot$ the mass

loss effects dominate the stellar evolution, while for lower mass stars the convection effects are dominant.

Different prescriptions are used in literature to describe the way in which compositional mixing is handled. The PARSEC code, whose tracks are used for this work, considers the *convective overshooting*. The main characteristic of convective overshooting for massive stars models can be summarized as follow:

- The mass of convective core is considerably higher with respect to the classical models. Consequently, semiconvection and/or convection effects do not develop in the core. This fact is true both for stars with and without mass loss.
- The stellar tracks obtained with overshooting models experience higher luminosity (L) with respect to the tracks derived using classical models.
- The time interval that corresponds to core H-burning increases with the overshooting, because of more availability of fuel dominates to the effect of high luminosity, which corresponds to high energy losses. The effect of overshooting to the duration of core H-burning is higher than the effect provoked by the mass loss.
- The duration of core He-burning phase is weakly sensible to the overshooting effect.

2.1.3 Evolution of massive stars in the HR diagram

The evolution of the massive stars is well represented in fig. 2.1, which shows the evolution of PARSEC tracks with initial masses between 14 to $350\,M_{\odot}$, for two different metallicities. The figure 2.1 is taken from Tang et al. (2014). As revealed by this figure, the evolutionary path of a massive star through the HRD can be rather complicated. Evolution proceeds at nearly constant luminosity, because massive stars do not develop degenerate cores and most of the mass is in radiative equilibrium. However, the evolution tracks show several left-right excursions and loops which depend on the mass of the star.
The relation between the theoretical evolution tracks and the observed types of massive stars is described by the *evolution scenario*, originally proposed by Peter Conti:

- $M_i \lesssim 15\,M_{\odot}$: the main sequence stars (MS), which are of spectral type O or B, evolve as red supergiant (RSG), or can experience a blue loop. During this phase these stars enter in the blue supergiant phase (BSG) and then return to the RSG region of HRD. The final fate can be a core collapse supernova type II (SNII)

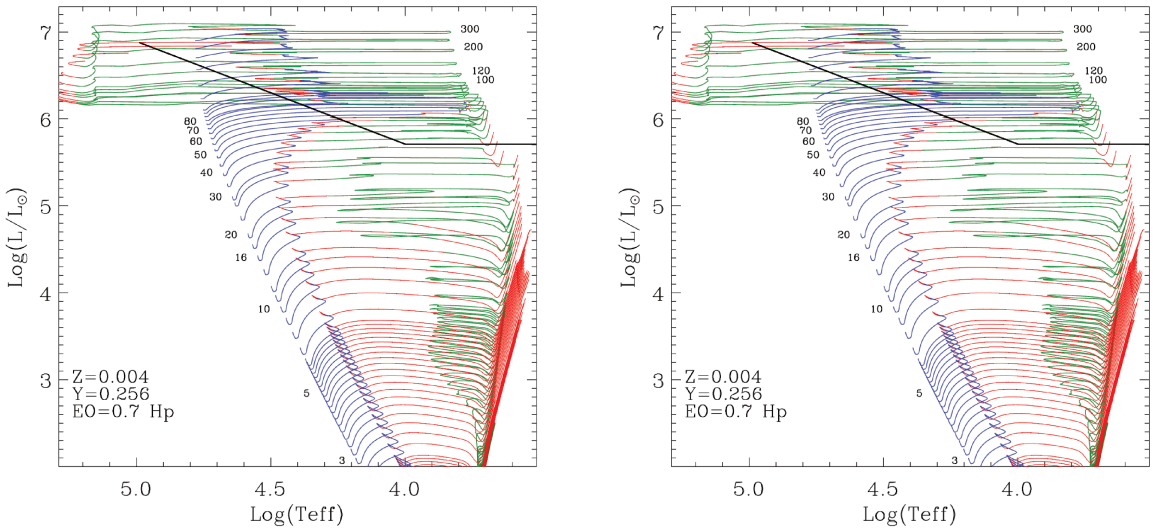

Figure 2.1: HR diagram of PARSEC tracks, for initial mass from $14\,M_\odot$ to $350\,M_\odot$ and initial metallicities Z=0.0001 (upper panel) and Z=0.004 (lower panel). The figure is taken from Tang et al. (2014)

- $15\,M_\odot \lesssim M_i \lesssim 25\,M_\odot$: MS (O) → BSG → RSG → SNII
- $25\,M_\odot \lesssim M_i \lesssim 40\,M_\odot$: MS (O) → BSG → RSG → WNL → WNE → WC → SNIb
- $M_i \gtrsim 40\,M_\odot$: MS (O) → BSG → LBV → WNL → WNE → WC → SNIb/c

The limiting masses given above are only indicative, and can be implicated to massive stars of Population I composition (near solar). Since mass-loss rates decrease with decreasing Z, the mass limits are higher for stars at lower metallicity. The relation between the final fate and the relative progenitors are discussed in section 4.0.3.

For stars with initial mass higher than $60\,M_\odot$, great episodes of mass loss are experienced also during the main sequence. The mass loss exposes layers that belonged to the large convective core. Thus CNO-cycling products are revealed, and the surface He-abundance increases at the expense of H. During the very short phase between central H and He burning, several solar masses are lost during the LBV phase. During the first part of the core-He burning the star appears as a WNL stars, and subsequently as a WNE star after the mass loss has removed the last H-rich layers outside the H-burning shell. The result is that the material that was formed during eh He-burning convective core is exposed at the surface: nitrogen, which was consumed in He-burning reactions, disappears while the products of He-burning, C and O, appear. Finally the star evolve as a WC star.

Generally, the mass loss rates experienced by stars with $M \gtrsim 30\,M_\odot$ increase with stellar mass, resulting in timescales for mass loss that are less that the nuclear timescale. As a result, there is a convergence of the final pre-supernova masses to $\sim 5-10\,M_\odot$. However, this effect is much diminished for metal-poor stars because the mass loss rates are generally lower at low metallicity.

2.1.4 Advanced evolution of massive stars

Once the carbon-oxygen core has formed after the He-burning, the subsequent evolution of the core is a series of alternating nuclear burning and core contraction cycles. Figure 2.2 shows the evolution of the central temperature (T_c) and the central density (ρ_c) during the stellar evolution. Both central temperature and density increase roughly following the law

$$T_c \propto \rho_c^{1/3} \tag{2.3}$$

as expected for homologous contraction. For central temperatures $\gtrsim 5 \cdot 10^8$K, the evolution tracks deviate from this trend, experiencing higher central temperature and density. This is the result of cooling the core by strong neutrino emission. The time interval between the onset of carbon burning and the formation of iron core is less than a few thousand years. During this time the mass of the CO-core remains fixed. Moreover, the stellar envelope has no time to respond to the rapid changes in the core, so that its evolution is completely disconnected from the evolution of the core. The result is that the position of a massive star in the HR diagram remains almost unchanged during the carbon burning and beyond.

2.1.5 The role of weak interactions and neutrino losses

The weak interactions play an important role in determining both the pre-supernova stellar structure and the nucleosynthesis. They affect the stellar structure because, during the whole evolution, the pressure is mostly due to electrons. These particles are, at first, non relativistic and non-degenerate, but later they can change the Y_e. Furthermore, they afffect the nucleosynthesis because the production of all nuclei with different values of neutrons and protons is sensitive to the neutron excess, η, which depends on the Y_e by the relation: $\eta = 1 - 2Y_e$. The neutrinos lost in weak interactions also affect the energy and entropy budgets of the star. These energy losses are especially important during the final collapse of the stars. The most dramatic decline in Y_e occurs early during silicon burning, but appreciable decreases continue as the iron core sits in hydrostatic equilibrium surrounded by active shells of silicon burning that impede its collapse. Some of the most important weak flows include electron capture on ^{35}Cl,^{32,33}S,^{53}Fe,^{55}Co and ^{56}Ni and, later,

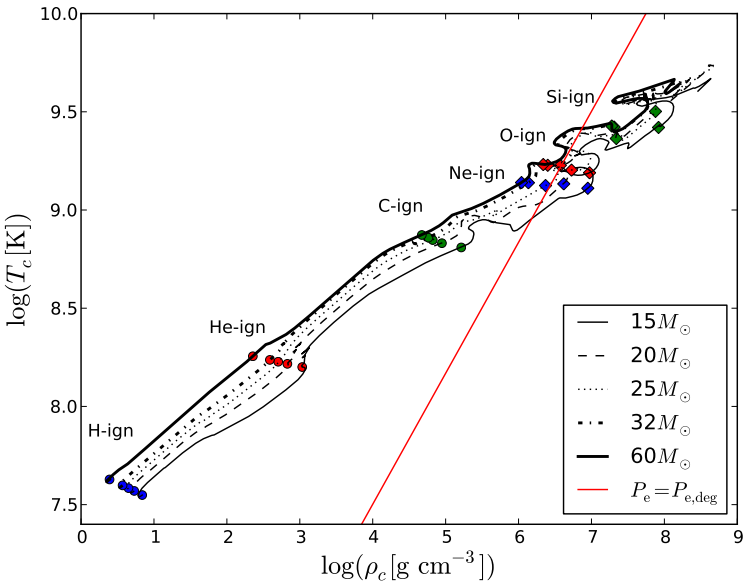

Figure 2.2: Evolution of central temperature and density of some massive stars at Z=0.02 through all nucelar burnings up to iron-core collapse. Ignition points for the core burning stages are indicated by the colored points, which are determined at the point when the principal fuel is depleted by 0.3% from its maximum value. Note that before the onset of the degeneracy condition ($P_e = P_{e,deg}$), all the tracks follow the trend $T_c \propto \rho_c^{1/3}$, which is expected from homologous contraction. The figure is taken from Pignatari et al. (2016).

the electron capture on ^{54,55,56}Fe and ^{61}Ni. The final value of Y_e is not particularly sensitive to the weak rates or to the stellar mass.

Before the oxygen ignition, the weak interactions play a minor role, because the change in neutron excess prior to O-burning has only a slight effect on the stellar structure. When the central temperature exceeds $\sim 5 \cdot 10^8$K the neutrinos losses are the most important energy leak from the stellar centre, taking away energy much more rapidly than photon diffusion or convection transport. From this point inwards the neutrino luminosity of the core (L_ν) far exceeds the luminosity radiated from the surface (L). During each nuclear burning phase, $L_{nuc} = \dot{E_{nuc}} \simeq L_\nu$, which thus results in a much shorter nuclear timescale in presence of neutrino losses: $\tau_{nuc} = E_{nuc}/L_\nu \ll E_{nuc}L$. Similarly, the rate of core contraction speeds up, favouring the core collapse acceleration. This loop condition is the cause if the core collapse event.

Table 2.1: Properties od nuclear burning stages in a $15\,M_{\odot}$ star, taken from Heger & Woosley (2002).

burning stage	T ($10^9\,K$)	($\rho(gcm^{-3})$	fuel	main products	timescale
hydrogen	0.035	5.8	H	He	$1.1 \cdot 10^7$ yr
helium	0.18	$1.4 \cdot 10^3$	He	C,O	$2.0 \cdot 10^6$ yr
carbon	0.83	$2.4 \cdot 10^5$	C	O,Ne	$2.0 \cdot 10^3$ yr
neon	1.6	$7.2 \cdot 10^6$	Ne	O,Mg	0.7 yr
oxygen	1.9	$6.7 \cdot 10^6$	O,Mg	Si,S	2.6 yr
silicon	3.3	$4.3 \cdot 10^7$	Si,S	Fe,Ni	18 d

2.1.6 Hydrostatic nuclear burnings

The following section is dedicated to the general description of the hydrostatic nuclear burning taking place inside the massive stars. The general properties of each nuclear burning experienced by massive stars is represented in table 2.1.

Hydrogen burning

A massive star spends about 90% of its life burning hydrogen in the core, and most of the rest burning helium. The quiescent phases when convection and radiation transport dominate over neutrino emission, also determine what follows during the advanced burning stages and explosion. The all aspects of massive stellar evolution during H- and He-burning phases are described in detail by Chiosi et al. (1992) and Maeder & Conti (1994). Grids of stellar models, including massive stars, have been evolved through hydrogen and helium burning by Schaerer et al. (1993b); Charbonnel et al. (1993); Hirschi et al. (2005b); Tang et al. (2014); Pignatari et al. (2016).

For massive stars, the main sequence core H-burning is characterized by a formation of convective core and the star grows radius, luminosity and decreases the effective temperature (T_{eff}). The size of the convective core is usually fixed by the classical Schwarzschild (1958) criterion, and increases with stellar mass, while the duration of the core H-burning phase decreases with increasing mass owning to the overwhelming effect of increasing luminosity. The main sequence lifetime of massive stars is of the order of 10^6yr and decrease with increasing initial mass. Massive stars may be affected by semi-convection instability, which has been considered the main feature of the structure of massive stars evolved at constant mass, while to date the most important signature of the massive stars evolution is the occurrence of mass loss by stellar wind Chiosi et al. (1992). After exhausting H in the core, massive stars evolve rapidly in red giant region of HR diagram. In this region the stars burn hydrogen in a shell above a rapidly contracting and heating core, composed essentially of helium. As the star approaches the Hayashi line, the hydrogen shell

envelope develops, and its base inward until it reaches the carbon-nytrogen-oxygen cycle (CNO) takes place. The H-shell provides both the stellar luminosity and adds matter to the H-exhausted core, which continues to grow. When the temperature and density in the core reach the suitable values, the core starts to burn helium.

The relevant nuclear reactions for H-burning in massive stars are the CNO cycle reactions, especially $^{12}C(p,\gamma)^{13}N(e^{+}\nu)^{13}C(p,\gamma)^{14}N(p,\gamma)^{15}O(e^{+}\nu)^{15}N(p,\alpha)^{12}C$ (see Rolfs & Rodney (1988) for details). The energy released by H-burning depends on initial composition, but for a star with 70% of hydrogen it is 26.7MeV (Heger & Woosley 2002), of which 1.71 MeV per helium atom is carried away by neutrinos. The reaction rates that govern the energy generation and stellar structure (in contrast to nucleosynthesis) are relatively well determined by the CNO cycle (Caughlan & Fowler 1988; Rolfs & Rodney 1988; Angulo et al. 1999b).

Other important cycles of reactions experienced by the star during H-burning are the Ne-Na and Mg-Al cycles. These reactions take place at the base of the convective envelope, where the hydrogen burns at $T_c \gtrsim 0.07$GK, e.g. during the thermally-pulsing Asymptotic-Giant Branch phase, in the supernovae-Ia explosions and classiv novae (José et al. 1999; Marigo et al. 2003a; José 2012; Marigo et al. 2013; Ventura et al. 2016; Slemer et al. 2017).

The reactions of the Ne-Na cycle are:

$$
\begin{aligned}
^{20}\mathrm{Ne} + \mathrm{p} &\longrightarrow {}^{21}\mathrm{Na} + \gamma \\
^{21}\mathrm{Na} &\longrightarrow {}^{21}\mathrm{Ne} + \beta^{+} + \nu \\
^{21}\mathrm{Ne} + \mathrm{p} &\longrightarrow {}^{22}\mathrm{Na} + \gamma \\
^{22}\mathrm{Na} &\longrightarrow {}^{22} + \beta^{+} + \nu \\
^{22}\mathrm{Ne} + \mathrm{p} &\longrightarrow {}^{23}\mathrm{Na} + \gamma \\
^{22}\mathrm{Na} + \mathrm{p} &\longrightarrow {}^{23}\mathrm{Mg} + \gamma \\
^{23}\mathrm{Mg} &\longrightarrow {}^{23}\mathrm{Na} + \beta^{+} + \nu \\
^{23}\mathrm{Na} + \mathrm{p} &\longrightarrow {}^{20}\mathrm{Ne} + \alpha
\end{aligned}
$$

The slowest reaction if this cycle is the $^{22}Ne(p,\gamma)^{23}Na$, whose reaction rate has been recent measured (Cavanna et al. 2015a; Iliadis 2010; Angulo et al. 1999a), so it determines the amount of product of the cycle. The NeNa cycle is important also for the production of ^{21}Ne, because it is involved in the n-production by the reaction $^{21}Ne(^{4}He,n)^{24}Mg$.

If the temperature at the bottom of the elvelope reaches the values $\sim 4 \cdot 10^{7}$K, the Mg-Al cycle

can ignite in the deepest H-burning zone. This cycle is ignited in massive stars ($M_i \gtrsim 40\,M_\odot$), as well as in the H-burning shells or red giant branch (RGB), asymptotic giant branch (AGB), and red supergiant stars (Straniero et al. (2013)). The reactions that form the Mg-Al cycle are:

$$
\begin{aligned}
^{23}\mathrm{Na} + \mathrm{p} &\longrightarrow {}^{24}\mathrm{Mg} + \gamma \\
^{24}\mathrm{Mg} + \mathrm{p} &\longrightarrow {}^{25}\mathrm{Al} + \gamma \\
^{25}\mathrm{Al} &\longrightarrow {}^{25}\mathrm{Mg} + \beta^+ + \nu \\
^{25}\mathrm{Mg} + \mathrm{p} &\longrightarrow {}^{26}\mathrm{Al} + \gamma \\
^{26}\mathrm{Al} &\longrightarrow {}^{26}\mathrm{Mg} + \beta^+ + \nu \\
^{26}\mathrm{Mg} + \mathrm{p} &\longrightarrow {}^{27}\mathrm{Al} + \gamma \\
^{26}\mathrm{Al} + \mathrm{p} &\longrightarrow {}^{27}\mathrm{Al} + \gamma
\end{aligned}
$$

$$
\begin{aligned}
^{27}Si &\longrightarrow {}^{27}Al + \beta^- + \tilde{\nu} \\
^{27}Al + p &\longrightarrow {}^{28}Si + \gamma \\
^{27}Al + p &\longrightarrow {}^{24}Mg + \alpha
\end{aligned}
$$

Massive stars do not produce a large amount of elements during H-burning. Indeed, massive stars produce one-fifth of the ^{14}N in the Sun, and even less amount of ^{13}C and ^{15}N. Another interesting element is the ^{26}Al, which is produced by proton capture on ^{25}Mg in massive stars during H-burning phase and ejected in the wind during the Wolf Rayet phase when it occurs Heger & Woosley (2002). Meynet et al. (1997) estimates that from the 20% to 70% of the total ^{26}Al existing in the interstellar medium (ISM) could be produced by massive star winds.

Helium burning

The He-burning in massive stars ignites in non degenerate conditions when the central temperature and central density reach the values of 10^8 K and $10^4 \mathrm{gcm}^{-3}$, respectively. During the core He-burning, the H-shell still exists, and the rate at which the H is burn into a shell is about the same as it did during the main sequence. The rate as which the He is burnt in the convective core determines the rate at which the star evolves. The duration of the core He-burning phase is typically the 20%

or 30% with respect to main sequence.

The first nuclear reaction that takes place during the core He-burning is the $3\alpha \rightarrow ^{12}$ C. The energy produced during this phase is 7.275MeV (Heger & Woosley 2002). The 3α reaction progresses through two intermediate steps:

$$\begin{aligned} ^4\mathrm{He} + ^4\mathrm{He} + \gamma &\longleftrightarrow ^8\mathrm{Be} \\ ^8\mathrm{Be} + ^4\mathrm{He} &\longrightarrow ^{12}\mathrm{C}^* \\ ^{12}\mathrm{C}^* &\longrightarrow ^{12}\mathrm{C} + 2\gamma \end{aligned}$$

The term $^{12}C^*$ indicates the isotope ^{12}C at second level of excitation, which decades in three different ways. The first way is the decay in the 3α particles; the second way is the cascade dis-excitation by the reaction $^{12}C^* \rightarrow ^8$ Be $+ ^4$ He with subsequent emission of γ rays; the last way is the direct decay to the fundamental state followed by an emission of $e^+ - e^-$ pair with total angular momentum equal to zero. The preferred channel is the first one, because the reaction $^{12}C^* \rightarrow ^8$ He $+ ^4$ He is esothermic .

Once the star has produced carbon, others α – capture reactions take place:

$$\begin{aligned} ^{12}\mathrm{C} + \alpha &\longrightarrow ^{16}\mathrm{O} + \gamma \\ ^{16}\mathrm{O} + ^4\mathrm{He} &\longrightarrow ^{20}\mathrm{Ne} + \gamma \\ ^{16}\mathrm{O} + ^4\mathrm{He} &\longrightarrow ^{24}\mathrm{Mg} + \gamma \end{aligned}$$

These reactions rates critically affect the chemical composition of He-burning products, and hence for the ejecta. The most efficient reaction is the $^{12}C(\alpha,\gamma)^{16}O$. The $^{16}O(^4He,\gamma)^{20}Ne$ is less rapid then the third reaction $^{20}Ne(^4He,\gamma)^{24}Mg$. This explains the low amount of ^{20}Ne produced during the He-burning.

Other important reactions are represented by the sequence
$^{14}N(\alpha,\gamma)^{18}F(\beta^+\nu)^{18}O$ that taking place before the beginning of core He-burning.

The rates of 3α, $^{14}N(\alpha,\gamma)^{18}F$, and the α – capture reactions (eq. 2.4) are well determined (Caughlan & Fowler 1988; Rolfs & Rodney 1988; Angulo et al. 1999b). This is not true for the reaction rate the of $^{12}C(\alpha,\gamma)^{16}O$, whose difficult measurement (Buchmann 1996; Kunz et al. 2002)

is due to sub-threshold resonances that must be determined indirectly. The reaction $^{12}C(\alpha,\gamma)^{16}O$ is important because it affects not only the ratio of carbon and oxygen at the end of He-burning, but indirectly the nucleosynthesis of many other species and the structure of supernova star.

If the products of the $\alpha-$capture reactions countain also free protons, and if there are traces of ^{20}Ne, the star can experience the Ne-Na cycle, at the base of the convective envelope.

The principal products of helium burning are ^{12}C and ^{16}O. The ratio between these two elements affects both their own nucleosynthesis and the future evolution of the star during the subsequent core nuclear burnings of carbon, neon and oxygen. This ratio is determined by competition between the 3α reaction and $^{12}C(\alpha,\gamma)^{16}O$, as shown in the equation (Heger & Woosley 2002):

$$\frac{Y(^{12}C)}{dt} = Y_{\alpha}^{3}\rho^{2}\lambda_{3\alpha} - Y(^{12}C)Y_{\alpha}\rho\lambda_{\alpha\gamma}(^{12}C) \tag{2.4}$$

The total amount of carbon and oxygen produced in a massive star is also sensitive to the treatment of convective boundary layers and mass loss (Langer et al. 1985). The former instability is removed in recent models by the theory of rotation (Hirschi et al. 2005b; Chieffi & Limongi 2013). Carbon nucleosynthesis from He-core can also be increased by mass loss: Timmes et al. (1995) find that, ignoring mass loss, about 1/3 of solar carbon is made in stars more massive than $8\,M_{\odot}$. The other products of helium nucleosynthesis are ^{18}O, ^{19}F, and $^{21,22}Ne$.

The neutron rich isotope of oxygen, is synthesized by massive stars in the reaction sequence $^{14}N(\alpha,\gamma)^{18}F(e^{+}\nu)^{18}O$ and at high temperature is destroyed by $^{18}O(\alpha,\gamma)^{22}Ne$. These two reactions are very rapid: the consequence is that all the residual ^{14}N synthesized by CNO cycle is transformed in ^{22}Ne. The reaction rate of $^{18}O(\alpha,\gamma)^{22}Ne$ can influence the production of ^{18}O yield (Aubert et al. (1996),Woosley & Weaver (1995)). At $T > 3\cdot10^{8}K$ the ^{22}Ne is processed by the reaction $^{22}Ne(\alpha,\gamma)^{25}Mg$, inducing a proton production, which is important for the synthetization of heavy elements by s-processes.

The production ^{19}F during He-burning in massive stars is determined by the reaction $^{15}N(\alpha,\gamma)^{19}F$, in which ^{15}N comes from $^{18}O(p,\alpha)^{15}N$ (Meynet & Arnould 1993, 2000). However, most of ^{19}F is produced by the neutrino processes taking place during the subsequent stages.

The s-processes are reactions in which the slow neutron capture prevail over the beta-decay lifetime. Analysis of solar abundances shows that there are two kind of s-processes that contribute to the synthesis of elements heavier than iron (Walter et al. 1986b,a; Ward & Newman 1978): the one is characterized by weak neutron irradiation at relatively low temperature, and the other is stronger and hotter. The stronger s-proesses are believed to occur in lower mass stars found on the asymptotic giant branch during a series of He-shell flashes.

The weak s-processes take place in massive stars during the He-burning phase, producing isotopes up to mass number A ~ 88, and contributing to the production of other light elements as ^{36}S,^{37} Cl,^{40} Ar,^{40} K and ^{45}Sc. The s-processes in massive stars have been studied largely in literature (Hoffman et al. 2001; The et al. 2000; Prantzos et al. 1990). The main source of neutrons for s-processes in massive stars is the reaction ^{22}Ne$(\alpha,\mathrm{n})^{25}$Mg that takes place during Ne-Na cycle. The ^{22}Ne comes from two α captures on the ^{14}N, which derives from CNO cycle. The amount of ^{22}Ne scales linearly with star metallicity. The ^{22}Ne$(\alpha,\mathrm{n})^{25}$Mg reaction requires high temperature to start: this is the reason why the s-processes occur mostly at the last stages of core He-burning. The complete consumption of ^{22}Ne occurs only in most massive stars. The ^{22}Ne can be converted also in ^{26}Mg by the reaction ^{22}Ne$(\alpha,\gamma)^{26}$Mg, which does not liberate free neutrons. The rates of these two reactions were object of many measurements (Kaeppeler et al. 1994; Jaeger et al. 2001; Rauscher & Thielemann 2000) determine the strength of the s-processes.

Carbon burning

Once the He available in the core finishes, the core contraction causes an enhancement of central temperature til $6-7\cdot10^8$K, igniting carbon in the core. The principal nuclear reaction of carbon burning is the fusion of two ^{12}C nuclei producing ^{23}Mg* (in which the "*" stands for "exited state"), which decades in different ways:

$$\begin{aligned} {}^{12}\mathrm{C}+{}^{12}\mathrm{C} \longrightarrow \quad {}^{24}\mathrm{Mg}^* \quad &\longrightarrow {}^{23}\mathrm{Mg}+\mathrm{n}-2.62\mathrm{MeV} \\ &\longrightarrow {}^{20}\mathrm{Ne}+\alpha+4.62\mathrm{MeV} \\ &\longrightarrow {}^{23}\mathrm{Na}+\mathrm{p}+2.24\mathrm{MeV} \end{aligned}$$

The probability of decay through proton channel is approximately the same as througth α channel (Caughlan & Fowler (1988)). The production of ^{23}Mg is important because is can decay in ^{23}Na trough ^{23}Mg$(\mathrm{n},\mathrm{p})^{23}$Na changing the neutron excess. The others reactions that increase the neutron excess during carbon burning are ^{20}Ne$(\mathrm{p},\gamma)^{21}$Na$(\mathrm{e}^+\nu)^{21}$Ne and ^{21}Ne$(\mathrm{p},\gamma)^{22}$Na$(\mathrm{e}^+\nu)^{22}$Ne. The principal nuclei produced during this evolutionary phase are ^{16}O,^{20,21,22} Ne,^{23} Na,^{24,25,26} Mg,^{26,27} Al, and a little amount of ^{29,30}Si and ^{31}P (Thielemann & Arnett 1985; Heger & Woosley 2002).

Neon burning

The composition after carbon burning consists mainly on ^{16}O,^{20}Ne and ^{24}Mg. The oxygen nuclei have the smallest coulomb barrier, but the temperature required for the fusion of two atoms of ^{16}O is too high. Therefore, before that the $^{16}\mathrm{O}+^{16}\mathrm{O}$ fusion reaction takes place, the reaction $^{20}\mathrm{Ne}(\gamma,\alpha)^{16}\mathrm{O}$ become efficient, and it is responsible of the neon burning ingition. The α particle produced in this reaction is rapidly captured by ^{16}O through the reaction $^{16}\mathrm{O}(\alpha,\gamma)^{20}\mathrm{Ne}$, restoring ^{20}Ne. Soon the two reactions reach the equilibrium, so that the α particles react with ^{20}Ne, producing ^{24}Mg. The net result of the photo-dissociation is that two ^{20}Ne form one ^{16}O nucleus and one ^{24}Mg. Others important reactions for the nucleosynthesis are:

$$\begin{aligned}
^{24}\mathrm{Mg}+\alpha &\longrightarrow {}^{28}\mathrm{Si}+\gamma \\
^{25}\mathrm{Mg}+\alpha &\longrightarrow {}^{28}\mathrm{Si}+\mathrm{n} \\
^{26}\mathrm{Mg}+\alpha &\longrightarrow {}^{29}\mathrm{Si}+\mathrm{n} \\
^{26}\mathrm{Mg}+\alpha &\longrightarrow {}^{30}\mathrm{Si}+\gamma
\end{aligned}$$

The main products of neon burning are ^{16}O,^{24}Mg and ^{28}Si with traces of ^{25}Mg,^{26}Mg,^{26,27}Al,^{29,30}Si,^{31}P and ^{32}S (Woosley & Weaver 1995; Heger & Woosley 2002).

Oxygen burning

When the central temperature after neon burning reaches the value of $2\cdot10^9$K, oxygen fusion is favoured over its photo-disintegration. The oxygen fusion reaction in hydrostatic equilibrium produces compound nuclear states of ^{32}S that has four different decay channels:

$$\begin{aligned}
^{16}\mathrm{O}+^{16}\mathrm{O} \longrightarrow {}^{32}\mathrm{S}^{*} &\longrightarrow {}^{31}\mathrm{S}+\mathrm{n}+1.45\mathrm{MeV} \\
&\longrightarrow {}^{31}\mathrm{P}+\mathrm{p}+7.68\mathrm{MeV} \\
&\longrightarrow {}^{30}\mathrm{P}+\mathrm{d}-2.41\mathrm{MeV} \\
&\longrightarrow {}^{28}\mathrm{Si}+\alpha+9.59\mathrm{MeV}
\end{aligned}$$

These reactions produce protons and α particles that are captured by other isotopes, forming nuclei with mass number $25 \le \mathrm{A} \le 32$, which include mostly ^{28}S,^{32,33,34}S,^{35,37}Cl,^{36,38}Ar,^{39,41}K

with traces of ^{40,42}Ca (Heger & Woosley 2002). When the central temperature reaches the values of $T \sim 2-3 \cdot 10^9$K, the oxygen photodisintegration and fusion reactions can occur at comparable rates. The nuclei heavier than nickel, which had undergone substantial s processing during neon, carbon and helium burning, now are destroyed by photodisintegration reactions producing the iron group elements.

Other important reactions taking place during core O-burning are the weak interactions experienced by the isotopes ^{30}P,^{30} S,^{33} S,^{33} P,^{35} Cl,^{35} S,^{37} Ar,^{37} CL, which are responsible of the neutron excess. When the oxygen available in the core runs out, oxygen can burn in shell at higher temperature and lower density. Under these conditions less electron captures occur. As a result the nucleosynthesis outside the core retains a memory of initial neutron excess.

Another interesting phenomenon that occurs during O-burning is the formation of a number of *quasi-equilibrium clusters*, which are groups of nuclei coupled by strong and electromagnetic reactions. These reactions are nearly balanced by their inverses (Heger & Woosley 2002). When the temperature rises, more nuclei join this groups and the smaller groups merge in larger ones. At the time when silicon burning ignites, there are two large clusters of isotopes: one with mass number in the range between ~ 24 and ~ 46, and the other is composed by the iron group elements. After a little quantity of silicon burns in the core these two groups merge into one (Woosley et al. 1973).

Silicon burning

Unlike carbon and oxygen burning, the silicon burning does not occur predominantly as a fusion reaction. We expected that the fusion reaction after the Si-burning involves two atoms of ^{24}Mg, because the product of the nuclear number of the reagents (Z_1Z_2) is minimum. Despite this fact, the coulomb barrier is so high that this reaction requires too high temperature and it is anticipated by the photo-disintegration of the main nuclei with consequent production of free protons, nucleons and α particles. A portion of ^{28}Si is processed by the sequence of photo-disintegration reactions $^{28}\mathrm{Si}(\gamma,\alpha)^{24}\mathrm{Mg}(\gamma,\alpha)^{20}\mathrm{Ne}(\gamma,\alpha)^{16}\mathrm{O}(\gamma,\alpha)^{12}\mathrm{C}(\gamma,2\alpha)\alpha$ (Heger & Woosley 2002). Other reaction chains maintain the equilibrium between α particles and free nucleons. The α particles and their associated nucleons released by these reactions add onto the big quasi-equilibrium group above ^{28}Si, increasing its mean atomic weight. In this way, most of the material is concentrate in bound species within the iron group. The consequence is that the silicon abundance becomes small.

In massive stars, the fuel of core silicon burning consists of a mixture of ^{28,29,30}Si in comparable amounts (the presence of this mixture can be explaied by a substantial electron capture

occurred). The consequence of this is that the burning is not governed by ^{28}Si and ^{24}Mg photo-disintegration, but also by (p,α) and (n,α) reactions on ^{25}Mg and ^{26}Mg. Moreover, the main product is not ^{56}Ni, but ^{54}Fe or ^{56}Fe.

The composition after silicon burning is governed by tightly bound iron-group nuclei allowed at given temperature, density and neutron excess. In the case of explosive Si-burning, the products depend on how much silicon was burned in the explosion and agrees with solar abundances only for the neutron excess $\eta \lesssim 0.006$, which permits the production of ^{48,49}Ti,^{51}V,^{50,52,53}Cr,^{55}Mn,^{54,56,57}Fe and traces of ^{28}Si,^{32}S,^{36}Ar and ^{40}Ca. Once the iron group elements have been produced, the fusion reactions stop, because heavier nuclei have a lower binding energy, and the reactions become endothermic. Once the iron has been synthesized in the core, the star exhausts the source of thermonuclear energy and begin to collapse. The final fate of stars it is discussed in detail in chapter 4. The elements heavier then iron can be produced during the core-collapse by r-processes.

2.1.7 Explosive nucleosynthesis

When the abundance of ^{28}Si becomes very small at the end of silicon burning, the non-equilibrated reactions that link Mg to Ne, C to O, and C with α-particles finally become balanced by their inverses. Thus, the abundances are given by a Saha equations for nucleons (see Heger & Woosley (2002) for details).
The Saha equation has the property of favouring, for temperature lower than 10^{10}K, the most tightly bound nuclei of the given neutron excess η. If there is a neutron-proton equality in the stellar composition, the favourite species is ^{56}Ni, which is important both nucleosynthesis and the light curves of supernovae. For neutron excess $\eta \sim 0.07$, which is more characteristic of the matter near the valley of β-stability, the most tightly bound nucleus is ^{56}Fe, and for composition containing still greater neutron-to-proton ratios, the equilibrium shifts to heavier isotopes (Heger & Woosley 2002) (e.g ^{62}Ni).
At temperature higher than 10^{10} K, the binding energy decreases with respect to the phase space and partition function of three α-particles and nucleons. This fact favours the formation of lighter particles.

Summarising, the nuclear statistical equilibrium condition favours the formation of Fe nuclei at lower temperature, while it requires the break-down into α-particles, protons and neutrons at higher temperature.

This photo-disintegration is of great importance for two reasons: it triggers the collapse of the iron core of the massive stars, and it causes energy losses of the shock wave generated by the core bounce. This photodisintegration does not end during the collapse of the iron core. Indeed, as

explained first in Bethe et al. (1979), the reservoir of energy in exited stated coupled with the large partition function assigned to those states allows the discrete bound nuclei to persists and remain relatively cool until the core has collapsed to nuclear density.

Silicon explosive burning

The explosive nucleosynthesis of silicon take place in the internal areas where the temperature reach the value $4-5\cdot10^9$K. Depending on the temperature and density of the shock, there are three different explosion ways:

- If the temperature is higher than $5\cdot10^9$K the star experiences the complete Si-burning, producing the iron group elements. The most abundant product is the ^{56}Ni, which decades in ^{56}Co and ^{56}Fe. The ^{56}Ni decay is responsable of the light curve of type II supernovae.
- If the temperature is sufficiently high to permitt the complete Si-burning but the density is too low, the 3α-chain can not maintain the statistical equilibrium with other nuclei during the rapid expansion and cooling, generating the so called *α-rich freeze out*. This phenomenon enhances the He abundances to levels higher than those predicted by nuclear statistical equilibrium.
- At temperature of 4-5$\cdot10^9$K the nuclear burning is incomplete; the chemical composition of the core consists mainly of ^{28}Si,^{32}S,^{40}Ca and a small amount of ^{56}Ni.

Oxygen explosive burning

If the central temperature at the beginning of core O-burning is higher than $3.3\cdot10^9$K, the O-burning products nuclei in quasi-statitical equilibrium with mass number $28 < A < 45$. These newly synthesized elements do not reach the statistical equilibrium with iron group elements. The main products of the explosive O-burning are ^{28}Si,^{32}S,^{40}Ca and trace of ^{56}Ni where the temperature reaches $4\cdot10^9$K.

Neon and carbon explosive burning

The explosive neon burning takes place if the temperature at the ignition of Neon in the core is higher than $2.1\cdot10^9$K. The main reactions are $^{20}\mathrm{Ne}(\gamma,\alpha)^{16}\mathrm{O}$ and the chain $^{20}\mathrm{Ne}(\alpha,\gamma)^{24}\mathrm{Mg}(\alpha,\gamma)^{28}\mathrm{Si}$, which product ^{16}O,^{24}Mg,^{28}Si.

At these temperature the only reactions that take place are those that burn the carbon in degenerate conditions, which products ^{20}Ne,^{23}Na and ^{24,25,26}Mg.

2.1.8 Core collapse supernova explosion

Nuclear fusion can not continue after the formation of iron core because of the high binding energy of iron nuclei, and the iron core continues to contract. The gravitaional energy released during the dynamical collapse of the core generates an intense neutrino flux. The neutrinos interact with the sourrounding matter generating a bounce and strong shock, which can produce the explosion known as core collapse cupernova. The gravitational collapse of the core stops when the core density reaches the values of $\rho_c = 10^{14} - 10^{15} \mathrm{gcm}^{-3}$, leaving a neutron star or a black hole.

Massive stars contribute about a 75% of the total number of all esploding supernovae. The other 25% is represented principally by white dwarf in binary system, which explode as SN Ia (Smartt 2009; Arcavi et al. 2010; Li et al. 2011; Smith et al. 2011; Mackey et al. 2003). A large fraction of faint core-collapse supernovae are invisible because of strong selection effect and limited observational capabilities (Mannucci et al. 2007; Botticella et al. 2008; Young et al. 2008; Mattila et al. 2012; Gal-Yam et al. 2013).

The explosion mechanism is largely discussed in literature. Great success has been achieved recently for low and intermediate energy explosion driven by neutrino transport (Bruenn et al. 2009; Kuroda et al. 2012; Müller et al. 2012; Bruenn et al. 2013; Frayer & Taylor 2012; Janka 2012). The explosion models available in literature are one, two or three dimensional. There is discrepancy between two and three dimensional CCSN simulation (Dolence et al. 2013).

The one-dimensional models parametrize the explosion with parameters as explosion energy and mass cut (Umeda & Nomoto 2002; Woosley & Weaver 1995). More recent methods are provided by Frayer & Taylor (2012), whose model links the mass of the C-O core at the end of core he-burning to the mass of the remnant. Another one-dimensional model is provided by Ertl et al. (2016), who uses two parameters to predict the explodability of the stars and to derive the remnant mass after the explosion event. We will describe in detail the last two models in sections 4.0.1 and 4.0.1, in which we explain how we used these models to derive the remnant masses from PARSEC tracks.

Light curve in core collapse supernovae

After the bounce of the collapsing core and strong neutrino interaction, a shock wave in generated in the silicon burning shell, generating the supernova explosion event. A large fraction of explosion energy is converted into kinetic and thermal energy of the shock. It takes from hours to days for the shock to get to the surface of the star, depending on the radius of progenitor. This time is

expressed by the equation:

$$t_{shock} = \frac{R_{pre-SN}}{v_s} \tag{2.5}$$

where v_s is the sound velocity and R_{pre-SN} is the radius of the progenitor. When the shock wave reaches the surface of the star, the temperature of the shock increases until billion of Kelvin, so it can be seen as a short X-ray/UV flash. This phenomenon is called *shock breakout*. The duration of the flash depends on the radius of the progenitor:

$$\Delta t_{shock} = \frac{R_{pre-SN}}{c} \tag{2.6}$$

where c is the speed of light.

Since the envelpe matter is optically thick, the opacity is dominated by electron scattering. The shock wave propagates into the envelope leaving into the matter a fraction of its thermal and kinetic energy.

During the first days after the explosion event the radius of progenitor increases, and the envelope expands adiabatically and cools. This causes the electron recombination and the formation of cooling wave, which propagates inwards through the envelope with a velocity exeding the sound speed. The photosphere, following the recombination and the cooling wave, propagates through the various chemical layers. Consequently, the radiation coming from the chemical layers that are crossed by the photospere generates the light curve.

The characteristics of light curve can be summarised in some main factors:

- *Photospheric phase*, which is related to the time when the light curve traces the front of photosphere, and it takes place after the shock breakout.
- *Plateau phase*. The shock-deposited energy is released and the luminosity remains constant. This phase is of the order of one hundred of days for stars with H-rich extended envelope. The light curve of H-rich compact stars and for those stars without H-envelope is characterised by prominent maximum but no plateau.
- *Re-brightening*. When the moving inward photosphere encounters the high energy photons synthesized during the $^{56}\mathrm{Ni} \rightarrow ^{56}\mathrm{Co} + \gamma$ decay, the luminosity increases, causing the re-brightening effect.

At later time the envelope becomes transparent and then the light curve follows the instant deposition of energy produced in the radioactive decay of nickel in cobalt.

The core collapse supernovae are divided in different classes by different observational properties.

- Tipe II Plateau (SN IIP). The progenitors of these explosions are stars with initial mass in the range between 7-8 $M_\odot$ and 20 $M_\odot$, H-rich envelope and stellar radius that exceeds several hundreds the solar radii. These supernovae are characterised by the plateau phase, during which the luminosity remains constant. The duration of the plateau phase depends on the radius of progenitor, the explosion energy and the ejected mass.

- Type II peculiar (SN II-pec). In this case the envelope of the progenitors is H-rich but it is more compact respect to the progenitors of SNe IIP. The classical example is the SN 1987A, which is characterised by a prominent bump-like curve.

- Type IIn (SN IIn). The letter "n" stands for "narrow lines", which are due to the supernova explosion in a dense medium. The interaction between the ejected material and the surrounding material slows down: consequently the chemical ejecta produce narrow emission lines observed in the supernova spectrum. The progenitors are stars characterised by H-rich envelope, as in the first case.

- Type II lineas (SN IIL). The progenitors of these supernovae are stars with no more than 1-2 $M_\odot$ of hydrogen in the envelope, and very high radius before the explosion. It is supposed that the envelope of these stars just before the explosion is characterized by a thin layer, which produces the SN IIL. The light curve is characterised by a linear decayed luminosity after the peak value.

- Type IIb (SN IIb). The progenitors of these supernovae has lost almost the entire hydrogen envelope before the explosion event. Consequently, the hydrogen lines appear in the spectrum only before the maximum.

- Type Ib or Ic (SN Ib/Ic). In this case the envelope of progenitors is completely absent. The spectrum of these supernovae does not exhibit hydrogen lines, but has strong helium lines. The SN Ic are those with helium lines-deficient spectrum. The explosion of SN Ib/Ic can originated from the helium core of massive stars or, most probably, from a companion of binary system that transferred its mass via Roche lobe overflow to the second star.

2.2 Very massive stars

Depending on the nuclear processes that take place in the stars during the pre-supernova evolution, massive stars can experience a different kind of supernova explosions. In this section we will describe the explosion mechanism that can be experienced by VMOs.

The pre-SN evolution of VMOs goes through the hydrostatic hydrogen, helium, carbon and neon core burning. After the carbon exhaustion and neon burning phase, these stars undergo a thermonuclear explosion due to dynamical instability generated by the creation of electron-positron pairs in their oxygen cores.

Following the criterion of Heger & Woosley (2002); Nomoto et al. (2013), we classify as VMOs all stars that develop an helium core more massive than $40\,M_\odot$. The initial mass ranges from 80-100 $M_\odot$ to 200-250 $M_\odot$, depending on initial chemical composition. Since the VMOs can experience high mass loss episodes during the pre-SN evolution, the initial mass interval is strongly dependent on initial metallicity. The VMOs are the progenitors of two different types of explosions: the *pulsation-pair instability SNe* (PPISNe), and the *pair instability SNe* (PISNe).

Stars that develop a helium core in the range between $\sim 40\,M_\odot$ to $\sim 133\,M_\odot$ lie in the domain of pair instability supernovae. This objects have initial mass between $100\,M_\odot \lesssim M_i \lesssim 260\,M_\odot$. Since the minimum value of M_i depends on the metallicity of the star, we define M_{VMO} as the lower limit of the M_i interval for the VMO regime. After the core He-burning, the central entropy and temperature of the star increase enough to lead to $e^+ - e^-$ pair creation. The creation of these particles drives the adiabatic index below 4/3, causing the runaway collapse. The collapse can be halted when the oxygen ignites in the core (because of the energy release by very temperature-dependent nuclear reactions). In some cases the energy released by nuclear reactions is more than necessary for an elastic bounce, reversing the collapse in explosion of the star. The depth and the temperature of bounce increase with the mass of $He-$core, therefore pair instability supernovae can be divided into three subgroups.

Stars that develop a helium core between $\sim 40\,M_\odot$ and $\sim 65\,M_\odot$ ($100\,M_\odot \lesssim M_i \lesssim 140\,M_\odot$), resolve the adiabatic instability with violent mass-ejection pulsations, without complete disruption (Heger & Woosley 2002). These stars are the pulsation instability supernovae (PPISN). The PPISN may end their life producing an iron core (Woosley 1986). Explosion energy is typically of 10^{51} erg, higher than normal CCSN, but the lack of ^{56}Ni ejected produce less bright light curves. Therefore these stars are also considered as faint core-collapse supernovae (Heger & Woosley 2002).

Stars with helium core in the range between $\sim 65\,M_\odot$ and $\sim 133\,M_\odot$ ($140\,M_\odot \lesssim M_i \lesssim 260\,M_\odot$) experience a violent pair instability, which causes the complete disruption of the star after the bounce (Ober et al. 1983; Heger & Woosley 2002). The explosion energy is of the order of $10^{52} - 10^{53}$ erg and the ejected ^{56}Ni could reach $50\,M_\odot$ (Heger & Woosley 2002). The pair instability mechanism for supernova explosion was discussed diffusely in literature (Fowler & Hoyle 1964; Bisnovatyi-Kogan & Kazhdan 1967; Rakavy & Shaviv 1967a; Fraley 1968; Zel'dovich & Novikov 1971). These stars are considered as members of first generation of stars at low metallic-

ity. Furthermore, recent stellar models suggest that pair-instability supernovae could occur also for stars at initial metallicity $Z_{\odot}/3$, which implies that it is possible to observe PISNe in local universe (Kozyreva et al. 2014b).

Finally, if the star is massive enough to develop a helium core greater than $133M_{\odot}$ ($M_i \gtrsim 260\,M_{\odot}$)the amount of mass is too high to lead to escaping of material, so it causes a direct collapse into black hole, without producing ejecta (Fryer & Kalogera 2001; Heger & Woosley 2002; Nomoto et al. 2013).

2.2.1 The pair-instability explosion mechanism

The high mass stars are characterised by lower central density (ρ_c) for a given central temperature (T_c), following the relation (Kippenhahn et al. 2012):

$$T_c \sim M^k \rho_c^{1/3} \tag{2.7}$$

where the term k depends on the equation of state (EoS). k is equal to $1/6$ for radiation dominated pressure, and equal to $1/3$ for gas dominated pressure Kippenhahn et al. (2012). Note that for dominant ideal gas pressure, the density-temperature equation depends also on molecular weight:

$$\rho_c = \frac{T_c^3}{\mu_c M^{3k}} \tag{2.8}$$

where μ_c is the molecular weight in the centre of the star.

Figure 2.3 shows the evolutionary tracks of the central density and temperature. Both quantities increase rapidly during the dynamical contraction of the core induced by the pair instability. The latest pre-SN evolution of very massive stars is characterised by core C-burning and central temperature $T_c \sim 10^9$K. During this phase, the photons are distributed according to Plank's law, but a fraction of the photons in the high energy tail exceed the rest mass energy for the electrons (which is ~ 511KeV), leading the production of electron-positron pairs via the reaction $2\gamma \leftrightarrow e^+e^-$. The transition between photons and matter causes a drop in the radiation pressure that compensate the gravitational force, and breaks the hydrostatic equilibrium. The dominant radiation pressure and the emerging relativistic electrons reduce the resistance of the matter to the gravitational force. The adiabatic index γ_{AD} drops below 4/3 and the system evolves with the collapse of the core. The collapse of the oxygen core occurs only if a large fraction of core enters in the instability region with $\gamma_{AD} < 4/3$ (at least 40% in mass of the star). The minimum O-core necessary for massive stars to enter in the instability is $\sim 30\,M_{\odot}$. The corresponding initial mass depends on the initial

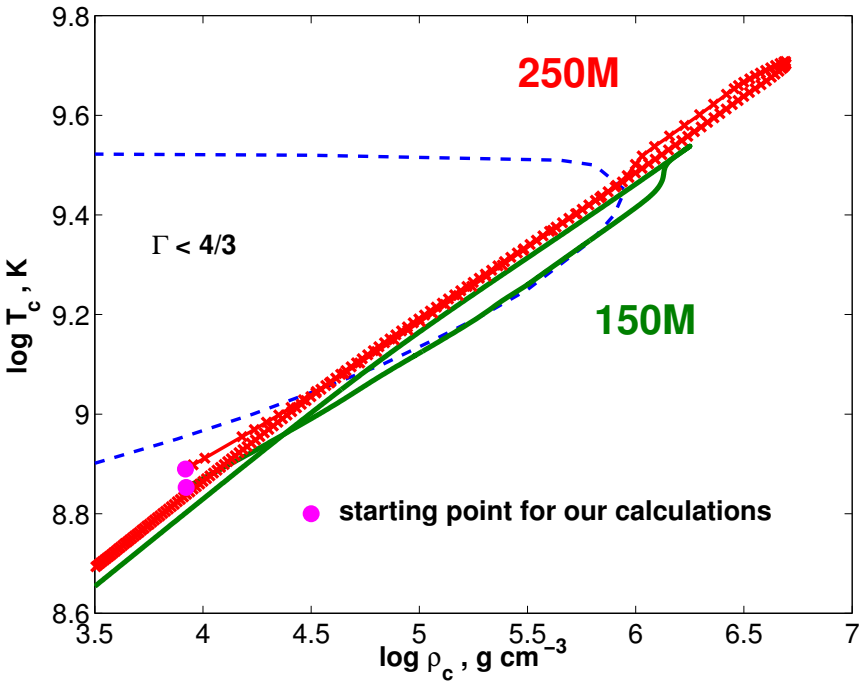

Figure 2.3: Evolutionary tracks of $150\,M_\odot$ and $150\,M_\odot$ modesl in central density-temperature diagra.The area enclosed by the dashed line indicates the pair-instability regime where $\Gamma < 4/3$. The filled circles mark the starting points for each model sequence. The figure is taken from Kozyreva et al. (2014b).

chemical composition of the stars and the mass loss episodes experienced during the evolution.

When the O-core starts to collapse, the central temperature increases till $T > 2 \cdot 10^9$K. The result is the ignition of explosive O-burning in the core. If the remaining stellar mass is sufficiently high, the star undergoes a second pair creation episode. During each eruption the star loses mass, so that finally it cannot undergo the pair instability anymore and collapses to a black hole. This final fate is the PPISN. The progenitors of PPISNe develop an He-core contained in the range $40\,M_\odot - 65\,M\odot$, which corresponds to stars with initial mass $100\,M_\odot \lesssim M_i \lesssim 140\,M_{odot}$. The limits of this range depend on initial metallicity.

If the M_{He} is higher than $65\,M_\odot$ (Heger & Woosley 2002) the energy generated during the explosive oxygen burning and Si-burning is sufficient to hold the collapse and reverse it to an explosion, which is so violent that all the pre-SN mass is ejected in the interstellar medium and there is no remnant left behind. This thermonuclear explosion is the PISN.

During the pair instability explosion event tens of solar masses of heavy elements are produced. The mass expelled reflects the chemical structure of these stars, which is showed in figure 2.4.

The pair instability ejected mass consists of about $30-40\,M_\odot$ of H, $50-60\,M_\odot$ of He, $2\,M_\odot$ of C, $40-50\,M_\odot$ of O, $10-15\,M_\odot$ of Si and up to $55\,M_\odot$ of Ni (Umeda & Nomoto 2002; Heger & Woosley 2002; Kozyreva et al. 2014b). Note that for normal CCSNe the maximum amount of ^{56}Ni mass is about $0.5\,M_\odot$ (Woosley & Weaver 1995; Chieffi & Limongi 2004).

The radioactive ^{56}Ni affects the SN light curve and governs the late time luminosity. The high mass of radioactive Ni expelled after pair instability explosion produce the so called *super-luminous supernovae* (SLSNe), which are characterized by a peak of luminosity of $M_v < -21$mag $L > 10^{44}$erg/s, 2 or 3 magnitudes lower than normal CCSNe.

2.2.2 Direct collapse to Black-hole

The stars that develop a He-core more massive than $133\,M_\odot$ start the main sequence with initial mass $M_i \gtrsim 260\,M_\odot$ (Heger & Woosley 2002). The inclusion of rotationally induced chemical mixing in stellar models can change the threshold value of He-core mass, because the chemical mixing lead to an increase of the He-core (Heger et al. 2000a; Hirschi et al. 2004; Yoon & Langer 2005).

All the energy generated by the oxygen and silicon explosion burnings is equal to the binding energy of the star (Bond et al. 1984), leading the collapse of the core after the pair instability phase.

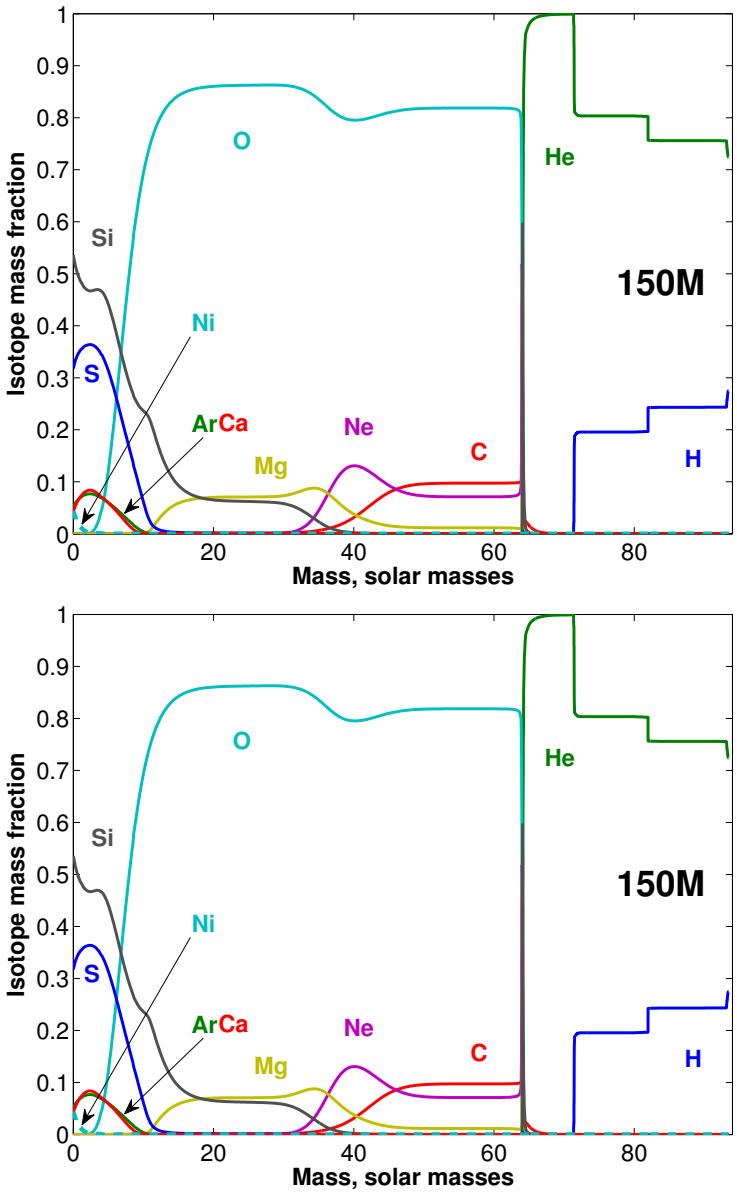

Figure 2.4: Final chemical structure of two models with initial mass of $150\,M_{\odot}$ (upper panel) and $250\,M_{\odot}$ (lower panel). The two plots are taken from Kozyreva et al. (2014b).

Chapter 3

PARSEC evolution models for massive stars

This chapter describes the main characteristics of PARSEC (**PA**dova & **TR**ieste **S**tellar **E**volution **C**ode, e.g. the main input parameters, the initial mass range and initial chemical composition used in this work.

In this work we used the new massive tracks computed with PARSEC (Bressan et al. 2012; Tang et al. 2014; Chen et al. 2015),for a wide range of initial mass and metallicities. The initial masses ranges from $8\,M_{\odot}$ to $350\,M_{\odot}$, and the initial metallicity considered is from Z=0.0001 to Z=0.02. The stellar evolution begins from the pre-main sequence to the end of core He-burning.

3.1 Basic input physics

the input physics used in PARSEC is described in detailed in Bressan et al. (2012); Tang et al. (2014) and Chen et al. (2015). We briefly summarize the main points with particular attention to more relevant to the massive stars. The *PARSEC* code computes stellar tracks from pre-main sequence to the beginning of central carbon burning, with initial mass ranging from low masses ($M = 0.1\,M_{\odot}$) to $350\,M_{\odot}$. The initial metallicities considered are scaled solar and range from $Z = 1 \cdot 10^{-4}$ to $Z = 0.02$. In this work we considered only the stars with initial mass greater than $M_{mas} \sim 8\,M_{\odot}$, which are represented in figure 3.1.

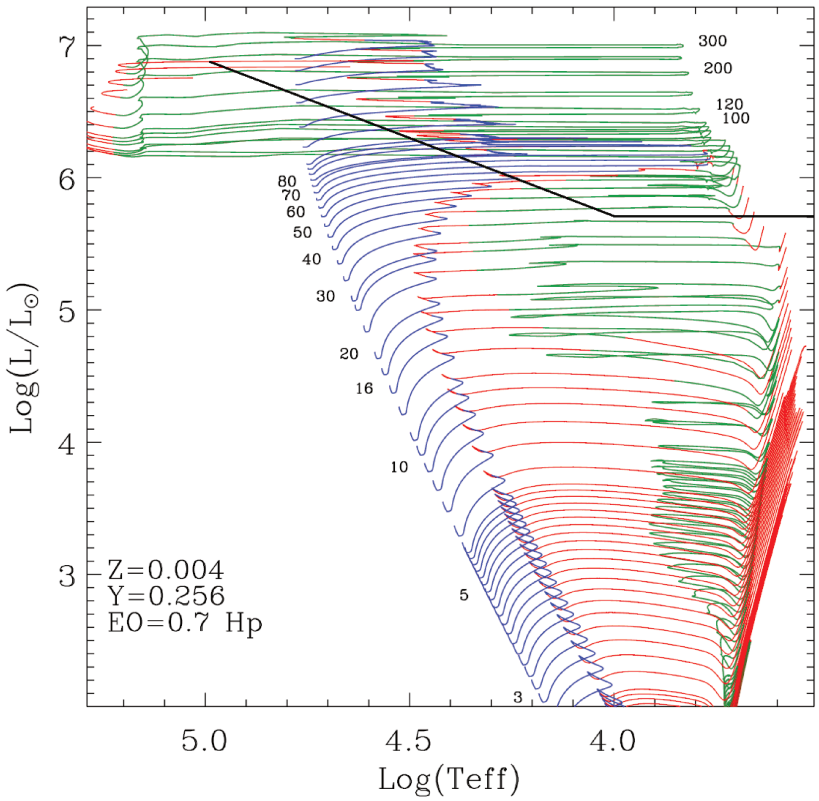

Figure 3.1: Example of HR diagram for massive stars tracks taken from PARSEC code.

3.1.1 The solar distribution of heavy elements

The solar distribution of heavy elements adopted in PARSEC. For each element heavier than ^{4}He its fractional abundances relative to the total solar metallicity is adopted.

The reference solar distribution of metals consists of 90 chemical elements from Li to U, with abundances taken from Grevesse & Sauval (1998), except for a subset of species for which the revision of Caffau et al. (2011) is adopted. According to this abundance compilation, the Sun's metallicity used is $Z_\odot = 0.01524$.The solar abundances for the main elements are listed in table 3.1

3.1.2 Opacities

The absorption properties of matter in the gas phase are described by means of pre-computed, static tables of Rosseland mean opacities, $k_R(\rho, T)$.

Table 3.1: Solar abundances of a few elements adopted in this work, following the values recommended by Caffau et al. (2011) and references therein. Abundances are expressed with the standard notation $A(Y) = \log(n_Y/n_H) + 12$. For all other species we adopt the compilation of Grevesse & Sauval (1998).

Element	Abundance $A(Y)$	Reference
Li	1.03	Caffau et al. (2011)
C	8.50	Caffau et al. (2010)
N	7.86	Caffau et al. (2009)
O	8.76	Caffau et al. (2008b)
P	5.46	Caffau et al. (2007)
S	7.16	Caffau & Ludwig (2007)
K	5.11	Caffau et al. (2011)
Fe	7.52	Caffau et al. (2011)
Eu	0.52	Mucciarelli et al. (2008)
Hf	0.87	Caffau et al. (2008a)
Os	1.36	Caffau et al. (2011)
Th	0.08	Caffau et al. (2008a)

The temperature T and density ρ depend on the chemical composition of the gas, which is commonly specified by the total metallicity (Z), the hydrogen abundance (X), and the distributions X_i/Z of the heavy elements in the mixture. The latter depends on the specific case considered, e.g scaled-sola mixture with $X_i/Z = X_{i,\odot}/Z_\odot$, or others X_i/Z derived from various constraints such as the enhancement/depletion of α-elements, or the over-abundances in primary C and O necessary to describe the He-burning regions.

In the high-temperature regime ($4.2 \leq \log(T/K) \leq 8.7$), the opacity tables provided by (Iglesias & Rogers 1996, OPAL tables) are adopted. In low temperature regime ($3.2 \leq \log(T/K) \leq 4.1$ the `AESOPUS` tool of Marigo & Aringer (2009) is used to generate opacity tables for any specified set of chemical abundances of 92 elements from H to U.

In the interval $4.0 < \log(T/K) < 4.1$ a linear interpolation between the opacities derived from the `OPAL` and `AESOPUS` is adopted.

Conductive opacities are included following Itoh et al. (2008). In the computation, for any specified chemical mixture, the total thermal conductivity accounts for the contribution of 11 atomic species (^{1}H,^{4}He,^{12}C, ^{16}O, ^{20}Ne,^{24}Mg, ^{28}Si), ^{32}S, ^{40}Ca and ^{56}Fe), each weighted by the corresponding abundance (by number).

Given the total reference metallicity Z and the distribution of heavy elements X_i/Z, two sets of opacity tables are constructed, namely the "H-rich" and "H-free". The former set comprises N_X opacity tables, where N_X is the number of hydrogen abundance values, which range from X=0 to X=1-Z. The latter set is characterized by X=0, while the helium content assumes N_Y values,

ranging from Y=0 to Y=1-Z.

3.1.3 Equation of state

The equation of state (EOS) is computed with FreeEOS core developed and updated over a years by A.W. Irwind, and freely available under GPL licence [1]. The FreeEOS package is fully implemented in PARSEC. The EOS calculation is performed accounting for the contributions of several elements, namely: H,He,C, N, O, Ne,Na Mg, Al, Si, P, S, Cl, Ar, Ca, Ti, Cr, Mn, Fe, Ni. For any specified distribution of heavy elements, several values of metallicity Z have been considered, and, for each value of Z, the tables with all thermodynamic quantities have been pre-computed over a suitably wide ranges of temperature and pressure (e.g. mass density, mean molecular weight, entropy, specific heats and their derivatives, etc.). Exactly in the same fashion as for the opacity, a "H-rich" and a "H-free" set of tables are used.

3.1.4 Nuclear reaction rates

The nuclear reaction network included in PARSEC consists of p-p chains, the CNO tri-cycle, the Ne-Na and Mg-Al chains,and the most important α-reactions, including the $\alpha-$n reactions. The network solves for the abundances of 26 chemical species: H, D, ^{3}He, ^{4}He, ^{7}Li, ^{7}Be, ^{12,13}C,^{14,15}N, ^{16,17,18}O, ^{19}F, ^{20,21,22}Ne,^{23}Na ^{24,25,26}Mg, ^{26m,26g,27}Al, ^{28}Si. The latter nucleus act as the "exit element", which ends the network. The total number of reaction rate considered is 42. The reaction rates and the corresponding Q-values are taken form JINA recommended database (Cyburt et al. (2010)), and electron screening factors are from Dewitt et al. (1973) and Graboske et al. (1973). The complete set of nuclear reactions and the relative reaction rate adopted in PARSEC are showed in table 2. The reference solar abundances used are those provided by Caffau et al. (2011), with the current solar metallicity Z = 0.01524.

Energy losses by electron neutrinos are taken from Munakata et al. (1985) and Itoh & Kohyama (1983), while for plasma neutrinos the fitting relations formulas of Haft et al. (1994) are adopted.

3.2 Convection, overshooting and mixing

The mixing length-theory is described according to Böhm-Vitense (1958a) with mixing-length parameter $\alpha_{\rm MLT}$ = 1.74. The Schwarzschild criterion is adopted to test the stability of radiative zones against convection. In presence of a gradient. Where a gradient of chemical composition is

[1] http://freeeos.sourceforge.net/

Table 3.2: Nuclear reaction rates adopted in PARSEC (Bressan et al. 2012).

Reaction	Reference
$p(p,\beta^+\nu)D$	Cyburt et al. (2010)
$p(D,\gamma)^3He$	Descouvemont et al. (2004)
$^3He(^3He,\gamma)2p+^4He$	Angulo et al. (1999a)
$^4He(^3He,\gamma)^7Be$	Descouvemont et al. (2004)
$^7Be(e^-,\gamma)^7Li$	Caughlan & Fowler (1988)
$^7Li(p,\gamma)^4He+^4He$	Descouvemont et al. (2004)
$^7Be(p,\gamma)^8B$	Angulo et al. (1999a)
$^{12}C(p,\gamma)^{13}N$	Angulo et al. (1999a)
$^{13}C(p,\gamma)^{14}N$	Angulo et al. (1999a)
$^{14}N(p,\gamma)^{15}O$	Imbriani et al. (2005)
$^{15}N(p,\gamma)^4He+^{12}C$	Angulo et al. (1999a)
$^{15}N(p,\gamma)^{16}O$	Angulo et al. (1999a)
$^{16}O(p,\gamma)^{17}F$	Angulo et al. (1999a)
$^{17}O(p,\gamma)^4He+^{14}N$	Chafa et al. (2007)
$^{17}O(p,\gamma)^{18}F$	Chafa et al. (2007)
$^{18}O(p,\gamma)^4He+^{15}N$	Angulo et al. (1999a)
$^{18}O(p,\gamma)^{19}F$	Angulo et al. (1999a)
$^{19}F(p,\gamma)^4He+^{16}O$	Angulo et al. (1999a)
$^{19}F(p,\gamma)^{20}Ne$	Angulo et al. (1999a)
$^{20}Ne(p,\gamma)^{21}Na$	Angulo et al. (1999a)
$^{21}Ne(p,\gamma)^{22}Na$	Iliadis et al. (2001)
$^{22}Ne(p,\gamma)^{23}Na$	Hale et al. (2002)
$^{23}Na(p,\gamma)^4He+^{20}Ne$	Hale et al. (2004)
$^{23}Na(p,\gamma)^{24}Mg$	Hale et al. (2004)
$^{24}Mg(p,\gamma)^{25}Al$	Iliadis et al. (2001)
$^{25}Mg(p,\gamma)^{26}Al^g$	Iliadis et al. (2001)
$^{25}Mg(p,\gamma)^{26}Al^m$	Iliadis et al. (2001)
$^{26}Mg(p,\gamma)^{27}Al$	Iliadis et al. (2001)
$^{26}Al^g(p,\gamma)^{27}Si$	Iliadis et al. (2001)
$^{27}Al(p,\gamma)^4He+^{24}Mg$	Iliadis et al. (2001)
$^{27}Al(p,\gamma)^{28}Si$	Iliadis et al. (2001)
$^4He(2^4He,\gamma)^{12}C$	Fynbo et al. (2005)
$^{12}C(^4He,\gamma)^{16}O$	Buchmann (1996)
$^{14}N(^4He,\gamma)^{18}F$	Görres et al. (2000)
$^{15}N(^4He,\gamma)^{19}F$	Wilmes et al. (2002)
$^{16}O(^4He,\gamma)^{20}Ne$	Angulo et al. (1999a)
$^{18}O(^4He,\gamma)^{22}Ne$	Dababneh et al. (2003)
$^{20}Ne(^4He,\gamma)^{24}Mg$	Angulo et al. (1999a)
$^{22}Ne(^4He,\gamma)^{26}Mg$	Angulo et al. (1999a)
$^{24}Mg(^4He,\gamma)^{28}Si$	Caughlan & Fowler (1988)
$^{13}C(^4He,n)^{16}O$	Angulo et al. (1999a)
$^{17}O(^4He,n)^{20}Ne$	Angulo et al. (1999a)
$^{18}O(^4He,n)^{21}Ne$	Angulo et al. (1999a)
$^{21}Ne(^4He,n)^{24}Mg$	Angulo et al. (1999a)
$^{22}Ne(^4He,n)^{25}Mg$	Angulo et al. (1999a)
$^{25}Mg(^4He,n)^{28}Si$	Angulo et al. (1999a)

present, an alternative criterion is that of Ledoux. This condition can happen during the evolution od massive stars when the convective core grows in mass or when an intermediate radiative region of varying chemical composition becomes unstable to the convection.

The overshooting from the convecting core is estimated with the mixing-length theory, which allows the penetration of convective elements into the stable regions (Bressan et al. 1981). The overshooting is described by the mean free-path of convective elements across the border of convective region, $l_c = \Lambda_c H_p$. The parameter of core overshooting adopted is $\Lambda_c = 0.5$ in units of H_p. The adopted mean free-path l_c is obtained from the calibration of intermediate age clusters and individual stars (Girardi et al. 2009; Deheuvels & Michel 2010; Kamath 2010; Torres et al. 2014). The overshooting at the base of the convective envelope is simply modeled by mixing the radiative region down to a distance of $l_c = 0.7H_p$ from the Schwarzschild border (Alongi et al. 1991). We warn that the extent of the overshooting regions and the corresponding mixing efficiencies are still a matter of debate (Tang et al. 2014; Bossini et al. 2015).
Finally, the rotational mixing has not been included in PARSEC.

3.3 Mass loss rates

The mass loss is included in PARSEC using different laws. The blue supergiant (BSG) phase, during which the surface temperature of the stars is higher than 12000 K, the Vink et al. (2000) relation has been used. The formulation of Vink et al. (2000) (R_{V01}) shows an almost linear overall dependence of the mass-loss rates on the metallicity: $\dot{M} \propto (Z/Z_\odot)^{0-85}\, M_\odot yr^{-1}$. The red supergiant (RSG) phase with $T_{eff} \leq 12000$ K is treated using the mass-loss rates provided by de Jager et al. (1988),R_{dJ}, assuming the same dependence on the surface metalliciy of R_{V01}. Fro Wolf Rayet (WR) stars, the Nugis & Lamers (2000) formalism, R_{NL}, has been adopted.
Furthermore, during the transition phase between O-phase to Luminous Blue Variables (LBV) and RSG, and finally to Wolf Rayet (WR), the behaviour of mass loss follows the laws of Gräfener (2008) and Vink et al. (2011). In the old PADOVA models (Bressan et al. 1993, e.g), the transition to the super-wind phase corresponding to LBV stars is artificially set at the stages when the models cross the Humphreys & Davidson (1979) limit in HR diagram. This is justified by the evidence that in the Galactic Magellanic Clouds massive stars near this limit show mass loss rates that may reach $\dot{M} \simeq 10^{-3}\, M_\odot yr^{-1}$. The Humphreys-Davidson limit is an observed property of the HR diagram of massive stars in near solar environments. Despite this, it is used independently from the metallicity of the galaxy, in spite of the fact that the mass loss rates themselves depend on the abundance of heavy elements (Kudritzki & Puls 2000; Puls et al. 2000; Mokiem et al. 2007; Smith

2014). This approximation becomes critical at very low metallicities.

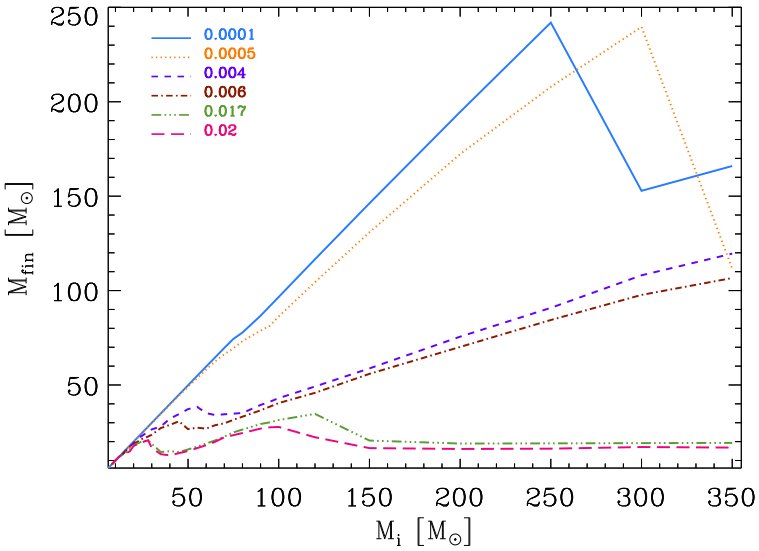

Figure 3.2: M_{fin} as function of M_i for different values of Z. Different line-styles are referred to different values of Z. Stellar tracks are taken from *PARSEC* VI.1 models.

The mass loss rate is strongly enhanced when the star reaches the Eddingthon limit for luminosity:

$$\Gamma = \frac{kL}{4\pi cGM} = 1 \tag{3.1}$$

where L is the surface luminosity of the star, k is the medium opacity, c is the speed of light, G the gravitational constant and M the ZAMS mass of the star. For the most massive stars at solar metallicity this may happen near the Humphreys-Davidson limit. As consequence, the above formalism could provide a modern description of the transition from O-type through LBV/RSG-type to WR-types (Vink & Gräfener 2012). It also included in PARSEC the recent formation of mass-rates provided bt Vink et al. (2011). The resulting HR diagram of massive stars is shown in upper panel of fig 3.3. The strength of mass loss rate is along the pre-supernova evolution is indicated with different colours. The Humphreys-Davidson limit is indicated with black solid line. The time spent in the region beyond the Humphreys-Davidson limit, when it is exceeded, is very short because the mass loss rate becomes so high that the stars rapidly lose their envelopes and turn into the hotter region of the HR diagram. This effect is explained by considering that when the star reaches the Humphreys-Davidson limit, the Γ_e rises close to 1 and. As described in Vink et al. (2011), when Γ_e is larger than 0.7, the mass-loss dependence on Γ_e becomes high,

and, correspondingly, the mass-loss rates are significantly enhanced. Interestingly, the luminosity of the tracks with $M_i \gtrsim 150\,M_\odot$ falls with tima much more than those of the less massive ones. This effect is explained by the relation between the over-luminosity and the main-sequence-mass-luminosity, which gives large values of Γ_e at larger masses. Thus the brightest massive stars are not necessarily those with the largest initial masses.

The dependence of mass-loss rates on the metallicity is a strong function of Γ_e, as shown by Gräfener (2008). While at low values of Γ_e the mass loss rates obey to the realtion:

$$\dot{M} \propto (Z/Z_\odot)^{0.85}\, M_\odot yr^{-1} \tag{3.2}$$

at increasing Γ_e the metallicity dependence decreases, and it disappears as Γ_e approaches 1. In the absence of a more comprehensive analysis of the dependence pf the mass-loss rates on the metallicity and Γ_e, and since there is a continuity between the models of Vink et al. (2011) and those of WNL stars provided by Gräfener (2008), the dependence of the mass loss to the metallicity used in PARSEC is:

$$\dot{M} \propto (Z/0.02)^{\alpha} \tag{3.3}$$

where the coefficient α obeys to the relation published by Gräfener (2008)

$$\alpha = 2.45 - 2.4 * \Gamma_e \quad (2/3 \leq \Gamma_e < 1) \tag{3.4}$$

and with the supplementary condition $0 < \alpha \leq 0.85$.
The evolutionary stages after core He-burning are very short in time, so mass loss has no effects at all. Therefore the mass of the star is frozen with which it will undergo to final supernova explosion.

The figure 3.2 represents the pre-SN mass (M_{fin}) as function of initial mass (M_i), for 13 sets of models with initial mass ranging from $\sim 8\,M_\odot$ to $350\,M_\odot$. The pre-SN mass is related to the final fate of the star and to the remnant mass. The other important values for our work are the mass of He-core (M_{He}) after the end of H-burning and the CO-core (M_{CO}) at the beginning of core C-burning. The figure 3.4 shows the CO-core mass as function of initial mass (left panel) and the He-core mass versus initial mass (right panel). Both M_{He} and M_{CO} increase with increasing initial mass and decreasing initial metallicity. The behavior of M_{CO} and M_{He} determine the final fate scenario of massive stars, which we will describe in detail in chapter 4.

My contribution in the PARSEC evolutionary code is reported in Tang et al. (2014) and Tang et al. (2016). In Tang et al. (2014) the PARSEC library os stellar evolutionary tracks is extended untill $350\,M_\odot$. The input physics is the same as PARSEC VI.1 version (Bressan et al. 2012), but for the mass-loss rate have been considered the most recent updated in the literature. This work

is focused on lower metallicity Z=0.001 and Z=0.004, for which the metal-poor dwarf irregular star-forming galaxies Sextans Am the Wolf-Lundmark-Melotte galaxy and NGC 6822 provide simple but powerful workbenches. The models reproduce fairly well the observe color-magnitude diagrams but the predicted blue loop is not hot enough extended in models with a canonical extent of overshooting. Therefore, the way to reconcile the discrepancy is to enhance the overshooting at the base of the convective envelope (envelope overshooting, EO) during the first dredge-up. The mixing scales required to reproduce the loop are EO=$2H_p$ and EO=$4H_p$ are larger than those derived from the observed location of the red-giant branch bump in low mass stars. This effect imply a strong dependence of the mixing scale below the usual Schawazschild border, on the stellar mass on luminosity.

The work of Tang et al. (2016) checked the performance of PARSEC tracks in reproducing the blue loops of intermediate age and young stellar populations. The tracks considered are those correspondent to intermediate and high initial mass (from 2 to 350 $M_\odot$ at very low metallicity. The synthetic color-magnitude diagrams (CMDs) obtained from the different sets of models with EO=$0.7H_p$, $2H_p$ and $4H_p$ are compared with the observations of Sagittarius dwarf irregular galaxy- The result is that the overshooting scale EO=$2H_p$ best reproduces the observe loops. It has been discussed also the dependence of the blue loop on the instability criterion. The result of the last analysis is that the Ledoux criterion favors the development of the blue loops with respect the classical Schwarzschild criterion. Thus, in presence of overshooting during the H-burning phase, a large EO is needed to reproduce the main features of the central He-burning phase of intermediate and high mass stars.

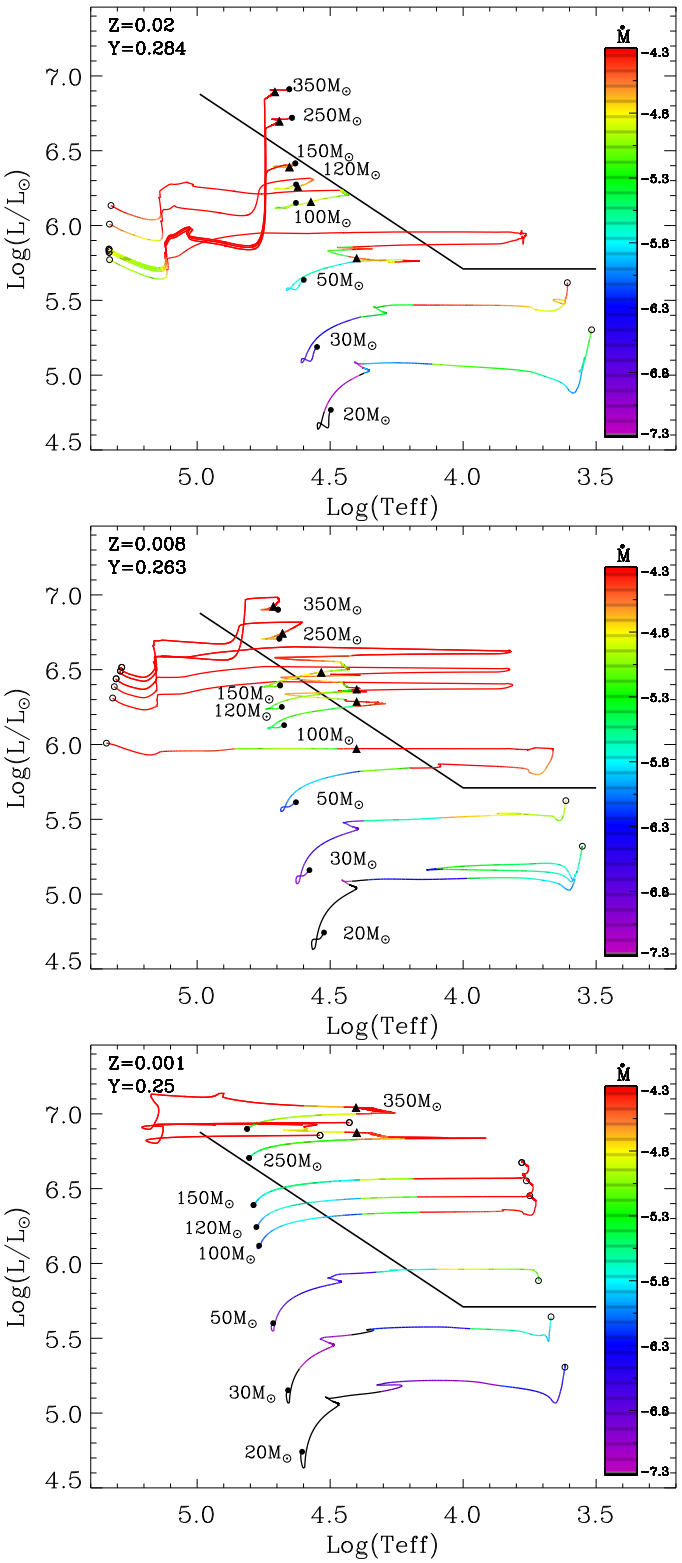

Figure 3.3: Some evolutionary tracks of massive stars at initial metallicity Z=0.02 (upper panel), Z=0.008 (middle panel) and Z=0.001 (lower panel). The plots are taken from Chen et al. (2015). The mass-loss rate is indicated with the colour bar. The black solid lines represent the Humphreys-Davidson limit (Humphreys & Davidson 1979) which delimits the forbidden region above which only very few stars are observed in the Hertzsprung-Russell (HR) diagram of the Galactic massive stars. The solid circles indicate the ZAMS, while the empty ones mark the end of the tracks. The triangles are positioned at the beginning of WR phase.

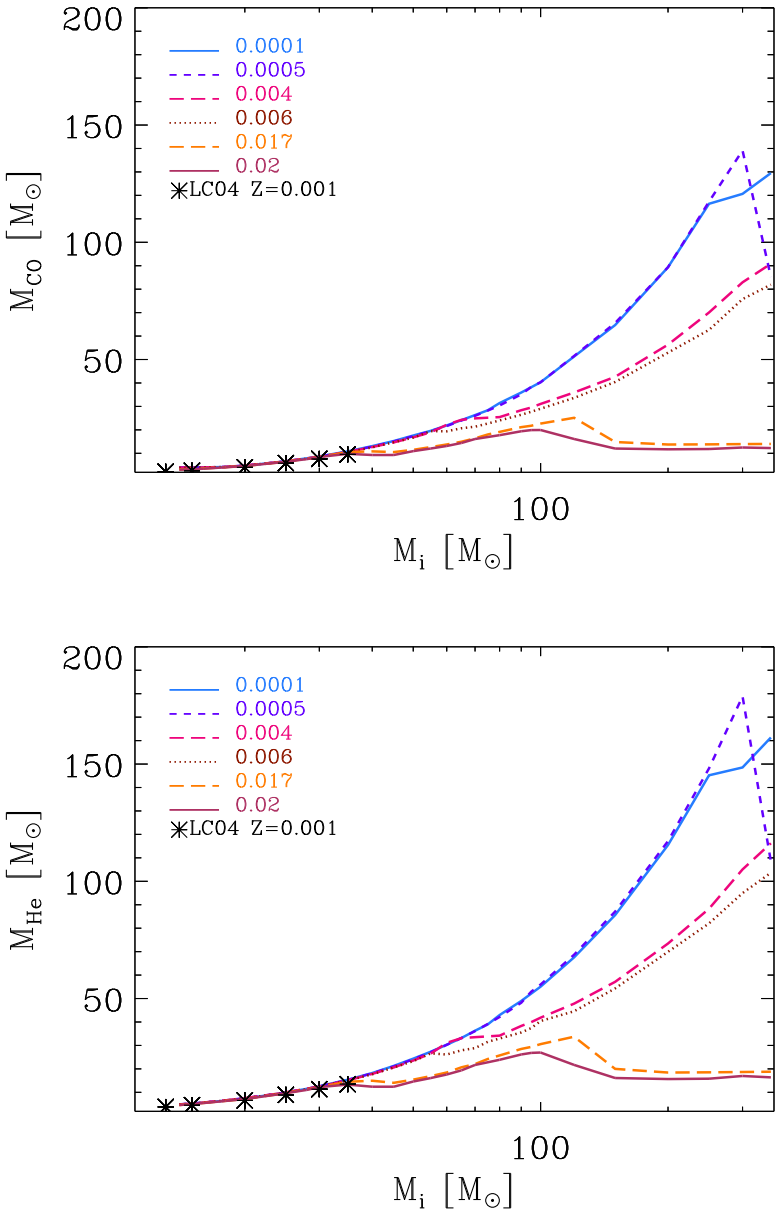

Figure 3.4: M_{He} and M_{CO} mass as function of M_i, for different values of Z. Lines represents the dataset of *PARSEC* VI.I stellar evolution models, while dots represent the values obtained from Chieffi & Limongi (2004) data.

Chapter 4

Final fates and chemical ejecta from massive stars

This chapter describes the method that we used to derive the final fate scenario of massive and very massive stars, and the relative ejecta. The first section of this chapter performs different explosions methods to derive the remnant masses of PARSEC stellar tracks, and discusses the different scenarios obtained. Once the remnant masses are obtained, the ejecta of stars are calculated, dividing in explosion and winds.

The final fate of stars primarily depends on their initial mass M_i and metallicity Z_i. It is convenient to define M_{mas} as the minimum value of M_i for a star to proceed through all nuclear stages up to silicon burning, with consequent formation of an iron core. These conditions require that carbon burning is ignited in non-degenerate conditions in the centre and that a oxygen-neon core is built up with a mass larger than $\simeq 1.37\,M_\odot$, as indicated by detailed stellar models (Nomoto 1984). This behaviour is experienced by the so called *massive stars*, whose initial mass spans from M_{mas} to $\sim 80-100\,M_\odot$. The upper limit decreases with initial metallicity. Recent stellar evolution calculations (e.g., Siess 2007; Hurley et al. 2000) indicate that M_{mas} corresponds to a minimum mass of the CO core formed at the end of the He-burning phase, M_{CO}, with a relatively small dependence on the initial metallicity. Following the detailed analysis of Siess (2007) this critical value is $M_{CO} \simeq 1.179 \pm 0.001\,M_\odot$ and $M_{CO} \simeq 1.246 \pm 0.015\,M_\odot$ for stellar models without and with

convective overshoot, respectively. As our *PARSEC* tracks include overshoot from the convective cores of massive stars, we adopt the latter criterion to define the class of massive stars, i.e. all models with $M_{CO} > 1.246\,M_{\odot}$. We find that M_{mas} is an increasing function of the metallicity, ranging from $M_{mas} \simeq 6\,M_{\odot}$ at $Z_i = 0.0001$ to $M_{mas} \simeq 8\,M_{\odot}$ at $Z_i = 0.02$

Stars more massive than $80 - 100\,M_{\odot}$ belong to the class of very massive objects (VMOs), and may not complete all nuclear stages before ending their evolution. Detailed evolutionary calculations that include the latest stages of VMOs show that the mass of He-core, M_{He}, at the end of pre-supernova phase critically controls their final fate and remnant (Heger & Woosley 2002; Heger et al. 2003; Nomoto et al. 2013). For more detailed see section 2.

In this sections we will analyze in detail the different final fates of massive and very massive stars belonging to the various groups, focusing on the nature (NS, BH) and mass of their remnants. Mass limits and many other relevant quantities used throughout the paper are defined in table 4.1.

4.0.1 Core-collapse supernovae

The core collapse events represent the final fates of stars that develop $M_{He} \lesssim 40\,M_{\odot}$, which corresponds to initial mass from M_{mas} to $\sim 100\,M_{\odot}$, depending on mass loss. As explained section 2, these objects synthesize the iron in the core before ending the evolution. The final fate can be either supernova explosion or a direct to collapse into a black hole.

The physics of supernovae explosions is extremely complex, and the hydro-dynamical code that investigate the explosion mechanism are computationally challenging (Fryer 1999; Fryer et al. 2006; Fryer & Kalogera 2001; Heger & Woosley 2002; Heger et al. 2003; Frayer & Taylor 2012; Janka 2012; Ugliano et al. 2012; Ertl et al. 2016, e.g). In particular, the relation between the last stage of pre-supernova evolution and the supernova remnants is still a matter of debate.

In this section, we discuss the explodability and the estimation of remnant mass of this class of objects, using the formalism provided by Frayer & Taylor (2012) and the criteria obtained from Ertl et al. (2016), combined with an empirical relation between the pre-supernova mass and ^{56}Ni ejection of type IIP supernovae. Moreover, we estimate the remnant mass using a relation between the ^{56}Ni ejection of type IIP supernovae.

The determination of the final fate scenario is affected by two problems. The first one concerns the explodabiliy, i.e. to determine either when stars explode as supernova (*successful SN*) or directly collapse into a black hole (*failed SN*).

Successful SNe is characterized by ejection of material in the interstellar medium after the explosion, and the formation of a remnant mass (M_{rem}). The remnant formation process can be divided into three phases: stellar collapse and bounce, convective engine, and post-explosion fall-

Table 4.1: Description of the main quantities used in this work.

Name	description
Z	Initial metallicity
M_i	Mass of the star at the beginning of main sequence
M_{fin}	Mass of the star at the end of core He-burning
M_{He}	Mass of the He-core at the end of core H-burning
M_{CO}	Mass of CO-core at the end of core He-burning
M_{cut}	Mass-cut, which enclose the entire mass that will collapse to form the remnant
M_{proto}	Mass of the proto-remnant, before the fallback. In absence of fallback $M_{proto} = M_{cut}$
M_{fb}	Amount of material that fall on to the surface of the M_{proto} immediately after the bounce
M_{rem}	Mass of the remnant, which is related to M_{proto} by the relation $M_{rem} = M_{proto} + M_{fb}$
M_{up}	Maximum mass for a star to develop a C-O degenerate core at the end of the core He burning phase
M_{mas}	Minimum mass for the formation of an iron core collapse supernova
M_{VMO}	Mass that divides the CCSNe and the VMOs
CCSN	Core collapse Supernovae
PPISN	Pulsation-pair Instability Supernovae
PISN	pair instability Supernovae
DBH	Direct collapse to black hole
$X^S_j(t)$	Surface abundance of the element j as function of time
$E^x_{j,M_i}/Y^x_{j,M_i}$	ejecta/yield of element j relative to star of initial mass M_i. The superscript x stands for wind(w), overlayer(ov) or explosion(sn)
$E^{x,int}_j/Y^{x,int}_j$	ejecta/yield of element j integrated over the mass range, from $M_i = 14\,M_\odot$ to $M_{max} = 350\,M_\odot$. The Label x stands for wind(w), overlayer(ov) or explosion(sn)
τ_H/τ_{He}	time at which the star starts burning H/He in the core

back (Heger & Woosley 2002; Frayer & Taylor 2012). The M_{rem} left behind can be a neutron star (NS) or a black hole (BH). According to Oppenheimer & Volkoff (1939), we assume that if $M_{rem} < 3\,M_\odot$, the remnant is a NS, otherwise it is a BH. Failed SNe includes stars that end their life forming a BH, without ejection of material.

The second problem deals with the material that falls back onto the surface of the proto-neutron star (M_{proto}) after the explosion. Once the material falls onto the surface of M_{proto} the remnant mass is formed. Therefore, we may consider the remnant mass as the sum of the proto-remnant (M_{proto}) and the amount of infalling material after the bounce (M_{fb}):

$$M_{rem} = M_{proto} + M_{fb} \quad \text{with} \quad M_{rem} \leq M_{fin}\,. \tag{4.1}$$

If the fallback is massive enough to include the entire mass of the star, the core collapse event is characterized by absence of ejecta. It is a failed supernova.

Mono-parametric prescription

The mono-parametric method of Frayer & Taylor (2012) describes the final fates of CCSNe on the base of analytic relations that express both M_{proto} and M_{fb} as a function of M_{CO}. Depending on

the amount of fall-back, the exploding star can either produce a NS or eventually collapse to a BH in case of a sufficiently large M_{fb}.

These relations were derived combining the predictions of stellar evolutionary calculations and supernova models of Hurley et al. (2000); Timmes et al. (1996). The result is the remnant mass distribution as a function of CO-core and initial mass. In order to obtain the remnant mass, Frayer & Taylor (2012) consider a wide range of explosion mechanisms based on the current understanding of supernova and gamma ray burst explosions. They adopt the convection-enhanced neutrino driven explosion model, dividing the analysis in fast-convection explosion and delayed-convection explosion. The former describes the explosions that happen in the first 250ms after the bounce, while the latter is relative to explosions that occur over a much longer timescale (e.g. explosions dominated by the standing accretion shock instability). In both cases the energy input used in Fryer's model is assumed to be limited by the convective region, as already done by Colgate et al. (1993), so that the energy of the explosion does not exceed $0.5 - 2 \cdot 10^{51}$ erg, even though the potential energy released in the stellar collapse is $\sim 10^{53}$erg. The explosion energy estimated by Frayer & Taylor (2012) is a derivation of the previous estimation of Fryer et al. (2006). The peculiarity of the convection-enhanced-neutrino-driven supernova engine is that it describes well the majority of observed supernovae.

The estimation of remnant provided by Frayer & Taylor (2012) is showed in figure 4.1, where M_{rem} is a function of the initial mass, for fast-convection and delayed-convection explosion supernova. For initial mass above the $\sim 30\,M_{\odot}$, the metallicity dependence of winds alters the final remnant mass. For these high masses the explosion energy is weak, and a considerable amount of the hydrogen and helium envelope falls back onto the compact remnant. At high metallicities, the rapid explosions produce slightly less massive remnants across a wide range of initial progenitor mass because the stronger explosions have less fallback, while at low Z the remnant masses produced by the two methods are identical. The jagged nature of the solid lines of figure 4.1, which indicates the remnant mass estimated by Frayer & Taylor (2012), comes from instabilities in the mixing within the stellar evolution code. In this point of view, the core masses are not a smooth function of progenitor mass.

As a first assumption, we use the prescritpions of Frayer & Taylor (2012) to derive the remnant masses relative to PARSEC tracks. In particular, from our values of CO-core (M_{CO}), we obtain M_{proto} and M_{fb} for each stellar track, and then the M_{rem}. Finally we obtain two different scenarios of core-collapse events, for fast-convection explosions and delayed-convection explosion respectively.

Figure 4.2 shows the different final fates of *PARSEC* tracks as a function of initial metallicity

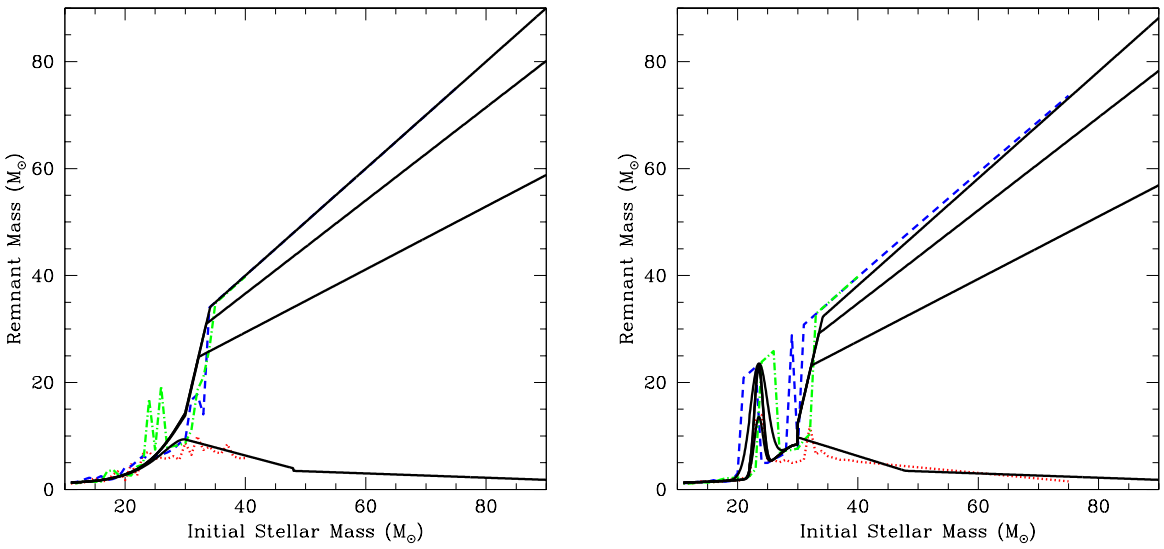

Figure 4.1: Remnant mass as a function of initial mass, for delayed model (left panel) and rapid model (right panel), for three different stellar model suites from Woosley et al. (2002), taken from Frayer & Taylor (2012). The different line-styles are relative to different initial metallicity models of Woosley et al. (2002): Z=0.02 (dot-dashed line), 10^{-4} (dashed), and zero metallicity (dotted). The solid lines are the fitting models of Frayer & Taylor (2012).

and initial mass. The left plot represents the final fate scenario obtained with delayed-convection explosion model, while the right plot shows the scenario deduced with fast-convection explosion model. The two plots show also the final fate of very massive objects obtained using the Heger & Woosley (2002) criterion that is described in detail in section 4.0.2. Different final fates are labelled with different symbols, as reported in the legend of figure 4.2.

The main result emerging from the two plots is that the final fate of CCSNe does not depends significantly on the metallicity. Indeed, the factor that influences the final fate of CCSNe is the amount of fallback, which depends on the explosion model used, and it causes the main differences observed in the two plots.

As seen in figure 4.1, the remnant masses obtained with a fast-convection explosion model have a jagged trend, which is observed also in our derivations. Indeed, the right panel of figure 4.2 shows a narrow interval of M_{CO} in which the fallback is very efficient. This range corresponds to $24\,M_\odot \lesssim M_i \lesssim 28\,M_\odot$. The remnant mass of this range is the same as the pre-SN mass, so these stars evolve as failed supernovae.

In the delayed explosion model there is a smooth transition from successful SN and failed SN (see figure 4.1, left panel), as the M_{rem} grows slowly with M_i.

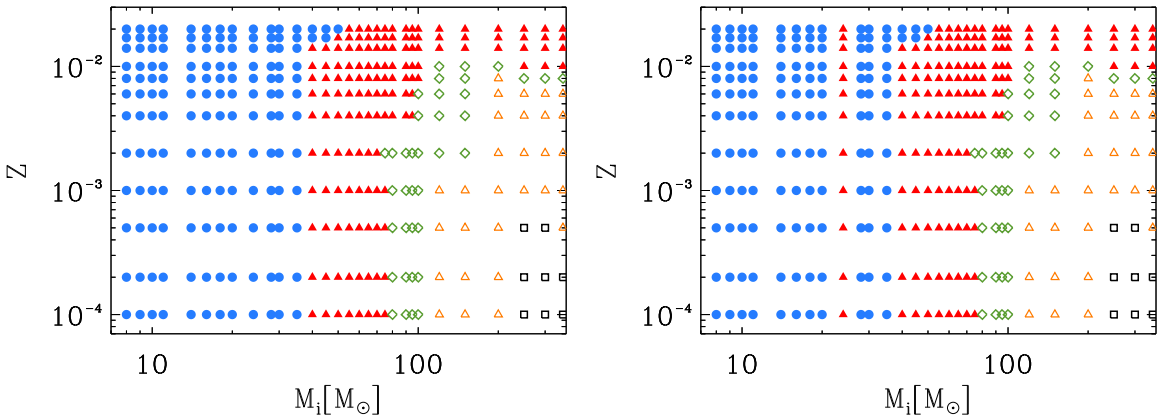

Figure 4.2: Different final fates, as function of Z and M_i, derived using delayed explosion model (left panel) and rapid explosion model (right panel). Filled symbols represent CCSNe, while empty symbols are the VMOs. Blue circles represent successful CCSNe, red triangles are the failed SNe, green diamonds are the Pulsation instability supernovae (PPISNe), yellow triangles represent the PISNe and black squares are stars that collapse into a BH without explosion.

Table 4.2: Final fates of *PARSEC* stellar tracks, obtained using Frayer & Taylor (2012) and Ertl et al. (2016) prescriptions for CCSNe, and the Heger et al. (2003) prescriptions for VMOs.

Final fate	M_{He}	**Frayer & Taylor (2012)**	**Ertl et al. (2016)**
CCSN with ejecta	$< 40\,M_\odot$	$M_{rem} < M_{co} < M_{fin}$	$M_{co} < 8.26\,M_\odot$
CCSN with only envelope ejecta	$< 40\,M_\odot$	$M_{co} < M_{rem} < M_{fin}$	$M_{co} < 8.26\,M_\odot$
CCSN wihtout ejecta	$< 40\,M_\odot$	$M_{co} < M_{rem} = M_{fin}$	$M_{co} > 8.26 M_\odot$
PPISN	$40\,M_\odot - 65\,M_\odot$		
PISN	$65\,M_\odot - 133\,M_\odot$		
DBH	$> 133\,M_\odot$		

Another characteristic of the final fates scenario deduced with mono-parametric prescriptions is that in both case the value of M_i that divides the successful SN from failed SN is constant til $Z \simeq Z_\odot/2$ and equal to $35 M_\odot$. For higher Z the threshold value is around $50\,M_\odot$.

Bi-parametric method

Recently it has been suggested that the dependence of the mass of the compact remnant on M_{fin} and M_{CO} might be more complex (Ugliano et al. 2012; O'Connor & Ott 2011; Janka 2012; Ertl et al. 2016). In particular, Ugliano et al. (2012) and Sukhbold & Woosley (2014) found that the pre-supernova properties (e.g Fe-core and CO-core, binding energies and density or entropy

profiles above the Fe-core), and the explosion properties (e.g explosion energy, nickel mass and remnant mass) vary non-monotonically with the initial mass. Moreover, these properties can differ considerably even between progenitors with a little different initial mass.

Ugliano et al. (2012) and O'Connor & Ott (2011) used the compactness as the explosion parameter. The compactness is the normalized enclosed mass-radius ratio, and it is defined by the equation:

$$\xi_{M} \equiv \frac{M/M_{\odot}}{R(M)/1000\,km} \tag{4.2}$$

where R(M) is the radius with enclosed mass M.

The work of Ertl et al. (2016) suggests that there are characteristic parameters of the pre-SN star that control the success of the failure of the supernova explosion with respect to a single value of the compactness or other useful parameters like the iron-core mass, CO-core mass or the binding energy outside the iron core. Indeed, while all measurements obtained with a single parameter reflect that the BH formation is favored for high compactness, there are still many outliers that do not obey the correlations. For example, a chosen mass M of the compactness ξ_{M} lead us to correctly predict explosions in $< 90\%$ of the cases (Pejcha & Thompson 2015), but the best choice of M is merely empirical, and the physical justification of ξ_{M} as good diagnostic is unclear (Ertl et al. 2016). Furthermore, for none of the single parameters expressed before does exists a sharp boundary value that discriminates between explosions and non explosions. Finally, stars with same initial mass (M_{i}) and CO-core mass (M_{CO}) can have different internal structure, therefore they can form different remnant masses. From this point of view, it is inappropriate to use a bi-univocal relation between remnant mass and M_{CO} to discriminate between successful and failed SN.

The explosion model provided by Ertl et al. (2016) distinguishes between successful and failed supernova using a bi-parametric analysis.

Figure 4.3, shows the explodability scenario obtained with bi-parameter prescription. The separation between successful and failed explosion can be understood by considering the neutrino-driven mechanism, in which the expansion of the SN shock is obstructed by the ram pressure of the infalling stellar-core matter and shock expansion is pushed by neutrino-energy deposition behind the shock. For neutrino luminosity above the critical value $L_{\nu,crit}$, which depends on the mass accretion rate ($\dot{M}$) of the shock, the runaway of the shock wave and the explosion are triggered by neutrino heating (Janka 2001, 2012; Pejcha & Thompson 2012; Müller & Janka 2015). The explosion is favored for high neutrino-luminosities and high $\dot{M}$. The relation:

$$L_{\nu} \propto R_{\nu}^{2} T_{\nu}^{4} \tag{4.3}$$

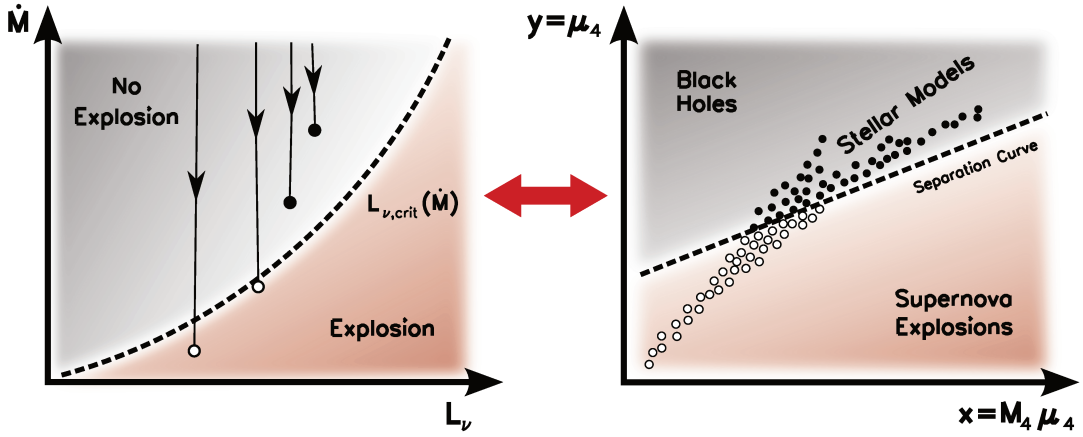

Figure 4.3: Correspondence of $L_\nu - \dot{M}$ plane with critical neutrino luminosity $L_{\nu,crit}(\dot{M})$ (left panel) and x-y plane with separation curve $y_sep(x)$ (right panel). in both panels, the white circles indicate the exploding models, while the black circles stands for the non exploding ones. The figure is taken directly from Ertl et al. (2016).

shows the dependence of the neutrino-luminosity on the temperature (T_ν^4) and radius (R_ν^2) of the neutrinosphere. Since both R_ν and T_ν increase roughly linearly with M_{proto}, we conclude that the strength of gravitational potential and the neutrino luminosity are determined by the mass of the proto-neutron star (M_{proto}) and the mass of the iron core. The Ertl et al. (2016) simulations show that the neutrino-driven explosions set short after the moment when infalling matter, which reaches at the shock wave position, has the adimensionless entropy ~ 4. Therefore, the parameters chosen are M_4, which is defined as the enclosed mass per dimensionless entropy per nucleon s=4, and μ_4, which is a measure of the mass accretion rate at this time and is id defined by the relation:

$$\mu_4 = \frac{\Delta M}{\Delta r}\Big|_{s=4} = \frac{[(M_4 + \Delta M) - M_4]\,/M_\odot}{[r(M_4 + \Delta M) - r(s=4)]\,/1000\mathrm{Km}} \tag{4.4}$$

The parameter M_4 is normalized to $M_\odot$ and μ_4 is normalized to $10^3\,\mathrm{km}/M_\odot$. As showed in figure 4.3, there is a separation curve that divides the exploding and non-exploding stars in the plane with x= $M_4\,\mu_4$ and y=μ_4, which is given by the equation:

$$y_{sep}(x) = k_1 x + k_2 \tag{4.5}$$

The coefficients k_1 and k_2 depend on the calibrations of the free parameters of Ertl et al. (2016) 1D hydrodynamic simulations. Since we verified that changing the separation curve there are no significant variations in the results, we use the calibration line with $k_1 = 0.283$ and $k_2 = 0.0430$.

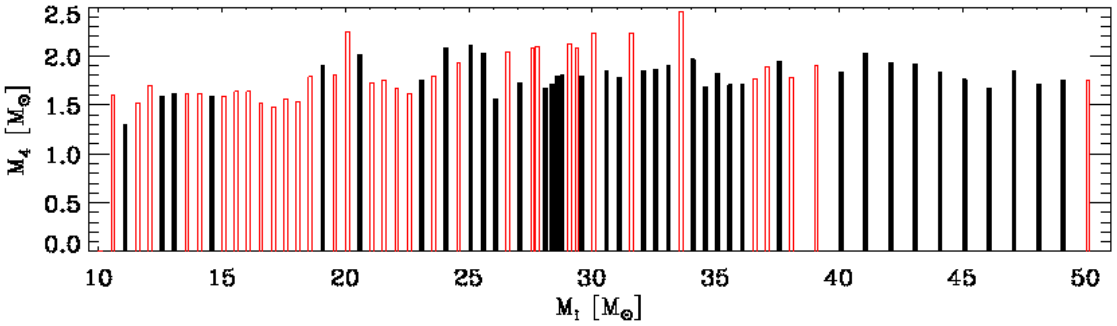

Figure 4.4: M_4 values derived from of MESA tracks with included *PARSEC* mass loss prescriptions, as function of M_i. The models have initial metallicity Z = 0.02. Red bars indicate the stars which evolve as successful supernovae, while black bars are relative to stars which direct collapse to black hole.

We clarify that we used the bi-parametric method only to separate the successful SNe from failed SNe. we clarify that we use the bi-parametric method obly to investigate the explodability of our tracks.The remnant mass of PARSEC tracks are obtained with the relation that links the remnant mass to the amount of nickel ejected, which is described in detail in sec. 4.0.1.

The values M_4 and μ_4 depend on the internal structure immediately before the explosion, thus it is not possible to obtain these values directly from *PARSEC* code because it computed stellar evolution until the end of He-burning. We extracted M_4 and μ_4 from the grid of simulations ran with MESA (Paxton et al. 2011), upgraded with *PARSEC* winds prescriptions. We computed the MESA tracks for stars of initial mass between $10\,M_\odot$ and $50\,M_\odot$ and metallicity Z = 0.02. The results are represented in figure 4.4. From the figure it can be deduced that the majority of stars with $M_i \gtrsim 28\,M_\odot$ form BHs through direct collapse, without leaving ejecta. These results are in agreement with those derived by Spera et al. (2015). The constrain on M_i determines the limit in M_{CO}, over which the final fate is failed SN. About this topic, we precise that we have made a simplified approximation to the explodability method of Ertl et al. (2016). The threshold value obtained from the fig. 4.4, does not represent a net limit between successful and failed CCSNe. This is validated by the fact that the explosions occur also for stars more massive than $28\,M_\odot$, but their low frequency lead us to choose this as a reasonable limit.
We applied this criteria to the *PARSEC* tracks. Due to the slightly dependence of the CO-core on the initial metallicity, it is reasonably safe to extend the threshold value of M_{CO} (see fig. 3.4) to the tracks of Z < 0.02 to predict the final fate for CCSN. Therefore, according to Ertl et al. (2016) method, we divided the CCSN final fate in two subgroups:

- $M_i \lesssim 28\,M_\odot$ ($M_{CO} \lesssim 8.26\,M_\odot$) : most of stars explode as core collapse supernovae, ejecting

material in the ISM and leaving behind a NS.

- $M_i \gtrsim 28\,M_\odot$ ($M_{CO} \gtrsim 8.26\,M_\odot$): most of stars in this range end the life with a core-collapse into a BH, without polluting the ISM with any element.

These results are showed in figure 4.5, in which the CCSN and VMO final fates are illustrated. The main difference between bi-parametric method and mono-parametric prescriptions is represented by the values of M_i that separates the successful from failed SN. This threshold value is around $28\,M_\odot$ for bi-parametric method, and it is lower than the separation value between successful and failed SN derived with Frayer & Taylor (2012) prescriptions. Moreover, these trashold value of $28\,M_\odot$ is constant with Z.

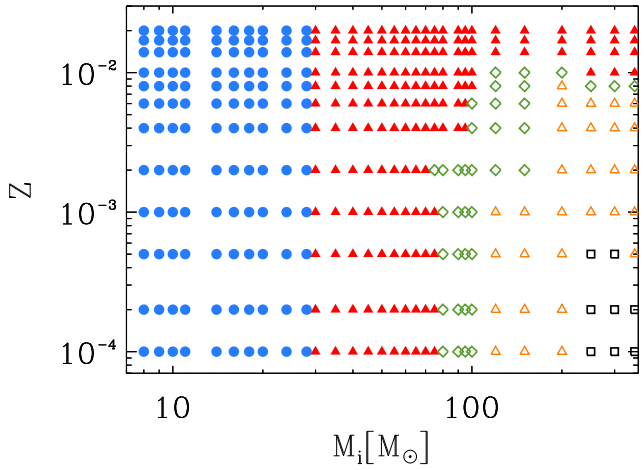

Figure 4.5: The same as figure 4.2, but obtained using bi-parametric method for CCSNe and Heger & Woosley (2002) prescriptions for VMOs. The legend is the same as in figure 4.2.

Remnant mass estimation using ^{56}Ni ejection

To estimate of M_{rem} we adopt a criterion based on the amount of ^{56}Ni produced during the supernova event. A fraction of this mass is ejected during the explosion, which is observed in the light curve. Indeed, the decay chain $^{56}Ni \longrightarrow {}^{56}Co \longrightarrow {}^{56}Fe$ produces gamma rays with energies of about 1 MeV, which release their energy through Compton scattering with bound and free electrons. Then, the Compton electrons lose the energy acquired through ionization and excitation of atoms and ions, producing the light curve. From the radioactive tail of the light curve it is possible to estimate the amount of ^{56}Ni ejected, and therefore the remnant mass left behind by the supernova after the explosion.

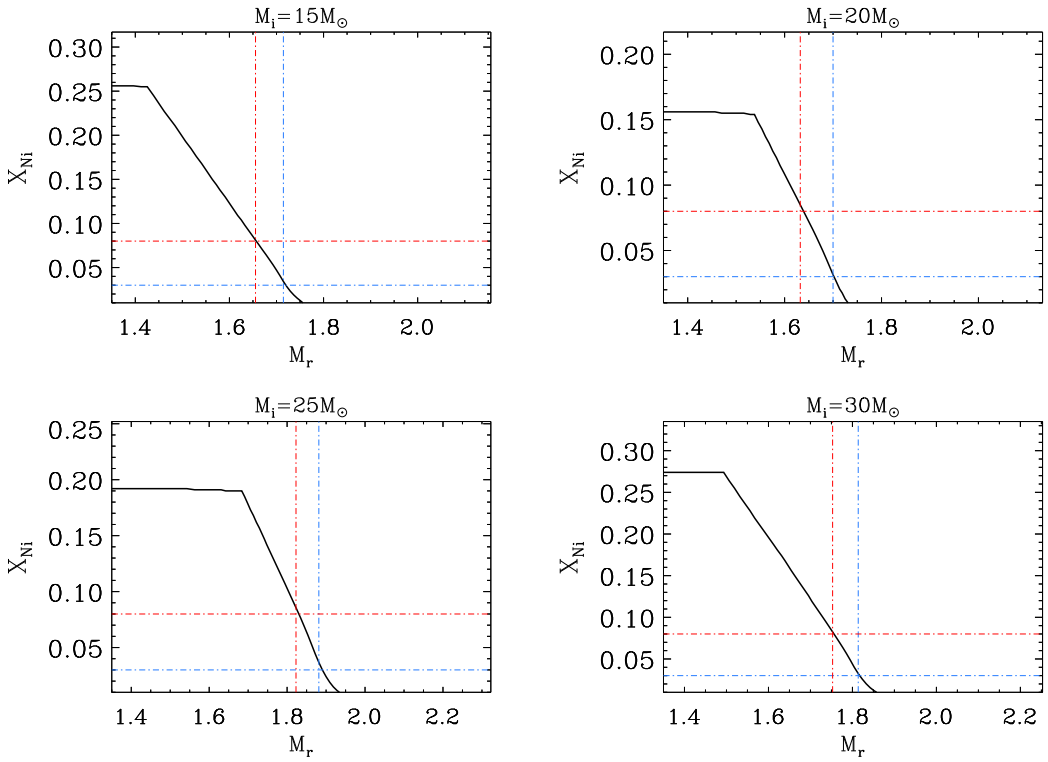

Figure 4.6: ^{56}Ni integrated abundance profile for stars with initial mass 15, 20, 35 and 30$M_{\odot}$, at Z=0.02, taken from Chieffi & Limongi (2004) database. The blue and red dashed orizontal lines indicate are positioned at two different values of ^{56}Ni ejected: E_{Ni} = 0.02 and $E_{N}i$ = 0.08 respectively. The vertical lines indicate the corresponding M_{cut} obtained from the Ni-ejecta.

The amount of ^{56}Ni ejected depends on the presence of an H-rich envelope before the explosion, the pre-supernova mass and the explosion energy (Heger et al. 2003; Hamuy 2003). Recently, a possible relation between initial mass and the amount of ^{56}Ni ejecta had been investigated (Umeda & Nomoto 2008). In our work we used the relation between the ^{56}Ni ejected and the mass of the star immediately before the explosion, using the data of a set of type IIP supernova with the plateau of $\sim$ 100 days, obtained by Utrobin & Chugai (2009),Utrobin et al. (2010). These plateau supernovae are believed to be an outcome of a core collapse of stars with M_i between 9 and 25$M_\odot$ stars (Heger et al. 2003).
In the figure 4.7 we represent the ^{56}Ni ejected mass as function of pre-supernova mass. We derived the relation between the amount of ^{56}Ni ejected and the pre-supernova mass:

$$Y = aX + b \tag{4.6}$$

where *Y* is the amount of ^{56}Ni ejected and *X* is M_{fin}, both of them in solar masses. The coefficient *a* and *b* are obtained by chi-square minimization, and are, respectively a=0.00656 and b=-0.0930.

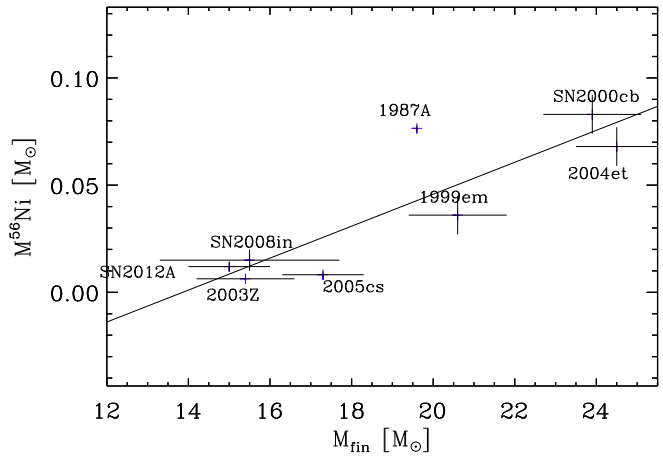

Figure 4.7: Ejecta of ^{56}Ni in solar masses as function of pre-supernova mass for a set of observed core collapse supernovae. The data are taken from Utrobin & Chugai (2009) and Utrobin et al. (2010).

Using this relation we obtained the mass cut of our set of tracks with initial mass between 9 $M_\odot$ and 25 $M_\odot$. For the stars with higher initial mass we consider the maximum amount of ^{56}Ni ejected derived from equation 4.6. The criteria that we used is valid only for normal CCSN, for which the explosion energy is of the order of 10^{51} erg. We proceed as follow. From the values of

^{56}Ni ejected we derived the correspondent M_{cut} in Chieffi & Limongi (2004) database (hereafter CL04), observing that the remnant masses derived from this database include the Si-shell. The CL04 database does not include univocal values of remnant mass for each model, but Chieffi & Limongi (2004) provide the integrated-nickel profile (before decay) for each track. In this way, given the value of the Ni-ejected during the explosion, it is possible to obtain an estimation of the mass that remains after the explosion (M_{cut}). Figure 4.6 shows the integrated abundance profiles of ^{56}Ni before decay, for four different values of initial mass taken from CL04 data base. The initial metallicity of these tracks is Z=0.02. Blue and red horizontal lines indicate two different values of Ni-ejected during the explosion. By the intersection between these lines and the Ni-profile it is possible to estimate the mass-cut M_{cut}. We note that the minimum and maximum values of remnant masses vary slightly with the value of ^{56}Ni ejected.

Once it is known the mechanism to obtain the remnant mass from CL04 database, we used this method to estimate the remnant masses relative to PARSEC tracks. Starting with a value of CO-core mass of PARSEC tracks (M_{CO}), we chose in the CLO4 database those tracks which have the M_{CO} immediately preceding and consecutive ($M_{CO,A}$ and $M_{CO,B}$, respectively). Then we selected the relative final masses ($M_{fin,A}$ and $M_{fin,B}$), and with the $^{56}Ni - M_{fin}$ relation we found the amount of nickel ejected. Thus, from the nickel profile we derived the remnant masses correspondent to $M_{CO,A}$ and $M_{CO,B}$: $M_{rem,A}$ and $M_{rem,B}$, respectively. Finally, using our M_{CO} as independent parameter, we interpolate the remnant masses just calculated to find our remnant mass (M_{rem}),

We repeated the procedure also for the other metallicities included in the CL04 database, and finally we interpolate in the metallicity to find the remnant masses for all the PARSEC tracks.

4.0.2 Very Massive Objects (VMO)

As seen in section 2, stars with initial mass higher than $\sim 100\,M_{\odot}$ have a different explosion mechanism in respect to the core-collapse supernovae.

We derived the final fate of VMOs from *PARSEC* tracks using the M_{He} classification of Heger & Woosley (2002). The remnant masses of PPISNe are derived interpolating the data of Woosley (1986). Figures 4.2 and 4.5 show that VMOs occur at low metallicity, while are absent at near solar Z. We find also that PISNe as final fate of massive stars for initial metallicity up to Z = 0.006. This result is in agreement with the recent studies of Kozyreva et al. (2014b).

4.0.3 Evolutionary type before explosion/collapse

In this section we briefly analyze the surface properties of the *PARSEC* tracks at the ignition of C-burning in the core. Given the extremely short timescales of the subsequent evolutionary phases

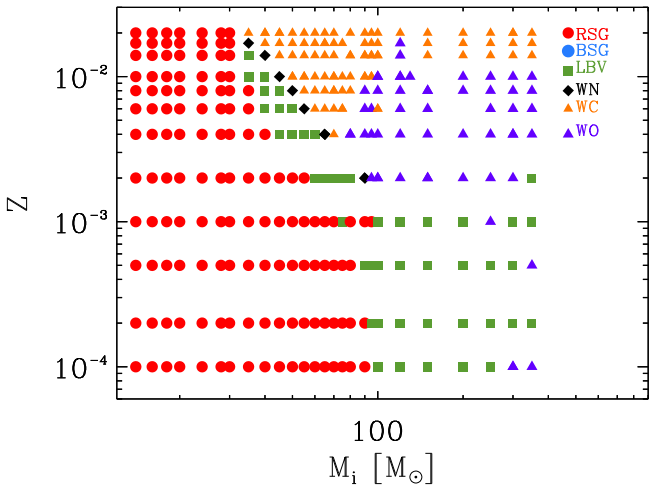

Figure 4.8: Predicted evolutionary stage (RSG, BSG, LBV, WR) at the onset of core C-burning as function of initial mass and metallicity. This eventually determines the characteristics of the progenitors of successful/failed SN of different types. The symbols are explained in the legend.

and the decoupling between core and envelope evolution, the surface properties are expected to remain essentially frozen until the explosion or collapse events take place. This information is particularly relevant, for instance, to assign a stellar progenitor to a core collapse supernova, or BH.

We have seen that stars with high initial mass and/or high initial metallicity experience strong mass loss episodes (Fig. 3.2). The powerful stellar winds can remove the entire H-rich envelope, eventually exposing at the surface H-deficient layers that were previously processed by the H- and He-burnings. These facts explain the existence of Wolf-Rayet (WR) stars (Conti 2000; Smith & Maeder 1989), a class of hot stars showing high-ionization emission lines in their H-deficient spectra (Barlow & Hummer 1982; Crowther et al. 1998; Crowther 2008).

These stars are usually grouped in three main classes, depending on their surface abundances, namely: WN, WC, and WO. The WN abundance patterns are consistent with material processed by CNO cycle, so that H, C and O are depleted in favor of N. The ratio H/He (by number) typically varies in the range between 0.1 and 4. WC and WO stars show the products of He-burning, so that the abundances of C, O and Ne are enhanced.

In the present study we adopt the following criteria to assign the WR class (Smith & Maeder 1991):

- $0 \leq$ n(H)/n(He) < 4 for WN stars;

- n(H) = 0 & 0.01 < n(C + O)/n(He) < 1 for WC stars;
- n(H) = 0 & n(C + O)/n(He) > 1 for WO stars;

In all cases the effective temperature should be $log(T_{\rm eff}) > 4.8$ (Maeder & Meynet 1987).
For models with H-rich envelopes (operatively defined by the relation n(H)/n(He) > 4), we use the following classification based on the position in the HR diagram. The red super giant (RSG) stars ($T_{\rm eff} \lesssim 12000\,K$) occupy the red region of HR diagram, while the blue super giant (BSG, $T_{\rm eff} > 12000K$) are located in the left part of HRD. In both cases the surface luminosity is below the Humphreys & Davidson (1979) instability limit. Stars that are in the region near this limit experience the luminous blue variable (LBV) phase (Humphreys & Davidson 1994). These stars are characterized by super-Eddington winds and explosive mass loss (Smith 2015). The Humphreys & Davidson (1979) limit depends on effective temperature and luminosity of the star, and it is described by the relation:

$$\log(L) = 1.18 \cdot \log(T_{\rm eff}) + 0.99 \tag{4.7}$$

which is defined at solar metallicity. We used this limit also for $Z < Z_\odot$, because when the star approaches the Eddington limit the metallicity dependence of the mass-loss becomes weaker, and disappears as the Eddington luminosity (Γ) approaches 1.

The results are presented in Fig. 4.8, that shows the predicted evolutionary stage at the onset of core C-burning as a function of initial mass and metallicity. At very low metallicity ($Z \lesssim 0.001$), the pre-supernova scenario is dominated by RSG stars, up to $M_i \sim 100\,M_\odot$, while more massive stars evolve as LBV, except rare cases. This behavior can be connected to the mass loss varying the initial mass and metallicity (see Fig. 3.2). The consequence is that for $Z < 10^{-3}$ the is absence of WR stars in the progenitors both of CCSNe and VMOs, except rare cases. The scenario changes for $10^{-3} \lesssim Z \lesssim 0.006$ in which WN and WO progenitors appear for SNe originating from stars with initial mass higher than $100\,M_\odot$. This fact means that the progenitors of failed SNe could be stars in LBV, WN or WO phases. At increasing metallicity there is a reduction of LBV progenitor stars, while the WC and WO progenitors increase, and for near solar metallicity the quasi totality of stars with $M_i \gtrsim 30\,M_\odot$ evolve as WC stars. We can conclude that for $Z \gtrsim Z_\odot/4$ the progenitors of supernovae/collapse events are mostly WC stars for failed SNe and WO stars for VMOs.

4.0.4 Discussion

The figures 4.9, 4.10 and 4.11 show the remnant mass as function of M_i, for initial metallicity $Z = 0.0001, 0.004, 0.006$ and 0.02. The initial mass ranges from $0.9\,M_\odot$ to $350\,M_\odot$. For completeness we included also the AGB models in the plots (magenta regions), which are taken from

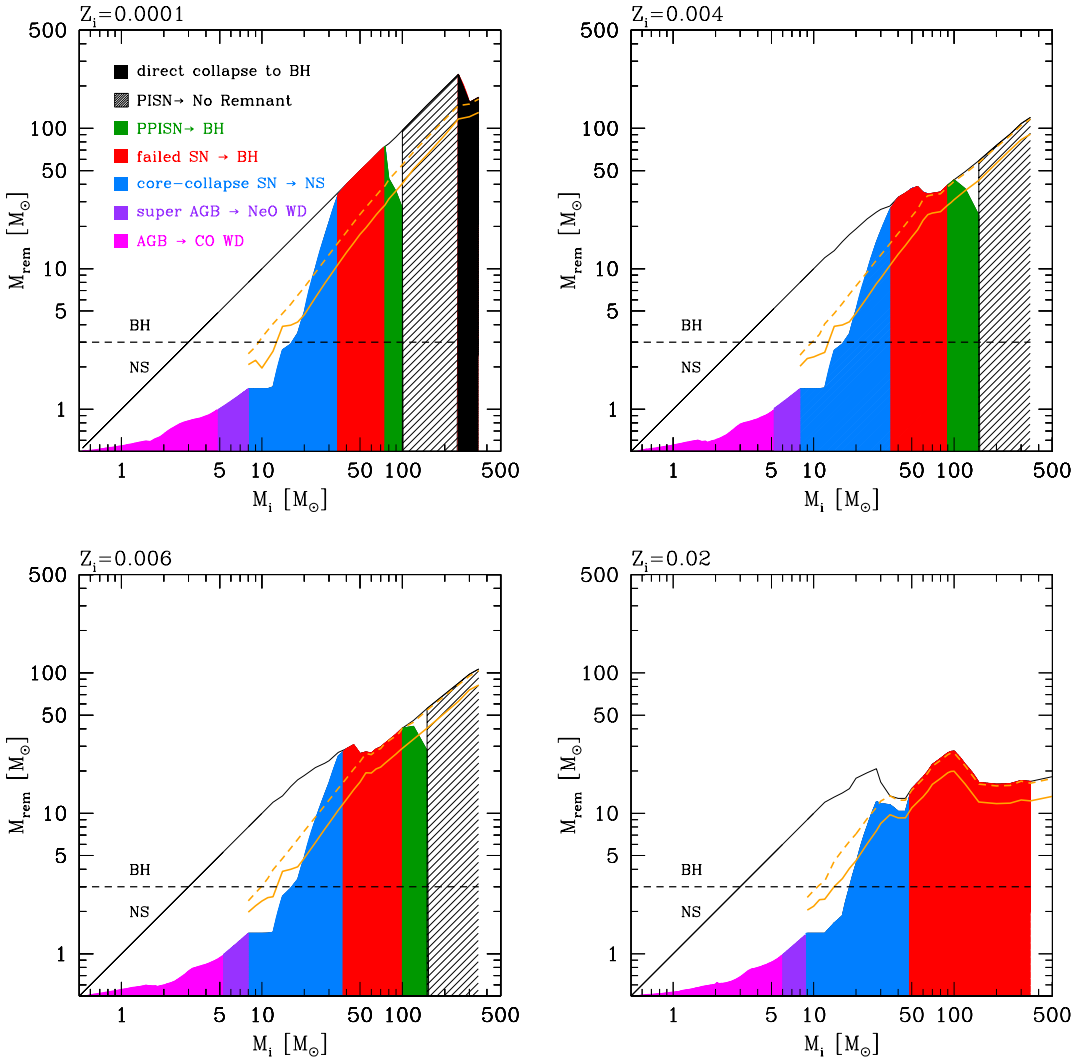

Figure 4.9: Remnant mass estimation and final fate scenario obtained with delayed explosion model of the mono-parametric method. Each plot is relative to a different metallicity: Z = 0.0001 in upper left panel, Z = 0.004 in upper right panel, Z = 0.006 in bottom left panel and Z = 0.02 in bottom right panel. The Black solid line represents the stellar mass at the end of the core He-burning. The orange solid line shows the value of C-O core of massive stars at the end of core He-burning, while the orange dashed line is the mass of M_{He} at the same evolutionary time. The dashed horizontal black line separates the NS and BH domains and it is placed at $M_{rem} = 3\,M_{\odot}$.

calculations of Marigo et al. (2013). The super-AGB stars (purple regions) are not treated explicitly in this work, so that to fill the gap between AGB and massive stars the remnant masses are obtained by linearly interpolating between M_{up} and M_{mas}. In any case the following discussion is limited to massive stars.

The blue and red regions include the CCSNe. The regions that correspond VMOs are colored with green (for PPISNe), dashed (PISNe) and black (DBHs). The orange solid line indicates the mass of the C-O core as function of M_i, while the dashed orange line is the value of He core. Both M_{CO} and M_{He} are obtained from PARSEC tracks at the termination of core He-burning. The black solid line connects the mass of the each star at the same evolution time. For massive stars this value coincides with the pre-SN mass. The dashed black line divides the domains of neutron stars ($M_{rem} < 3\,M_\odot$) and black holes ($M_{rem} \gtrsim 3\,M_\odot$).

Let us first analyze the results for massive stars (blue and red regions). The figures clearly show that their final fate and remnant mass vary with both the initial metallicity and the adopted model prescriptions (explodability criterion, characteristic explosion time-scales, efficiency of fall-back, etc.).

Interestingly, the critical value of the initial mass that marks the boundary between successful (blue region) and failed CCSNe (red region) is affected. While adopting the bi-parametric model of Ertl et al. (2016) this limit is found around $M_i \simeq 28\,M_\odot$ with a small metallicity dependence, a somewhat larger limiting mass ($M_i \simeq 35 \div 50\,M_\odot$) is predicted with the mono-parametric criterion of Frayer & Taylor (2012). In the latter case we also expect that the mass limit shift towards larger values at increasing metallicity.

Likewise, the relation between M_{rem} and M_i is influenced by the explosion model prescriptions (see Spera et al. (2015) for a thorough discussion). In the framework of the delayed-explosion model (see figure 4.9), the remnant mass increases gradually with M_i reflecting the linear relation between the amount of fallback and M_{CO} (see Frayer & Taylor (2012)), which increases with M_i. Adopting the rapid-explosion model (see figure 4.10) the remnant mass exhibits a non-monotonic and steeper relation with M_i. In both cases the group of successful SN produces both neutron stars (for initial masses in range between $M_{mas} \lesssim M_i \lesssim 20-25M_\odot$) and black holes (for $20-25M_\odot \lesssim M_i \lesssim 40-50M_\odot$).

The above predictions appear to be significantly different from the final fate scenario obtained using the bi-parametric method coupled with ^{56}Ni-M_{fin} relation. Indeed, a sharp transition of M_{rem} shows up between the blue and red regions. Given the minor efficiency of the fall-back process, successful SN produce remnants masses that are comparable to those of the iron cores (Ertl et al. 2016). As a consequence all successful SNe leave behind a neutron star (with $M_{rem} < 3\,M_\odot$).

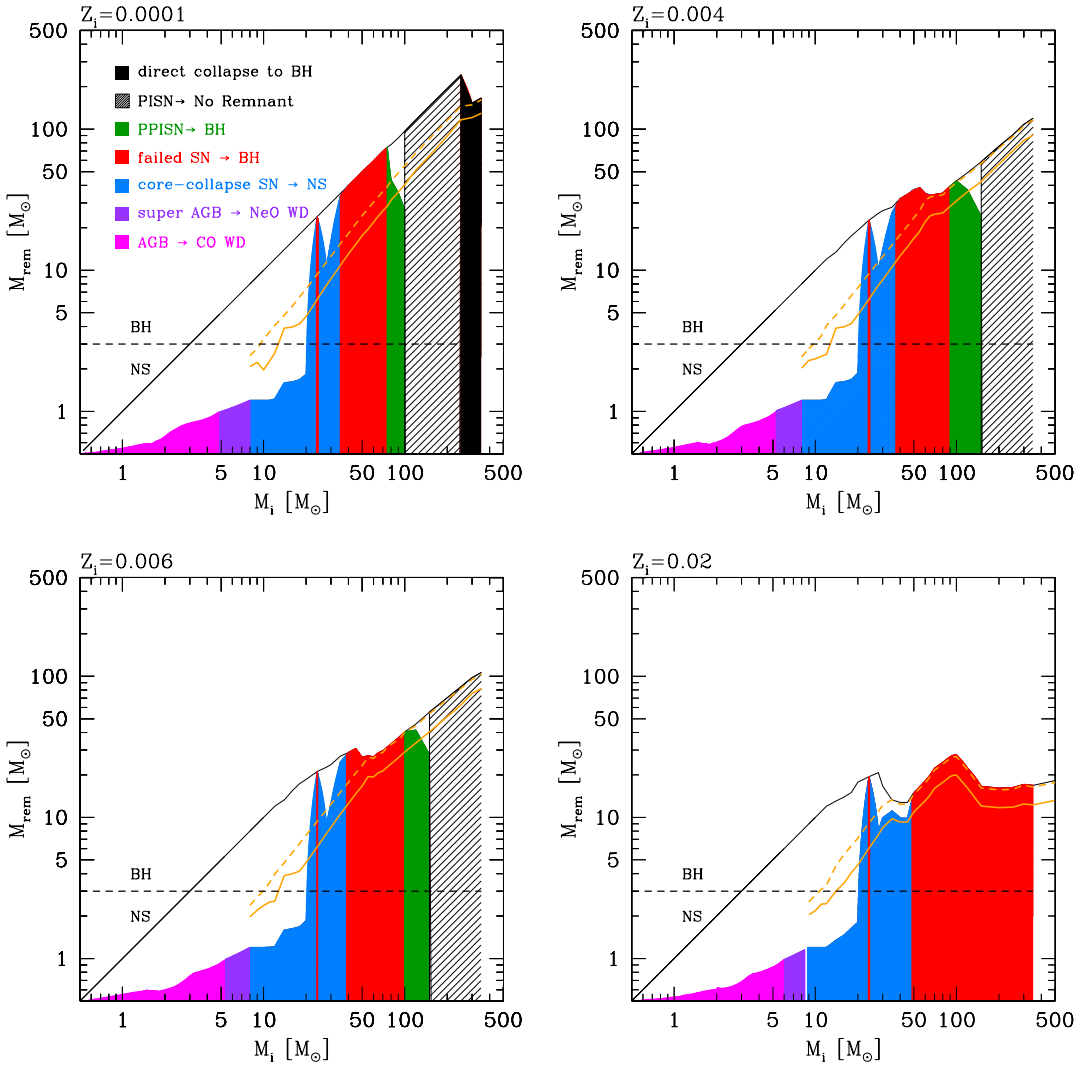

Figure 4.10: Remnant mass estimation and final fate scenario obtained with the rapid explosion model of the mono-parametric method. The legend is the same as that of figure 4.9.

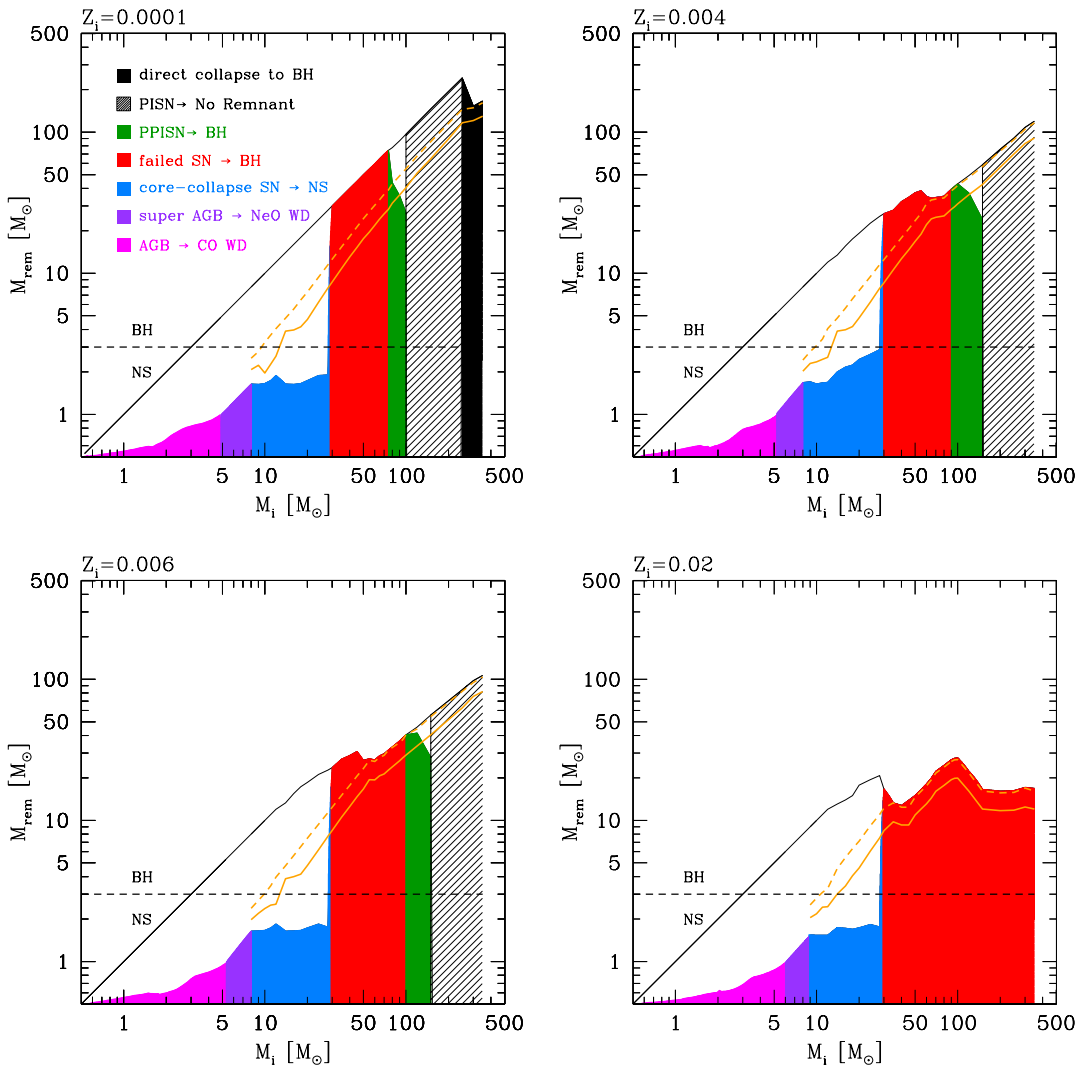

Figure 4.11: Remnant mass estimation and final fate scenario obtained with the bi-parametric method coupled with the ^{56}Ni.M$_{fin}$ relation for M$_{rem}$ estimation. The legend is the same of figure 4.9.

Furthermore, interesting considerations can be maiden from the values of the neutron stars obtained with the three different scenarios. Figures 4.9 and 4.10 show that the mass of neutron stars produced by successful SNe is $\sim 1.8-2\,M_\odot$, while the masses of NS observed in fig. 4.11 are around the value $\sim 1.4\,M_\odot$.
Several recent observations of neutron stars have direct bearing on the determination of the NS mass. The most accurately measured masses are from timing observations of the double neutron star binaries, but the neutron star masses are obtained also by observing the white dwarf neutron star binaries and X-ray binary systems (Lattimer & Prakash 2007). Therefore, the values of NS mass obtained from observations varies from $1.4414 \pm 0.0002\,M_\odot$ (Weisberg & Taylor 2005, radio-binary pulsar PSR 1913+16) to $2.44 \pm 0.27\,M_\odot$ (Clark et al. 2002, X-ray binary 4U1700-37). In light of this considerations, we conclude that our values of NS masses are in agreement with the most recent observations.

In summary, within the initial mass range of massive stars that are potential progenitors of CCSNe, (i.e. that form an iron core at the completion of the silicon burning phase), the contribution in dark remnants depends on the adopted explosion criterion. Black holes are generated by both successful and failed SNe in the case of the mono-parametric model (over a range of initial stellar masses from 25-30 $M_\odot$ to $50\,M_\odot$), while in the bi-parametric scenario only stars that are unable to drive the explosion generate black holes ($M_\mathrm{i} \gtrsim 28-30\,M_\odot$).

As to the class of VMOs, comparing the plots, we notice the absence of VMOs at high initial metallicity. This is linked to the behavior of M_He, which is larger at decreasing metallicity for the same initial stellar mass (see Fig. 3.4). In particular, this is more evident for the DBH objects, which occur only at very low metallicity. This result is in agreement with previous studies (Portinari et al. 1998; Umeda & Nomoto 2002; Heger et al. 2003; Nomoto et al. 2013).

It is interesting to note that the at $Z = 0.006$ stars with $M_\mathrm{i} > 100\,M_\odot$ evolve as PPISNe and PISNe (upper right panel). This result seems supported by recent observations of overluminous supernovae at metallicity $Z_\odot/3$, that are interpreted as the occurrence of PISNe by stellar models (Kozyreva et al. 2014b). This would imply the occurrence, hence the chemical enrichment, of pair instability events in the local Universe.

4.1 Chemical ejecta

In this section we present the chemical ejecta of massive and very massive stars. The reference grid of models is extracted from the *PARSEC* database (Bressan et al. 2012; Tang et al. 2014), for initial mass from M_mas to $350\,M_\odot$ and initial metallicity which ranges between $Z = 1 \cdot 10^{-4}$ and

Z = 0.02.

For each stellar model we computed the amount of ejected material, E_j, in the form of the elemental species *j*, summing up the contributions due to the stellar winds (E_j^w), the overlying layers above the CO core just before the explosion (E_j^{ov}), and the supernova (E_j^{sn}):

$$E_j = E_j^w + E_j^{ov} + E_j^{sn} \tag{4.8}$$

We note that, depending on the assumed final fate scenario, some terms may be null, e.g. $E_j^{ov} = 0$ for WC stars, $E_j^{sn} = 0$ for failed SN (see Sects 4.0.3).

The elements here considered include most important species and related isotopes from H to Ge. It is worth recalling that the elements explicitly considered in the nuclear networks adopted in *PARSEC* are all the isotopes from ^{1}H to ^{28}Si. Heavier elements are present in the initial chemical composition, according to the adopted scaled-solar mixture (see Sect. 3), and are not affected by the nuclear reactions and mixing events during the hydrostatic H- and He-burning phases. The contribution of the subsequent explosive nucleosynthesis is tailored to the *PARSEC* models with the aid of proper calculations taken from the literature, as detailed below.

4.1.1 Wind ejecta

The mass in the form of the element *j* ejected by stellar winds from a star with initial mass M_i is calculated using the equation:

$$E^w_{jM_i} = \int_0^{\mathcal{T}_H+\mathcal{T}_{He}} \dot{M}(M_i, t) X_j^S(t) dt, \tag{4.9}$$

where the integral is performed over the H- and He-burning phases (with lifetimes $\mathcal{T}_H$ and $\mathcal{T}_{He}$, respectively), $\dot{M}(t)$ is the current mass loss rate, and $X_j^S(t)$ is the surface abundance (in mass fraction) of species *j* at current time *t*.

Figures 4.12 and 4.13 show the wind ejecta of the main elements considered in the *PARSEC* models, as function of initial stellar mass, for different metallicities. For $M_i \leq 100\,M_\odot$ the general behavior is the increase of the wind ejecta with initial mass and metallicity, which is related to the strengthening of stellar winds at higher luminosities and larger abundances of metals. This applies to H, He, N, Ne, Na, Mg, Al, and Si. The trend is inverted in the case of C and O. At metallicities Z =0.004, 0.006 the wind ejecta from stars more massive than $100\,M_\odot$ are higher by up to one order of magnitude for C and up to two orders of magnitude for O, compared to those contributed at Z=0.017, 0.02. This result is explained considering the stage at which stars of different initial

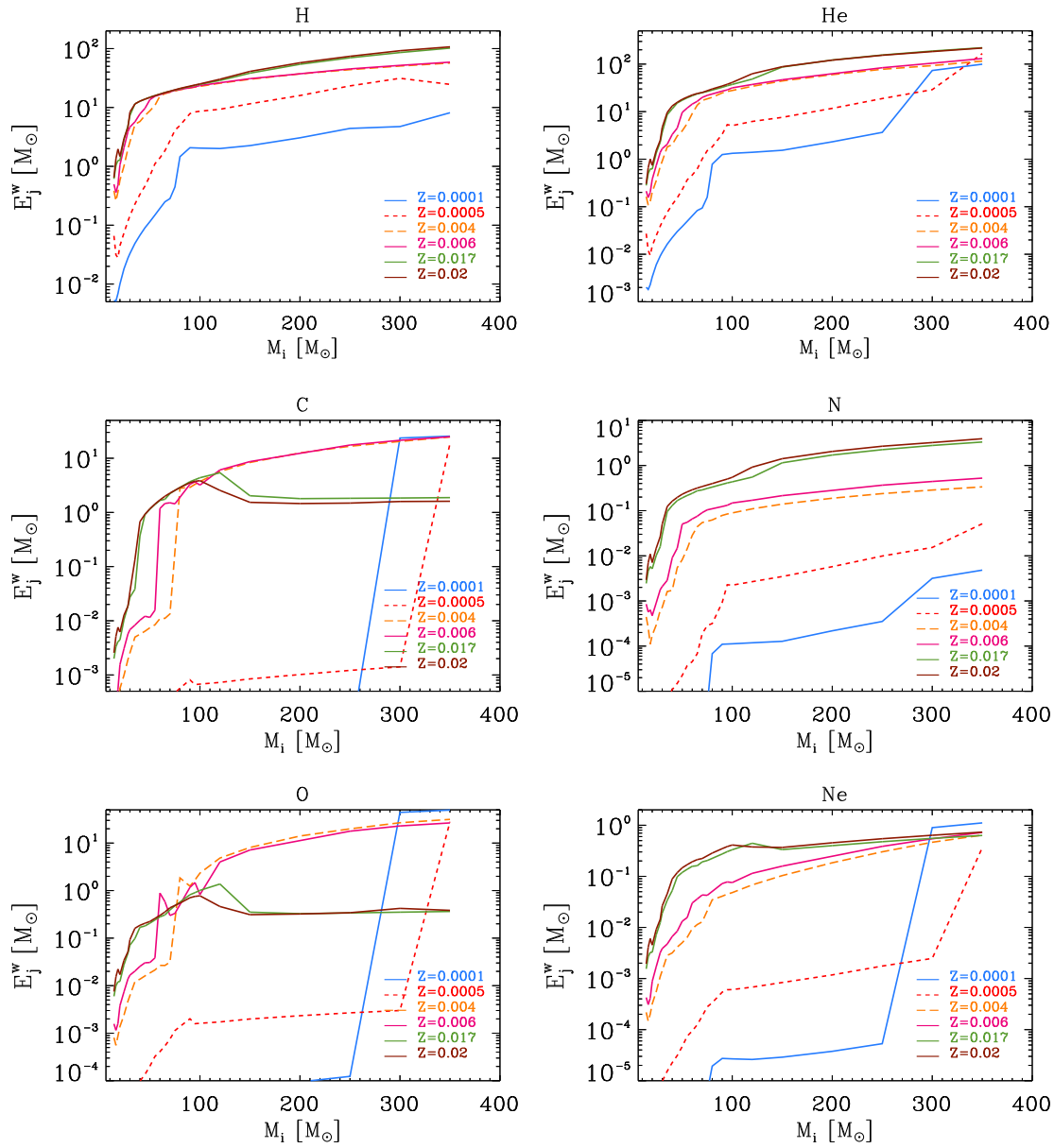

Figure 4.12: Wind ejecta of H, He, C, N, O, Ne as function of M_i, for mass range between M_{mas} to 350$M_\odot$. Models are taken from the last version of *PARSEC* [Tang et al. (2014)].

masses and metallicities enter the WC and WO phases, which are characterized by strong winds enriched in C and O.

Figure 4.14 shows the reduction of the total stellar mass as function of time for very massive

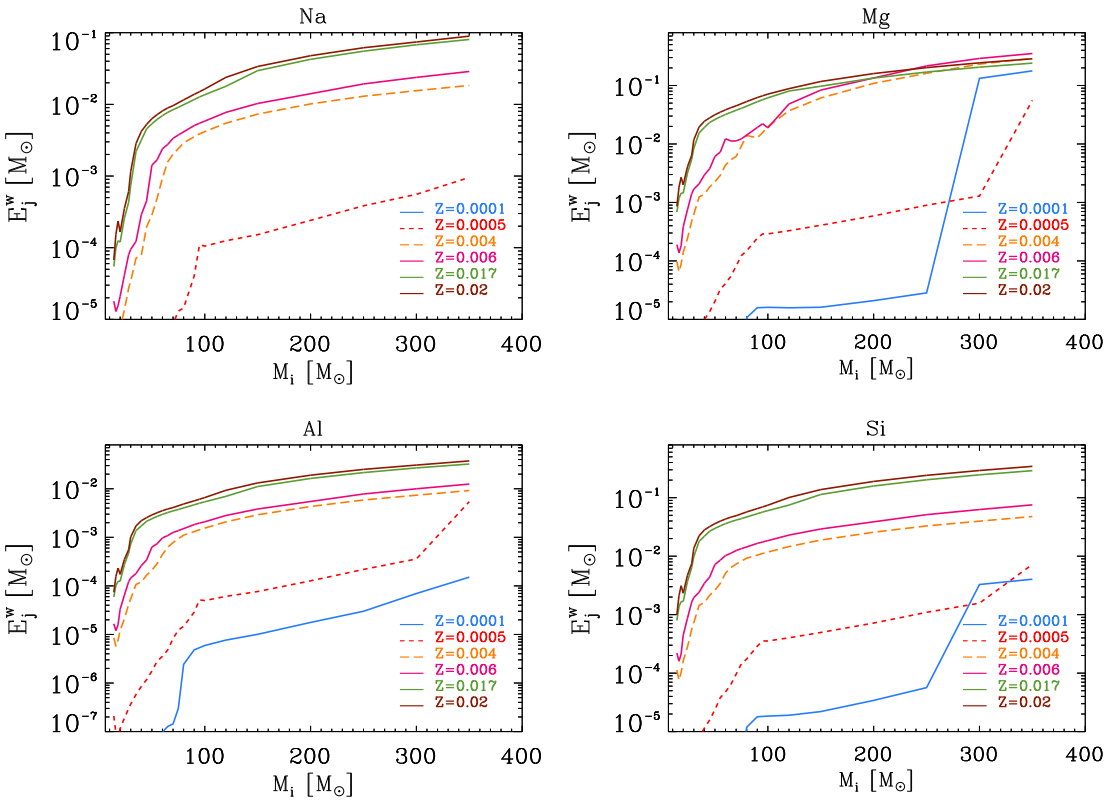

Figure 4.13: Wind ejecta of Na, Mg, Al and Si as function of M_i, as the figure 4.12.

stars with M_i = 150, 250, 350 $M_\odot$ and three choices of the initial metallicity. At Z=0.02 all VMOs experience high mass loss before entering in the WC regime, which is attained close to the end of the He-burning phase. We note that these models are not expected to go through the WO regime. As a consequence, the ejecta are characterized by low amounts of primary C and O. Conversely, at lower metallicities, Z=0.0001 and 0.004, due to the relatively weak stellar winds during the early evolutionary stages, VMOs reach the WC and WO regimes with a much larger stellar mass, hence producing higher ejecta of C and O.

4.1.2 Explosion ejecta

For stars that undergo successful SN explosions we calculated the chemical ejecta coupling the *PARSEC* models to explosion nucleosynthesis calculation available in the literature, depending on the type of explosion (CCSN, PISN or PPISN).

Concerning the CCSNe, we adopted the supernova ejecta provided by Chieffi & Limongi

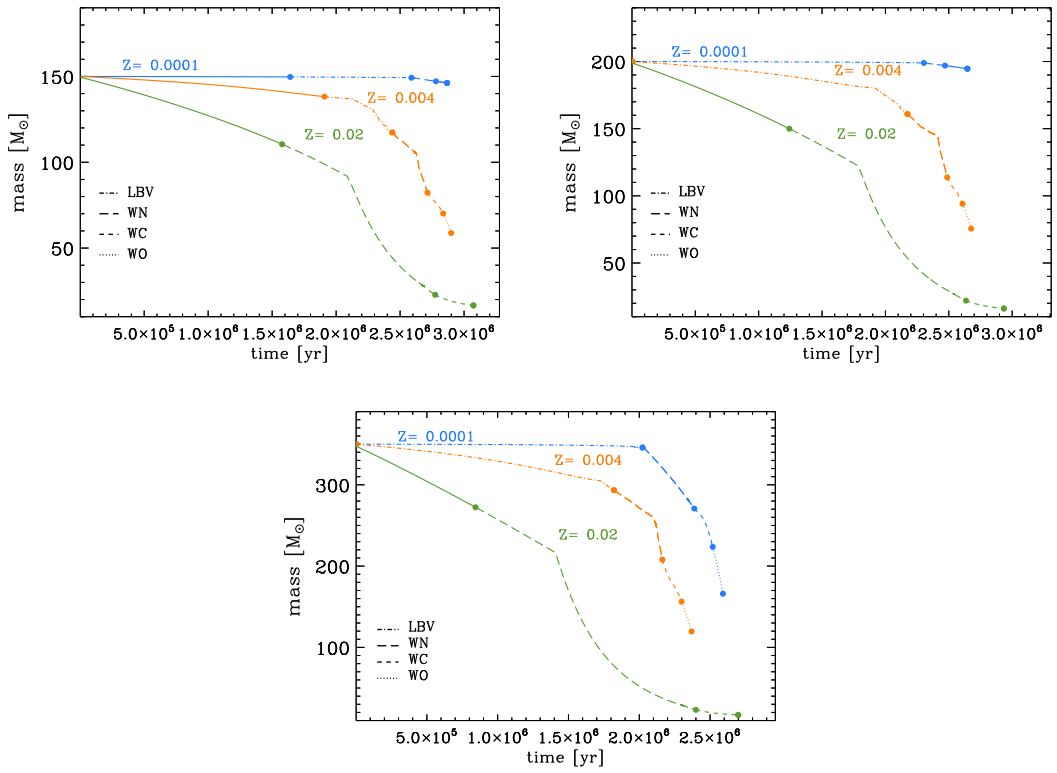

Figure 4.14: Stellar mass as function of time, for initial metallicity Z=0.0001, 0.004 and 0.02 and initial mass $150\,M_\odot, 200\,M_\odot, 300\,M_\odot$ and $350\,M_\odot$. Different evolutionary phases are labeled with different line-styles, as indicated in the legenda. Continuum lines represent the evolution prior to Wolf Rayet phase or LBV phase.

(2004) (hereafter CL04), which consist of tables of isotopes obtained from models with initial mass between $13\,M_\odot$ and $35\,M_\odot$, with initial metallicity $Z = 10^{-4}$, $Z = 10^{-3}$, $Z = 6 \cdot 10^{-3}$, $Z = 2 \cdot 10^{-2}$. A few simplifying assumptions are adopted.

First, we assume that the amount of mass surrounding the CO core at the time just before the explosion is ejected during the SN event keeping its chemical composition unchanged. This seems reasonable since, as discussed by Limongi & Chieffi (2003), when the shock front reaches the outer edge of CO-core, its temperature has dropped down to $\sim 10^9$ K and the explosive nucleosynthesis is essentially extinguished. This fact is confirmed by figure 4.15, which shows the abundance profile of the elements ^{12}C, ^{14}N, ^{15}N, ^{16}O, ^{24}Mg, ^{26}Al, ^{28}Si and ^{32}S obtained from Limongi & Chieffi (2006) database. The values of M_{He} and M_{CO} are obtained from CL04 data using, respectively, the depletion of H and ^{4}He radial profile, with the threshold value of 10^{-4}. The plot of Fig. 4.15 con-

firms that all the abundance profiles remain unchanged out of M_{CO}. However, we do not take into account the possible production of ^{15}N from neutrino nucleosynthesis and a possible formation of an α-rich freeze-out in the ejecta of ^{4}He.

As consequence of this assumption, the elements ejected by the supernova explosion are divided in two groups: those that is nuclearly processed by the shock wave passage (included in the region between M_{CO} and M_{rem}), and those whose abundances remain unchanged nuclear composition remain unchanged (outside the CO-core at the time just before the explosion). The latter group forms the so called *overlayer*.

Second, for the same M_{CO}, the kinetic energy of our ejecta at infinity may be different from those of CL04 models, as the mass and the physical structure of the layers above the core are not the same. This issue is alleviated by the fact that, following the analysis of Limongi & Chieffi (2003), for sufficiently large stellar masses the supernova yields are found to be mainly controlled by the adopted mass-cut, rather than the kinetic energy. This important result mitigates the inconsistency and allows us to explore various assumptions on the mass location of the mass-cut and their impact on the chemical yields (see Sect. 4.0.1).

Third, another difference is related to the choice of the rate for the critical reaction $^{12}C(\alpha,\gamma)^{16}O$. In our *PARSEC* models we use the rate from Buchmann (1996), while in Chieffi & Limongi (2004) the rate of Kunz et al. (2002). In the range of temperature $0.1 - 1.0$ GK the relative difference between the two versions is relatively small (within 10 and 30%).

In order to obtain the explosion ejecta, we proceed as follows. The overlayer ejecta are estimated directly from PARSEC tracks, using the structure profiles. The explosion ejecta are obtained using the CL04 database. We first estimated the remnant masses (see sec. 4.0.1). Then, we interpolate the ejecta of CL04 database using the CO-core mass and remnant masses as parameter, since the explosion ejecta are included between these mass coordinates. Finally, for each track and each element considered, we summed up the explosion ejecta with the correspondent overlayer. The PARSEC tracks for which we obtained the explosion ejecta are the progenitors of the successful CCSNe. We remind that the initial masses included in this group are from $8\,M_{\odot}$ to $\sim 30-50\,M_{\odot}$, depending on the initial metallicity and the explosion model used to classify them. The corresponding CO-core-masses range from $2.2-2.5\,M_{\odot}$ to $7.8-10.9\,M_{\odot}$, depending on initial metallicity and explosion model used. Since the CO-core interval cof CL04 database spans from $\sim 2.01\,M_{\odot}$ to $\sim 10.23\,M_{\odot}$, the extrapolation is small.

The ejecta of PPISNe are obtained by the pure He-core ejecta of Woosley & Heger (2015), using the mass of He-core as parameter. We assume that the explosive nucleosynthesis of PPISNe is entirely included in the He-core, as confirmed by Heger & Woosley (2002); Woosley & Heger

(2015); Woosley (2016). Also the remnant masses of PPISNe are obtained by interpolating the values of Woosley & Heger (2015), using the mass of He-core as parameter. The explosion ejecta are then summed up with those that form the envelope, which are pushed away by the explosion. The overlayer ejecta are obtained only using *PARSEC* tracks, considering as *overlayer* the region out of He-core.

Concerning the PISNe, we used the databases of Heger & Woosley (2002) and Kozyreva et al. (2014b), which provide the explosion ejecta for stars with He core in the range between $65\,M_\odot$ and $133\,M_\odot$ ($150\,M_\odot \lesssim M_i \lesssim 270\,M_\odot$) at Z=0 and Z=0.001 respectively.

Since the explosive nucleosynthesis of PISNe can be reasonably considered as confined in the He-core region (Woosley & Heger 2015), we consider the ejecta of pure He-cores, derived from Heger & Woosley (2002) for Z=0 and Kozyreva et al. (2014b) for Z=0.001. We first estimate the contribution of helium ejecta that come from the He-core (E_{He}^{core}) from those of the envelope (E_{He}^{env}). Assuming that all the hydrogen ejected comes from the envelope, we derive the average abundance of hydrogen from the relation $< H >= E_H/(M_{fin} - M_{He})$, in which E_H is the hydrogen ejected during the pair instability event. With the hypothesis that the metallicity in the envelope remains constant, we can derive the average abundance of helium in the envelope using the relation $< He >= 1 - Z - < H >$. Therefore, the helium ejecta that become from the envelope are $E_{He}^{env} =< He > (M_{fin} - M_{He})$. We precise that the ejecta of Kozyreva et al. (2014b) also include the stellar winds, which we separate from the pure-He core ejecta. Finally, we obtained the contribution of helium that comes from the He-core using the relation $E_{He}^{core} = E_{He}^{tot} - E_{He}^{env}$, in which E_{He}^{tot} is the total amount of He ejecta. For the elements heavier than helium, we used the relation $E_i^{core} = E_i - X_{i,0}(M_{fin} - M_{He})$, where $X_{i,0}$ is the initial abundance of the elements *i*. We assume that the envelope initial metallicity does not vary during the pre-supernova evolution.
After deriving the pure-helium-core ejecta from the data of Kozyreva et al. (2014b), we interpolate in the mass of He-core to obtain the ejecta relative to our models. Also for the PISNe, we added the overlayer ejecta, obtained from *PARSEC* code, to the elements ejected in the explosion.

Results and comparison with other authors

Figures 4.16 and 4.17 compare the wind ejecta of our models to those provided by Portinari et al. (1998), Hirschi et al. (2005b) and Pignatari et al. (2016) (labeled as Po98, Hi05 and Pi16, respectively), for stars at initial metallicity Z=0.02. The main characteristics of the models used are represented in the table 4.3.

From the comparison between our wind ejecta with other sets of winds we derive some considerations. For stars less massive than $30\,M_\odot$ the stellar rotation enhances the amount of mass

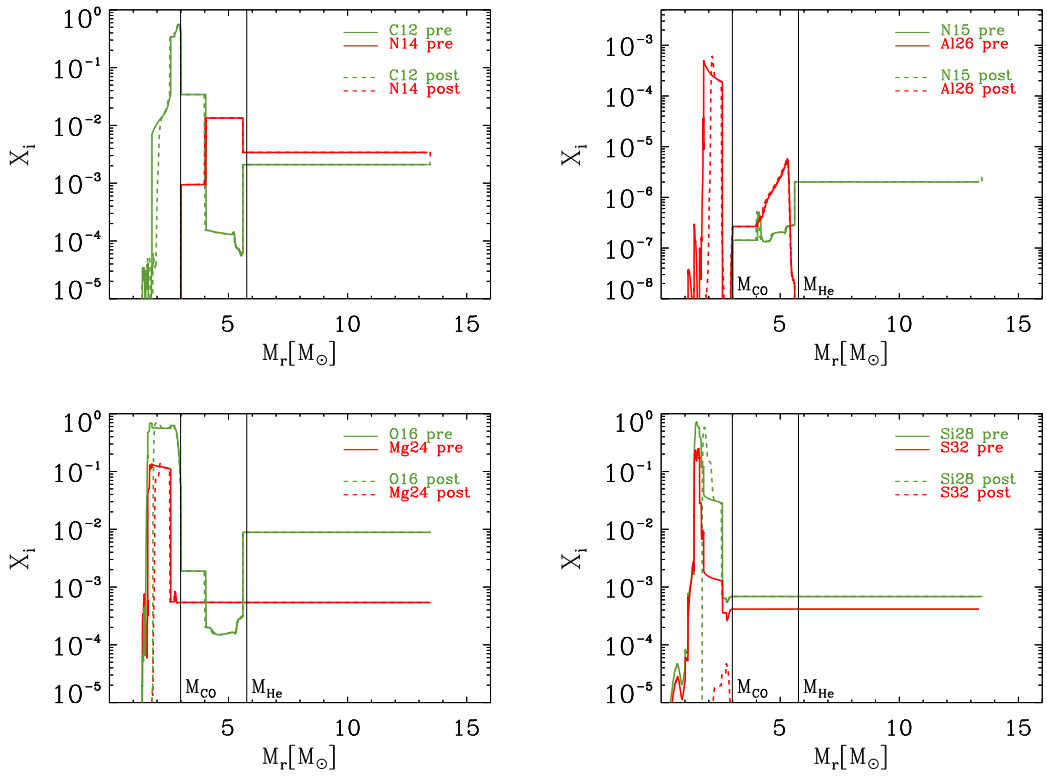

Figure 4.15: Structure profile of some elements ejected in the supernova explosion of a star with $M_i = 15\,M_\odot$ and $Z = Z_\odot$. Solid lines represent the profiles before explosion, while dotted lines are relative to profiles after explosion. The data are taken from Limongi & Chieffi (2006) dataset.

ejected (e.g., models of Hirschi et al. 2005b), because the mass-loss rate is directly proportional to the equatorial surface rotation velocity (Heger et al. 2000b). Moreover, the rotational mixing increases the helium core masses and enriches the stellar envelopes with products of hydrogen burning (Heger et al. 2000b). The effect is more evident for the elements produced by the CNO and Ne-Na cycles, which are mixed up in the envelope and dredged-up to the surface of the star.

In absence of rotation the figures 4.16 and 4.17 show similar trends in the amount of wind ejecta provided by different authors. Differences are more evident for carbon wind ejecta, for which the maximum difference is about one order of magnitude. The reason of different behaviors can be attributed to different amount of mass lost during the pre-SN evolution. Figure 4.18 shows the values of pre-SN mass obtained by different evolution models. We note that stars with initial mass higher than $\sim 20\,M_\odot$ develop pre-SN masses that differ by a factor 2-3 and even a factor of 5 for stars more massive than $\sim 60\,M_\odot$. If stara experience strong mass loss episodes, a large part of

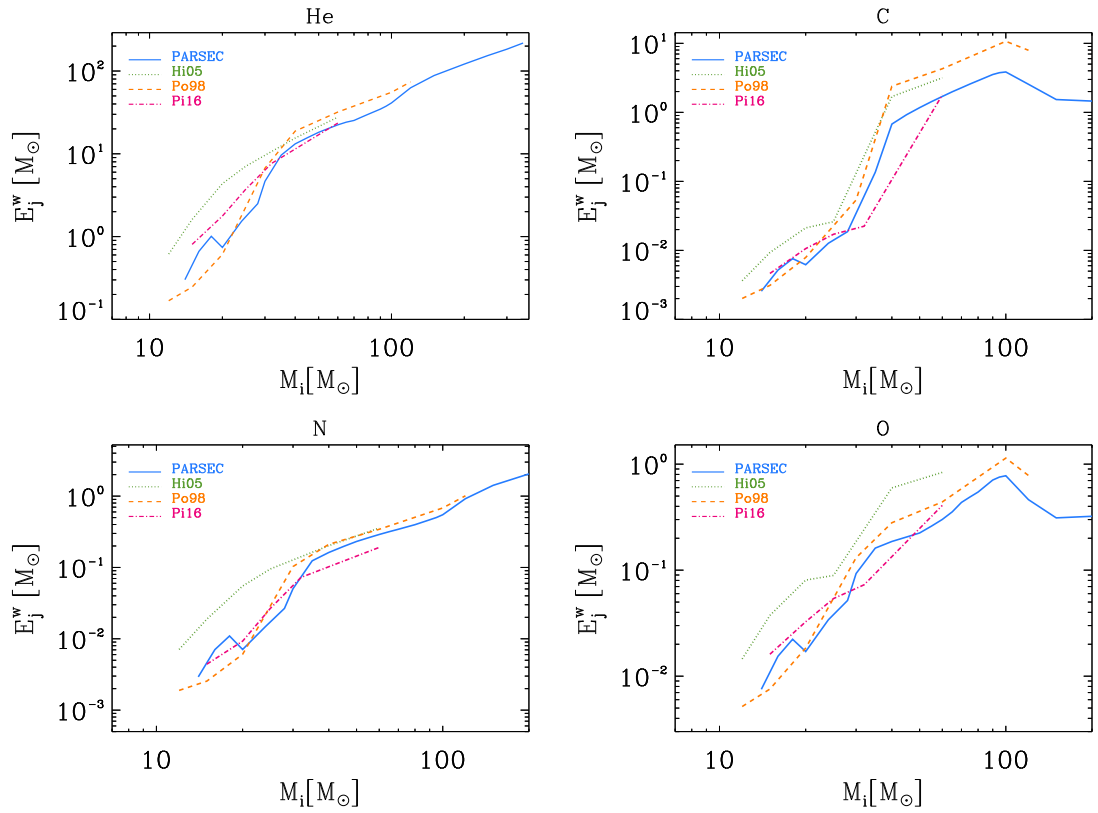

Figure 4.16: Comparison between our wind ejecta of He, C, N, O and those provided by Portinari et al. (1998); Hirschi et al. (2005b); Pignatari et al. (2016), labeled as Po98, Hi05 and Pi16, respectively.

the envelope is removed and the products of nucleosynthesis may be exposed to the surface. This circumstance applies to the WR phase that is experienced by stars more massive that $\sim 40\,M_\odot$ at Z=0.02. Other sources of discrepancies can be attributed to different initial chemical composition adopted. For instance, the solar C abundance measured by Anders & Grevesse (1989) is 8.56 (expressed in standard notation $A(Y) = \log(n_y/n_H) + 12$), while the abundance of Caffau et al. (2011) is 8.50. The fractional mass abundances are $X_C = 4.356 \cdot 10^{-3}$ and $X_C = 2.548 \cdot 10^{-3}$, respectively.

Additional effects can be due to input parameters of different models, such as overshooting parameter, initial chemical composition, and stellar opacities.

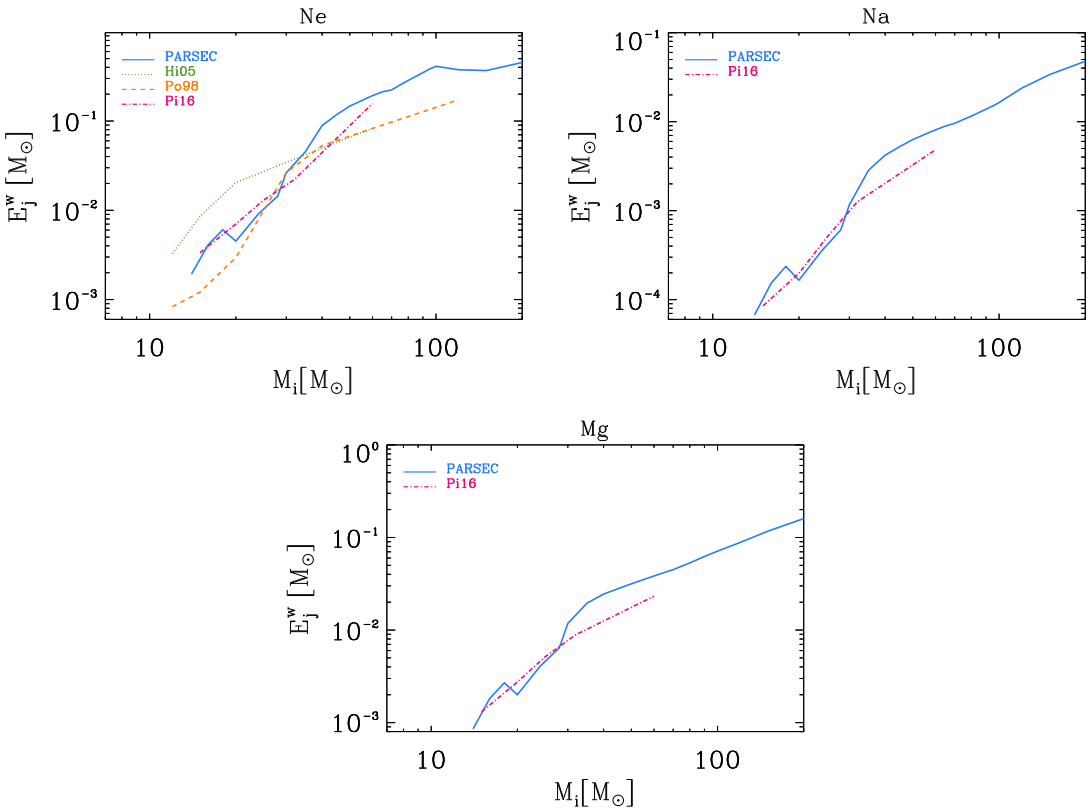

Figure 4.17: Comparison between our wind ejecta of Ne, Na, Mg and those provided by Portinari et al. (1998); Hirschi et al. (2005b); Pignatari et al. (2016), labeled as Po98, Hi05 and Pi16, respectively. All authors adopt an initial metallicity Z=0.02

4.2 Integrated ejecta and production factors

We calculate the wind and explosion ejecta integrated over the initial mass function (IMF) of Kroupa (2001), for a single stellar population (SSP) of $10^6\,M_\odot$. The IMF adopted is the equation (2) of Kroupa (2001). It follows the relation

$$\phi(M) = A \cdot M^{-\alpha_i} \tag{4.10}$$

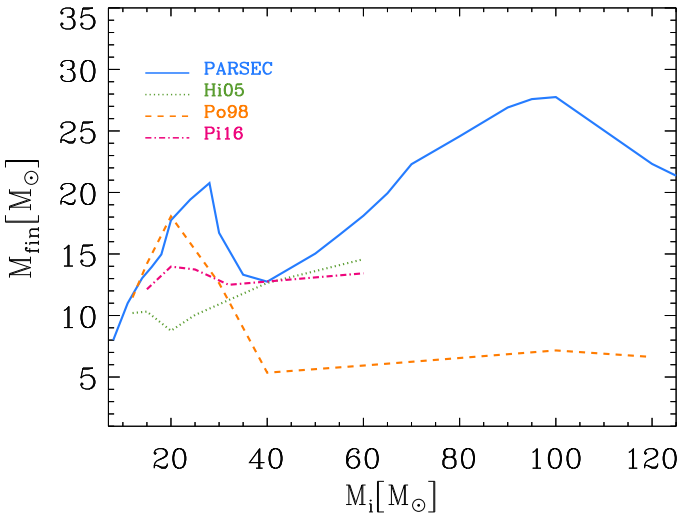

Figure 4.18: Comparison between our pre-SN masses with those obtained by, Portinari et al. (1998); Hirschi et al. (2005b); Pignatari et al. (2016), labeled as Po98, Hi05 and Pi16, respectively.

where:

$$\begin{aligned} \alpha_0 &= 0.3 \pm 0.7, \quad 0.01\,M_\odot \leq M_i < 0.08\,M_\odot \\ \alpha_1 &= 1.3 \pm 0.5, \quad 0.08\,M_\odot \leq M_i < 0.50\,M_\odot \\ \alpha_2 &= 2.3 \pm 0.3, \quad 0.50\,M_\odot \leq M_i < 1\,M_\odot \\ \alpha_3 &= 2.3 \pm 0.7, \quad M_i \geq 1\,M_\odot \end{aligned} \tag{4.11}$$

The value of the constant A is obtained by the relation:

$$\int_{0.1}^{350} \phi(M_i) dM_i = 10^6\,M_\odot \tag{4.12}$$

where the quantity $10^6\,M_\odot$ is the mass of SSP considered in this case.

The equations used to obtain the integrated yields are:

$$E_j^{w,int} = \int_{0.1}^{350} \phi(M_i) E_j^w(M_i) dM_i \tag{4.13}$$

Table 4.3: Stellar model used for our wind comparison and their main characteristics.

Input physics	Portinari et al. (1998)	Hirschi et al. (2005)	Pignatari et al. (2016)
evolution code	Padova evolution code (Bressan et al. 1993)	Geneva stellar evolution code (Hirschi et al. 2004)	GENEC (Eggenberger et al. 2008a; Bennett et al. 2012)
nitial mass range	0.6-120 $M_\odot$	12-60 $M_\odot$	from low mass to 60 $M_\odot$
initial metallicity range	$0.0004 \leq$ Zle0.05	Z=0.02	Z=0.02 and Z=.01
initial chemical abundances	Anders & Grevesse (1989) and Hannaford et al. (1992)	Maeder & Meynet (2001) for elements lighter than Mg, Anders & Grevesse (1989) otherwise	Anders & Grevesse (1989)
nuclear reaction rates	Caughlan & Fowler (1988), including the rate of $^{12}C(\alpha,\gamma)^{16}O$	NACRE compilation (Angulo et al. 1999b)	NACRE compilation (Angulo et al. 1999b)
opacities	OPAL opacity tables (Iglesias & Rogers 1993)	OPAL type 2 opacity tables and Ferguson et al. (2005) opacity tables	OPAL type 2 opacity tables and Ferguson et al. (2005) opacity tables
mass loss prescriptions	de Jager et al. (1988) for stars under the Humphreys-Dadivdson limit. For Wolf-Rayet stars,the laws of (Langer 1989) are used. The $\dot{M}$-Z relation is obtained from Kudritzki et al. (1989)	Vink et al. (2001) and Vink et al. (2000) for BSG, and the law of de Jager et al. (1988) for RSG	Vink et al. (2001) for stars with $T_{eff} \geq 3.9$ K and from de Jager et al. (1988) otherwise. During the WR phase, the mass loss rates of Nugis & Lamers (2000) are used
core overshooting parameter	0.25H_p in the range $1.0\,M_\odot \leq M_i \leq 1.5\,M_\odot$ and 0.5 H_p above it	0.1H_p for H- and He-burnings	0.2H_p for H- and He-burning
initial rotation velocity	0 Km/s	0 Km/s	0 Km/s and 300 Km/s

for stellar winds, and

$$E_j^{sn,int} = \int_{0.1}^{350} \phi(M_i) E_j^{sn}(M_i) dM_i \tag{4.14}$$

for the explosion ejecta. The quantities $E_j^w(M_i)$ and $E_j^{sn}(M_i)$ are, respectively, the wind and explosion ejecta of element j, as function of M_i.

The integrals of equations 4.13 and 4.14 are calculated separately for the three classes of supernovae: CCNSe, PPISNe and PISNe. In each case the chemical contribution comes from specific mass intervals, being null elsewhere.

The results for three values of the initial metallicity, namely Z=0.0001, 0.004, and 0.014, are shown in figures 4.19, 4.20 and 4.21, for the entire set of chemical elements. For each class of stars we distinguish the wind (blue squares) and the explosion (red circles) components. The

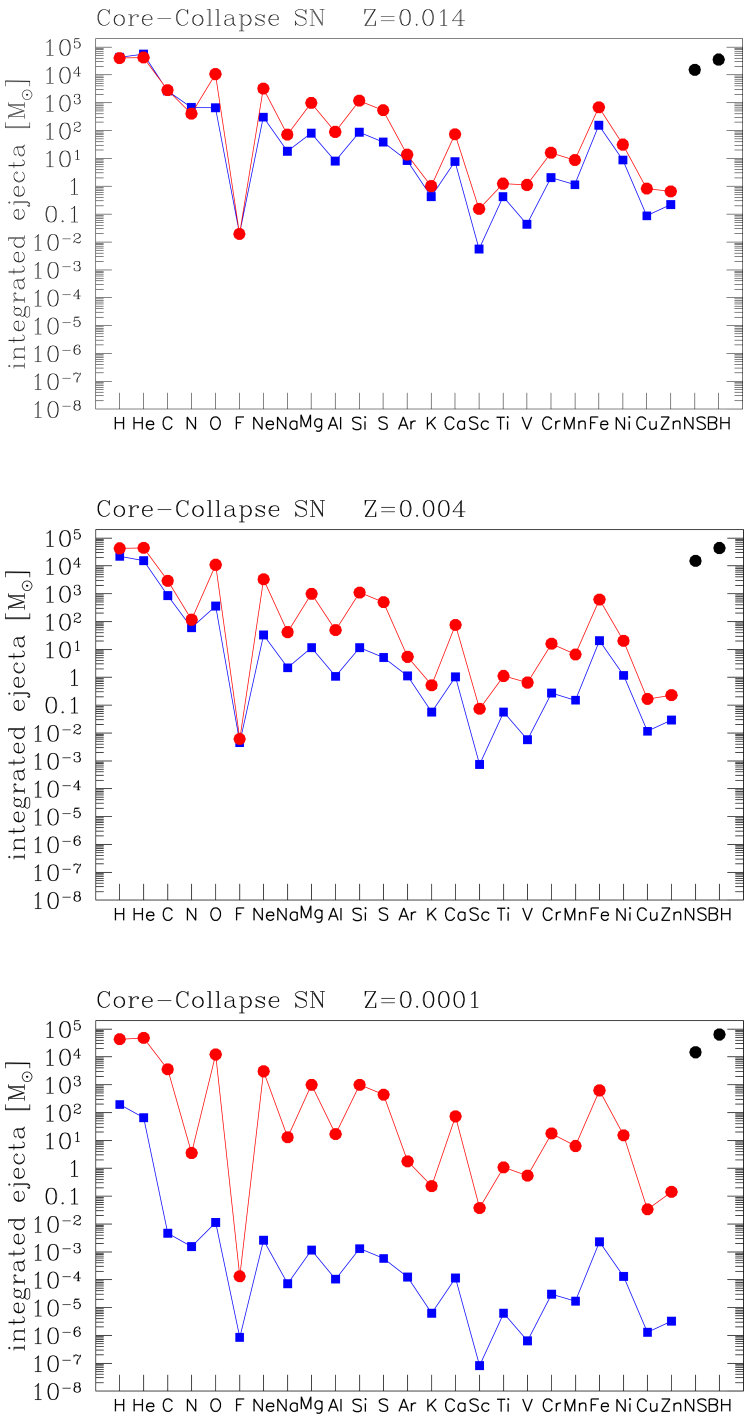

Figure 4.19: Ejecta of massive stars that end their evolution as CCSNe. Stellar ejecta (winds and explosion) are integrated over the Kroupa IMF (Kroupa 2001) for simple stellar population of $10^6\,M_\odot$, and three choices of the initial metallicity Z=0.001,0.006 and 0.014. The IMF limits are $8\,M_\odot$ and $\sim 30\,M_\odot$. Red circles indicate the explosion ejecta, while blue squares show the wind ejecta. Black circles are the contributions in the form of NS and BH. The supernova ejecta are obtained with a criterion based on the bi-parametric method of Ertl et al. (2016) for explosion.

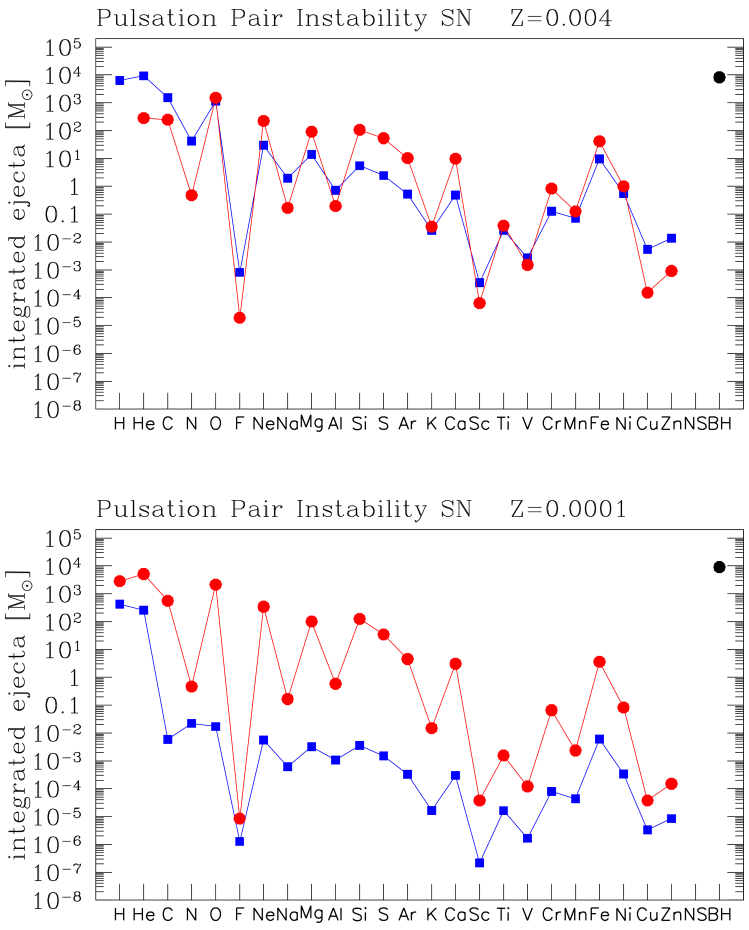

Figure 4.20: The same as in figure 4.19, but for the stars that experience the PPISN events. Note the absence of the case with Z = 0.014. The IMF limits are $M_i \sim 77\,M_\odot$ and $M_i \sim 115\,M_\odot$ for Z = 0.0001, and $M_i \sim 99\,M_\odot$ and $M_i \sim 190\,M_\odot$ for Z = 0.004.

.

contribution in compact remnants (neutron stars and black holes) is also shown.

A few aspects are worthy of consideration for each class of stars. Let us start with CCSN. We recall that, given the adopted criterion for the final fate (see sections 4.0.1 and 4.0.2), successful CCSNe correspond to almost the same initial mass range, $\sim 8\,M_\odot - 30\,M_\odot$, for the three metallicities.

Most of the integrated explosion ejecta from CCSNe appear to be weakly sensitive to the initial metallicity, a fact that was already discussed by Chieffi & Limongi (2004); Prantzos (2011). This

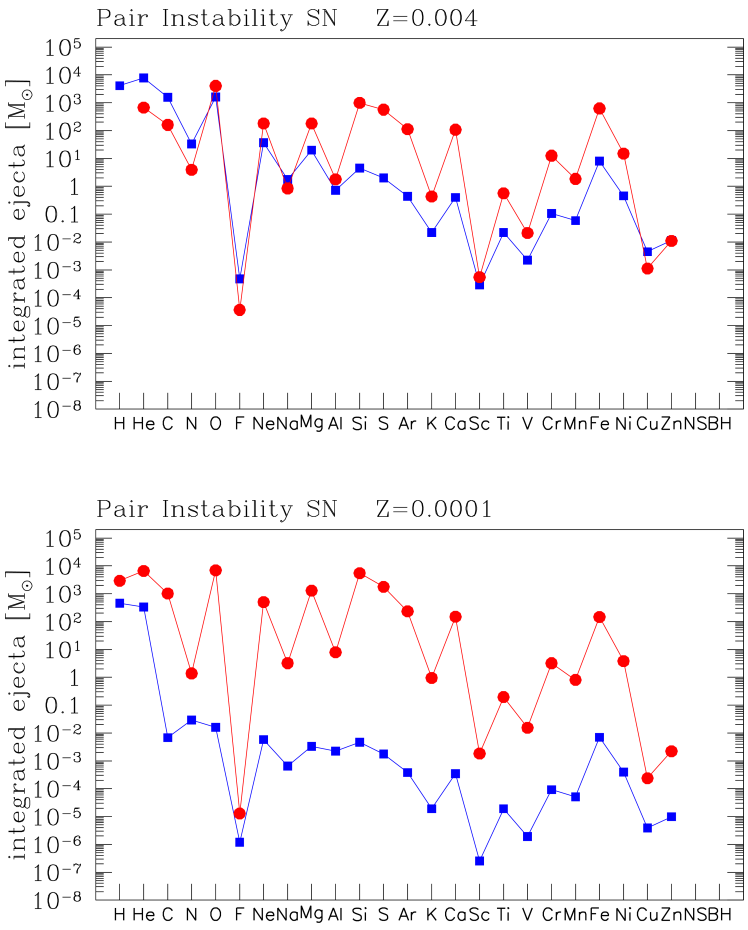

Figure 4.21: he same as in figure 4.19, but for the stars that experience the PISN events. Note the absence of the case with Z = 0.014. The initial mass window chosen is from $M_i \sim 116\,M_\odot$ to $M_i \sim 230\,M_\odot$ for Z = 0.0001, and from $M_i \sim 190\,M_\odot$ to $M_i \sim 350\,M_\odot$ for Z = 0.004

can be understood considering the secondary and primary origin of the elements. In brief, while the most abundant isotope of each even element is of primary origin (explosive and/or hydrostatic), the ejecta of the odd elements always have a combination of a primary and a secondary contributions. For the odd species the primary component is present also when the secondary component tends to decrease at lower metallicities. A notable exception is nitrogen, which is produced mainly by the CNO cycle, and its abundance depends directly on the initial abundances of carbon and oxygen in the original composition. Conversely, the integrated wind ejecta prior to the CCSN explosion are clearly correlated to the initial metal content. This can be explained considering that at decreasing

Z the elemental abundances in the initial chemical mixture are lower, and more importantly, the efficiency of the stellar winds is also weaker.

As to the class of PPISNe, the relevant range of initial masses goes from $M_i \sim 77\,M_\odot$ to $M_i \sim 115\,M_\odot$ at Z = 0.0001, and from $M_i \sim 99\,M_\odot$ to $M_i \sim 190\,M_\odot$ at Z = 0.004. The PISN events are expected to occur in the initial mass window from $M_i \sim 116\,M_\odot$ to $M_i \sim 230\,M_\odot$ at Z = 0.0001, and from $M_i \sim 190\,M_\odot$ to $M_i \sim 350\,M_\odot$ at Z = 0.004. No PISNe and PPISNe are predicted to occur at Z = 0.014.

Looking at figures 4.20 and 4.21 we note that the integrated ejecta show the typical odd-even pattern, similarly to the CCSNe. Although the number of these stars is expected to be less than that of the CCSN class, the integrated chemical contribution is not negligible at all. For instance, large amounts of oxygen are ejected as a significant fraction of the oxygen core remains unburnt during the explosive events (Kozyreva et al. 2014c). Also the wind contributions from PPISN and PISN progenitors appear to be comparable to those from CCSN progenitors. It is clear that also in this case the wind ejecta show a direct dependence on the initial metallicity, mostly set by the efficiency of mass loss. As seen in section 4.0.3, at Z=0.0001 the progenitors of PPISNe and PISNe are LBV stars, while at Z=0.004 we found that the VMOs evolve as Wolf-Rayet stars. This fact explains the significant amounts of helium, carbon, oxygen and nitrogen expelled by these stars with Z=0.004. At this metallicity, the wind ejecta for these elements are even larger than the SN contributions, a condition not met at Z=0.0001.

Production factors

We calculated also the production factors of the all elements from H to Zn. The figures 4.22, 4.23 and 4.24 show the production factors integrated over a Kroupa (2001) IMF of our ejecta, for the metallicities Z=0.0001 (rel dashed line), Z=0.004 (blue dot-dashed line) and Z=0.014 (near solar; black solid line). The solid horizontal line is placed at the production factor of oxygen (at $Z = Z_\odot$), and the two dotted black lines are placed at half and twice that value, respectively. For each element, we used the equation (1) of Goswami & Prantzos (2000):

$$p_{f,j} = \frac{\int_{M_{inf}}^{M_{sup}} \Phi(M) E_j(M) dM}{\int_{M_{inf}}^{M_{sup}} \Delta M \Phi(M) X_{j,\odot} dM} \tag{4.15}$$

where, $\Phi(M)$ is the IMF with lower and upper limits M_{inf} and M_{sup}, respectively. ΔM is the total mass lost, and $X_{j,\odot}$ is the solar composition of element j, taken from Caffau et al. (2011). The IMF used is the same as for the integrated ejecta (equation (2) of Kroupa (2001)).

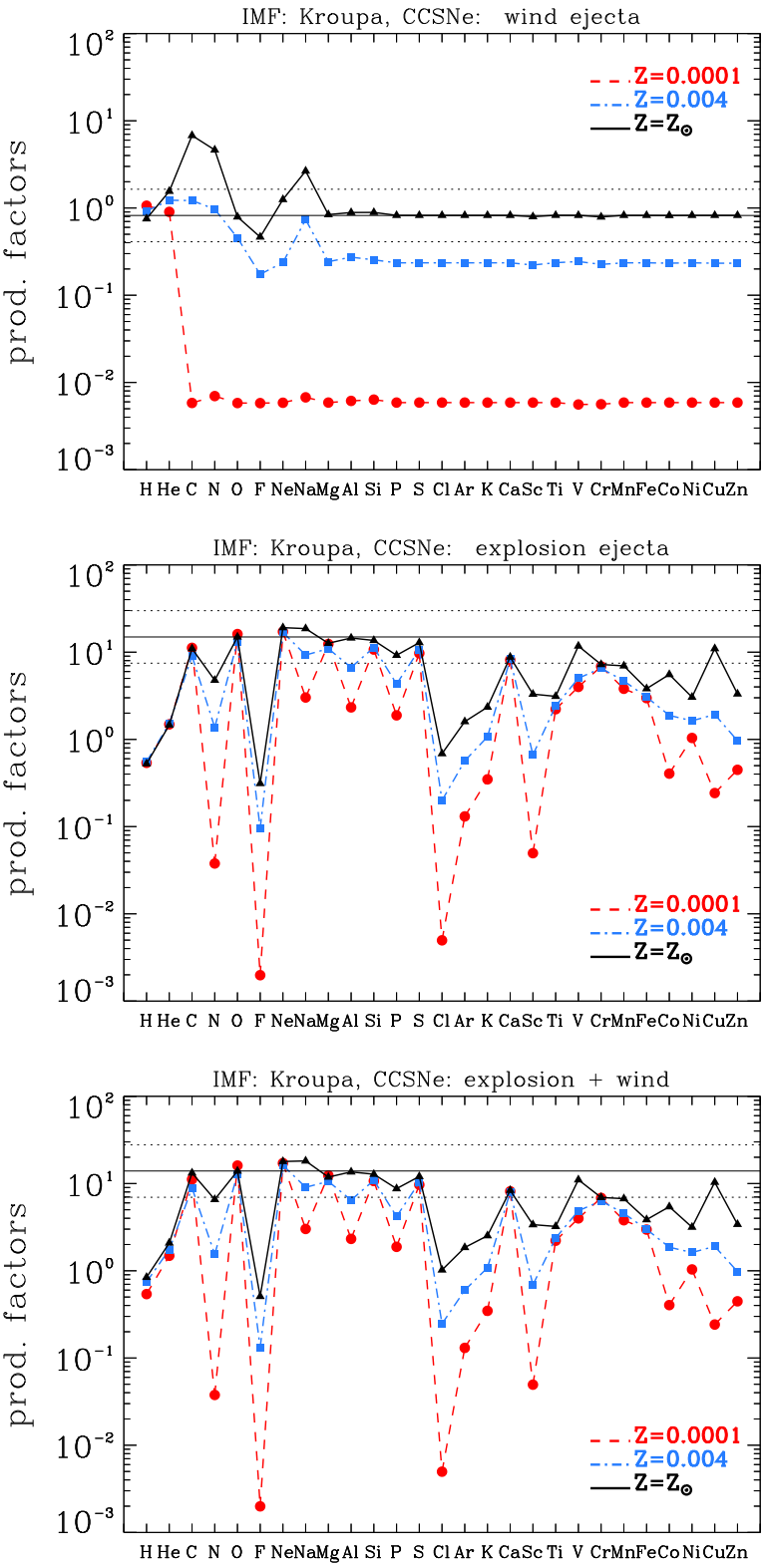

Figure 4.22: Production factors (over a Kroupa (2001) IMF) of CCSNe ejecta for three different initial metallicities (labeled with three different line-style). The contribution of stellar winds (uper panel), explosion ejecta (middle panel) and total ejecta (bottom panel) is represented. The supernova ejecta are obtained with a criterion based on the bi-parametric method of Ertl et al. (2016) for explosion. The solid horizontal lines indicate value of the solar oxygen production factor ($P_{f,O}$), while the dotted horizontal lines are placed at half and twice that value, respectively.

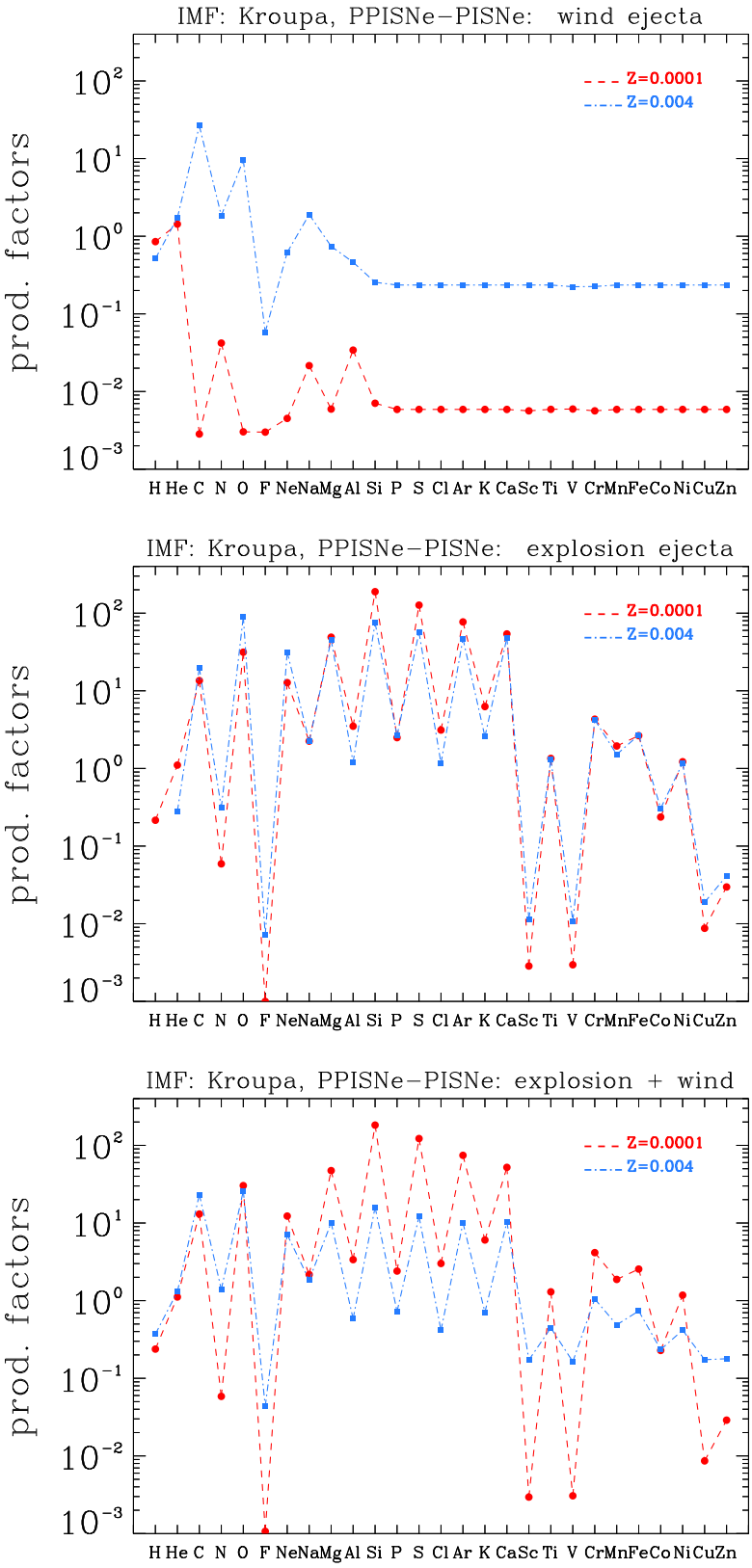

Figure 4.23: The same as in figure 4.22, but for the stars that evolve as PPISNe or PISNe. The supernova ejecta of PISNe are taken from Heger & Woosley (2002) and from Kozyreva et al. (2014b) while for PPSINe we used the data of Woosley & Heger (2015). Note the absence of the case with Z = 0.014.

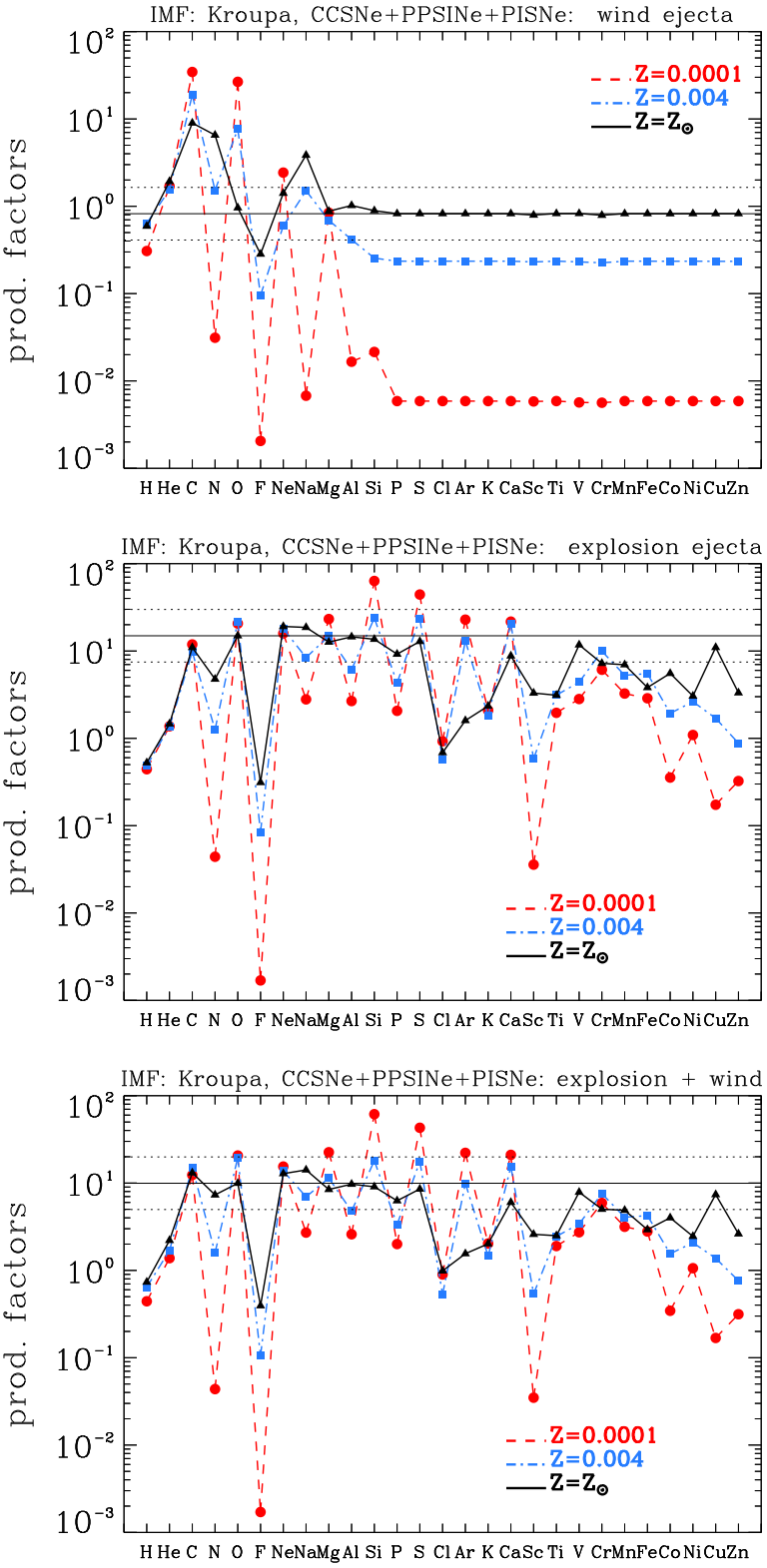

Figure 4.24: The same as in figure 4.22, but in this case the production factors are integrated ove the whole IMF, from $8\,M_{\odot}$ to $350\,M_{\odot}$.

We considered three different choices of lower and upper mass limits, depending on the class of stars considered:

- The class of CCSNe is defined by $M_{inf} = 8\,M_{\odot}$ and $M_{sup} \sim 30\,M_{\odot}$. The upper limit depends weakly on the initial metallicity, for the metallicities here considered.
- The classes of PPISNe and PISNe span over a initial mass interval that varies with initial Z. The mass interval of PPISNe and PISNe is from $M_{inf} \sim 80\,M_{\odot}$ to $M_{sup} \sim 200\,M_{\odot}$ for Z=0.0001 and $M_{inf} \sim 100\,M_{\odot}$ to $M_{sup} = 350\,M_{\odot}$ for Z=0.004. The PPISNe and PISNe do not occur at Z = 0.014.
- As to the the contribution from all classes, i.e. CCSNe, PPISNe and PISNe, the integration is performed from $M_{inf} = 8\,M_{\odot}$ to $M_{sup} = 350\,M_{\odot}$ for all three metallicities.

For each class we produced three different plots, which show the contribution of stellar winds (first plot), explosion ejecta (second plot), and both winds and explosion (third plot).

It is interesting to compare the values of production factors relative to different elements showed in figures 4.22, 4.23 and 4.24.

Core collapse SNe

We first consider the contribution of CCSNe (fig. 4.22).
The upper panel shows the winds contribution due to the progenitor of CCSNe. We consider in the analysis only the progenitors of successful CCSNe. From this plot we deduce that the progenitors of CCSNe contribute to the synthetisation of the light elements He, C, N, O Ne and Na, which are ejected as stellar winds. Furthermore, this contribution enhance with the initial metallicity, as expected by the increasing of the mass loss with Z. In particular, the contribution of carbon and nitrogen ejected in the winds with respect to the total ejecta vary from $\sim 5\%$ at low Z, to $\sim 20\%$ at near solar Z, and from $\sim 15\%$ to $\sim 35\%$, respectively.
Concerning the contribution of explosion ejecta, it is interesting to compare the contribution due to the CCSNe with respect to the VMOs. Figures 4.25 shows the explosion metal yields multiplied by the initial mass function probability $\Phi(M) \propto M^{alpha}$, for two values of metallicities (Z=0.0001 and Z=0.02, respectively). From these plots we deduce that the contribution of metal yields is mostly due to the CCSNe rather than the PISNe or PPISNe, confirming the results of Kozyreva et al. (2014b).

The middle panel of fig. 4.22 shows the explosion ejecta of the successful CCSNe. The CCSNe ejecta are obtained from Chieffi & Limongi (2004) (hereafter CL04). We applied the

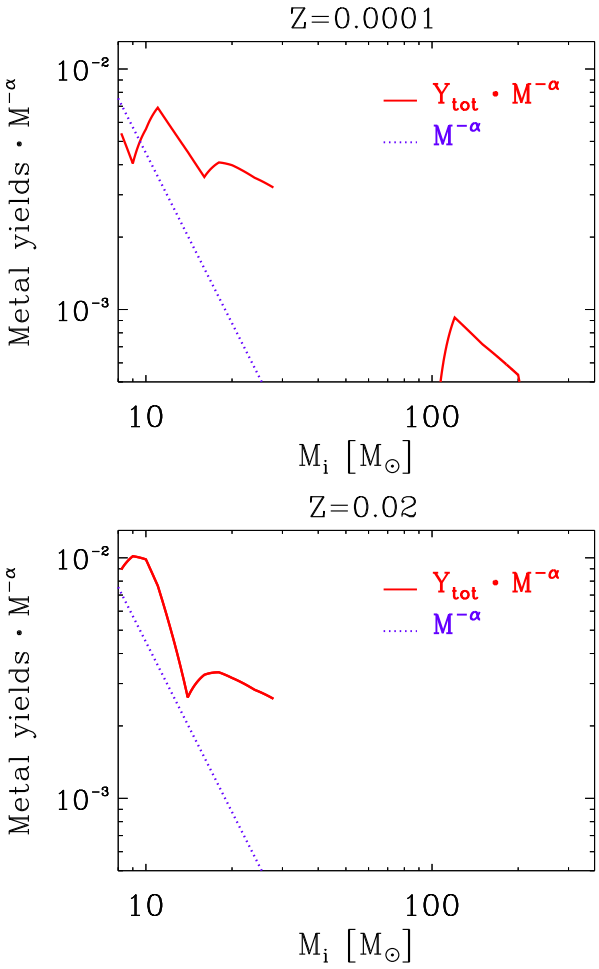

Figure 4.25: Metal yields (red solid line) multiplied by the initial mass function probability ($\Phi(M) \propto M^{alpha}$) as function of initial mass, for metallicities Z=0.0001 and Z=0.02. Dotted violet lines represent the IMF $\phi(M) = M^{-\alpha}$. The y-axis is in arbitrary units.

explodability criterion of Ertl et al. (2016) coupled with the relation between the pre-SN mass and M_{cut} (Umeda & Nomoto 2008) for the remnant mass estimation. We note that the general behavior of our values is similar to those showed in fig. 1 of Goswami & Prantzos (2000), The odd-even effect is pronounced at lower Z. Observations indicate that the dependence of C and N abundance with respect to the metallicities is [C/Fe] ~ 0 and [N/Fe] ~ 0 both in the halo and in the disk (Goswami & Prantzos 2000, fig. 7). This fact implies that the production factors of these two elements do not depend on initial metallicity. We confirm this result for carbon, but not for nitrogen. The discrepancy between our result and the observations is explained by considering that, in massive stars, nitrogen can be produced not only by the original carbon present in the star (secondary nitrogen), but also by the C produced in He-burning zones (primary nitrogen). This second mechanism requires a proton-mixing in He-burning zones, which is not included in the models of LC04. Therefore, the p_f of nitrogen is strongly dependent on initial Z. This result is in agreement with previous the studies of Woosley & Weaver (1995) and Limongi et al. (2000). The α-elements O, Mg, Si, S, Ca and Ti have the [α/Fe]-ratio constant in the halo ([α/Fe] $\sim$ 0.3-0.5), and it declines gradually in the disk (Goswami & Prantzos 2000). This imply that all these elements should not depend on initial metallicity. This is true for O, Si, Ca and S, which are true primaries and our results are in agreement with those provided by (Woosley & Weaver 1995) and Limongi et al. (2000). The elements Mg and Ti seems to show a weakly dependence on the initial Z. The elements K, Sc and V are odd-elements produced mainly by oxygen burning. The first one is produced during the hydrostatic burning while the other two are synthesized during the explosive burning. These three elements are underproduced with respect to the values obtained by (Woosley & Weaver 1995) and Limongi et al. (2000). This is explained by the results of CCSN nucleosynthsis, as discussed in CL04. The iron peak elements are Cr, Mn, Co, Fe, Ni, Cu and Zn. The isotopes with mass number lower than 57 are mainly produced during explosive O and Si burning and in nuclear statistical equilibrium, while the isotopes with A > 57 are produced mostly by the α -rich freeze out, but also by neutron capture during hydrostatic He- and C-burnings (Goswami & Prantzos 2000; Heger & Woosley 2002). Our result for CCSNe shows that the odd-even effect is more evident at low metallicity. Furthermore, the dependence on Z of iron peak elements is stronger for the odd-elements Co and Cu. The production factors of Co at different Z are not in agreement with the observed data showed in fig. 7 of Goswami & Prantzos (2000), in which the Co increases with decreasing Z. Despite this, our result is in agreement with those obtained by Woosley & Weaver (1995), but not with those of Limongi et al. (2000).

Pair instability and pulsation-pair instability supernovae

The contribution of the production factors due to PISNe and PPISNe is showed in fig. 4.23. The ejecta of PISNe are estimated using the data of Heger & Woosley (2002), who provides explosion ejecta at Z=0, and from Kozyreva et al. (2014b), who gives the ejecta at Z=0.001. Concerning the PPISNe, the values of ejecta and remnant masses are estimated using the data of Woosley & Heger (2015). A more detailed explanation of how we obtained these values is given in section 4.1.2.

The first panel of fig 4.23 shows the contribution of the stellar winds produced by the progenitors of PISNe and PPISNe. The behavior is similar to the winds of CCSNe-progenitors: the production id favored at high metallicity for light elements.

Lets consider the second panel of 4.23 show an excess of production of even-charged elements compared to odd-charged elements, which is present both at very low Z and intermediate Z. The odd-even effect of α-element is higher than those produced by CCSNe. Langer et al. (2007) and Yoon et al. (2012) show that the odd-even effect is controlled by the neutron excess. The value of neutron excess of PISNe is $\eta \sim 10^{-5}$, much smaller than the neutron excess achieved in the Si-shell of a typical CCSN ($\eta \sim 10^{-2}$), where explosive nuclear burning occurs during the supernova explosion. Concerning the heavier elements, the nucleosynthetic pattern of iron group-elements is critically determined by the neutronization during the explosive burning and therefore less affected by the initial metallicity, so the odd-even effect is less evident. Furthermore, the second panel of fig. 4.23 shows that the impact of the PISNe on the overall nucleosynthesis pattern is weaker at Z=0.004 than at very low Z (Z=0.0001).

Figure 4.24 shows the production factors of all elements from H to Zn, integrated in the whole IMF, with $M_{inf} = 8\,M_{\odot}$ and $M_{sup} = 350\,M_{\odot}$. It is interesting to compare the two plots: CCSNe explosion+winds (fig. 4.22, third panel) and CCSNe+PPISNe+PISNe explosion+winds (fig. 4.24, third panel). We derive that the PISNe and PPISNe give a major contribution to the production of α-elements with respect to CCSNe, while the iron group elements are mostly produced by explosive nuclear burning of CCSNe.

The PISNe and PPISNe give a large contribution also to the production of light elements. This result is showed in second panel of figures 4.22 and 4.24. The two plots show the production factors of winds due to the progenitors of only CCSNe, and CCNSe+PISNe+PPISNe, respectively. We obtain that, at low metallicities, the progenitors of PISNe and PPISNe give a large contribution to the production of light elements. This fact is explained by considering that these stars experience

violent mass loss episodes during the pulsations that occur at the ignition of core O-burning. These pulsations are the consequence of pair-instability, and they can expell away the entire H-rich envelope. This fact justifies the high amount of wind ejecta produced by these stars.

4.3 Tables of ejecta

In this section we describe in detail the content of the ejecta tables that will be available on-line. Each table includes the ejecta in solar masses for initial mass from M_{mas} to $350\,M_{\odot}$ of a specific initial metallicity, including also the main structure values such as the pre-SN mass (M_{fin}), the mass of He-core (M_{He}), CO-core mass (M_{CO}) and remnant mass (M_{rem}). The pre-SN phase and the type of explosion are also included using the following legenda:

- RSG: red supergiant
- BSG: blue supergiant
- WC: Wolf-Rayet stars with envelope rich in carbon
- WN: Wolf-Rayet stars with envelope rich in nitrogen
- WO: Wolf-Rayet stars with envelope rich in oxygen
- LBV: luminous blue variables

for the pre-SN evolutionary stage (see sec. 4.0.3 for details), and

- sCCSN: successful core collapse SN
- fCCSN: failed core collapse SN
- PISN: pair instability SN
- PPISN: pulsation-pair instability SN
- DBH: stars that direct collapse to black hole without explosion

for the type of explosion. The row named X_i shows the initial composition scaled from the solar abundances of Caffau et al. (2011). The ejecta tables are separated in wind contribution and explosion contribution.
The tables of wind ejecta contain the amount of mass lost by stars during the evolution prior to the supernova event. The elements ejected are both those initially present in the star and those synthesized during the evolution. We produced two versions of winds tables. The first one contains all the wind ejecta of elements from H to Zn, while the second one includes also the isotopes contribution for elements lighter than ^{28}Si. It is important to note that the mass loss prescriptions of *PARSEC* code are included for stars with $M_i \geq 14\,M_{\odot}$. For this reason, the wind ejecta of less massive stars are set to zero.

The tables of explosion ejecta contain the elements ejected by the supernova, which include both those produced by the explosion nucleosynthesis and those that form the envelope. For each metallicity we produced three different tables, depending on the explosion method used to calculate the CCSN ejecta. Two tables are obtained using the mono-parametric prescriptions of Frayer & Taylor (2012), with delayed and rapid explosion models. The third one results from the application of bi-parametric method of Ertl et al. (2016) for explodability, coupled with the $^{56}\mathrm{Ni} - \mathrm{M_{fin}}$ relation for remnant mass estimation. Since we consider the fCCSNe as "non-explosion" events, the ejecta of these stars are set to zero and the value of the remnant masses is set as equal to the correspondent pre-SN mass.

Here we present an example of the tables that will be available on line. We give two tables, one for winds and one for explosion ejecta, for models at Z=0.02 (tables 4.4 and 4.5) Note that, only for stylistic reasons, here we divide the two tables in two parts. Moreover, in the second part of tables 4.4 and 4.5 we repeat the column relative to the initial mass, in order to simplify the reading.

Table 4.4: Wind ejecta in $M_\odot$ for Z=0.02 for elements from H to Zn.

Z_i	Y_i	M_i	M_{fin}	M_{He}	M_{CO}	M_{rem}	pre-SN	SN-type	H	He	C	N	O	F	Neon	Na	Mg	Al
Xi	–	–	–	–	–	–	–	–	6.96e-01	2.84e-01	3.60e-03	9.73e-04	8.82e-03	6.61e-07	2.02e-03	4.71e-05	8.86e-04	7.63e-05
0.02	0.284	8	8.00	2.54	2.26	1.58	RSG	sCCSN	0.00e+00	0.00e+00	0.00e+00	0.00e+00	0.00e+00	0.00e+00	0.00e+00	0.00e+00	0.00e+00	0.00e+00
0.02	0.284	9	9.00	3.14	2.82	1.66	RSG	sCCSN	0.00e+00	0.00e+00	0.00e+00	0.00e+00	0.00e+00	0.00e+00	0.00e+00	0.00e+00	0.00e+00	0.00e+00
0.02	0.284	10	10.00	3.30	2.96	1.66	RSG	sCCSN	0.00e+00	0.00e+00	0.00e+00	0.00e+00	0.00e+00	0.00e+00	0.00e+00	0.00e+00	0.00e+00	0.00e+00
0.02	0.284	11	11.00	3.80	3.40	1.66	RSG	sCCSN	0.00e+00	0.00e+00	0.00e+00	0.00e+00	0.00e+00	0.00e+00	0.00e+00	0.00e+00	0.00e+00	0.00e+00
0.02	0.284	14	13.03	4.56	3.01	1.74	RSG	sCCSN	6.44e-01	3.02e-01	2.56e-03	2.92e-03	7.52e-03	5.49e-07	1.93e-03	6.76e-05	8.55e-04	7.37e-05
0.02	0.284	16	13.95	5.45	3.43	1.72	RSG	sCCSN	1.35e+00	6.64e-01	5.18e-03	7.05e-03	1.54e-02	1.13e-06	4.10e-03	1.53e-04	1.82e-03	1.57e-04
0.02	0.284	18	14.96	6.32	4.05	1.69	RSG	sCCSN	1.97e+00	1.01e+00	7.59e-03	1.09e-02	2.23e-02	1.63e-06	6.06e-03	2.36e-04	2.69e-03	2.32e-04
0.02	0.284	20	17.74	7.12	4.60	1.74	RSG	sCCSN	1.47e+00	7.40e-01	6.20e-03	7.08e-03	1.71e-02	1.26e-06	4.52e-03	1.66e-04	2.00e-03	1.73e-04
0.02	0.284	24	19.42	9.15	6.06	1.83	RSG	sCCSN	2.96e+00	1.53e+00	1.27e-02	1.48e-02	3.40e-02	2.48e-06	9.15e-03	3.53e-04	4.06e-03	3.51e-04
0.02	0.284	28	20.76	11.02	7.52	1.76	RSG	sCCSN	4.59e+00	2.50e+00	1.87e-02	2.67e-02	5.17e-02	3.75e-06	1.44e-02	6.09e-04	6.41e-03	5.56e-04
0.02	0.284	30	16.72	12.23	8.45	16.72	RSG	fCCSN	8.36e+00	4.66e+00	3.45e-02	5.04e-02	9.30e-02	6.71e-06	2.64e-02	1.16e-03	1.18e-02	1.02e-03
0.02	0.284	35	13.31	13.31	9.78	13.31	WO	fCCSN	1.15e+01	9.63e+00	1.36e-01	1.24e-01	1.61e-01	8.19e-06	4.54e-02	2.85e-03	1.95e-02	1.72e-03
0.02	0.284	40	12.75	12.39	9.28	12.75	WC	fCCSN	1.28e+01	1.32e+01	6.77e-01	1.62e-01	1.86e-01	9.12e-06	8.88e-02	4.20e-03	2.44e-02	2.20e-03
0.02	0.284	45	13.89	13.50	10.11	13.89	WC	fCCSN	1.38e+01	1.57e+01	9.23e-01	1.97e-01	2.05e-01	9.25e-06	1.18e-01	5.25e-03	2.80e-02	2.54e-03
0.02	0.284	50	15.03	14.61	10.93	15.03	WC	fCCSN	1.48e+01	1.82e+01	1.17e+00	2.31e-01	2.24e-01	9.37e-06	1.47e-01	6.30e-03	3.16e-02	2.89e-03
0.02	0.284	55	16.55	16.09	12.04	16.55	WC	fCCSN	1.59e+01	2.03e+01	1.43e+00	2.61e-01	2.60e-01	9.72e-06	1.69e-01	7.20e-03	3.50e-02	3.21e-03
0.02	0.284	60	18.11	17.60	13.13	18.11	WC	fCCSN	1.68e+01	2.24e+01	1.70e+00	2.90e-01	3.01e-01	1.00e-05	1.93e-01	8.10e-03	3.84e-02	3.54e-03
0.02	0.284	65	19.93	19.38	14.41	19.93	WC	fCCSN	1.79e+01	2.41e+01	1.99e+00	3.17e-01	3.55e-01	1.02e-05	2.13e-01	8.92e-03	4.17e-02	3.84e-03
0.02	0.284	70	22.30	21.67	16.10	22.30	WC	fCCSN	1.89e+01	2.53e+01	2.27e+00	3.43e-01	4.35e-01	1.04e-05	2.23e-01	9.59e-03	4.49e-02	4.10e-03
0.02	0.284	75	23.43	22.78	16.92	23.43	WC	fCCSN	2.00e+01	2.76e+01	2.58e+00	3.71e-01	4.90e-01	1.10e-05	2.54e-01	1.06e-02	4.90e-02	4.48e-03
0.02	0.284	80	24.57	23.88	17.73	24.57	WC	fCCSN	2.11e+01	3.00e+01	2.88e+00	3.98e-01	5.45e-01	1.16e-05	2.85e-01	1.15e-02	5.31e-02	4.86e-03
0.02	0.284	90	26.91	26.15	19.40	26.91	WC	fCCSN	2.31e+01	3.47e+01	3.53e+00	4.66e-01	7.08e-01	1.14e-05	3.48e-01	1.38e-02	6.22e-02	5.64e-03
0.02	0.284	95	27.59	26.81	19.90	27.59	WC	fCCSN	2.41e+01	3.76e+01	3.75e+00	5.01e-01	7.55e-01	1.17e-05	3.82e-01	1.50e-02	6.67e-02	6.08e-03
0.02	0.284	100	27.75	26.98	19.94	27.75	WC	fCCSN	2.51e+01	4.12e+01	3.85e+00	5.48e-01	7.77e-01	1.19e-05	4.10e-01	1.64e-02	7.12e-02	6.59e-03
0.02	0.284	120	22.32	21.70	16.11	22.32	WC	fCCSN	3.02e+01	6.27e+01	2.55e+00	9.21e-01	4.62e-01	1.08e-05	3.76e-01	2.38e-02	8.84e-02	9.30e-03
0.02	0.284	150	16.57	16.11	12.03	16.57	WC	fCCSN	4.10e+01	8.82e+01	1.53e+00	1.42e+00	3.11e-01	9.79e-06	3.68e-01	3.38e-02	1.17e-01	1.32e-02
0.02	0.284	200	16.12	15.67	11.71	16.12	WC	fCCSN	5.75e+01	1.21e+02	1.46e+00	2.05e+00	3.22e-01	9.19e-06	4.53e-01	4.77e-02	1.60e-01	1.90e-02
0.02	0.284	250	16.26	15.81	11.83	16.26	WC	fCCSN	7.40e+01	1.54e+02	1.49e+00	2.67e+00	3.42e-01	8.44e-06	5.44e-01	6.16e-02	2.02e-01	2.51e-02
0.02	0.284	300	17.14	16.97	12.47	17.14	WC	fCCSN	9.21e+01	1.84e+02	1.59e+00	3.22e+00	4.22e-01	1.16e-05	6.36e-01	7.42e-02	2.44e-01	3.07e-02
0.02	0.284	350	16.84	16.37	12.24	16.84	WC	fCCSN	1.07e+02	2.18e+02	1.61e+00	3.92e+00	3.84e-01	7.28e-06	7.33e-01	8.95e-02	2.86e-01	3.74e-02

Table 4.4-continued.

M_i	Si	P	S	Cl	Ar	K	Ca	Sc	Ti	V	Cr	Mn	Fe	Co	Ni	Cu	Zn
Xi	9.25e-04	8.56e-06	4.44e-04	1.07e-05	9.62e-05	4.83e-06	8.78e-05	1.65e-07	4.62e-06	2.50e-07	2.38e-05	1.29e-05	1.77e-03	4.70e-06	1.00e-04	9.88e-07	2.50e-06
8	0.00e+00	0.00e+00	0.00e+00	0.00e+00	0.00e+00	0.00e+00	0.00e+00	0.00e+00	0.00e+00	0.00e+00	0.00e+00	0.00e+00	0.00e+00	0.00e+00	0.00e+00	0.00e+00	0.00e+00
9	0.00e+00	0.00e+00	0.00e+00	0.00e+00	0.00e+00	0.00e+00	0.00e+00	0.00e+00	0.00e+00	0.00e+00	0.00e+00	0.00e+00	0.00e+00	0.00e+00	0.00e+00	0.00e+00	0.00e+00
10	0.00e+00	0.00e+00	0.00e+00	0.00e+00	0.00e+00	0.00e+00	0.00e+00	0.00e+00	0.00e+00	0.00e+00	0.00e+00	0.00e+00	0.00e+00	0.00e+00	0.00e+00	0.00e+00	0.00e+00
11	0.00e+00	0.00e+00	0.00e+00	0.00e+00	0.00e+00	0.00e+00	0.00e+00	0.00e+00	0.00e+00	0.00e+00	0.00e+00	0.00e+00	0.00e+00	0.00e+00	0.00e+00	0.00e+00	0.00e+00
14	9.65e-04	8.26e-06	4.29e-04	1.04e-05	9.28e-05	4.66e-06	8.48e-05	1.59e-07	4.46e-06	2.41e-07	2.20e-05	1.25e-05	1.71e-03	4.53e-06	9.66e-05	9.53e-07	2.41e-06
16	2.05e-03	1.76e-05	9.12e-04	2.21e-05	1.97e-04	9.91e-06	1.80e-04	3.38e-07	9.48e-06	5.13e-07	4.68e-05	2.65e-05	3.64e-03	9.65e-06	2.05e-04	2.03e-06	5.12e-06
18	3.04e-03	2.60e-05	1.35e-03	3.26e-05	2.92e-04	1.47e-05	2.67e-04	5.00e-07	1.40e-05	7.59e-07	6.92e-05	3.92e-05	5.38e-03	1.43e-05	3.04e-04	3.00e-06	7.57e-06
20	2.26e-03	1.93e-05	1.00e-03	2.43e-05	2.17e-04	1.09e-05	1.98e-04	3.72e-07	1.04e-05	5.65e-07	5.15e-05	2.92e-05	4.00e-03	1.06e-05	2.26e-04	2.23e-06	5.64e-06
24	4.58e-03	3.92e-05	2.04e-03	4.92e-05	4.41e-04	2.21e-05	4.02e-04	7.54e-07	2.12e-05	1.15e-06	1.04e-04	5.92e-05	8.12e-03	2.15e-05	4.58e-04	4.53e-06	1.14e-05
28	7.24e-03	6.20e-05	3.22e-03	7.78e-05	6.96e-04	3.49e-05	6.36e-04	1.19e-06	3.34e-05	1.81e-06	1.65e-04	9.35e-05	1.28e-02	3.40e-05	7.24e-04	7.15e-06	1.81e-05
30	1.33e-02	1.14e-04	5.90e-03	1.43e-04	1.28e-03	6.41e-05	1.17e-03	2.19e-06	6.14e-05	3.32e-06	3.03e-04	1.72e-04	2.35e-02	6.24e-05	1.33e-03	1.31e-05	3.31e-05
35	2.17e-02	1.86e-04	9.64e-03	2.33e-04	2.09e-03	1.05e-04	1.90e-03	3.57e-06	1.00e-04	5.42e-06	4.94e-04	2.80e-04	3.84e-02	1.02e-04	2.17e-03	2.14e-05	5.41e-05
40	2.73e-02	2.33e-04	1.21e-02	2.93e-04	2.62e-03	1.32e-04	2.39e-03	4.48e-06	1.26e-04	6.81e-06	6.21e-04	3.52e-04	4.83e-02	1.28e-04	2.73e-03	2.69e-05	6.80e-05
45	3.12e-02	2.66e-04	1.38e-02	3.34e-04	2.99e-03	1.50e-04	2.73e-03	5.12e-06	1.44e-04	7.78e-06	7.09e-04	4.02e-04	5.51e-02	1.46e-04	3.11e-03	3.07e-05	7.76e-05
50	3.50e-02	2.99e-04	1.55e-02	3.76e-04	3.36e-03	1.69e-04	3.07e-03	5.75e-06	1.62e-04	8.74e-06	7.97e-04	4.52e-04	6.20e-02	1.64e-04	3.50e-03	3.45e-05	8.72e-05
55	3.85e-02	3.29e-04	1.71e-02	4.13e-04	3.70e-03	1.86e-04	3.38e-03	6.33e-06	1.78e-04	9.62e-06	8.76e-04	4.97e-04	6.81e-02	1.81e-04	3.85e-03	3.80e-05	9.59e-05
60	4.20e-02	3.59e-04	1.86e-02	4.50e-04	4.03e-03	2.02e-04	3.68e-03	6.89e-06	1.94e-04	1.05e-05	9.55e-04	5.41e-04	7.42e-02	1.97e-04	4.19e-03	4.14e-05	1.05e-04
65	4.51e-02	3.86e-04	2.00e-02	4.84e-04	4.33e-03	2.18e-04	3.96e-03	7.42e-06	2.08e-04	1.13e-05	1.03e-03	5.83e-04	7.99e-02	2.12e-04	4.51e-03	4.45e-05	1.12e-04
70	4.78e-02	4.08e-04	2.12e-02	5.13e-04	4.59e-03	2.30e-04	4.19e-03	7.85e-06	2.20e-04	1.19e-05	1.09e-03	6.17e-04	8.45e-02	2.24e-04	4.77e-03	4.71e-05	1.19e-04
75	5.17e-02	4.42e-04	2.29e-02	5.54e-04	4.96e-03	2.49e-04	4.54e-03	3.29e-06	2.48e-04	2.52e-05	1.20e-03	6.67e-04	9.14e-02	2.43e-04	5.16e-03	5.14e-05	1.16e-04
80	5.55e-02	4.75e-04	2.46e-02	5.96e-04	5.33e-03	2.68e-04	4.87e-03	9.12e-06	2.56e-04	1.39e-05	1.26e-03	7.17e-04	9.82e-02	2.60e-04	5.55e-03	5.48e-05	1.38e-04
90	6.32e-02	5.40e-04	2.80e-02	6.78e-04	6.07e-03	3.05e-04	5.54e-03	1.04e-05	2.91e-04	1.58e-05	1.44e-03	8.16e-04	1.12e-01	2.96e-04	6.31e-03	6.23e-05	1.57e-04
95	6.76e-02	5.77e-04	3.00e-02	7.24e-04	6.48e-03	3.25e-04	5.92e-03	1.11e-05	3.11e-04	1.69e-05	1.54e-03	8.71e-04	1.19e-01	3.17e-04	6.74e-03	6.66e-05	1.68e-04
100	7.24e-02	6.19e-04	3.21e-02	7.76e-04	6.95e-03	3.49e-04	6.35e-03	1.19e-05	3.34e-04	1.81e-05	1.65e-03	9.34e-04	1.28e-01	3.39e-04	7.23e-03	7.14e-05	1.80e-04
120	9.79e-02	8.36e-04	4.34e-02	1.05e-03	9.39e-03	4.72e-04	8.58e-03	1.61e-05	4.51e-04	2.44e-05	2.23e-03	1.26e-03	1.73e-01	4.59e-04	9.77e-03	9.65e-05	2.44e-04
150	1.34e-01	1.14e-03	5.93e-02	1.43e-03	1.28e-02	6.44e-04	1.17e-02	2.20e-05	6.16e-04	3.34e-05	3.04e-03	1.72e-03	2.36e-01	6.27e-04	1.33e-02	1.32e-04	3.33e-04
200	1.84e-01	1.57e-03	8.17e-02	1.98e-03	1.77e-02	8.88e-04	1.62e-02	3.03e-05	8.49e-04	4.60e-05	4.19e-03	2.38e-03	3.26e-01	8.64e-04	1.84e-02	1.82e-04	4.59e-04
250	2.34e-01	2.00e-03	1.04e-01	2.51e-03	2.25e-02	1.13e-03	2.05e-02	3.85e-05	1.08e-03	5.85e-05	5.33e-03	3.02e-03	4.14e-01	1.10e-03	2.34e-02	2.31e-04	5.83e-04
300	2.83e-01	2.42e-03	1.26e-01	3.04e-03	2.72e-02	1.37e-03	2.48e-02	4.65e-05	1.31e-03	7.07e-05	6.45e-03	3.66e-03	5.01e-01	1.33e-03	2.83e-02	2.79e-04	7.06e-04
350	3.34e-01	2.85e-03	1.48e-01	3.58e-03	3.20e-02	1.61e-03	2.93e-02	5.48e-05	1.54e-03	8.33e-05	7.59e-03	4.31e-03	5.90e-01	1.57e-03	3.33e-02	3.29e-04	8.31e-04

Table 4.5: Explosion ejecta in $M_\odot$ for Z=0.0001. The values are obtained using the bi-parametric method (Ertl et al. 2016) for exploidability coupled with the $^{56}Ni - M_{fin}$ relation for remnant mass estimation.

Z_i	Y_i	M_i	M_{fin}	M_{He}	M_{CO}	M_{rem}	pre-SN	SN-type	H	He	C	N	O	F	Neon	Na	Mg	Al
Xi	–	–	–	–	–	–	–	–	6.51e-01	3.49e-01	1.80e-05	4.86e-06	4.41e-05	3.31e-09	1.01e-05	2.36e-07	4.43e-06	3.82e-07
0.0001	0.35	8	8.00	2.50	2.18	1.39	RSG	sCCSN	2.68e+00	3.13e+00	6.71e-02	2.21e-04	3.19e-01	9.08e-09	1.27e-01	7.40e-04	5.19e-02	1.15e-03
0.0001	0.35	9	9.00	2.79	2.43	1.24	RSG	sCCSN	3.06e+00	3.51e+00	4.70e-02	2.49e-04	2.56e-01	1.03e-08	1.73e-01	1.05e-03	5.06e-02	1.47e-03
0.0001	0.35	10	10.00	3.25	1.96	1.46	RSG	sCCSN	3.32e+00	4.26e+00	3.46e-01	3.23e-04	5.35e-01	9.19e-09	1.08e-01	6.20e-04	5.25e-02	1.02e-03
0.0001	0.35	11	11.00	3.65	2.27	1.68	RSG	sCCSN	3.51e+00	4.55e+00	4.48e-01	3.14e-04	7.51e-01	1.17e-08	4.26e-02	1.82e-04	5.45e-02	5.54e-04
0.0001	0.35	14	13.99	4.81	3.89	1.64	RSG	sCCSN	5.06e+00	5.05e+00	1.37e-01	4.14e-04	1.27e+00	1.42e-08	4.53e-01	1.70e-03	1.62e-01	2.78e-03
0.0001	0.35	16	15.99	5.59	3.97	1.63	RSG	sCCSN	5.66e+00	6.28e+00	2.18e-01	4.64e-04	1.33e+00	1.64e-08	4.78e-01	1.79e-03	1.69e-01	2.92e-03
0.0001	0.35	18	17.99	6.47	4.18	1.66	RSG	sCCSN	5.98e+00	6.70e+00	7.06e-01	4.76e-04	2.03e+00	1.88e-08	5.09e-01	1.95e-03	1.69e-01	2.89e-03
0.0001	0.35	20	19.99	7.37	4.70	1.74	RSG	sCCSN	6.46e+00	7.20e+00	9.33e-01	5.22e-04	2.62e+00	1.84e-08	5.66e-01	2.32e-03	1.61e-01	2.56e-03
0.0001	0.35	24	23.98	9.39	6.23	1.89	RSG	sCCSN	8.20e+00	7.65e+00	1.02e+00	5.88e-04	3.86e+00	2.52e-08	7.75e-01	3.41e-03	1.65e-01	2.20e-03
0.0001	0.35	28	27.96	11.47	7.85	1.91	RSG	sCCSN	8.98e+00	8.90e+00	1.11e+00	6.61e-04	5.27e+00	2.73e-08	1.08e+00	4.38e-03	2.25e-01	2.99e-03
0.0001	0.35	30	29.96	12.59	8.68	29.96	RSG	fCCSN	0.00e+00	0.00e+00	0.00e+00	0.00e+00	0.00e+00	0.00e+00	0.00e+00	0.00e+00	0.00e+00	0.00e+00
0.0001	0.35	35	34.93	15.35	10.81	34.93	RSG	fCCSN	0.00e+00	0.00e+00	0.00e+00	0.00e+00	0.00e+00	0.00e+00	0.00e+00	0.00e+00	0.00e+00	0.00e+00
0.0001	0.35	40	39.91	18.22	13.07	39.91	RSG	fCCSN	0.00e+00	0.00e+00	0.00e+00	0.00e+00	0.00e+00	0.00e+00	0.00e+00	0.00e+00	0.00e+00	0.00e+00
0.0001	0.35	45	44.88	21.28	15.25	44.88	RSG	fCCSN	0.00e+00	0.00e+00	0.00e+00	0.00e+00	0.00e+00	0.00e+00	0.00e+00	0.00e+00	0.00e+00	0.00e+00
0.0001	0.35	50	49.85	24.37	17.58	49.85	RSG	fCCSN	0.00e+00	0.00e+00	0.00e+00	0.00e+00	0.00e+00	0.00e+00	0.00e+00	0.00e+00	0.00e+00	0.00e+00
0.0001	0.35	55	54.80	27.31	19.59	54.80	RSG	fCCSN	0.00e+00	0.00e+00	0.00e+00	0.00e+00	0.00e+00	0.00e+00	0.00e+00	0.00e+00	0.00e+00	0.00e+00
0.0001	0.35	60	59.74	30.30	21.90	59.74	RSG	fCCSN	0.00e+00	0.00e+00	0.00e+00	0.00e+00	0.00e+00	0.00e+00	0.00e+00	0.00e+00	0.00e+00	0.00e+00
0.0001	0.35	65	64.67	33.18	24.15	64.67	RSG	fCCSN	0.00e+00	0.00e+00	0.00e+00	0.00e+00	0.00e+00	0.00e+00	0.00e+00	0.00e+00	0.00e+00	0.00e+00
0.0001	0.35	70	69.62	36.27	26.31	69.62	RSG	fCCSN	0.00e+00	0.00e+00	0.00e+00	0.00e+00	0.00e+00	0.00e+00	0.00e+00	0.00e+00	0.00e+00	0.00e+00
0.0001	0.35	75	74.39	38.97	28.35	74.39	RSG	fCCSN	0.00e+00	0.00e+00	0.00e+00	0.00e+00	0.00e+00	0.00e+00	0.00e+00	0.00e+00	0.00e+00	0.00e+00
0.0001	0.35	80	77.76	42.96	31.42	39.25	RSG	PPISN	1.20e+01	1.97e+01	1.35e+00	1.55e-03	4.36e+00	3.26e-08	8.37e-01	2.86e-05	2.62e-01	1.26e-04
0.0001	0.35	90	86.68	48.97	35.91	41.22	RSG	PPISN	1.27e+01	2.23e+01	2.39e+00	1.66e-03	6.29e+00	3.40e-08	1.46e+00	2.82e-05	3.22e-01	1.47e-04
0.0001	0.35	95	91.66	52.02	38.11	46.42	LBV	PPISN	1.32e+01	2.39e+01	2.41e+00	1.76e-03	4.34e+00	3.37e-08	1.29e+00	3.00e-05	2.03e-01	1.65e-04
0.0001	0.35	100	96.63	55.07	40.32	51.61	LBV	PPISN	1.38e+01	2.55e+01	2.42e+00	1.86e-03	2.39e+00	3.35e-08	1.12e+00	3.17e-05	8.31e-02	1.83e-04
0.0001	0.35	120	116.60	67.57	51.28	0.00	LBV	PISN	1.46e+01	3.10e+01	6.08e+00	6.15e-03	5.22e+01	8.37e-08	4.55e+00	6.92e-03	2.33e+00	2.40e-02
0.0001	0.35	150	146.21	85.60	64.69	0.00	LBV	PISN	1.79e+01	3.75e+01	1.41e+00	7.88e-03	4.08e+01	8.11e-08	1.50e+00	1.27e-02	7.18e+00	2.67e-02
0.0001	0.35	200	194.63	115.47	89.36	0.00	LBV	PISN	1.59e+01	4.21e+01	1.16e+01	9.34e-03	2.16e+01	4.74e-08	2.88e+00	3.84e-02	1.30e+01	9.41e-02
0.0001	0.35	250	241.93	145.20	116.41	241.93	LBV	DBH	0.00e+00	0.00e+00	0.00e+00	0.00e+00	0.00e+00	0.00e+00	0.00e+00	0.00e+00	0.00e+00	0.00e+00
0.0001	0.35	300	152.83	148.55	120.64	152.83	LBV	DBH	0.00e+00	0.00e+00	0.00e+00	0.00e+00	0.00e+00	0.00e+00	0.00e+00	0.00e+00	0.00e+00	0.00e+00
0.0001	0.35	350	165.97	161.32	129.52	165.97	LBV	DBH	0.00e+00	0.00e+00	0.00e+00	0.00e+00	0.00e+00	0.00e+00	0.00e+00	0.00e+00	0.00e+00	0.00e+00

Table 4.5-continued.

M_i	Si	P	S	Cl	Ar	K	Ca	Sc	Ti	V	Cr	Mn	Fe	Co	Ni	Cu	Zn
Xi	4.63e-06	4.28e-08	2.22e-06	5.37e-08	4.81e-07	2.41e-08	4.39e-07	8.23e-10	2.31e-08	1.25e-09	1.19e-07	6.46e-08	8.86e-06	2.35e-08	5.00e-07	4.94e-09	1.25e-08
8	7.77e-02	1.19e-04	3.78e-02	3.13e-07	2.87e-04	3.55e-05	6.18e-03	1.22e-07	1.16e-04	2.00e-05	1.97e-03	9.00e-04	7.72e-02	6.24e-05	2.65e-03	1.29e-06	1.18e-05
9	5.77e-02	6.31e-05	3.12e-02	3.53e-07	3.36e-04	4.36e-05	5.38e-03	1.48e-07	1.02e-04	2.66e-05	2.03e-03	1.17e-03	7.74e-02	8.52e-05	3.22e-03	3.97e-06	1.31e-05
10	8.61e-02	1.42e-04	4.05e-02	4.32e-07	2.67e-04	3.21e-05	6.52e-03	1.14e-07	1.23e-04	1.73e-05	1.94e-03	7.87e-04	7.71e-02	5.29e-05	2.42e-03	3.27e-06	1.76e-05
11	1.15e-01	2.22e-04	5.00e-02	4.69e-07	1.97e-04	2.06e-05	7.66e-03	7.92e-08	1.43e-04	8.01e-06	1.86e-03	4.00e-04	7.68e-02	2.05e-05	1.62e-03	9.98e-06	3.70e-05
14	1.11e-01	2.20e-04	4.42e-02	5.43e-07	8.56e-05	1.18e-05	7.15e-03	7.02e-08	8.86e-05	1.09e-05	1.46e-03	4.92e-04	3.88e-02	1.03e-05	5.68e-04	1.32e-07	1.12e-06
16	1.12e-01	2.20e-04	4.44e-02	6.46e-07	7.98e-05	1.13e-05	7.29e-03	7.16e-08	9.17e-05	1.13e-05	1.52e-03	5.12e-04	4.07e-02	1.10e-05	5.97e-04	1.45e-07	1.20e-06
18	1.18e-01	2.13e-04	4.82e-02	7.42e-07	8.49e-05	1.26e-05	8.03e-03	7.97e-08	1.01e-04	1.16e-05	1.70e-03	5.34e-04	4.55e-02	1.11e-05	6.12e-04	2.62e-07	1.44e-06
20	1.36e-01	1.92e-04	5.97e-02	8.21e-07	1.09e-04	1.72e-05	1.01e-02	1.01e-07	1.25e-04	1.21e-05	2.14e-03	5.73e-04	5.72e-02	1.03e-05	6.14e-04	5.94e-07	2.04e-06
24	1.71e-01	1.62e-04	8.06e-02	9.53e-07	1.38e-04	2.44e-05	1.41e-02	1.41e-07	1.76e-04	1.17e-05	2.94e-03	5.96e-04	8.57e-02	1.04e-05	8.71e-04	4.04e-06	1.81e-05
28	1.81e-01	1.93e-04	8.20e-02	1.08e-06	9.49e-05	2.03e-05	1.50e-02	1.43e-07	1.94e-04	8.30e-06	2.94e-03	4.83e-04	9.93e-02	1.27e-05	1.39e-03	1.01e-05	5.07e-05
30	0.00e+00	0.00e+00	0.00e+00	0.00e+00	0.00e+00	0.00e+00	0.00e+00	0.00e+00	0.00e+00	0.00e+00	0.00e+00	0.00e+00	0.00e+00	0.00e+00	0.00e+00	0.00e+00	0.00e+00
35	0.00e+00	0.00e+00	0.00e+00	0.00e+00	0.00e+00	0.00e+00	0.00e+00	0.00e+00	0.00e+00	0.00e+00	0.00e+00	0.00e+00	0.00e+00	0.00e+00	0.00e+00	0.00e+00	0.00e+00
40	0.00e+00	0.00e+00	0.00e+00	0.00e+00	0.00e+00	0.00e+00	0.00e+00	0.00e+00	0.00e+00	0.00e+00	0.00e+00	0.00e+00	0.00e+00	0.00e+00	0.00e+00	0.00e+00	0.00e+00
45	0.00e+00	0.00e+00	0.00e+00	0.00e+00	0.00e+00	0.00e+00	0.00e+00	0.00e+00	0.00e+00	0.00e+00	0.00e+00	0.00e+00	0.00e+00	0.00e+00	0.00e+00	0.00e+00	0.00e+00
50	0.00e+00	0.00e+00	0.00e+00	0.00e+00	0.00e+00	0.00e+00	0.00e+00	0.00e+00	0.00e+00	0.00e+00	0.00e+00	0.00e+00	0.00e+00	0.00e+00	0.00e+00	0.00e+00	0.00e+00
55	0.00e+00	0.00e+00	0.00e+00	0.00e+00	0.00e+00	0.00e+00	0.00e+00	0.00e+00	0.00e+00	0.00e+00	0.00e+00	0.00e+00	0.00e+00	0.00e+00	0.00e+00	0.00e+00	0.00e+00
60	0.00e+00	0.00e+00	0.00e+00	0.00e+00	0.00e+00	0.00e+00	0.00e+00	0.00e+00	0.00e+00	0.00e+00	0.00e+00	0.00e+00	0.00e+00	0.00e+00	0.00e+00	0.00e+00	0.00e+00
65	0.00e+00	0.00e+00	0.00e+00	0.00e+00	0.00e+00	0.00e+00	0.00e+00	0.00e+00	0.00e+00	0.00e+00	0.00e+00	0.00e+00	0.00e+00	0.00e+00	0.00e+00	0.00e+00	0.00e+00
70	0.00e+00	0.00e+00	0.00e+00	0.00e+00	0.00e+00	0.00e+00	0.00e+00	0.00e+00	0.00e+00	0.00e+00	0.00e+00	0.00e+00	0.00e+00	0.00e+00	0.00e+00	0.00e+00	0.00e+00
75	0.00e+00	0.00e+00	0.00e+00	0.00e+00	0.00e+00	0.00e+00	0.00e+00	0.00e+00	0.00e+00	0.00e+00	0.00e+00	0.00e+00	0.00e+00	0.00e+00	0.00e+00	0.00e+00	0.00e+00
80	2.87e-04	1.49e-06	7.73e-05	1.87e-06	1.67e-05	8.40e-07	1.53e-05	2.86e-08	8.04e-07	4.35e-08	4.14e-06	2.25e-06	3.08e-04	8.18e-07	1.74e-05	1.72e-07	4.34e-07
90	1.86e-04	1.61e-06	8.38e-05	2.03e-06	1.81e-05	9.10e-07	1.66e-05	3.10e-08	8.71e-07	4.71e-08	4.49e-06	2.44e-06	3.34e-04	8.86e-07	1.89e-05	1.86e-07	4.70e-07
95	2.38e-01	1.70e-06	3.97e-02	2.13e-06	4.67e-03	9.57e-07	3.50e-03	1.26e-08	9.52e-07	9.68e-08	4.62e-06	2.56e-06	3.51e-04	8.86e-07	1.98e-05	1.96e-07	4.95e-07
100	4.76e-01	1.78e-06	7.93e-02	2.23e-06	9.32e-03	1.00e-06	6.99e-03	3.42e-08	9.60e-07	5.20e-08	4.95e-06	2.69e-06	3.68e-04	9.76e-07	2.08e-05	2.05e-07	5.19e-07
120	4.30e+00	2.78e-03	1.31e+00	7.50e-04	1.73e-01	6.39e-04	1.15e-01	4.03e-08	5.81e-05	6.13e-08	2.81e-03	8.13e-05	1.53e-01	3.90e-05	3.42e-03	6.41e-08	2.50e-06
150	2.98e+01	3.59e-03	9.64e+00	5.76e-03	1.27e+00	5.19e-03	8.11e-01	4.99e-08	1.02e-03	7.58e-08	1.54e-02	4.27e-03	6.85e-01	1.60e-04	1.83e-02	1.24e-06	1.03e-05
200	6.13e+01	4.18e-03	1.99e+01	1.19e-02	2.62e+00	1.08e-02	1.67e+00	5.53e-08	2.39e-03	8.41e-08	3.88e-02	9.75e-03	1.76e+00	4.15e-04	4.61e-02	2.89e-06	2.68e-05
250	0.00e+00	0.00e+00	0.00e+00	0.00e+00	0.00e+00	0.00e+00	0.00e+00	0.00e+00	0.00e+00	0.00e+00	0.00e+00	0.00e+00	0.00e+00	0.00e+00	0.00e+00	0.00e+00	0.00e+00
300	0.00e+00	0.00e+00	0.00e+00	0.00e+00	0.00e+00	0.00e+00	0.00e+00	0.00e+00	0.00e+00	0.00e+00	0.00e+00	0.00e+00	0.00e+00	0.00e+00	0.00e+00	0.00e+00	0.00e+00
350	0.00e+00	0.00e+00	0.00e+00	0.00e+00	0.00e+00	0.00e+00	0.00e+00	0.00e+00	0.00e+00	0.00e+00	0.00e+00	0.00e+00	0.00e+00	0.00e+00	0.00e+00	0.00e+00	0.00e+00

Table 4.6: Explosion ejecta in $M_\odot$ for Z=0.02. The values are obtained using the bi-parametric method (Ertl et al. 2016) for explodability coupled with the $^{56}Ni - M_{fin}$ relation for remnant mass estimation.

Z_i	Y_i	M_i	M_{fin}	M_{He}	M_{CO}	M_{rem}	pre-SN	SN-type	H	He	C	N	O	F	Neon	Na	Mg	Al
Xi	–	–	–	–	–	–	–	–	6.96e-01	2.84e-01	3.60e-03	9.73e-04	8.82e-03	6.61e-07	2.02e-03	4.71e-05	8.86e-04	7.63e-05
0.02	0.284	8	8.00	2.54	2.26	1.58	RSG	sCCSN	2.55e+00	2.60e+00	3.43e-01	3.12e-02	5.26e-01	2.17e-06	4.92e-02	1.44e-03	3.78e-02	1.94e-03
0.02	0.284	9	9.00	3.14	2.82	1.66	RSG	sCCSN	2.87e+00	2.68e+00	3.83e-01	3.21e-02	9.00e-01	2.42e-06	1.95e-01	4.98e-03	7.60e-02	6.92e-03
0.02	0.284	10	10.00	3.30	2.96	1.66	RSG	sCCSN	3.25e+00	3.14e+00	4.08e-01	3.78e-02	1.13e+00	2.72e-06	3.31e-01	8.16e-03	1.11e-01	1.15e-02
0.02	0.284	11	11.00	3.80	3.40	1.66	RSG	sCCSN	3.48e+00	3.42e+00	4.12e-01	4.12e-02	1.11e+00	2.90e-06	3.06e-01	7.65e-03	1.05e-01	1.07e-02
0.02	0.284	14	13.03	4.56	3.01	1.74	RSG	sCCSN	4.57e+00	5.19e+00	1.69e-01	7.01e-02	7.11e-01	3.08e-06	2.12e-01	5.73e-03	8.32e-02	7.54e-03
0.02	0.284	16	13.95	5.45	3.43	1.72	RSG	sCCSN	4.39e+00	5.37e+00	4.26e-01	7.02e-02	1.17e+00	3.28e-06	3.49e-01	8.81e-03	1.19e-01	1.19e-02
0.02	0.284	18	14.96	6.32	4.05	1.69	RSG	sCCSN	4.54e+00	5.48e+00	5.16e-01	7.28e-02	1.58e+00	3.28e-06	5.40e-01	1.32e-02	1.70e-01	1.83e-02
0.02	0.284	20	17.74	7.12	4.60	1.74	RSG	sCCSN	5.54e+00	6.52e+00	6.34e-01	8.67e-02	1.98e+00	3.82e-06	6.13e-01	1.70e-02	1.80e-01	2.24e-02
0.02	0.284	24	19.42	9.15	6.06	1.83	RSG	sCCSN	5.14e+00	7.13e+00	7.54e-01	9.37e-02	2.85e+00	3.19e-06	8.13e-01	2.68e-02	2.05e-01	3.39e-02
0.02	0.284	28	20.76	11.02	7.52	1.76	RSG	sCCSN	5.01e+00	7.08e+00	7.56e-01	1.02e-01	3.96e+00	2.87e-06	1.23e+00	3.79e-02	2.94e-01	5.32e-02
0.02	0.284	30	16.72	12.23	8.45	16.72	RSG	fCCSN	0.00e+00	0.00e+00	0.00e+00	0.00e+00	0.00e+00	0.00e+00	0.00e+00	0.00e+00	0.00e+00	0.00e+00
0.02	0.284	35	13.31	13.31	9.78	13.31	WO	fCCSN	0.00e+00	0.00e+00	0.00e+00	0.00e+00	0.00e+00	0.00e+00	0.00e+00	0.00e+00	0.00e+00	0.00e+00
0.02	0.284	40	12.75	12.39	9.28	12.75	WC	fCCSN	0.00e+00	0.00e+00	0.00e+00	0.00e+00	0.00e+00	0.00e+00	0.00e+00	0.00e+00	0.00e+00	0.00e+00
0.02	0.284	45	13.89	13.50	10.11	13.89	WC	fCCSN	0.00e+00	0.00e+00	0.00e+00	0.00e+00	0.00e+00	0.00e+00	0.00e+00	0.00e+00	0.00e+00	0.00e+00
0.02	0.284	50	15.03	14.61	10.93	15.03	WC	fCCSN	0.00e+00	0.00e+00	0.00e+00	0.00e+00	0.00e+00	0.00e+00	0.00e+00	0.00e+00	0.00e+00	0.00e+00
0.02	0.284	55	16.55	16.09	12.04	16.55	WC	fCCSN	0.00e+00	0.00e+00	0.00e+00	0.00e+00	0.00e+00	0.00e+00	0.00e+00	0.00e+00	0.00e+00	0.00e+00
0.02	0.284	60	18.11	17.60	13.13	18.11	WC	fCCSN	0.00e+00	0.00e+00	0.00e+00	0.00e+00	0.00e+00	0.00e+00	0.00e+00	0.00e+00	0.00e+00	0.00e+00
0.02	0.284	65	19.93	19.38	14.41	19.93	WC	fCCSN	0.00e+00	0.00e+00	0.00e+00	0.00e+00	0.00e+00	0.00e+00	0.00e+00	0.00e+00	0.00e+00	0.00e+00
0.02	0.284	70	22.30	21.67	16.10	22.30	WC	fCCSN	0.00e+00	0.00e+00	0.00e+00	0.00e+00	0.00e+00	0.00e+00	0.00e+00	0.00e+00	0.00e+00	0.00e+00
0.02	0.284	75	23.43	22.78	16.92	23.43	WC	fCCSN	0.00e+00	0.00e+00	0.00e+00	0.00e+00	0.00e+00	0.00e+00	0.00e+00	0.00e+00	0.00e+00	0.00e+00
0.02	0.284	80	24.57	23.88	17.73	24.57	WC	fCCSN	0.00e+00	0.00e+00	0.00e+00	0.00e+00	0.00e+00	0.00e+00	0.00e+00	0.00e+00	0.00e+00	0.00e+00
0.02	0.284	90	26.91	26.15	19.40	26.91	WC	fCCSN	0.00e+00	0.00e+00	0.00e+00	0.00e+00	0.00e+00	0.00e+00	0.00e+00	0.00e+00	0.00e+00	0.00e+00
0.02	0.284	95	27.59	26.81	19.90	27.59	WC	fCCSN	0.00e+00	0.00e+00	0.00e+00	0.00e+00	0.00e+00	0.00e+00	0.00e+00	0.00e+00	0.00e+00	0.00e+00
0.02	0.284	100	27.75	26.98	19.94	27.75	WC	fCCSN	0.00e+00	0.00e+00	0.00e+00	0.00e+00	0.00e+00	0.00e+00	0.00e+00	0.00e+00	0.00e+00	0.00e+00
0.02	0.284	120	22.32	21.70	16.11	22.32	WC	fCCSN	0.00e+00	0.00e+00	0.00e+00	0.00e+00	0.00e+00	0.00e+00	0.00e+00	0.00e+00	0.00e+00	0.00e+00
0.02	0.284	150	16.57	16.11	12.03	16.57	WC	fCCSN	0.00e+00	0.00e+00	0.00e+00	0.00e+00	0.00e+00	0.00e+00	0.00e+00	0.00e+00	0.00e+00	0.00e+00
0.02	0.284	200	16.12	15.67	11.71	16.12	WC	fCCSN	0.00e+00	0.00e+00	0.00e+00	0.00e+00	0.00e+00	0.00e+00	0.00e+00	0.00e+00	0.00e+00	0.00e+00
0.02	0.284	250	16.26	15.81	11.83	16.26	WC	fCCSN	0.00e+00	0.00e+00	0.00e+00	0.00e+00	0.00e+00	0.00e+00	0.00e+00	0.00e+00	0.00e+00	0.00e+00
0.02	0.284	300	17.14	16.97	12.47	17.14	WC	fCCSN	0.00e+00	0.00e+00	0.00e+00	0.00e+00	0.00e+00	0.00e+00	0.00e+00	0.00e+00	0.00e+00	0.00e+00
0.02	0.284	350	16.84	16.37	12.24	16.84	WC	fCCSN	0.00e+00	0.00e+00	0.00e+00	0.00e+00	0.00e+00	0.00e+00	0.00e+00	0.00e+00	0.00e+00	0.00e+00

Table 4.6-continued.

Si	P	S	Cl	Ar	K	Ca	Sc	Ti	V	Cr	Mn	Fe	Co	Ni	Cu	Zn	
Xi	9.25e-04	8.56e-06	4.44e-04	1.07e-05	9.62e-05	4.83e-06	8.78e-05	1.65e-07	4.62e-06	2.50e-07	2.38e-05	1.29e-05	1.77e-03	4.70e-06	1.00e-04	9.88e-07	2.50e-06
8	1.03e-01	7.78e-04	4.72e-02	6.17e-05	1.55e-03	8.58e-05	6.05e-03	2.24e-06	1.93e-04	2.30e-05	1.76e-03	9.48e-04	9.46e-02	2.62e-04	7.05e-03	3.42e-05	5.64e-05
9	1.40e-01	1.07e-03	6.43e-02	6.64e-05	1.91e-03	1.05e-04	8.02e-03	4.12e-06	1.82e-04	3.05e-05	2.20e-03	1.24e-03	9.82e-02	3.20e-04	5.54e-03	8.52e-05	6.55e-05
10	1.48e-01	1.17e-03	6.58e-02	7.56e-05	1.92e-03	1.18e-04	8.13e-03	5.39e-06	1.81e-04	3.10e-05	2.15e-03	1.24e-03	9.93e-02	4.12e-04	5.81e-03	1.26e-04	8.64e-05
11	1.47e-01	1.16e-03	6.58e-02	8.16e-05	1.99e-03	1.19e-04	8.17e-03	5.25e-06	1.85e-04	3.11e-05	2.18e-03	1.25e-03	1.00e-01	3.97e-04	5.83e-03	1.18e-04	8.40e-05
14	1.40e-01	1.11e-03	6.19e-02	1.08e-04	2.27e-03	1.21e-04	6.60e-03	4.86e-06	1.27e-04	2.46e-05	1.30e-03	8.31e-04	4.59e-02	2.71e-04	2.52e-03	9.27e-05	6.65e-05
16	1.49e-01	1.21e-03	6.48e-02	1.13e-04	2.25e-03	1.32e-04	7.34e-03	6.01e-06	1.47e-04	2.77e-05	1.62e-03	9.99e-04	5.82e-02	3.63e-04	3.02e-03	1.31e-04	8.74e-05
18	1.61e-01	1.35e-03	6.90e-02	1.17e-04	2.20e-03	1.47e-04	8.42e-03	7.67e-06	1.74e-04	3.22e-05	2.09e-03	1.24e-03	7.58e-02	4.97e-04	3.73e-03	1.88e-04	1.18e-04
20	1.90e-01	1.48e-03	8.73e-02	1.41e-04	3.13e-03	2.28e-04	1.10e-02	1.09e-05	2.23e-04	3.73e-05	2.46e-03	1.45e-03	9.22e-02	6.23e-04	4.62e-03	2.83e-04	1.71e-04
24	2.45e-01	1.80e-03	1.23e-01	1.44e-04	4.70e-03	3.80e-04	1.59e-02	1.81e-05	3.16e-04	4.63e-05	3.12e-03	1.81e-03	1.22e-01	9.15e-04	6.51e-03	5.23e-04	3.19e-04
28	2.07e-01	2.22e-03	8.97e-02	1.42e-04	3.37e-03	2.53e-04	1.16e-02	2.02e-05	3.31e-04	3.81e-05	2.91e-03	1.55e-03	1.32e-01	1.13e-03	8.77e-03	6.77e-04	5.46e-04
30	0.00e+00	0.00e+00	0.00e+00	0.00e+00	0.00e+00	0.00e+00	0.00e+00	0.00e+00	0.00e+00	0.00e+00	0.00e+00	0.00e+00	0.00e+00	0.00e+00	0.00e+00	0.00e+00	0.00e+00
35	0.00e+00	0.00e+00	0.00e+00	0.00e+00	0.00e+00	0.00e+00	0.00e+00	0.00e+00	0.00e+00	0.00e+00	0.00e+00	0.00e+00	0.00e+00	0.00e+00	0.00e+00	0.00e+00	0.00e+00
40	0.00e+00	0.00e+00	0.00e+00	0.00e+00	0.00e+00	0.00e+00	0.00e+00	0.00e+00	0.00e+00	0.00e+00	0.00e+00	0.00e+00	0.00e+00	0.00e+00	0.00e+00	0.00e+00	0.00e+00
45	0.00e+00	0.00e+00	0.00e+00	0.00e+00	0.00e+00	0.00e+00	0.00e+00	0.00e+00	0.00e+00	0.00e+00	0.00e+00	0.00e+00	0.00e+00	0.00e+00	0.00e+00	0.00e+00	0.00e+00
50	0.00e+00	0.00e+00	0.00e+00	0.00e+00	0.00e+00	0.00e+00	0.00e+00	0.00e+00	0.00e+00	0.00e+00	0.00e+00	0.00e+00	0.00e+00	0.00e+00	0.00e+00	0.00e+00	0.00e+00
55	0.00e+00	0.00e+00	0.00e+00	0.00e+00	0.00e+00	0.00e+00	0.00e+00	0.00e+00	0.00e+00	0.00e+00	0.00e+00	0.00e+00	0.00e+00	0.00e+00	0.00e+00	0.00e+00	0.00e+00
60	0.00e+00	0.00e+00	0.00e+00	0.00e+00	0.00e+00	0.00e+00	0.00e+00	0.00e+00	0.00e+00	0.00e+00	0.00e+00	0.00e+00	0.00e+00	0.00e+00	0.00e+00	0.00e+00	0.00e+00
65	0.00e+00	0.00e+00	0.00e+00	0.00e+00	0.00e+00	0.00e+00	0.00e+00	0.00e+00	0.00e+00	0.00e+00	0.00e+00	0.00e+00	0.00e+00	0.00e+00	0.00e+00	0.00e+00	0.00e+00
70	0.00e+00	0.00e+00	0.00e+00	0.00e+00	0.00e+00	0.00e+00	0.00e+00	0.00e+00	0.00e+00	0.00e+00	0.00e+00	0.00e+00	0.00e+00	0.00e+00	0.00e+00	0.00e+00	0.00e+00
75	0.00e+00	0.00e+00	0.00e+00	0.00e+00	0.00e+00	0.00e+00	0.00e+00	0.00e+00	0.00e+00	0.00e+00	0.00e+00	0.00e+00	0.00e+00	0.00e+00	0.00e+00	0.00e+00	0.00e+00
80	0.00e+00	0.00e+00	0.00e+00	0.00e+00	0.00e+00	0.00e+00	0.00e+00	0.00e+00	0.00e+00	0.00e+00	0.00e+00	0.00e+00	0.00e+00	0.00e+00	0.00e+00	0.00e+00	0.00e+00
90	0.00e+00	0.00e+00	0.00e+00	0.00e+00	0.00e+00	0.00e+00	0.00e+00	0.00e+00	0.00e+00	0.00e+00	0.00e+00	0.00e+00	0.00e+00	0.00e+00	0.00e+00	0.00e+00	0.00e+00
95	0.00e+00	0.00e+00	0.00e+00	0.00e+00	0.00e+00	0.00e+00	0.00e+00	0.00e+00	0.00e+00	0.00e+00	0.00e+00	0.00e+00	0.00e+00	0.00e+00	0.00e+00	0.00e+00	0.00e+00
100	0.00e+00	0.00e+00	0.00e+00	0.00e+00	0.00e+00	0.00e+00	0.00e+00	0.00e+00	0.00e+00	0.00e+00	0.00e+00	0.00e+00	0.00e+00	0.00e+00	0.00e+00	0.00e+00	0.00e+00
120	0.00e+00	0.00e+00	0.00e+00	0.00e+00	0.00e+00	0.00e+00	0.00e+00	0.00e+00	0.00e+00	0.00e+00	0.00e+00	0.00e+00	0.00e+00	0.00e+00	0.00e+00	0.00e+00	0.00e+00
150	0.00e+00	0.00e+00	0.00e+00	0.00e+00	0.00e+00	0.00e+00	0.00e+00	0.00e+00	0.00e+00	0.00e+00	0.00e+00	0.00e+00	0.00e+00	0.00e+00	0.00e+00	0.00e+00	0.00e+00
200	0.00e+00	0.00e+00	0.00e+00	0.00e+00	0.00e+00	0.00e+00	0.00e+00	0.00e+00	0.00e+00	0.00e+00	0.00e+00	0.00e+00	0.00e+00	0.00e+00	0.00e+00	0.00e+00	0.00e+00
250	0.00e+00	0.00e+00	0.00e+00	0.00e+00	0.00e+00	0.00e+00	0.00e+00	0.00e+00	0.00e+00	0.00e+00	0.00e+00	0.00e+00	0.00e+00	0.00e+00	0.00e+00	0.00e+00	0.00e+00
300	0.00e+00	0.00e+00	0.00e+00	0.00e+00	0.00e+00	0.00e+00	0.00e+00	0.00e+00	0.00e+00	0.00e+00	0.00e+00	0.00e+00	0.00e+00	0.00e+00	0.00e+00	0.00e+00	0.00e+00
350	0.00e+00	0.00e+00	0.00e+00	0.00e+00	0.00e+00	0.00e+00	0.00e+00	0.00e+00	0.00e+00	0.00e+00	0.00e+00	0.00e+00	0.00e+00	0.00e+00	0.00e+00	0.00e+00	0.00e+00

4.4 Conclusions

In this work we investigated different scenarios of chemical enrichment produced by massive and very massive stars. To this purpose, we first analyzed their final fates on the base of physical criteria suggested in the literature. As expected, the final fate of massive and very massive stars mainly depend on the initial mass, initial metallicity and the adopted explosion model.

Massive stars, ranging from $8\,M_\odot$ to an upper limit that depends on metallicity (from $\sim 100\,M_\odot$ at low Z to few$100\,M_\odot$ at $\simeq Z_\odot$), end their life as CCSNe, which are divided in successful and failed CCSNe. Several authors confirm this result (Heger & Woosley 2002; Umeda & Nomoto 2002; Nomoto et al. 2013; Ertl et al. 2016, e.g.). The contribution of dark remnants depends on the adopted explosion criterion. Results obtained using the mono-parametric model of Frayer & Taylor (2012) show that black holes are generated both by successful and failed SN, while following the bi-parametric analysis carried out by Ertl et al. (2016) the fall-back of material after the explosion is minor so that only failed CCSNe can leave behind a black hole. Moreover, the mass range of successful explosions is also affected by the explosion model used: the maximum mass for successful SN obtained with Frayer & Taylor (2012) method varies from $25-30\,M_\odot$ to $50\,M_\odot$, depending on Z, while those obtained with Ertl et al. (2016) models is about $30\,M_\odot$ independently on Z. In this respect, we should caution that the bi-parametric analysis of Ertl et al. (2016) does not indicate a net threshold stellar mass between successful and failed SNe. Successful explosions are predicted to occur also for masses larger than $30\,M_\odot$, though their frequency appears to decrease (see figure 4.4). For simplicity, in our models we adopt $30\,M_\odot$ as reasonable limit.

The presence of massive BHs, generated by failed CCSNe, is confirmed by the recent detection of gravitational waves originating from binary black hole merger GW150914 (Abbott et al. 2016). The two black holes of masses $29M_\odot$ and $36M_\odot$ of GW150914 are most likely formed in an environments with metallicity lower than $1/2\,Z_\odot$ and probably lower than $1/4\,Z_\odot$ (Abbott et al. 2016; Spera et al. 2015; Mapelli et al. 2013). The masses derived from these observations agree with the values predicted by our models at Z = 0.006.

Stars more massive than $\sim 100\,M_\odot$, at low metallicity, evolve as VMOs, which end their evolution as PPISNe, PISNe or DBHs. We find that suitable conditions for the occurrence of PPISN and PISN events are not limited to extremely low metallicities, as suggested by Heger & Woosley (2002); Umeda & Nomoto (2002); Nomoto et al. (2006), but they can occur up to $Z = Z_\odot/3$. This result confirms the recent studies of Kozyreva et al. (2014b) and Langer et al. (2007), which show that such explosions may indeed occur in the local Universe.

In the second part of this work we obtained the winds and explosion ejecta of massive and very massive stars, for the wide range of initial mass and metallicities provided by *PARSEC* models. As

a result we generated a database of chemical ejecta from massive and very massive stars covering a wide range of initial metallicities. The tables will be publicly released to the astronomical community.

The wind ejecta are obtained directly from the *PARSEC* stellar evolutionary calculations, and include all isotopes from ^{1}H to ^{28}Si and heavier elements up to Zn. As expected, we find that the winds contributions increase with initial mass and initial metallicity. This effect is more evident for the elements N, C, O,Ne and Mg, which are produced during the hydrostatic burning phases.

We also note that the behavior of wind ejecta for carbon and oxygen produced by very massive stars is peculiar, as they are inversely correlated to the initial metallicity. We explained this behavior considering the stage at which the stars of different initial mass and metallicity enter in the WC and WO phases, during which the stars eject high quantity of carbon and oxygen as winds.

We compared our predictions with the results from other authors. Clearly, the wind ejecta depend not only on the adopted mass loss prescription, but they also bear on various physical inputs, such as the treatment of convection, nuclear reaction rates, and rotation. This latter (considered in models of Hirschi et al. (2005b)) produces an amount of stellar winds systematically higher than those obtained from non rotating models. This effect is explained by the increase of the mass-loss rate as well by the larger envelope chemical pollution caused by rotational mixing.

Finally, we calculated the integrated yields of winds and explosion ejecta over a Kroupa IMF for a simple stellar population of $10^6\,M_\odot$, separating the contribution of CCSNe, PPISNe and PISNe. We note that even though the number of stars in the PPISNe and PISNe range is significantly smaller than the number of CCSNe progenitors, the total amount of integrated ejecta from VMOs appears not negligible compared to that from massive stars. Our result is confirmed by Kozyreva et al. (2014c). Furthermore, considering that the PISNe can occur at initial metallicity up to $Z = Z_\odot/3$, we can conclude that,in environments with $Z \lesssim Z_\odot/3$, both massive and very massive stars contribute significantly to the chemical enrichment of ISM.

Chapter 5

Nucleosynthesis in intermediate-mass stars: neon and sodium ejecta

This chapter includes the analysis of the chemical ejecta of intermediate-mass stars, with particular focus on the thermally-pulsing asymptotic giant branch (TP-AGB) stars that experience both the third dredge-up and hot-bottom burning.

Different from the stars considered in previous sections, low and intermediate mass stars do not complete the whole nuclear processes until the iron core formation: after the central helium burning phase, the CO-core becomes degenerate and these stars evolve along the so-called *asymptotic giant branch* (AGB), in the HR diagram. The AGB is a brief but interesting and important phase of evolution because it is the site of rich nucleosynthesis. AGB stars experience also strong mass-loss episodes, which eventually remove their entire envelope. Under this conditions, the CO-core, after a brief transition phase as central star of a planetary nebula, becomes a long-lived cooling white dwarf.

The AGB phase begins when the the star finishes the available fuel of He, and the CO-core contracts. During a brief transition all layers below the H-burning shell contract, until He-burning shifts to a shell around the CO core. The star has now two active shells and a double mirror effect operates: when the core contracts, the He-rich layers above expand and the outer envelope starts to contract. The expansion of the He-rich zone causes a drop of the temperature in the H-shell, so that the H-burning shell extinguishes. Thus only one ”mirror” remains and now the entire envelope

(He-rich layer plus H-rich outer envelope) starts expanding in response to core contraction. This phase is named *early AGB phase*.

The He-burning shell gradually adds mass to the growing CO core, which becomes degenerate due to its increasing density. As the envelope expands and cools, the convective envelope penetrates deeper until it reaches the composition discontinuity left by the extinct H-shell.

If the initial mass is higher than $\sim 4\,M_\odot$ a convective dredge-up episode can occur and it is called *second dredge up*. During this phase the convective envelope penetrates down into the helium-rich layers. This effect is due to the combination of the continuing expansion and cooling of these layers, which increases their opacity, and the growing energy flux produced by the He-burning shell. The material that is dredged-up is subject to a nuclear processing: the hydrogen is burned into helium, ^{12}C have been completely converted into ^{14}N by the CNO-cycle. The amount of material dredged up can varies from 0.2 $M_\odot$ to 1 $M_\odot$, depending on the initial mass of the star. After the dredge-up, the material appears to the surface. One of the most important effect of the second dredge-up is the reduction of the mass of the H-exhausted core. As consequence the mass of the white dwarf that remains is reduced.

When the He-burning shell approaches the H-He discontinuity, its luminosity decreases because of the lack of fuel. As consequence, the above layers contract and heat the extinguished H-burning shell until it is re-ignited. Now both shells produce energy: this phase is named *double shell burning*. However, the two shells do not burn at the same cadence: the He-burning shell becomes thermally unstable and undergoes periodic *thermal pulses*. The star enters in the phase called *Thermally pulsing AGB* (TP-AGB).

The stellar structure of the star during the TP-AGB phase is well represented in figure 5.1. The TP-AGB phase of the AGB has some main properties:

- There is alternation between the periodic thermal pulses and the mixing episodes. This processes give rise to a unique nucleosynthesis of ^{12}C,^{14}N and elements heavier than iron, which get rich the stellar envelope and atmosphere of carbon. Expansion and cooling of the intershell region can also lead to a deeper penetration of the outer convective envelope. In some cases convection can penetrate beyond the now extinct H-burning shell, such that material from the intershell region is mixed into the outer envelope. This phenomenon is called *third dredge-up*.

- Similar to the RGB stars, the stellar properties mainly depend on the size of the degenerate CO core. In particular there is a tight core mass luminosity relation Boothroyd & Sackmann

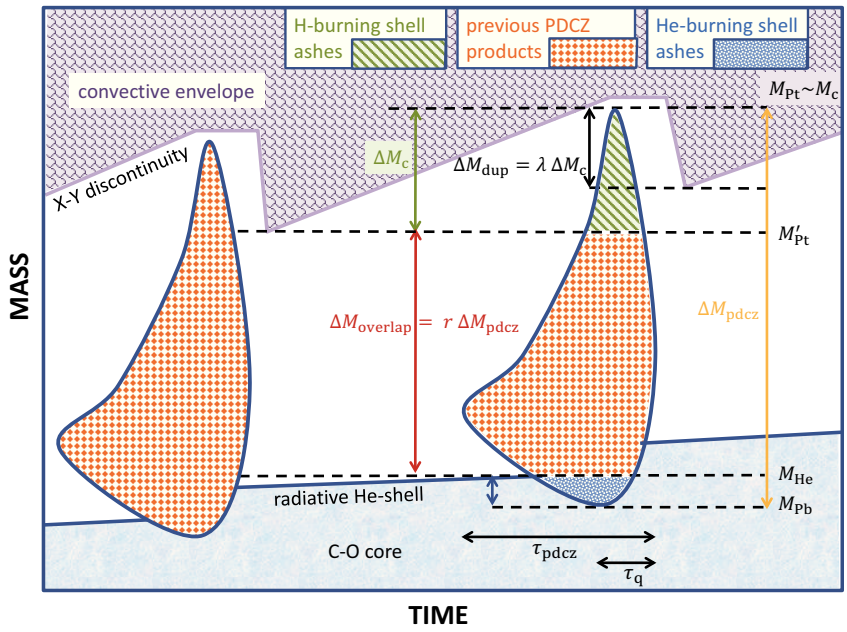

Figure 5.1: Kippenhahn diagram showing the evolution of the inner layers of a TP-AGB star during and between two consecutive thermal pulses. mass boundaries and relevant quantities (e.g degree of overlap r and the efficiency of the third dredge-up) are indicated. Note that the time coordinates are not in real scales, for graphical clarity. On the abscissa have been reported the lifetime of the convective pulse $\tau_{\rm PDCZ}$, and the quenching time $\tau_{\rm Q}$ counted from the maximum extension of the PDCZ. The figure is taken from Marigo et al. (2013)

(1988a):

$$L = 5.2 \cdot 10^4 L_{\odot} \left(\frac{M_c}{M_{\odot}} - 0.456 \right) \tag{5.1}$$

which is valid for $0.52 \lesssim \mathrm{M_c/M_{\odot}} \lesssim 0.7$ and for $3 \cdot 10^3 \lesssim \mathrm{L/L_{\odot}} 12 \cdot 10^4$.

- During the TP-AGB phase the stars experience strong mass loss episodes, up to $10^{-4}\mathrm{M_{\odot}/yr}$, which are probably driven by dynamical pulsations combined with radiation pressure on dust particles formed in the cool atmosphere. The mass loss gradually removes the envelope and replenishes the interstellar medium with the synthesized elements.

- The extended stellar atmosphere and circumstellar envelope are characterized by a rich molecular and dust chemistry. This is showed in their infra-red spectra, which have been observed by space telescope mission such as ISO and Spitzer.

The main effect of the thermal pulses operating in AGB stars is the appearance of the helium-burning products at the surface. Moreover, the surface abundances of many other elements and

isotopes change during the TP-AGB phase. The direct evidence for active nucleosynthesis in AGB stars was the detection the technetium ^{99}T, which decays in a timescale of $2 \cdot 10^5$yr, AGB stars are considered also the major producers of carbon, nitrogen and elements heavier than iron by the *s-process*. They also make an important contribution to the production of ^{19}F,^{25} Mg and ^{26}Mg and other isotopes.

Due to the large production of heavier elements, low- and intermediate-mass stars play a key role in the chemical evolution of the Universe. During their lives they experience a rich nucleosynthesis and various mixing episodes, eventually ejecting significant amounts of newly synthesized elements into the interstellar medium. Quantifying their chemical contribution is of key relevance to understand the chemical enrichment of galaxies and several theoretical studies were carried out to this purpose (Cristallo et al. 2015; Doherty et al. 2014a,b; Cristallo et al. 2011; Siess 2010; Ventura et al. 2013; Karakas & Lattanzio 2014; Ventura & Marigo 2010; Marigo 2001a; Forestini & Charbonnel 1997).

Despite the valuable efforts, large uncertainties still affect the yields of various elements, due to the uncertainties of the physical processes (i.e., mass loss, convection, mixing, nuclear reactions) that characterize the advanced evolutionary stages, in particular the thermally-pulsing asymptotic giant branch (TP-AGB).

In this study we will focus on the nucleosynthesis of ^{22}Ne and ^{23}Na and their ejecta produced by stars massive enough to experience the process of hot-bottom burning (hereinafter also HBB) during the AGB phase (M_i > 3-4 $M_\odot$). When, during the quiescent AGB evolution, the temperature at the base of convective envelope exceeds $\simeq 0.07$ GK, the CNO, NeNa and MgAl cycles are efficiently activated (Forestini & Charbonnel 1997), with the effect of significantly altering the abundances of the catalysts involved in the proton-capture reactions. The NeNa cycle is responsible for affecting the abundances of isotopes between ^{20}Ne and ^{24}Mg. The current uncertainties of the ^{22}Ne and ^{23}Na ejecta are dramatically high, up to factors of $\simeq 10$, given the large uncertainties that affect a few reaction rates involved in the NeNa cycle (e.g., Karakas 2010; Izzard et al. 2007; Ventura & D'Antona 2005b). The poor knowledge of resonances in ^{23}Na$(p,\alpha)^{20}$Ne and ^{23}Na$(p,\gamma)^{24}$Mg is critical (Hale et al. 2004). The rate of the NeNa cycle is determined by the slowest reaction of the chain, the ^{20}Ne$(p,\gamma)^{21}$Na (Rolfs & Rodney 1988), and most uncertainties are caused by the ^{22}Ne$(p,\gamma)^{23}$Na reaction. In fact, the systematic analysis carried out by Izzard et al. (2007) has shown that the ejecta of ^{23}Na is dominated by the uncertainties in the ^{22}Ne$(p,\gamma)^{23}$Na rate, with the destruction rates of ^{23}Na$(p,\gamma)^{24}$Mg and ^{23}Na$(p,\alpha)^{20}$Ne playing a

lesser role.

The contribution of resonances to the ^{22}Ne(p,γ)^{23}Na rate is still uncertain because of the large number of levels of ^{23}Na, the complexity of direct measurements and the interpretation of indirect data. This is particularly true for resonances at energies corresponding to the typical temperatures of hot-bottom burning in AGB stars, i.e. $0.07\,\mathrm{GK} \lesssim \mathrm{T} \lesssim 0.11\,\mathrm{GK}$ (e.g., Marigo et al. 2013; Boothroyd et al. 1995).

In this paper we analyze the impact on ^{22}Ne and ^{23}Na ejecta of the new rate for ^{22}Ne(p,γ)^{23}Na that has been recently revised following accurate measurements at LUNA (Cavanna et al. 2015b). We computed a large set of evolutionary models for stars that experience HBB and the third dredge-up during the AGB phase. The results are compared to those obtained with other versions of the rate in the literature, and also by varying other parameters that are critical for the evolution of AGB stars. The final aim is to re-evaluate the uncertainties that affect the ^{22}Ne and ^{23}Na ejecta, as well as to explore the implications we may draw on the hypothesis that metal-poor AGB stars are promising candidates to explain the O-Na anti-correlation exhibited by Galactic globular clusters' stars (e.g., D'Antona et al. 2016; D'Ercole et al. 2012; Ventura & D'Antona 2009).

The structure of the paper is organized as follows. In Section 5.1 we recall the main results and improvements obtained with recent LUNA data for the S-factor of the ^{22}Ne(p,γ)^{23}Na reaction. In Section 5.2 we outline the most relevant characteristics and input physics of the stellar evolutionary models. In Section 5.3 we discuss the evolution of the surface abundance of neon, sodium and magnesium isotopes in stars that experience HBB and the third dredge-up during the TP-AGB phase. A quantitative comparison of the ^{22}Ne and ^{23}Na ejecta as a function of the initial stellar mass and metallicity is provided in Section 5.4. In the context of the origin of the O-Na anti-correlation in Galactic globular clusters (GGCs), Section 5.5 analyzes the impact of the new LUNA rate on the AGB star hypothesis. Section 5.6 closes the paper providing a summary and a few final remarks.

5.1 The new LUNA rate for ^{22}Ne(p,γ)^{23}Na

In stellar models the ^{22}Ne(p,γ)^{23}Na reaction has usually been described according to one of the two popular rate compilations quoted in Table 5.1. They collect direct and indirect data on ^{22}Ne(p,γ)^{23}Na resonance strengths, namely: Angulo et al. (1999a, hereinafter NACRE); Iliadis et al. (2010a,b, hereinafter IL10). The latter was recently updated by the STARLIB group including new indirect data (Sallaska et al. 2013). It differs from the previous version by less than 3% in

the range of temperatures explored in this paper and we will still refer to IL10.

This situation was recently improved by direct measurements performed at LUNA in the underground facility of the Gran Sasso National Laboratory, where the low-background environment (Broggini et al. 2010; Costantini et al. 2009) and the available setup (Cavanna et al. 2014) offer the possibility to investigate nuclear reactions down to very low energies (Cavanna et al. 2015b).

In Cavanna et al. (2015b) three new resonances were observed for the first time, at 156.2, 189.5 and 259.7 keV laboratory energy. In addition, more precise ^{23}Na excitation energies corresponding to the new resonances were found, except for the 189.5 keV resonance. For other three resonances, at 71, 105, and 215 keV, new upper limits to the strengths were obtained.

In order to estimate the new total reaction rate a Monte Carlo method was used (see for more details Cavanna et al. 2015b). The new data were combined with previous direct measurement results for higher energy resonances (Depalo et al. 2015) and with literature resonant and non-resonant contributions (Iliadis et al. 2010a,b).

The new central value of the reaction rate lies between those of NACRE and IL10, see Fig. 5.2. The more precise excitation energies found for the 156.2 keV and 259.7 keV resonances are responsible for the increase of the reaction rate by a factor of $3-5$ with respect to IL10 at temperatures $0.12\,\mathrm{GK} \lesssim \mathrm{T} \lesssim 0.20\,\mathrm{GK}$. For $0.08\,\mathrm{GK} \lesssim \mathrm{T} \lesssim 0.25\,\mathrm{GK}$ the 1σ lower limit of the new reaction rate is above the upper limit calculated by IL10. Another effect of the direct observation of three new resonances in the range of temperatures $1.7\,\mathrm{GK} \lesssim \mathrm{T} \lesssim 2.5\,\mathrm{GK}$ is the reduction of the error bars of the total reaction rate, in comparison to NACRE and IL10. Nevertheless the new reaction rate has still larger uncertainties than IL10 for $0.05\,\mathrm{GK} \lesssim \mathrm{T} \lesssim 0.1\,\mathrm{GK}$. This is because of the different treatment of the 71 and 105 keV resonances, for which further investigation is necessary. As a matter of fact, in the range of temperatures of HBB in TP-AGB stars, see Fig. 5.2, the new reaction rate is higher than IL10 by about a factor of 20, which will significantly impact on model predictions.

5.2 Stellar evolutionary models

Stellar evolutionary models for intermediate-mass stars were calculated with the `PARSEC` and `COLIBRI` codes (Bressan et al. 2012; Marigo et al. 2013). The `PARSEC` tracks cover the evolution from the pre-main sequence up to the initial stages of the thermally-pulsing asymptotic giant branch (TP-AGB) phase. Starting from the first thermal pulse computed with `PARSEC`, the subsequent evolution up to the almost complete ejection of the envelope is followed with the `COLIBRI` code. The reader should refer to the aforementioned papers for all details about the two codes.

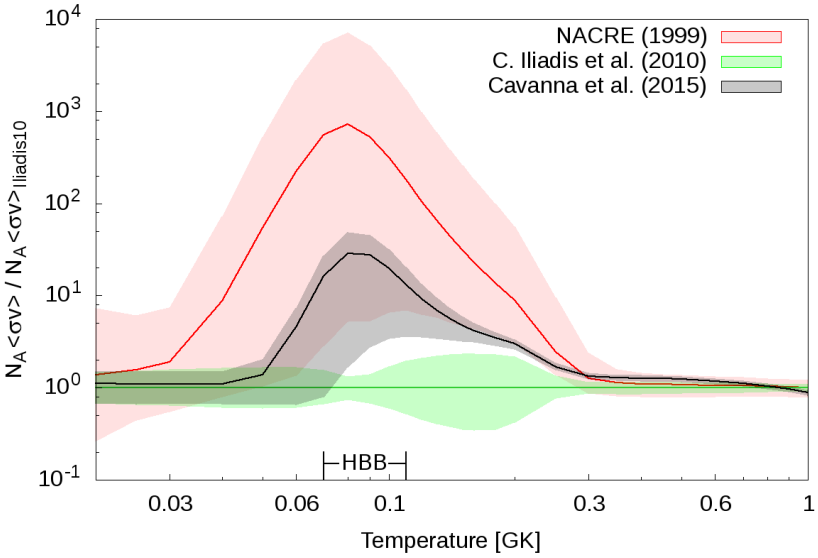

Figure 5.2: Total reaction rate normalized to IL10, as a function of temperature, calculated by NACRE (red line), IL10 (green line) and Cavanna et al. (2015b) (black line). The colored regions show the corresponding uncertainties. The range of temperatures relevant for the occurrence of HBB is also indicated.

We shortly recall the prescriptions for the adopted input physics which are mostly relevant for this work, common to both PARSEC and COLIBRI. Stellar convection is described by means of the classical mixing length theory (Böhm-Vitense 1958b). The mixing length is assumed to scale linearly with the pressure scale height, H_p, according to setting the proportionality factor $\alpha_{MLT} = 1.74$, following our recent calibration of the solar model (Bressan et al. 2012).

Overshoot is applied to the borders of convective cores as well as at the base of the convective envelope, and is described through the parameter Λ which sets its extension in units of H_p. In the range of intermediate stellar masses under consideration our default choice is $\Lambda_c = 0.5$ for convective core overshoot (across the classical Schwarzschild border) and $\Lambda_e = 0.7$ for envelope overshoot.

The network of nuclear reaction rates includes the proton-proton chains, the CNO tri-cycle, the NeNa and MgAl cycles, and the most important α-capture reactions, together with few α-n reactions. In the burning regions, at each time step, the network is integrated to derive the abundances of 26 chemical species: ^{1}H, D, ^{3}He, ^{4}He,^{7}Li, ^{8}Be, ^{4}He, ^{12}C, ^{13}C, ^{14}N, ^{15}N, ^{16}N, ^{17}N, ^{18}O, ^{19}F, ^{20}Ne, ^{21}Ne, ^{22}Ne, ^{23}Na, ^{24}Mg, ^{25}Mg, ^{26}Mg, ^{26}Al^{m}, ^{26}Al^{g}, ^{27}Al, ^{28}Si. Our initial reference set of nuclear reaction rates is taken from the JINA reaclib database (Cyburt et al. 2010), from which we also take the Q-value of each reaction. In total we consider 42 reaction rates (for

the complete list and references see Table 1 of Marigo et al. 2013). No neutron-capture reactions are included.

We computed the evolution of intermediate-mass stars with initial masses in the range between $3.0 M_\odot$ and $M_{\rm up}$ (in incremental steps of $0.2\,M_\odot$), the upper limit being the maximum mass for a star to develop a carbon-oxygen degenerate core at the end of the core helium burning phase. With the adopted input physics and prescriptions (e.g. the extension of convective core overshoot) we find that $M_{\rm up} \simeq 5-6\,M_\odot$ for the metallicity range under consideration. As for the chemical composition we consider three choices of the initial metallicity $Z_{\rm i}$ and helium content $Y_{\rm i}$, namely: $(Z_{\rm i}, Y_{\rm i}) = (0.0005, 0.249); (0.006, 0.0259); (0.014, 0.273)$. For each $Z_{\rm i}$ the corresponding $Y_{\rm i}$ is derived assuming a linear relation with a helium-to-metals enrichment ratio $\Delta Y/\Delta Z = 1.78$, a primordial helium abundance $Y_{\rm p} = 0.2485$, a Sun's metallicity at its birth $Z_\odot = 0.01774$, and a present-day Sun's metallicity $Z_\odot = 0.01524$ (more details can be found in Bressan et al. 2012). The initial distribution of metals is assumed to follow a scaled-solar pattern (Caffau et al. 2011) for $Z_{\rm i}$ =0.006, 0.014, while we adopt an α-enhanced mixture with [α/Fe]=0.4 for $Z_{\rm i} = 0.0005$. This latter is suitable to describe the chemical pattern of low-metallicity Halo stars and first-generation stars in Galactic globular clusters. The assumed chemical composition of the evolutionary models is summarized in Table 5.1.

Major effects on the NeNa nucleosynthesis show up during the TP-AGB phase of stars with hot-bottom burning. Therefore it is worth recalling the main features of the `COLIBRI` code, and our reference set of prescriptions according to Marigo et al. (2013, hereinafter also *M*13). Other model assumptions, summarized in Table 5.2, will be tested and discussed later in the paper (Sects. 5.4.1 and 5.5).

The evolution of the models presented in this work is followed at constant mass until the onset of the TP-AGB phase. To compute the mass-loss rate along the TP-AGB we first adopt the semi-empirical relation by Schröder & Cuntz (2005), modified according to Rosenfield et al. (2014), and then, as the star enters the dust-driven wind regime, we adopt an exponential form $\dot{M} \propto \exp(M^a R^b)$, as a function of stellar mass and radius (see for more details Bedijn 1988; Girardi et al. 2010; Rosenfield et al. 2014). The latter was calibrated on a sample of Galactic long-period variables with measured mass-loss rates, pulsation periods, masses, effective temperatures, and radii. We emphasize that the combination of the two mass-loss laws was calibrated through observations of resolved AGB stars in a large sample of nearby galaxies of low metallicities and various star-formation histories, observed with the HST/ACS Nearby Galaxy Survey Treasury (Rosenfield et al. 2016, 2014; Dalcanton et al. 2009), leading to a satisfactory reproduction of the measured star counts and luminosity functions.

In COLIBRI we account for the changes in the surface chemical composition caused by the occurrence of the third dredge-up and hot-bottom burning. As for the third dredge-up we adopt a hybrid approach that involves detailed physics as well as free parameters. We perform numerical integrations of the envelope structure at the stage of the post-flash luminosity peak to determine if and when the third dredge-up is expected to take place according to a temperature criterion (Marigo & Girardi 2007). The chemical composition of the pulse-driven convection zone is predicted by solving a nuclear network that includes the main α-capture reactions. The efficiency of the third dredge-up as a function of stellar mass and metallicity is computed with an analytic formalism based on full stellar models (Karakas et al. 2002). It includes adjustable parameters which are suitably modified in order to reproduce basic observables of AGB stars, such as carbon star luminosity functions, M-C transition luminosities, surface C/O ratios (e.g., Marigo 2015; Rosenfield et al. 2014; Marigo et al. 2013; Girardi et al. 2010; Marigo et al. 2008; Marigo & Girardi 2007; Marigo et al. 2003b).

The process of hot-bottom burning experienced by massive AGB stars (with initial masses $M_{\rm i} \geq 3-4\,M_{\odot}$, depending on metallicity and model details) is consistently taken into account in terms of energetics and nucleosynthesis.The nucleosynthesis of all species is coupled in time and in space with a diffusive description of convection.

A key characteristic of the COLIBRI code is that the equation of state for $\simeq 800$ atomic and molecular species, and the Rosseland mean of the gas opacities across the atmosphere and the deep envelope are computed on-the-fly, ensuring a full consistency with the changing abundances of all involved chemical elements (Marigo & Aringer 2009).

As for the nuclear reaction ^{22}Ne$(p,\gamma)^{23}$Na we mainly investigated three different experimental rates, namely: LUNA, IL10, and NACRE (see Table 5.1). Each selected option is adopted throughout the evolutionary calculations, from the main sequence to the end of the TP-AGB phase. For comparison, we also tested the theoretical rate from Cyburt et al. (2010), which was calculated with the version 5.0w of the NON-SMOKER$^{\rm WEB}$ code (Rauscher & Thielemann 2000). We note that in the temperature range of interest for HBB, $T \approx 0.07-0.12$ GK, the theoretical CYB10 rate is larger than IL10 by factors of $\sim 1\,000$.

5.3 Changes in the surface ^{22}Ne and ^{23}Na abundances

5.3.1 Prior to the TP-AGB: the second dredge-up

We will briefly discuss here the predicted changes in the surface Ne-Na abundances that may take place before the development of thermal pulses in intermediate masses, with $3M_{\odot} \lesssim M_{\rm i} \lesssim 6M_{\odot}$. We

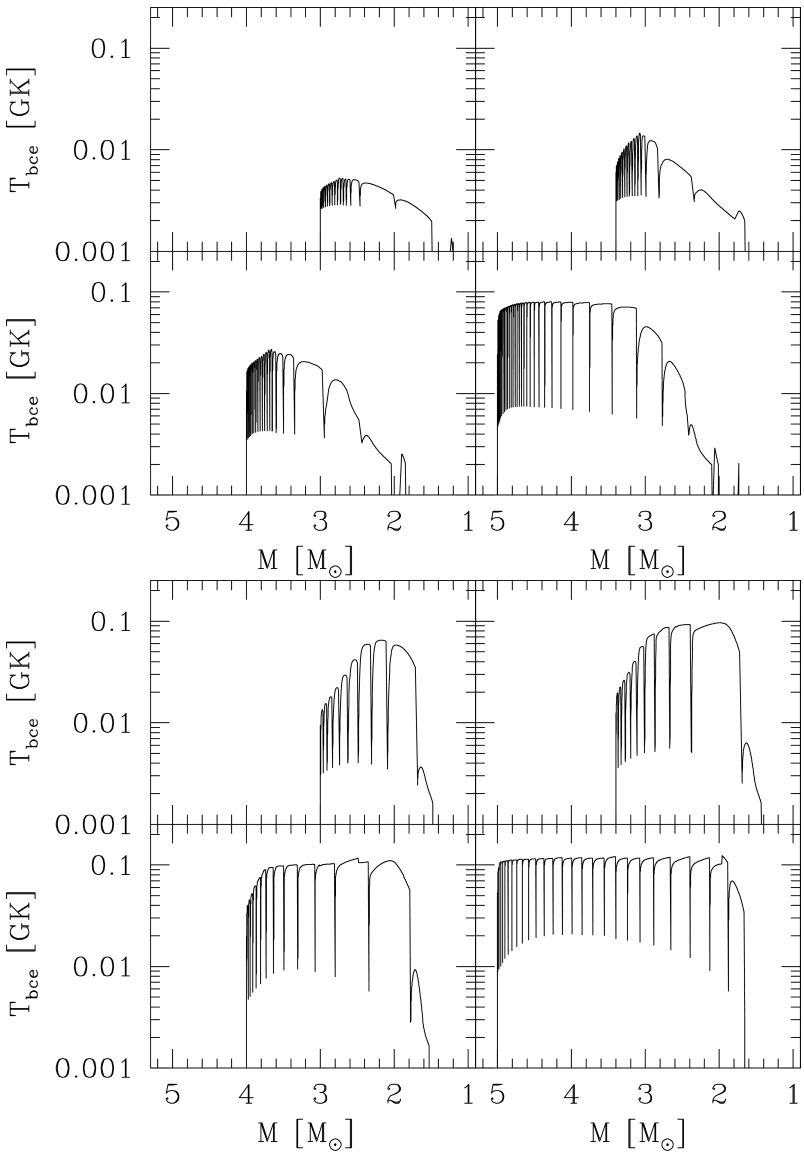

Figure 5.3: Evolution of the temperature at the base of the convective envelope as a function of the current stellar mass, during the TP-AGB phase of a few selected models with initial masses of 3.0, 3.4, 4.0, and 5.0 $M_{\odot}$, and metallicities $Z_{\rm i}$ = 0.014 (upper side) and $Z_{\rm i}$ = 0.0005 (lower side plot).

Table 5.1: Prescriptions adopted in the stellar evolutionary models (PARSEC and COLIBRI codes), namely: initial metallicity Z_i, initial helium abundance Y_i (both in mass fraction), distribution of metals, range of initial masses M_i. The upper mass limit corresponds to M_{up}, that is the maximum mass for a star to develop an electron-degenerate C-O at the end of the He-burning phase. Three experimental versions, together with a theoretical version for the rate of $^{22}Ne(p,\gamma)^{23}Na$, are reported. The ratio $\frac{<\sigma\upsilon>}{<\sigma\upsilon>_{IL10}}$ gives the value of a given rate at a temperature of 0.1 GK, normalized to the IL10 version.

Stellar parameters			
Z_i	Y_i	initial partition of metals	M_i [$M_\odot$] range (in steps of 0.2 $M_\odot$)
0.0005	0.249	[α/Fe]=0.4	3.0-5.0
0.006	0.259	scaled-solar	3.0-5.4
0.014	0.273	scaled-solar	3.0-5.6

Rate for $^{22}Ne(p,\gamma)^{23}Na$			
Reference	type	acronym	$\frac{<\sigma\upsilon>}{<\sigma\upsilon>_{IL10}}$
Iliadis et al. (2010a)	experimental	IL10	1.00e00
Cavanna et al. (2015b)	experimental	LUNA	1.80e01
Angulo et al. (1999a)	experimental	NACRE	3.13e02
Cyburt et al. (2010)	theoretical	CYB10	4.35e03

Table 5.2: Prescriptions for convection, mass loss and third dredge-up assumed in our TP-AGB models. The *M*13 set corresponds to our reference choice, initially adopted for all stellar models considered in this work. The *A*-*F* combinations are tested in stellar models with the lowest metallicity, i.e. Z_i = 0.0005, [α/Fe]=0.4, for which HBB is most efficient (see Section 5.5).

model class	α_{ML}	$\dot{M}$	λ_{max}	notes	
*M*13	1.74	*M*13	*M*13	reference set [a]	very efficient third dredge-up λ_{max} up to $\simeq$ 1
A	1.74	VW93	*M*13	popular mass-loss law	
B	1.74	B95	*M*13	efficient mass loss with η = 0.02	
C	2.00	*M*13	*M*13	efficient HBB	
D	1.74	*M*13	λ = 0	no third dredge-up	
E	2.00	*M*13	0.5	efficient HBB moderate third dredge-up $^{23}Na(p,\alpha)^{20}Na$ reduced by 5	
F	1.74	B95	λ = 0	efficient mass loss with η = 0.03 no third dredge-up $^{23}Na(p,\alpha)^{20}Na$ reduced by 3	

[a] Input prescriptions as in Marigo et al. (2013)

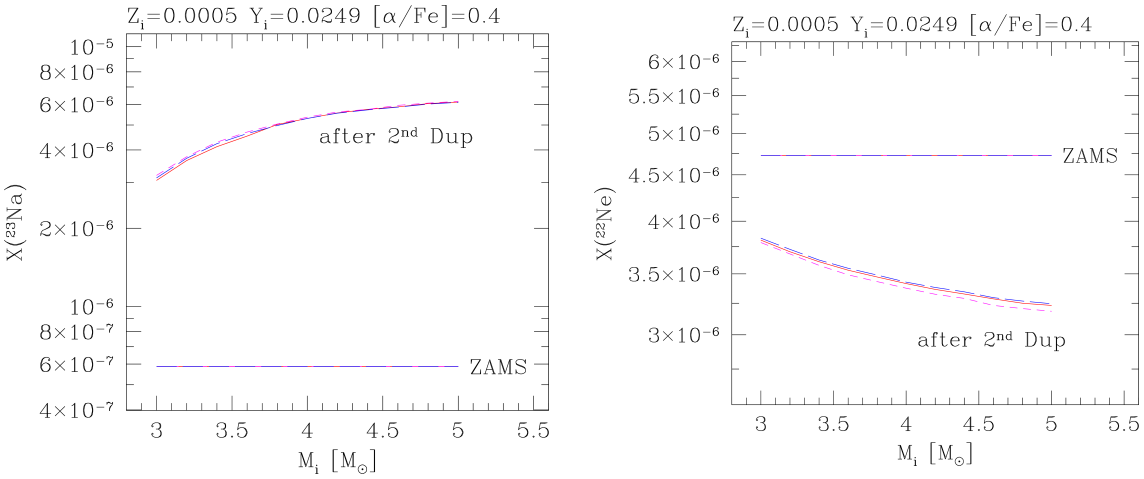

Figure 5.4: Surface abundances of ^{22}Ne (right) and ^{23}Na (left) as a function of the initial stellar mass at the zero-age main sequence (ZAMS) and after the second dredge-up on the E-AGB. Predictions are shown for three choices of the ^{22}Ne$(p,\gamma)^{23}$Na rate, namely: NACRE (magenta short-dashed line), IL10 (blue long-dashed line), LUNA (red solid line).

focus on the first and second dredge-up processes in the context of classical models, i.e. neglecting the possible contribution of extra-mixing events.

The first dredge-up takes place at the base of the red giant branch (RGB) when material that was processed through partial hydrogen burning via the CNO cycle and p-p chains is brought up to the surface. Models predict an increase of surface nitrogen, and a reduction of the isotopic ratio ^{12}C/^{13}C. As for the Ne-Na isotopes minor changes are expected, and their abundances remain essentially those of the initial chemical composition.

The situation is different when the second dredge-up occurs during the early-AGB (hereinafter also E-AGB) of stars with initial masses $M_{\rm i} > 3-4\,M_{\odot}$ (depending on metallicity and other model details). In these stars the base of the convective envelope deepens into the layers previously processed by the temporarily extinguished H-burning shell. The surface is enriched with material containing the products of complete H-burning. Significant variations in the surface concentrations of the Ne-Na isotopes are expected, as illustrated in Fig. 5.4 for a set of models with initial metal-poor composition. We see that ^{23}Na increases by a factor of 5-10 (larger for higher stellar masses), while ^{22}Ne is correspondingly reduced. These trends agree with the predictions of other stellar models in the literature (Karakas & Lattanzio 2014; Ventura & D'Antona 2006; Smiljanic et al. 2009; Mowlavi 1999b; Forestini & Charbonnel 1997).

The effects of different ^{22}Ne$(p,\gamma)^{23}$Na rates on the final Ne-Na abundances after the second dredge-up is minor. Comparing the results obtained with the rates quoted in Table 5.1, we find

that the relative differences with respect to the NACRE rate span a range $\simeq 1-4\%$ for ^{23}Na and to $\simeq 0.5-1\%$ for ^{22}Ne. This means that the Ne-Na surface concentrations after the second dredge-up are mainly controlled by the depth of the envelope penetration (e.g. through the mixing length, and/or the overshoot parameter). Conversely, the nuclear rates have a dramatic impact during the TP-AGB phase, when intermediate-mass stars are affected by the third dredge-up and hot-bottom burning. This aspect is discussed next, in Section 5.3.2.

5.3.2 During the TP-AGB: HBB nucleosynthesis and the third dredge-up

Evolutionary calculations of the TP-AGB phase indicate that the activation of the NeNa cycle at the base of the convective envelope requires relatively high temperatures, $T > 0.05$ GK, which can be attained in luminous and massive AGB and super-AGB stars, preferably at low metallicity (e.g., Doherty et al. 2014b; Marigo et al. 2013; Karakas & Lattanzio 2007; Forestini & Charbonnel 1997). Figure 5.3 compares the predicted temperatures at the base of the convective envelope, $T_{\rm bce}$, in TP-AGB models of various initial masses and two choices of the metallicity. Higher temperatures are reached by stars of larger mass and lower metallicity. The model with $\rm M_i = 5.0\,M_\odot$ and $\rm Z_i = 0.0005$ attains the highest temperatures, up to $\rm T_{bce} \sim 0.12$ K. In all models the final drop in temperature is caused by the reduction of the envelope mass by stellar winds, which eventually extinguishes HBB.

Provided that the NeNa cycle operates for a sufficiently long time, the main result is the synthesis of ^{23}Na at the expenses of the Ne isotopes. In general, the competition between production (through the reaction $^{22}\mathrm{Ne}(p,\gamma)^{23}\mathrm{Na}$) and destruction (through the reactions $^{23}\mathrm{Na}(p,\alpha)^{20}\mathrm{Ne}$ and $^{23}\mathrm{Na}(p,\gamma)^{24}\mathrm{Mg}$) depends on the temperature of the burning zone and the duration of the process.

The picture above becomes more complex if, in addition to HBB, the star experiences also the third dredge-up. During the power-down phase of a thermal pulse the base of the convective envelope may reach the region that was previously affected by the pulse-driven convective zone (hereafter PDCZ), which causes a rapid change in the surface chemical composition. The standard chemical composition of the PDCZ mainly consists of ^{12}C ($\simeq 20\%-25\%$), ^{16}O ($\simeq 1\%-2\%$), ^{22}Ne ($\simeq 1\%-2\%$), with ^{4}He practically comprising all the rest (Boothroyd & Sackmann 1988b; Mowlavi 1999b), almost regardless of metallicity and core mass.

Figure 5.5 (left panel) shows the predicted abundances in the PDCZ developing at each thermal pulse in TP-AGB stars with initial mass $M_{\rm i} = 5\,M_\odot$ and initial metallicity $Z_{\rm i} = 0.006$, computed with the `COLIBRI` code. We note that ^{4}He, ^{12}C, and ^{16}O achieve the typical concentrations that characterize the classical PDCZ composition. The amount of mass dredged-up at each thermal

pulse and the corresponding efficiency λ[1] are also illustrated in Fig. 5.5 (right panel). Similar results apply to the other metallicities here considered. In all models with $M_{\rm i} > 4\,M_{\odot}$ the the third dredge-up is predicted to become quite deep as thermal pulses develop, reaching a maximum around $\lambda \simeq 1$. These trends are obtained following the predictions of full stellar AGB calculations of Karakas et al. (2002), which are characterized by very efficient third dredge-up. Different prescriptions, i.e. lower values of λ, are adopted in additional sets of AGB models, which are discussed in Sections 5.4.1 and 5.5. The rapid decrease of λ takes place over the last stages, when the envelope mass is dramatically reduced by stellar winds.

In the context of this study it is interesting to analyze the abundances of ^{22}Ne and ^{23}Na in the PDCZ, and the effect of the envelope chemical composition on them. The ^{22}Ne isotope is relatively abundant in the PDCZ, increasing up to nearly 1% in mass fraction in the $Z_{\rm i} = 0.0005$ models, while it reaches up to $\simeq 2\%$ in the $Z_{\rm i} = 0.014$ models, where it exceeds the ^{16}O abundance. In the PDCZ ^{22}Ne is the product of the chain of α-capture reactions that starts from the ^{14}N, left over by the H-burning shell at the end of the inter-pulse period, i.e. $^{14}{\rm N}(^4{\rm He},\gamma)^{18}{\rm F}(\beta^+\nu)^{18}{\rm O}(^4{\rm He},\gamma)^{22}{\rm Ne}$. Therefore, at each thermal pulse the abundance ^{22}Ne in the PDCZ depends on the current CNO content in the envelope, and positively correlates with the efficiency of the third dredge-up. In fact, the injection of primary ^{12}C into the envelope by the third dredge-up increases the CNO abundance available to the H-burning shell, which will be mainly converted into ^{14}N during the quiescent inter-pulse periods.

Conversely, the abundance of ^{23}Na in the PDCZ is largely unaffected by He-burning nucleosynthesis during the thermal pulse (Forestini & Charbonnel 1997), while it is essentially determined by the shell H-burning during the previous inter-pulse period. In fact, when a thermal pulse develops, the associated PDCZ can reach the inter-shell region where some unburnt ^{23}Na survived against proton captures. Then, this secondary ^{23}Na is mixed out in the PDCZ and eventually injected into the envelope during the third dredge-up (see Mowlavi 1999b, for a thorough analysis). More recently, Cristallo et al. (2009) discussed the formation of a ^{23}Na-pocket in the transition region between the core and the envelope, which may provide an additional source of sodium. However, those results apply to low-mass stars and should not affect the ejecta of sodium from more massive AGB stars considered here.

In view of the above, it is clear that the third dredge-up and HBB nucleosynthesis are closely coupled and affect the surface abundances of ^{22}Ne and ^{23}Na, (see, e.g., Ventura & D'Antona 2006; Karakas & Lattanzio 2003; Mowlavi 1999a; Forestini & Charbonnel 1997, for similar results

[1] According to a standard notation the efficiency of the third dredge-up is expressed with $\lambda = \Delta M_{\rm dup}/\Delta M_{\rm c}$, which is the fraction of the core mass increment over an inter-pulse period that is dredged-up to the surface at the next thermal pulse.

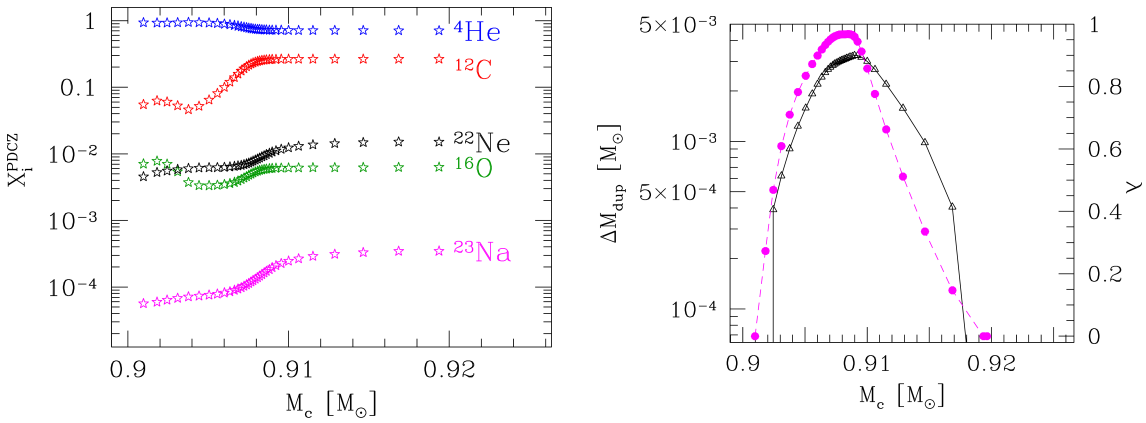

Figure 5.5: Characteristics of the third dredge-up as a function of the core mass during the TP-AGB evolution of a star with initial mass $M_i = 5\,M_\odot$ and metallicity $Z_i = 0.006$. Input prescriptions correspond to our reference set (*M*13; see Table 5.2), while other assumptions for the third dredge-up are discussed later in the paper (see Sections 5.4.1, 5.5 and Table 5.2). Left panel: Abundances (in mass fraction) left in the PDCZ after the development of each thermal pulse as a function of the core mass. Right panel: Amount of dredged-up material at each thermal pulse (black triangles connected by solid line), and efficiency parameter λ (filled magenta circles connected by dashed line). Similar trends hold for the other Z_i considered in this work.

discussed in the past literature). Each time a third dredge-up event takes place, some amounts of ^{22}Ne and ^{23}Na are injected into the convective envelope where they will be subsequently involved in the NeNa cycle when HBB is re-activated during the quiescent inter-pulse periods.

This is exemplified in Fig. 5.6, which shows the evolution of the surface abundances in low-metallicity stars that undergo both HBB during the quiescent inter-pulse periods and recurrent third dredge-up episodes at thermal pulses. The spikes of ^{22}Ne correspond to the quasi-periodic enrichment caused by the third dredge-up, while the subsequent decrease (particularly evident in the bottom-left panel) shows the destruction due to ^{22}Ne$(p,\gamma)^{23}$Na when HBB is reignited.

Comparing the four panels of Fig. 5.6, each corresponding to a different choice of the rate for ^{22}Ne$(p,\gamma)^{23}$Na, it is also evident that the abundance trends of ^{22}Ne, ^{23}Na, and ^{24}Mg are critically affected by this reaction. Note, for instance, how much the amplitude of the saw-teeth trend for ^{22}Ne is reduced when passing from CYB10 to LUNA. This simply reflects the fact that with the new LUNA rate proton captures on ^{22}Ne nuclei are much less frequent than predicted by CYB10 when HBB is active.

Besides the evolution of the surface abundances, it is particularly relevant to quantify the amount of the processed material AGB stars expel via stellar winds. Therefore, in the next section we will analyze the ejecta of ^{22}Ne and ^{23}Na and their uncertainties, with particular focus on the

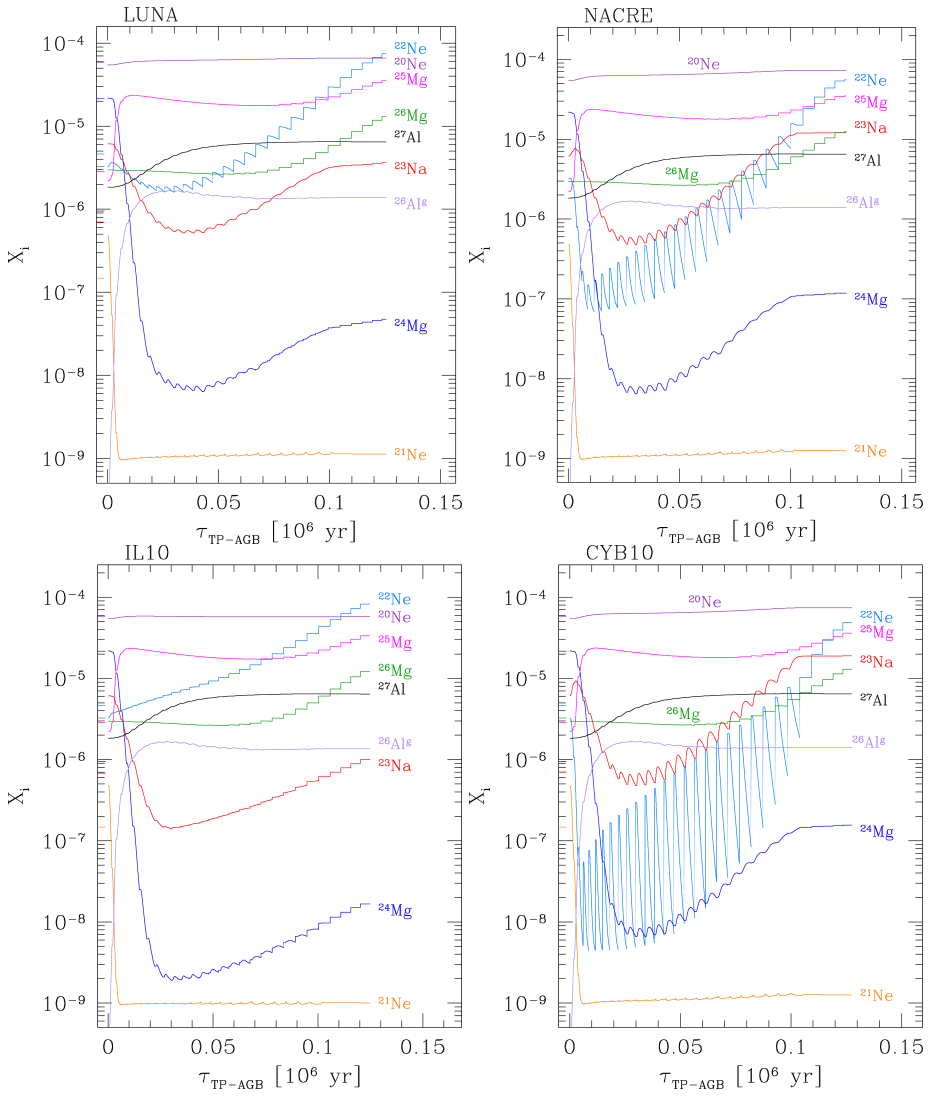

Figure 5.6: Evolution of envelope abundances of Ne, Na, and Mg isotopes (in mass fraction) during the whole TP-AGB phase of a star with initial mass $M_{\rm i} = 5\,M_{\odot}$, metallicity $Z_{\rm i} = 0.0005$, and α- enhancement $[\alpha/{\rm Fe}] = 0.4$. Time is counted since the first TP. The model experiences both HBB and third dredge-up events. All models share the same input physics but for the rate of ^{22}Ne$(p,\gamma)^{23}$Na, as indicated in the labels (see also Table 5.1). Major differences show up in the evolution of ^{22}Ne, ^{23}Na, and ^{24}Mg.

impact of the new LUNA rate.

5.4 AGB ejecta of ^{22}Ne and ^{23}Na

Figure 5.7 illustrates the ejecta of ^{22}Ne and ^{23}Na produced by all stellar models in our reference grid Marigo et al. (2013, *M*13, see also Table 5.2), for three choices of the initial composition and three choices of the ^{22}Ne$(p,\gamma)^{23}$Na rate. We do not present the results for ^{24}Mg since, contrarily to the evolution of the abundance, the time-integrated ejecta are found to be little affected by the adopted rate. This is due to two reasons. In stars of relatively low mass or high metallicity the temperature at the base of the convective envelope may not reach the values necessary to activate the Mg-Al cycle. In more massive and metal-poor stars, that attain the suitable temperature conditions, the main contribution to the time-integrated ^{24}Mg ejecta comes from the very initial stages when the abundance of this isotope starts to be quickly reduced by proton captures (see the initial steep decrease of ^{24}Mg in all panels of Fig. 5.6). The very initial drop of the ^{24}Mg abundance is practically independent of the assumed rate for the ^{22}Ne$(p,\gamma)^{23}$Na reaction. Then, when the abundance evolution of ^{24}Mg becomes affected by the ^{23}Na production rate (as the ^{24}Mg curve reaches a minimum and starts to increase), the ^{24}Mg concentration has already decreased by orders of magnitude, and the contribution to the ejecta of the subsequent stages remains small. The differences in the final ^{24}Mg ejecta are within $\sim 2-5\%$ for the models in Fig. 5.6.

We see that the LUNA results are intermediate between those predicted with NACRE and IL10. At a given initial stellar mass, the LUNA ejecta for ^{23}Na are lower than NACRE, but somewhat larger than IL10. The opposite is true for ^{22}Ne. The differences become prominent towards higher initial stellar masses and lower metallicities, conditions that favor the development of HBB.

In this respect the bar diagrams also show the minimum mass for the activation of HBB, in particular the NeNa cycle, in AGB stars as a function of the metallicity. We adopt an empirical definition, looking for the stellar mass above which the chemical yields of ^{22}Ne and ^{23}Na, calculated with different rates for the ^{22}Ne$(p,\gamma)^{23}$Na reaction, start to differ in the bar diagram of Fig. 5.7. At lower masses the yields are essentially the same because the nuclear rate remain too low during the TP-AGB phase. We see that this mass limit is $\sim 4.8\,M_\odot$ at $Z_\mathrm{i} = 0.014$, $\sim 4.2\,M_\odot$ at $Z_\mathrm{i} = 0.006$, and $\sim 3.0\,M_\odot$ at $Z_\mathrm{i} = 0.0005$.

We also see that the trend of the ^{22}Ne and ^{23}Na ejecta with the stellar mass is not monotonic. At increasing stellar mass, the ejecta initially increase, reach a maximum, and then decrease again. The maximum ^{22}Ne and ^{23}Na ejecta do not occur at the same initial mass, but a lower mass for ^{22}Ne, both decreasing with the metallicity.

These behaviors are the combined result of the strength of HBB, the efficiency of the third dredge-up, the TP-AGB lifetime, and their dependencies on stellar mass and metallicity.

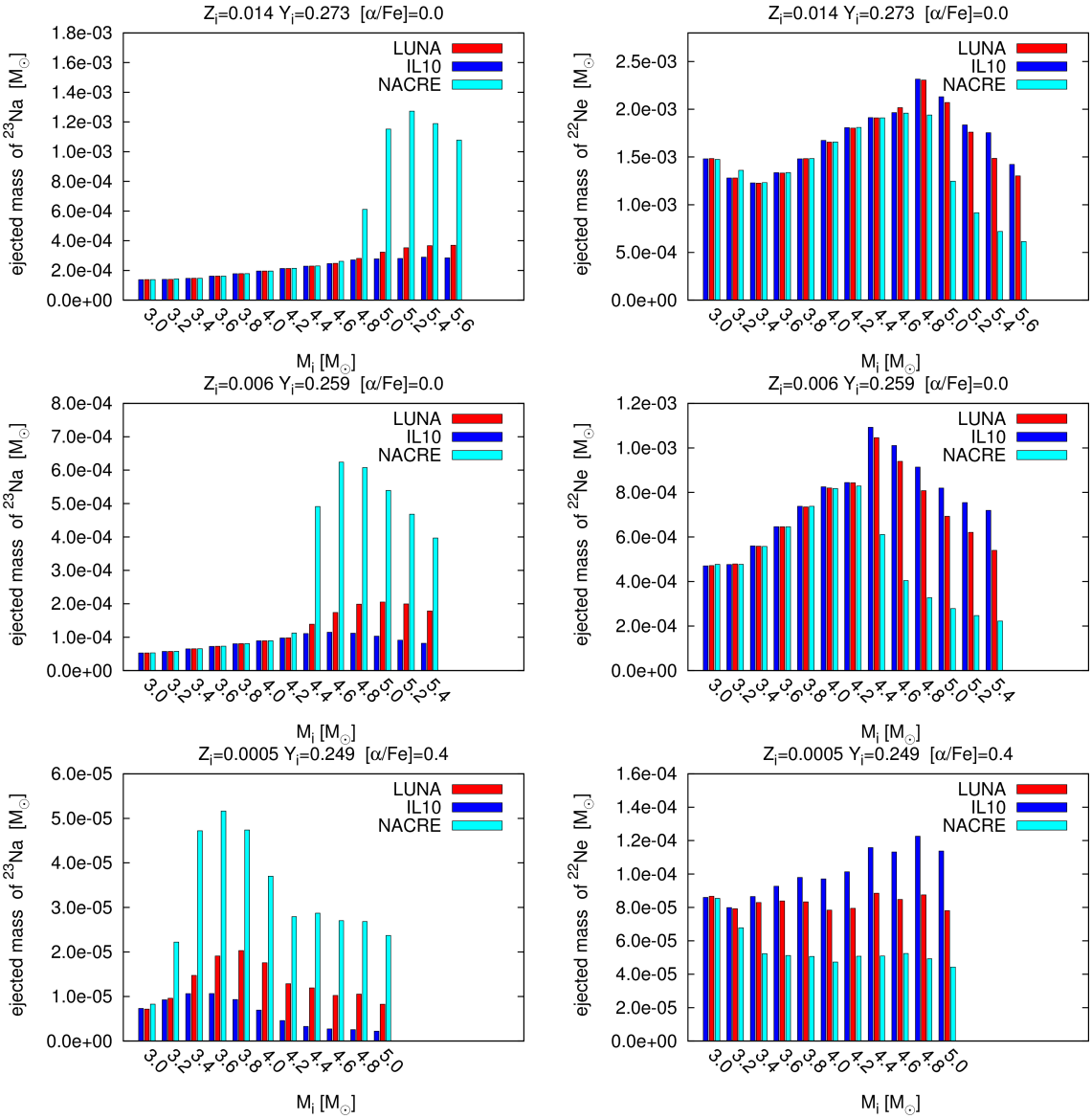

Figure 5.7: ^{22}Ne and ^{23}Na ejecta expelled into the interstellar medium by stellar winds during the whole TP-AGB phase by intermediate-mass stars with HBB as a function of the initial mass and for three choices of the original metallicity, namely: $Z_i = 0.014$, $Z_i = 0.006$, and $Z_i = 0.0005$. The plots compare the results obtained with four choices for the ^{22}Ne$(p,\gamma)^{23}$Na rate (as indicated in the upper labels).

5.4.1 Nuclear versus stellar model uncertainties

We discuss here the impact of the uncertainties associated to the nuclear rate cross sections, as well as those produced by evolutionary aspects that characterize the AGB evolution. As to super-AGB stars, the reader may refer to the studies of Doherty et al. (2014a,b).

Nuclear uncertainties

Figure 5.8 displays the uncertainties in the ^{22}Ne, ^{23}Na and ^{24}Mg ejecta ascribed only to the current uncertainties in the LUNA rate of the ^{22}Ne$(p,\gamma)^{23}$Na reaction, for our reference set of stellar model prescriptions. The error bars for ^{22}Ne and ^{23}Na increase in models with larger initial mass and lower metallicity. This is not surprising since these conditions favor the development of HBB due to the higher temperatures attained at the base of the convective envelope.

Let us denote with $f_{\rm L}$ and $f_{\rm U}$ the ratios between the ejecta obtained with the lower and upper limits of the LUNA rate and those obtained with the recommended LUNA rate. In the AGB models with $Z_{\rm i} = 0.0005$ and initial masses in the range $3.0 - 5.0\,M_{\odot}$ the error bars for the ^{22}Ne and ^{23}Na ejecta correspond to factor pairs $(f_{\rm L}, f_{\rm U})$ of $\simeq (0.92 - 0.97, 1.01 - 1.28)$ and $(0.43 - 0.95, 1.01 - 1.25)$, respectively. These values are significantly lower than the error bars estimated by Izzard et al. (2007), who reported much wider ranges $\sim (0.14 - 0.17, 1.00 - 1.01)$ and $\sim (0.53 - 0.62, 33 - 106)$ for the ^{22}Ne and ^{23}Na ejecta produced by the lowest metallicity set of their synthetic TP-AGB models[2] when varying the ^{22}Ne$(p,\gamma)^{23}$Na rate only.

The LUNA improvement is indeed striking for the upper limit of ^{23}Na ejecta, as the relative uncertainty has decreased from ~ 100 to ~ 1.25 in the worst case. No significant effect is predicted for the ejecta of ^{24}Mg.

To have a global evaluation of the nuclear uncertainties affecting the ejecta of ^{22}Ne and ^{23}Na we should consider other relevant reactions involved in the NeNa cycle, in particular ^{20}Na$(\mathrm{p},\gamma)^{21}$Ne, ^{23}Na$(\mathrm{p},\alpha)^{20}$Ne and ^{23}Na$(\mathrm{p},\gamma)^{24}$Mg. To this aim we refer to the results of detailed investigations carried out by Izzard et al. (2007) and more recently by Cesaratto et al. (2013).

In the work of Izzard et al. (2007) all reaction rates involved in the NeNa cycle were varied simultaneously in all possible combinations of lower and upper limits, available at that time. As to the ^{23}Na+p rates, the reference rates were taken from Rowland et al. (2004), and multiplicative factors of $/1.3, \times 1.3$ and $/40, \times 10$ were adopted to define the lower and upper limits for the rates of ^{23}Na$(\mathrm{p},\alpha)^{20}$Ne and ^{23}Na$(\mathrm{p},\gamma)^{24}$Mg, respectively.

A conclusion of the study by Izzard et al. (2007) was that the ejecta of ^{22}Ne and ^{23}Na are

[2]The quoted results of Izzard et al. (2007) refer to stellar models with $Z_{\rm i} = 0.0001$ and $M_{\rm i} = 4, 5, 6\,M_{\odot}$.

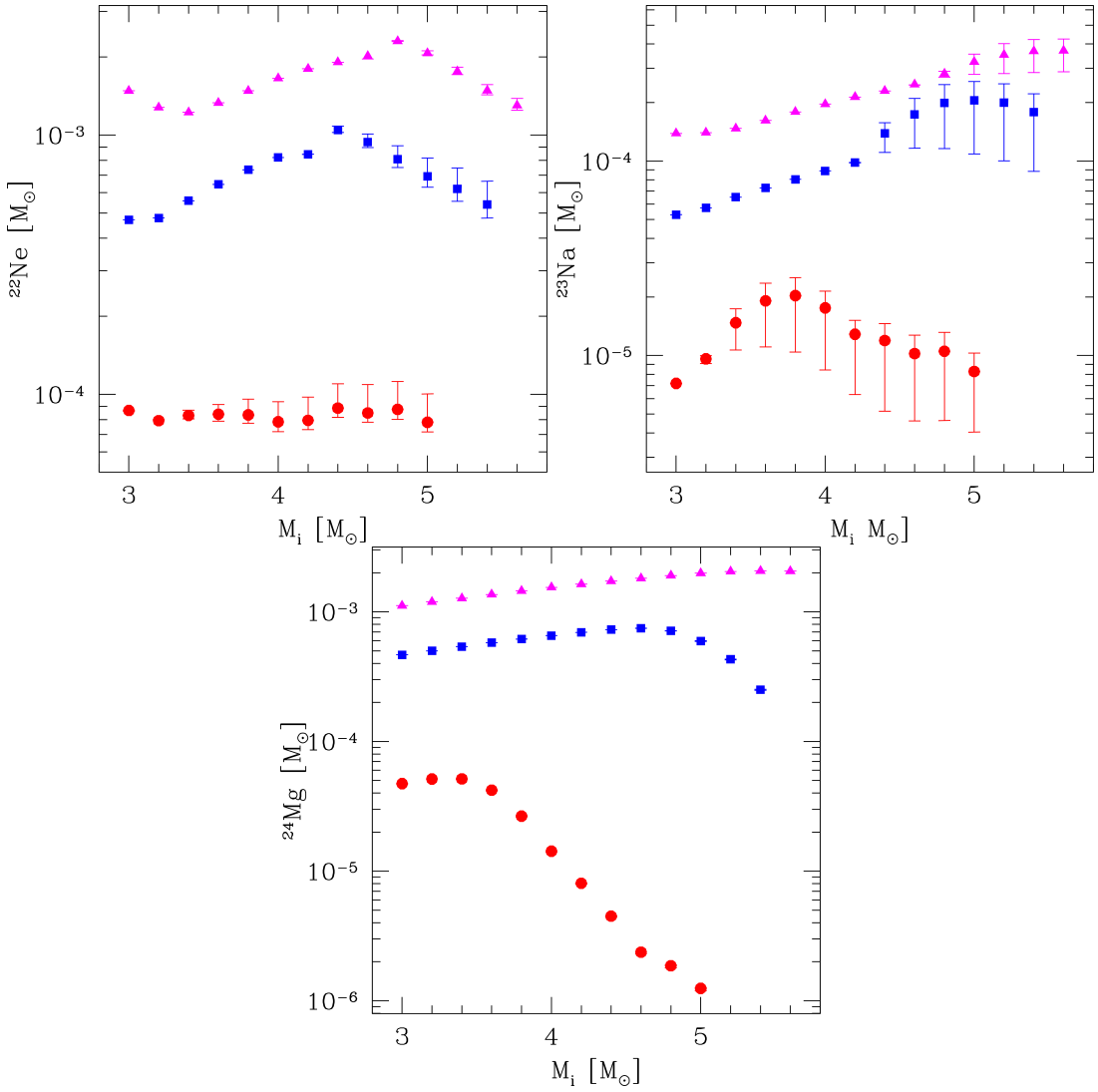

Figure 5.8: Ejecta and corresponding uncertainties of ^{22}Ne, ^{23}Na, and ^{24}Mg due to the uncertainties in the LUNA rate for the ^{22}Ne$(p,\gamma)^{23}$Na nuclear reaction, as a function of the initial stellar mass and metallicity (magenta triangles for $Z_i = 0.014$, blue squares for $Z_i = 0.006$, and read circles for $Z_i = 0.0005$). Symbols show the results obtained with the recommended rate, while the error bars correspond to the use of the lower and upper limits for the rate (see Fig. 5.2).

mainly affected by the uncertainties of the ^{22}Ne$(p,\gamma)^{23}$Na rate (see tables 6 and 7 of Izzard et al. (2007)). Only for ^{23}Na the lower-range uncertainties in the ejecta were found to be somewhat influenced by the uncertainties in the destruction rates ^{23}Na+p (see their table 7).

More recently, Cesaratto et al. (2013) calculated new rates for ^{23}Na$(p,\alpha)^{20}$Ne and ^{23}Na$(p,\gamma)^{24}$Mg

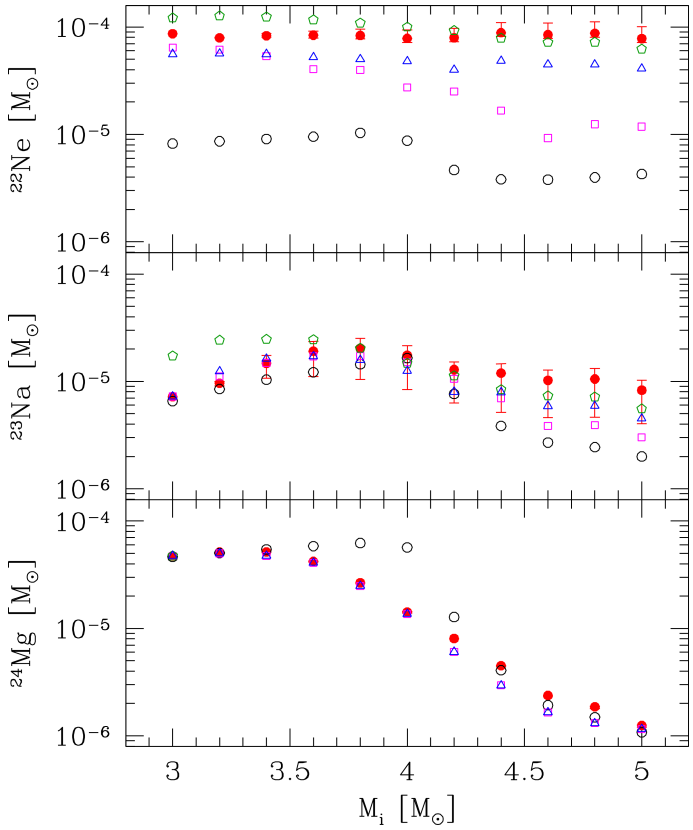

Figure 5.9: Uncertainties in the ^{22}Ne, ^{23}Na, and ^{24}Mg ejecta contributed by stars with initial masses in the range $M_i = 3.0 - 5.0\,M_\odot$ and metallicity $Z_i = 0.0005$. The red error bars represent the uncertainties in the LUNA rate and are the same as in Fig. 5.8. The empty symbols correspond to the ejecta obtained with the recommended LUNA rate while varying other model prescriptions, namely: Vassiliadis & Wood (1993) mass-loss law (green pentagons), Blöcker (1995) mass-loss law (magenta squares), mixing-length parameter $\alpha_{ML} = 2.0$ (blue triangles), no third dredge-up (black circles).

based on nuclear experiments which allowed, for the first time, to derive an upper limit estimate for the strength of a 138-keV resonance, until then neglected in previous studies. A consequence of this is that the recommended rate for ^{23}Na(p,γ)^{24}Mg has been reduced significantly (by over one order of magnitude at $T \simeq 0.07$ GK), compared to the IL10 version. At the same time, the contribution of the 138-keV resonance is found to be negligible for the ^{23}Na(p,α)^{20}Ne reaction and the revised rate of Cesaratto et al. (2013) is in excellent agreement with that of IL10.

As a result, the ^{23}Na destruction due to proton captures appears to be totally dominated by the ^{23}Na(p,α)^{20}Ne reaction over the temperature range relevant for HBB. The (p,α)/(p,γ) reaction rate ratio is $\gtrsim 100$ all over the temperature interval characteristic of HBB, so that a minor leakage

into the Mg-Al cycle is expected (see figure 16 of Cesaratto et al. 2013).

Therefore, despite the large reduction of the ^{23}Na(p,γ)^{24}Mg rate, the impact on the abundance of ^{23}Na is quite small. In their test nucleosynthesis calculations, applied to an AGB model with HBB, Cesaratto et al. (2013) derived an increase in the final ^{23}Na abundance by only $\simeq$ 13% compared the predictions obtained with the IL10 rate.

Concerning the present estimates for the lower and upper limit uncertainties of the ^{23}Na+p reactions over the range temperature range 0.07-0.1 GK, the typical dividing/multiplicative factors with respect to the recommended rate do not exceed $\simeq 1.20-1.25$ in the case of the IL10 rate for ^{23}Na(p,α)^{20}Ne, and are within the range $\simeq 1.4-3.0$ in the case of the rate for ^{23}Na(p,γ)^{24}Mg revised by Cesaratto et al. (2013). These values correspond to relatively small uncertainties and should be taken into consideration when discussing the role of AGB stars with HBB in the context of the observed O-Na anti-correlations of GGC stars (see Section 5.5).

Evolutionary uncertainties

It is instructive to compare now the current nuclear uncertainties with those that are driven by stellar evolution uncertainties. It is well known that the most problematic aspects to treat on theoretical grounds are those related to mass loss, third dredge-up and HBB, due to our still defective knowledge of the complex physics involved. Basically, we lack an accurate determination of the efficiency of these processes, and how they vary with the mass and the composition of the star.

Mass loss is commonly parameterized in AGB stellar models and several possible options are available. Depending on the adopted mass-loss rate prescription quite significant differences arise in the evolutionary models, mainly in terms of lifetimes, number of thermal pulses, chemical enrichment, final core mass, and HBB over-luminosity (see, e.g. Rosenfield et al. 2016; Kalirai et al. 2014; Ventura & D'Antona 2005b). HBB efficiency is also critically affected by the adopted theoretical framework to treat convection and its related parameters (e.g., Ventura & D'Antona 2005a). The depth of the third dredge-up is still much debated among AGB modelers (e.g., Marigo & Girardi 2007; Marigo 2015, for a review), as it critically depends also on technical and numerical details (Mowlavi 1999a; Frost & Lattanzio 1996). For massive AGB stars with $M_{\rm i} \gtrsim 4\,M_{\odot}$, the situation is particularly heterogeneous, as the predictions for the efficiency λ vary from high (≈ 1 or larger, e.g. Herwig 2004; Karakas et al. 2002; Vassiliadis & Wood 1993), to moderate (e.g., Cristallo et al. 2015; Ventura & D'Antona 2008). In this mass range direct constraints from observations are still lacking, making the overall picture rather unclear.

In view of the above, we estimated the impact of stellar evolution assumptions computing additional TP-AGB models with ($Z_{\rm i}$ = 0.0005, [α/Fe]=0.4), each time changing an input prescrip-

tion. The adopted prescriptions are summarized in Table 5.2. With respect to the reference model, calculated following $M13$, the changes were applied to the mixing-length parameter $\alpha_{\rm ML}$, the mass-loss rate $\dot{M}$, and the third dredge-up efficiency λ. The reference $M13$ model is characterized by a very efficient third dredge-up (with a maximum λ close to unity; see right panels of Fig. 5.5), a relatively efficient HBB which leads to the activation of the CNO, NeNa, MgAl cycles (see Fig. 5.6), and a mass-loss prescription that was calibrated on a sample of Galactic Miras.

The sequence of the four models $A-B-C-D$ was chosen to test the effect on the ejecta of ^{22}Ne, ^{23}Na, and ^{24}Mg when varying the strength of the aforementioned processes. It is worth noting that there is a strong coupling among them so that a change in one process may have a sizable impact also on the others. The main results are presented in Fig. 5.9 for the whole mass range considered and the lowest metallicity $Z = 0.0005$, for which HBB is expected to be most efficient.

Efficiency of mass loss: Models A and B differ from model $M13$ in terms of the mass-loss law. While model A adopts the popular mass-loss formula proposed by Vassiliadis & Wood (1993, hereinafter also VW93), model B uses the Blöcker (1995) prescription with the efficiency parameter $\eta = 0.02$, which gives much higher rates. We find that the VW93 model predicts chemical ejecta that are comparable with those of the $M13$ reference models. In fact the two mass-loss prescriptions, though based on different approaches and different calibration samples, share a similar functional dependence that predicts an exponential increase of $\dot{M}$ during the initial stages of the TP-AGB evolution (see the discussion in Marigo et al. 2013).

Large differences show up, instead, between the $M13$, A models, and the models B. As to this latter group, the higher mass-loss rates lead to a reduction of the TP-AGB lifetimes, particularly significant for the most massive and luminous AGB stars. For instance, the B model with $M_{\rm i} = 5.0\,M_{\odot}$ suffers a lower number of third dredge-up episodes (14 instead of 30) and HBB remains active for a shorter time. As a consequence, compared to the reference $M13$ models, the B models predict ejecta of ^{22}Ne and ^{23}Na that are lower by factors in the range $1.3-9.2$ and $1.1-2.7$, respectively. The reduction of the ^{24}Mg yield is smaller, by factors in the range $\simeq 1.02-1.5$.

Efficiency of HBB: Models C test the effect of increasing the strength of HBB. This is obtained setting the mixing length parameter to a higher value ($\alpha_{\rm ML} = 2.00$) compared to the reference value ($\alpha_{\rm ML} = 1.74$). As a consequence, hotter temperatures are attained in the deepest layers of the convective envelope so that nuclear reactions in NeNa cycle occur faster. Also, the maximum quiescent luminosity attained is larger (e.g., $\log(L)_{\rm max} \simeq 4.81$ instead of $\simeq 4.76$ for the reference $M13$ model with $M_{\rm i} = 5\,M_{\odot}$). Despite the stronger HBB, the integrated yields of ^{22}Ne, ^{23}Na,

and ^{24}Mg for *C* models are found to be lower than the *M*13 predictions (by factors in the range $\simeq 1.1-1.9$). This is explained considering that the higher luminosities reached by *C* models favor a more intense mass loss, which anticipates the termination of the AGB phase (e.g., 24 thermal pulses in *C* model compared to 30 in *M*13 model with $M_{\rm i} = 5\,M_{\odot}$).

Efficiency of the third dredge-up: As models *M*13, *A*, *B*, *C* are all characterized by a very efficient third dredge-up, we explored in the *D* models the case in which no dredge-up ($\lambda = 0$) is expected to take place during the entire TP-AGB evolution. In this way we may sample the overall uncertainty in the chemical yields bracketed by two opposite conditions. The main effect of taking $\lambda = 0$ is that no newly synthesized ^{22}Ne is injected into the convective envelope at thermal pulses. As a consequence, the production of ^{23}Na through the ^{22}Ne$(p,\gamma)^{23}$Na reaction during the inter-pulse phase is greatly reduced as it involves only the cycling of the NeNa isotopes that are originally present in the envelope when HBB is activated. This is evident in Fig. 5.9 where the ^{22}Ne and ^{23}Na yields predicted in models *D* are found to be lower than those produced by the reference models *M*13 by a factor in the ranges $\simeq 8-22$ and $\simeq 1.1-4.1$, respectively. The variation in the ^{24}Mg yields is not monotonic with the stellar mass. The absence of the third dredge-up favors larger ^{24}Mg yields at initial masses of $3.5-4.2\,M_{\odot}$, while smaller yields are predicted at larger masses, $M_{\rm i} \gtrsim 4.5\,M_{\odot}$. This complex trend is the time-integrated result of mass loss and HBB efficiency during the TP-AGB evolution in stars of different initial masses.

In summary, from this exercise it is evident that the improvements in the nuclear S-factor for the ^{22}Ne$(p,\gamma)^{23}$Na reaction achieved with LUNA have significantly reduced the uncertainties in the chemical ejecta of ^{22}Ne and ^{23}Na produced by intermediate-mass AGB stars with HBB. On the other hand, we conclude that remaining, not negligible, uncertainties are ascribed mainly to evolutionary aspects that still urge a substantial theoretical effort.

To give some representative numbers we refer to the ($M_{\rm i} = 5.0\,M_{\odot}, Z_{\rm i} = 0.0005$) model. The largest uncertainty factors for the ^{22}Ne yields due to the nuclear S-factor of ^{22}Ne$(p,\gamma)^{23}$Na have decreased from $\approx 5-7$ to $\approx 10-30\%$. As to the ^{23}Na yields, we go from ≈ 100 to ≈ 2. At the same time, the evolutionary uncertainties still make a large contribution, rising the factors up to ≈ 18 for ^{22}Ne and to ≈ 4 for ^{23}Na. As to the ^{24}Mg yields, the impact of ^{22}Ne$(p,\gamma)^{23}$Na is found to be smaller than in previous estimates (e.g., Izzard et al. 2007), and its nuclear uncertainties should be dominated by other nuclear reactions in the NeNa cycle (^{23}Na$(p,\gamma)^{24}$Mg, ^{24}Mg$(p,\gamma)^{25}$Al), not analyzed here.

5.5 The oxygen-sodium anti-correlation in GGCs

In recent years a number of studies have analyzed the hypothesis of metal-poor intermediate-mass AGB and super-AGB stars experiencing HBB as plausible candidates to explain the observed anti-correlations between light elements (C-N,O-Na, Al-Mg) that characterize the chemical patterns exhibited by the stars of Galactic globular clusters (e.g., D'Antona et al. 2016; Renzini et al. 2015; Conroy 2012; D'Ercole et al. 2010; Ventura & D'Antona 2009; Renzini 2008; Prantzos et al. 2007; Karakas et al. 2006; Ventura & D'Antona 2005c; Fenner et al. 2004; Herwig 2004; Denissenkov & Herwig 2003, and references therein). Though a uniform consensus on the AGB scenario has not been reached (other stellar candidates are discussed, for instance, by Denissenkov & Hartwick 2014; Krause et al. 2013; de Mink et al. 2009; Prantzos et al. 2007; Decressin et al. 2007), it is interesting to look at the patterns of the AGB chemical yields on the observed O-Na anti-correlation diagram. Relevant properties of the AGB ejecta are provided in Table 5.3.

In Fig. 5.10 we show the evolution drawn by a few selected low-metallicity models (with $Z_{\rm i} = 0.0005$, and $[\alpha/{\rm Fe}]= 0.4$), during their whole TP-AGB evolution, until the complete ejection of the envelope. This is the result of the combined effect of both HBB and the third dredge-up (if present), and mass loss.

The seventeen clusters included in the catalog of Carretta et al. (2009) span a large range in metallicity. Among them four clusters (NCG 1904, NGC 3201, NGC 6254, NGC 6752) have iron abundances ([Fe/H]≃ -1.579, -1.512, -1.575, -1.555, respectively) that are quite close (within the errors) to that of our set of low-metallicity models ([Fe/H]≃ -1.56)[3]. The abundance data for these clusters (grey dots), draw a well-defined O-Na anti-correlation, with a few stars extending into the upper region characterized by the highest Na enrichment, which is the main focus of the analysis that follows.

We note that the $M_{\rm i} = 3.6\,M_{\odot}$ model exhibits a modest abundance evolution, characterized by a little depletion of O, and some enrichment in ^{23}Na due to a relatively mild HBB. Moving to larger stellar mass (i.e. $M_{\rm i} = 4.4, 5.0\,M_{\odot}$) HBB becomes stronger and the models draw an extended loop, along which ^{23}Na is initially destroyed together with O, and later it is efficiently produced thanks to the periodic injection of fresh ^{22}Ne by the third dredge-up at thermal pulses, followed by the operation of the $^{22}{\rm Ne}(p,\gamma)^{23}{\rm Na}$ reaction during the inter-pulse periods (see also Fig. 5.6). As HBB becomes weaker and eventually extinguishes (due to the reduction of the envelope mass by stellar winds), some additional O enrichment may occur if a few final third dredge-up events

[3]Our reference solar mixture (Caffau et al. 2011), and that from Kurucz (1994) used in the spectroscopic work of Carretta et al. (2009) are characterized by similar metal abundances, corresponding to a total Sun's metallicity $Z_{\odot} \simeq$ 0.0152 and 0.0158, respectively.

take place before the termination of the TP-AGB phase. Conversely, if no third dredge-up occurs ($\lambda = 0$ as in models *F* and *D*; Table 5.2) the source of ^{22}Ne synthesized during thermal pulse is not at work so that the abundance loop does not show up and sodium is essentially destroyed by HBB with respect to its abundance after the second dredge-up. The significance of the different trends is discussed further in Section 5.5.1.

The left panels of Fig. 5.11 (from top to bottom) compare the results obtained with the *M*13 prescriptions but varying the rate of the ^{22}Ne$(p,\gamma)^{23}$Na reaction applied to the low-metallicity set of stellar models. Each stellar model is represented by a point in the diagram, whose coordinates are the surface abundance ratios computed as weighted averages, that is summing up the amounts of elements ejected at each time time step and then normalizing them to the total ejected mass. The range of initial masses goes from 3.0 $M_\odot$ to 5.0 $M_\odot$ in steps of 0.2 $M_\odot$.

A feature common to all panels of Fig. 5.11 is that, independently of the adopted input physics, the sequence of AGB models at increasing initial stellar mass runs crosswise the observed anti-

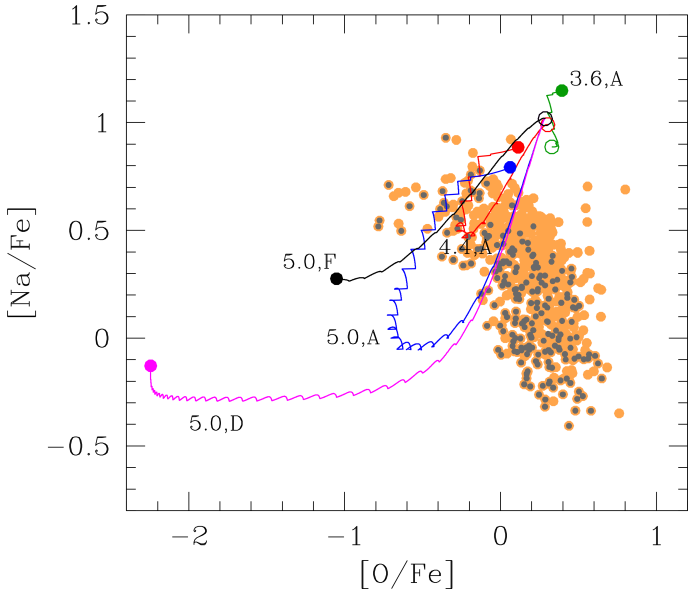

Figure 5.10: O-Na anti-correlation in stars of GGCs. Spectroscopic data (orange dots) for 17 clusters are taken from the catalog of Carretta et al. (2009). The data for clusters with iron content $-1.51 \lesssim$[Fe/H]$\lesssim -1.58$ are marked with grey dots. Standard spectroscopic notation is adopted, i.e. $[Y_i/\mathrm{Fe}] = \log(n_i/n_{\mathrm{Fe}}) - \log(n_{i,\odot}/n_{\mathrm{Fe},\odot})$ (with n_i being the number density of the element i). The curves display the evolution of abundance ratios during the whole TP-AGB phase for a few selected models with initial metallicity $Z_\mathrm{i} = 0.0005$. The corresponding stellar masses (in $M_\odot$) are indicated on the plot. All models correspond to the reference *M*13 prescriptions, except for those labeled with *F* and *D* (see Table 5.2 for details). In each curve the empty circle marks the abundances after the second dredge-up, while the filled circle indicates the final ratios at the termination of the TP-AGB phase.

Table 5.3: Properties of AGB models with initial metallicity $Z_i = 0.0005$ and composition of their ejecta, obtained with the LUNA rate. The prescriptions used in the different sets of models are also described in Table 5.1. From left to right the columns indicate: the initial stellar mass, the total number of thermal pulses, the final core mass, the average helium abundance (in mass fraction), the average abundance ratios expressed as $< [n_i/n(Fe)] >$ (with abundances by number) in the ejecta of C, N, O, the enhancement factor of the CNO content, and the average abundance ratios of Na, Mg, and Al. As to Li, the corresponding average abundance is expressed as $\log[n(Li)/n(H)] + 12$.

$Z_i = 0.0005$, $Y_i = 0.249$, [α/Fe]=0.4

Reference *M*13 prescriptions											
Efficient third dredge-up											
M_i [$M_\odot$]	N_{tp}	M_{fin} [$M_\odot$]	<X(He)>	<A(Li)>	<[C/Fe]>	<[N/Fe]>	<[O/Fe]>	R_{cno}	<[Na/Fe]>	<[Mg/Fe]>	<[Al/Fe]>
3.0	11	0.81	0.30	3.74	1.81	1.45	0.49	11.77	0.76	0.44	0.05
3.2	11	0.82	0.31	3.95	1.34	2.21	0.46	10.75	0.85	0.43	0.08
3.4	12	0.83	0.32	3.46	1.21	2.28	0.42	10.94	1.03	0.44	0.11
3.6	13	0.85	0.33	3.30	1.03	2.12	0.35	10.94	1.08	0.44	0.15
3.8	14	0.86	0.34	3.19	0.99	2.12	0.28	10.75	1.07	0.45	0.26
4.0	16	0.88	0.35	3.12	0.90	2.14	0.19	10.23	0.99	0.45	0.32
4.2	17	0.89	0.35	3.03	0.78	2.12	0.08	9.95	0.82	0.45	0.43
4.4	20	0.91	0.36	2.91	0.70	2.11	-0.04	10.26	0.75	0.45	0.56
4.6	23	0.93	0.36	2.77	0.57	2.07	-0.17	9.71	0.62	0.43	0.67
4.8	26	0.94	0.37	2.72	0.54	2.07	-0.22	9.76	0.58	0.42	0.71
5.0	30	0.97	0.37	2.72	0.48	2.01	-0.32	8.85	0.43	0.39	0.74
Models *B*: Efficient mass loss with Blöcker (1995) and $\eta = 0.02$											
M_i [$M_\odot$]	N_{tp}	M_{fin} [$M_\odot$]	<X(He)>	<A(Li)>	<[C/Fe]>	<[N/Fe]>	<[O/Fe]>	R_{cno}	<[Na/Fe]>	<[Mg/Fe]>	<[Al/Fe]>
3.0	10	0.80	0.30	4.00	1.37	2.23	0.46	10.36	0.76	0.42	0.05
3.2	10	0.81	0.31	3.66	1.01	2.31	0.44	9.78	0.94	0.42	0.09
3.4	10	0.82	0.32	3.38	1.31	2.22	0.38	8.86	1.03	0.42	0.12
3.6	10	0.84	0.33	3.15	0.27	2.27	0.30	7.30	1.06	0.41	0.16
3.8	11	0.85	0.34	2.97	1.19	2.14	0.23	7.18	1.01	0.42	0.26
4.0	11	0.87	0.35	2.83	0.19	2.18	0.10	5.62	0.91	0.41	0.32
4.2	12	0.89	0.35	2.70	0.98	2.04	-0.01	5.23	0.67	0.41	0.43
4.4	12	0.91	0.36	2.60	0.25	2.04	-0.21	3.91	0.46	0.39	0.55
4.6	13	0.92	0.36	2.65	-0.03	1.85	-0.37	2.81	0.23	0.36	0.65
4.8	13	0.94	0.37	2.55	0.07	1.92	-0.45	2.95	0.17	0.35	0.72
5.0	14	0.96	0.37	2.70	0.49	1.74	-0.48	2.52	0.02	0.33	0.72
Models *C*: Efficient HBB with α_{ML}=2.0											
M_i [$M_\odot$]	N_{tp}	M_{fin} [$M_\odot$]	<X(He)>	<A(Li)>	<[C/Fe]>	<[N/Fe]>	<[O/Fe]>	R_{cno}	<[Na/Fe]>	<[Mg/Fe]>	<[Al/Fe]>
3.0	10	0.81	0.30	3.82	1.38	2.03	0.46	8.77	0.77	0.41	0.05
3.2	10	0.82	0.31	3.41	1.27	2.11	0.40	8.82	1.00	0.42	0.10
3.4	11	0.83	0.32	3.31	1.04	2.19	0.33	8.76	1.08	0.43	0.14
3.6	12	0.84	0.33	3.18	0.72	2.06	0.26	8.41	1.03	0.42	0.18
3.8	13	0.86	0.34	3.13	0.73	2.04	0.16	8.18	0.97	0.42	0.31
4.0	14	0.87	0.35	3.05	0.70	2.04	0.04	7.82	0.83	0.42	0.42
4.2	15	0.89	0.35	2.94	0.49	1.96	-0.16	6.70	0.60	0.39	0.58
4.4	17	0.91	0.36	2.82	0.47	1.97	-0.24	7.22	0.57	0.38	0.66
4.6	19	0.93	0.36	2.74	0.33	1.91	-0.37	6.53	0.40	0.35	0.74
4.8	21	0.94	0.37	2.72	0.31	1.90	-0.42	6.42	0.36	0.34	0.75
5.0	24	0.97	0.37	2.76	0.24	1.83	-0.51	5.74	0.21	0.31	0.73
Models *D*: No third dredge-up (λ=0)											
M_i [$M_\odot$]	N_{tp}	M_{fin} [$M_\odot$]	<X(He)>	<A(Li)>	<[C/Fe]>	<[N/Fe]>	<[O/Fe]>	R_{cno}	<[Na/Fe]>	<[Mg/Fe]>	<[Al/Fe]>
3.0	17	0.85	0.29	-1.14	-0.29	0.68	0.36	1.00	0.72	0.40	0.06
3.2	20	0.86	0.31	-0.77	-0.29	0.72	0.35	1.00	0.79	0.40	0.08
3.4	24	0.88	0.32	0.68	-0.29	0.76	0.34	1.00	0.85	0.40	0.11
3.6	29	0.90	0.32	2.50	-0.30	0.79	0.33	1.00	0.89	0.40	0.13
3.8	34	0.92	0.33	3.47	-0.89	0.91	0.32	1.00	0.93	0.39	0.22
4.0	38	0.94	0.34	3.27	-0.99	1.10	0.17	1.00	0.96	0.39	0.25
4.2	41	0.96	0.35	3.03	-0.81	1.29	-0.43	1.00	0.51	0.39	0.48
4.4	42	0.97	0.35	2.89	-0.75	1.34	-1.08	1.00	0.15	0.32	0.79
4.6	44	0.99	0.36	2.77	-0.72	1.36	-1.50	1.00	0.00	0.23	0.89
4.8	47	1.00	0.36	2.72	-0.70	1.36	-1.64	1.00	-0.05	0.19	0.90
5.0	50	1.02	0.37	2.72	-0.67	1.36	-1.72	1.00	-0.15	0.14	0.80

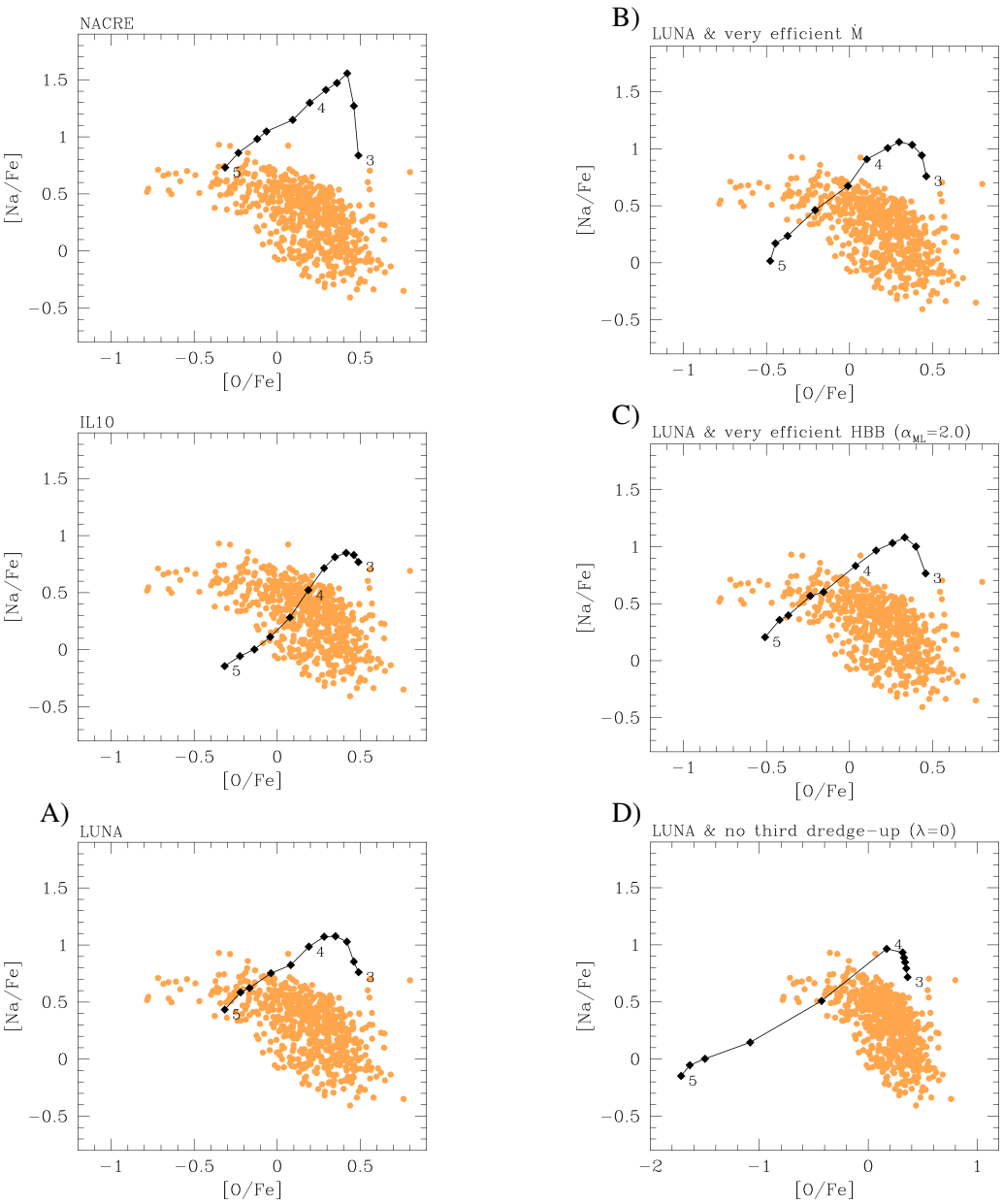

Figure 5.11: O-Na anti-correlation in stars of GGCs. Observed data are the same as in Fig. 5.10. In each panel the sequence of filled squares (from right to left) corresponds to the elemental ratios [Na/Fe] and [O/Fe] in the TP-AGB ejecta of stars with initial composition Z_i = 0.0005, [α/Fe]=0.4, and masses from 3.0 $M_\odot$ to 5.0 $M_\odot$ in steps of 0.2 $M_\odot$. Few selected values of the mass (in $M_\odot$) are indicated nearby the corresponding model. Panels of the left row: all models share the same AGB phase prescriptions (our reference case $M13$), but for the rate of ^{22}Ne$(p,\gamma)^{23}$Na (see Table 5.1). Panels of the right row (from top to bottom): results obtained with the LUNA rate, but varying other model assumptions, as described in Table 5.2 and marked by the corresponding capital letter on top-left. See the text for more explanation.

Table 5.4: Properties of AGB models with initial metallicity $Z_i = 0.0005$ and composition of their ejecta, obtained with the LUNA rate. The prescriptions used in the different sets of models are also described in Table 5.1. From left to right the columns indicate: the initial stellar mass, the total number of thermal pulses, the final core mass, the average helium abundance (in mass fraction), the average abundance ratios expressed as $< [n_i/n(Fe)] >$ (with abundances by number) in the ejecta of C, N, O, the enhancement factor of the CNO content, and the average abundance ratios of Na, Mg, and Al. As to Li, the corresponding average abundance is expressed as $\log[n(Li)/n(H)] + 12$.

Models *E*: Efficient HBB with $\alpha_{ML} = 2$, $\lambda_{max} = 0.5$, $^{23}Na(p,\alpha)^{20}Na$ / 5											
M_i [$M_\odot$]	N_{tp}	M_{fin} [$M_\odot$]	<X(He)>	<A(Li)>	<[C/Fe]>	<[N/Fe]>	<[O/Fe]>	R_{cno}	<[Na/Fe]>	<[Mg/Fe]>	<[Al/Fe]>
3.0	12	0.82	0.30	4.07	1.53	1.52	0.45	7.76	0.74	0.42	0.05
3.2	13	0.83	0.31	3.45	1.15	1.94	0.40	7.73	0.91	0.42	0.09
3.4	14	0.84	0.32	3.32	1.02	1.99	0.32	7.49	1.06	0.43	0.14
3.6	15	0.86	0.33	3.22	0.67	1.83	0.23	7.18	1.08	0.43	0.19
3.8	16	0.87	0.34	3.13	0.66	1.87	0.10	6.59	1.12	0.43	0.33
4.0	18	0.89	0.34	3.04	0.51	1.91	-0.05	6.58	1.08	0.43	0.45
4.2	20	0.91	0.35	2.94	0.45	1.88	-0.22	6.34	1.01	0.42	0.61
4.4	22	0.92	0.36	2.82	0.28	1.84	-0.41	5.73	0.89	0.39	0.73
4.6	24	0.94	0.36	2.74	0.21	1.78	-0.56	5.11	0.76	0.35	0.80
4.8	25	0.95	0.37	2.72	0.15	1.78	-0.63	4.75	0.71	0.33	0.81
5.0	29	0.98	0.37	2.76	0.09	1.72	-0.71	4.37	0.59	0.31	0.77
Models *F*: Efficient mass loss with Blöcker (1995) and $\eta = 0.03$, $\lambda = 0$, $^{23}Na(p,\alpha)^{20}Na$ / 3											
M_i [$M_\odot$]	N_{tp}	M_{fin} [$M_\odot$]	<X(He)>	<A(Li)>	<[C/Fe]>	<[N/Fe]>	<[O/Fe]>	R_{cno}	<[Na/Fe]>	<[Mg/Fe]>	<[Al/Fe]>
3.0	17	0.84	0.29	-1.41	-0.29	0.68	0.36	1.00	0.72	0.40	0.06
3.2	19	0.86	0.31	-0.21	-0.29	0.72	0.35	1.00	0.79	0.40	0.08
3.4	23	0.88	0.32	1.59	-0.29	0.76	0.34	1.00	0.85	0.40	0.11
3.6	23	0.89	0.32	3.46	-0.31	0.80	0.33	1.00	0.89	0.40	0.13
3.8	28	0.91	0.33	3.38	-1.20	0.94	0.31	1.00	0.94	0.39	0.22
4.0	29	0.92	0.34	3.09	-0.99	1.16	0.10	1.00	1.03	0.40	0.27
4.2	27	0.93	0.35	2.87	-0.83	1.30	-0.31	1.00	0.95	0.40	0.42
4.4	24	0.94	0.35	2.76	-0.77	1.35	-0.68	1.00	0.73	0.38	0.65
4.6	20	0.95	0.36	2.74	-0.74	1.36	-0.86	1.00	0.54	0.35	0.76
4.8	20	0.96	0.36	2.73	-0.71	1.36	-0.95	1.00	0.46	0.34	0.79
5.0	17	0.98	0.37	2.89	-0.71	1.35	-0.86	1.00	0.35	0.33	0.76

correlation, the higher-mass ones reaching lower [O/Fe] values. This trend has already been reported in the literature (see e.g., Ventura & Marigo 2010). The only way to make the stellar models bend over the populated region is to invoke a dilution process with gas of pristine composition, which basically shares the same chemical pattern as the field stars of the same [Fe/H].

According to a present-day scenario the observed anti-correlation would be the result of multiple star formation episodes within GGCs, in which the ejecta of AGB stars from a first generation polluted the gas involved in the subsequent secondary star formation events (Ventura & D'Antona 2008). In this framework GGC stars that populate the upper region of the anti-correlation (high Na, low O) would exhibit the chemical abundances of pure AGB ejecta, while stars on the opposite extreme (low Na, high O) would sample a pristine composition, typical of the first generation. In between are all the GGC stars born out of a mixture in which the AGB ejecta were partially diluted into a pristine gas.

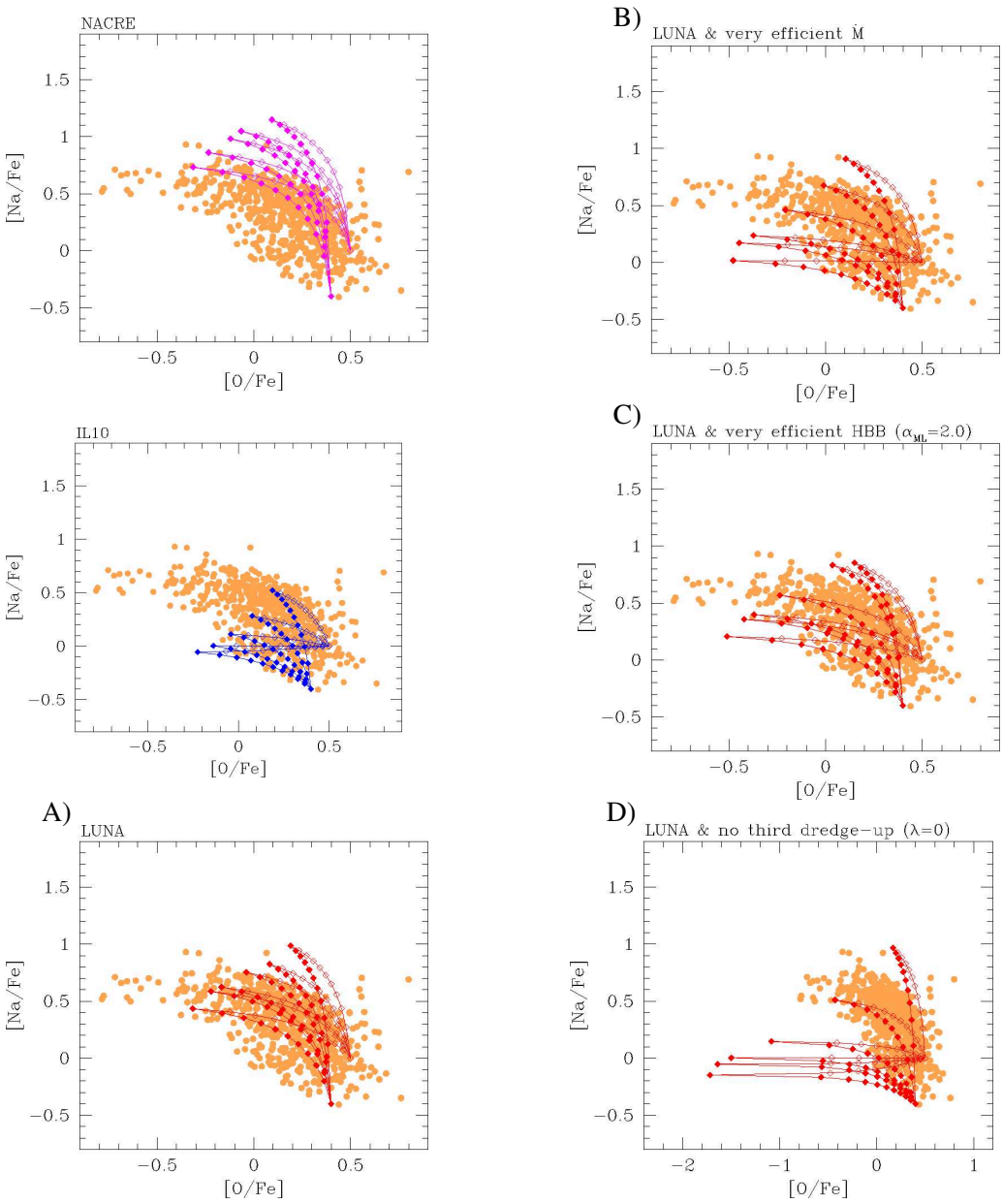

Figure 5.12: O-Na anti-correlation in stars of GGCs. Observed data are the same as in figure 5.11. The models correspond to a range of initial masses from 4.0 $M_{\odot}$ to 5.0 $M_{\odot}$ in steps of 0.2 $M_{\odot}$. Lower mass models, $M_{\rm i} < 4.0\,M_{\odot}$, are not included because mostly too far from the observed anti-correlation. Following equation (5.2) two dilution curves (solid and dashed lines) have been applied to each AGB model, corresponding to two choices of the pristine gas' composition. Each dot along the curves refers to a given value of the dilution fraction f_p, which is made increase from 0 (pure AGB ejecta) to 1 (pristine gas) in steps of 0.1. The models are the same as in Fig. 5.11. See the text for more explanation.

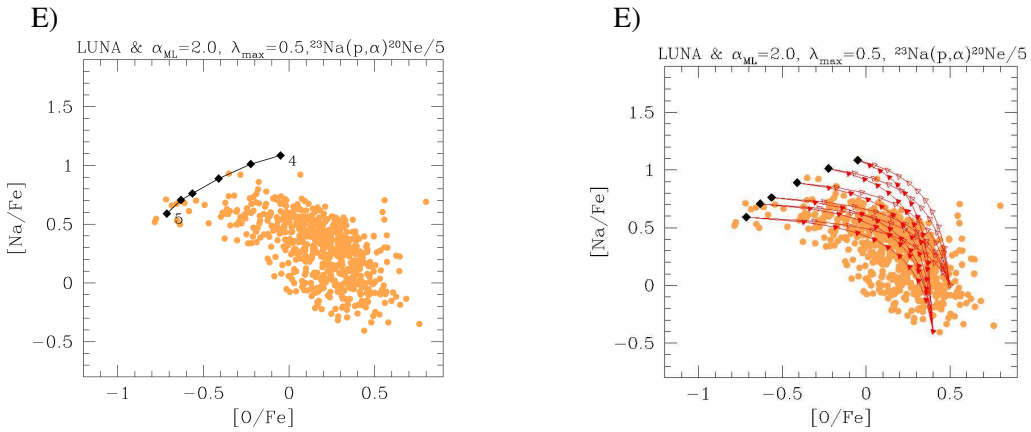

Figure 5.13: The same as in Figs 5.11 and 5.12, but referred to the set E of AGB models, characterized by a very efficient HBB, moderate third dredge-up, and a reduced rate for ^{23}Na$(p,\alpha)^{20}$Na by a factor of 5, so as to limit the destruction of sodium.The models correspond to a range of initial masses from 4.0 $M_{\odot}$ to 5.0 $M_{\odot}$ in steps of 0.2 $M_{\odot}$.

In this simplified picture low-metallicity AGB models should be found in the upper part of the observed anti-correlation. Looking at Fig. 5.11 we note that depending on the assumed rate ^{22}Ne$(p,\gamma)^{23}$Na, the sequence of AGB models change their location significantly. In particular, the NACRE models are characterized by high [Na/Fe] and hardly intersect the data but for the highest stellar masses, the IL10 models cross the anti-correlation in the middle not touching the Na-richest, O-poorest points, the LUNA sequence attain Na abundances consistent with the upper extreme of the anti-correlation, but fails to reach the points with the lowest oxygen abundance, i.e. [O/Fe]< -0.4. We address this point in Section 5.5.1.

It is now interesting to examine the behavior of the models when a simple dilution model is adopted. The dilution effect can be mimicked according to the formula (Conroy 2012):

$$[Y_{\rm i}/{\rm Fe}] = \log\left((1-f_p)10^{[Y_{\rm i}/{\rm Fe}]_o} + f_p 10^{[Y_{\rm i}/{\rm Fe}]_p}\right), \tag{5.2}$$

where the subscripts o and p refer to the original pristine gas and the pure AGB ejecta, and f_p is the fraction of the AGB ejecta mixed into the gas.

For each set of models we applied Eq. 5.2 to draw a dilution curve, which starts at $[Y_{\rm i}/{\rm Fe}]_p$ given by the AGB evolutionary calculations (with $f_p = 0$) and ends at a point having coordinates ([O/Fe]$_o$, [Na/Fe]$_o$); with $f_p = 1$). For this latter we assume two combinations (0.4,-0.3) and (0.5, 0.0) to mimic some dispersion in the [Na/Fe]$_o$ and [O/Fe]$_o$ ratios, which is present in the observed data.

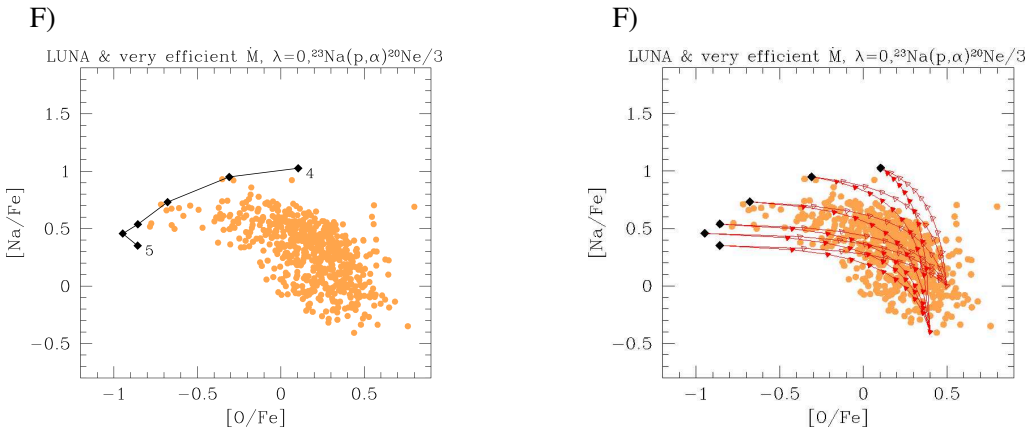

Figure 5.14: The same as in Figs 5.11 and 5.12, but referred to the set F of AGB models, characterized by efficient mass loss, no third dredge-up, and a reduced rate for ^{23}Na$(p,\alpha)^{20}$Na by a factor of 3, so as to limit the destruction of sodium.

By eye, the set of LUNA models at the bottom-left panel of Fig. 5.12 seems to reproduce better the trend of O-Na anti-correlation, compared to the other cases. However, we note that data at lower [Na/Fe] are not completely covered by our most massive TP-AGB models (up to $M_{\rm i} = 5M_{\odot}$). In this respect the impact of other AGB model prescriptions (i.e. efficiency of mass loss, HBB, and third dredge-up) may be important and are analyzed later in this section.

We caution that the relatively good match of our reference LUNA models cannot be taken as a full support to the AGB star hypothesis. In fact, these models are characterized by an efficient third dredge-up, which produces a net increase in the CNO abundance in the ejecta, at variance with the observational indication that in various GGCs stars that belong to the first and second populations, have constant CNO, within the errors, or relatively similar (e.g., Ivans et al. 1999; Carretta et al. 2005). Recent spectroscopic observations (e.g., Yong et al. 2009, 2015) have revealed a much more complex situation: there are stars belonging to the same clusters that exhibit non-negligible variations of the total CNO abundance, others that show a constant CNO abundance. Given this intricate picture we analyse various degrees of CNO enrichment in Section 5.5.1.

In order to keep the increase of the CNO abundance low in the AGB envelopes a possibility is to invoke that almost no third dredge-up took place at thermal pulses. In this way the ejecta would exhibit the nucleosynthesis fingerprint of an (almost) pure NeNa cycle. In the models this condition can be obtained assuming a very efficient mass-loss rate and/or imposing that depth of the third dredge-up events was small (low λ).

To explore the impact of these assumptions let us analyze the set of TP-AGB evolutionary calculations referred to as B, C, and D in Table 5.1. Relevant properties of the ejecta are presented

in Table 5.3.

The quantity $R_{\rm cno}$ is defined as the ratio between the average CNO abundance in the ejecta and the initial value at the time the star formed. We note that in our adopted definition of $R_{\rm cno}$ the abundances are expressed by number and not by mass fraction since during CNO cycle operation what is conserved is the number of the catalysts and not their mass.

The results of our calculations are shown in Figs 5.11 and 5.12 (see the label at the top of each panel for identification). As to the sets *B* and *C*, they are both characterized by a shorter TP-AGB evolution, which reduces the number of TPs, hence limiting the CNO increase at the surface. At the same time, the shortcoming is that the most massive AGB models considered here ($M_{\rm i} \geq 3.8\,M_{\odot}$) tend to produce sodium ejecta that are lower than the standard case, and do not reach the upper extreme of the anti-correlation. This would imply that the O-Na anti-correlation is caused by AGB stars within a very narrow mass range, which requires an extremely fine-tuned initial-mass function.

In the case *D* with $\lambda = 0$ the CNO abundance is unchanged, but on the O-Na diagram the agreement is poor as the most massive AGB stars experience a significant depletion of oxygen, whereas their sodium abundance becomes even lower. In fact no fresh ^{22}Ne is injected into the envelope at TPs and when the ^{22}Ne$(p,\gamma)^{23}$Na reaction is reactivated during HBB no significant amount of ^{23}Na is synthesized. Moreover, as already mentioned in Sec. 5.4.1, models without third dredge-up tend to have longer TP-AGB lifetimes (mass loss is less efficient because of their higher effective temperatures), so that a larger amount of oxygen is burnt into nitrogen.

5.5.1 Can we recover the Na-rich, O-poor extreme of the anti-correlation?

All AGB models described so far are not able to extend into the O-poor extreme of the anti-correlation, matching the sodium abundances at the same time. The inability of AGB models to reach [O/Fe]< -0.5 has been already reported by D'Ercole et al. (2012) who invoked the occurrence of an extra-mixing process during the red giant branch phase of GGC stars.

More generally, examining the available AGB ejecta in the literature we realize that three main issues affect their suitability to represent the extreme composition of the first stellar generation in GGCs (see also D'Antona et al. 2016). Namely, to our knowledge, no existing AGB (or super-AGB) model has shown to fulfill the whole set of conditions:

- [O/Fe] < -0.5
- $0.5 \lesssim$ [Na/Fe] $\lesssim 0.8$
- $R_{\rm cno} \lesssim 3-4$, or more stringently, $R_{\rm cno} \simeq 1$.

The first two conditions, which apply to the upper extreme of the anti-correlation, are difficult to meet since a more efficient destruction of oxygen via the ON cycle is usually accompanied by an efficient destruction of sodium through the ^{23}Na(p,α)^{20}Ne reaction, and to a lesser extent through the ^{23}Na(p,γ)^{24}Mg. This trend is more pronounced with increasing stellar mass, as clearly shown in all panels of Fig. 5.11.

A way to increase the overall sodium production is to assume an efficient third dredge-up, so that newly synthesized ^{22}Ne can be injected into the envelope and later burnt into ^{23}Na. But this brings along the problem of increasing the CNO abundance, yielding $R_{\rm cno} >> 1$, as shown in Table 5.3.

An alternative possibility is that of lowering the destruction of sodium, by reducing the current rate for ^{23}Na(p,α)^{20}Ne reaction. This suggestion has been put forward by Ventura & D'Antona (2006), and more recently by D'Antona et al. (2016); Renzini et al. (2015); D'Orazi et al. (2013).

In view of the above, we single out an optimal set of AGB model prescriptions that best reproduce the chemical constraints on Na, O, and CNO content, which characterize the upper extreme of the anti-correlation.

To achieve this goal we follow a sort of "calibration path", which requires several model calculations and tests. For a given level of third dredge-up efficiency, we first adjust the mixing-length parameter and the mass loss to obtain the right temperature evolution at the base of the convective envelope that produces the right O-depletion in the average ejecta. Clearly, some mild degeneracy between convection and mass loss efficiencies is present, but the uncertainty range is small for reasonable choices of the parameters. Then, we reduce the destruction rate of ^{23}Na(p,α)^{20}Ne by the suitable factor that allows to reach the required Na enrichment.

We summarize here the final results of our investigation. Let us start from the constraint on the CNO abundance, and consider two possible requirements expressed by $R_{\rm cno} \lesssim 3-4$ and $R_{\rm cno} = 1$, respectively. They define two classes of TP-AGB models.

The requirement $R_{\rm cno} \lesssim 3-4$ implies that some dredge-up is allowed to take place during the TP-AGB evolution. Under these conditions, our best set of models (named *E* in Table 5.2) is calculated assuming a moderate third dredge-up, with a maximum efficiency $\lambda_{\rm max} = 0.5$, which produces $R_{\rm cno} \lesssim 4-5$ for initial masses $M_{\rm i} \geq 4.4\,M_{\odot}$. We are able to reach the lowest [O/Fe] by increasing the mixing length parameter to $\alpha_{\rm ML} = 2.0$, which causes a very efficient HBB. At the same time, we prevent a large destruction of sodium by reducing the IL10 rate for ^{23}Na(p,α)^{20}Ne by a factor of 5. All other prescriptions are the same as in our reference *M*13 set.

The results are presented in Fig. 5.13 and the relevant characteristics of the ejecta are listed in Table 5.3. This set of AGB models is able, for the first time, to reproduce the Na-rich, O-poor

extreme of the O-Na anti-correlation, while keeping a mild CNO increase. The most massive AGB models, with $M_{\rm i} = 4.6 - 5.0\,M_{\odot}$ reach the stars with the lowest [O/Fe] as a consequence of a suitable combination of efficient HBB and mass loss, without the need of invoking extra-mixing episodes as suggested by D'Ercole et al. (2012). At the same time, we confirm previous suggestions (D'Antona et al. 2016; Renzini et al. 2015) about the need of decreasing the destruction rate of sodium.

The requirement $R_{\rm cno} = 1$ implies that no third dredge-up occurred. Under this stringent assumption, our best performing set of models (named *F* in Table 5.2), is calculated with $\alpha_{\rm ML} = 1.74$, adopting a more efficient mass-loss prescription (Blöcker 1995, with $\eta = 0.03$), and reducing the ^{23}Na(p,α)^{20}Ne rate by a factor of 3. As before, all other prescriptions are the same as in *M*13. The results are shown in Fig. 5.14 and the properties of the corresponding ejecta are summarized in Table 5.3. The upper extreme of the anti-correlation and its dispersion is also well described by the average abundance of the AGB models with initial masses $4.0\,M_{\odot} \lesssim M_{\rm i} \lesssim 5.0\,M_{\odot}$.

Compared to the set *E* with $R_{\rm cno} > 1$, in models *F* we apply a few changes in the input prescriptions which are explained as follows. The absence of dredge-up episodes in models *F* makes both the atmospheres and the convective envelopes somewhat hotter, as a consequence of the lower opacities[4]. This leads to increase the strength of HBB, so that $\alpha_{\rm ML} = 1.74$ (instead of 2) already allows us to obtain the required oxygen depletion. At the same time, the TP-AGB evolution is a little shorter which prevents an excessive destruction of both oxygen and sodium. Also in this case we have to limit the consumption of sodium by reducing the nuclear rate of proton captures.

Interestingly, independent indications towards a modest third dredge-up in stars with $M_{\rm i} \approx 3 - 4 M_{\odot}$ are also derived from the analysis of the Galactic initial-final mass relation (Kalirai et al. 2014). On observational grounds, the high Rb abundances measured in luminous AGB stars in the Magellanic Clouds and in the Galaxy hint that stars with HBB do experience the third dredge-up (Zamora et al. 2014; García-Hernández et al. 2009, 2006). It follows that quantifying the efficiency of the third dredge-up in massive AGB stars is still an open issue and it can be reasonably treated as a free parameter in AGB models to explore the impact of various assumptions, in a way similar to what we performed in this study.

For comparison, in Fig. 5.15 we show our best-fitting models (*E* and *F*) together with the predictions of other two theoretical studies, namely Ventura et al. (2013), and Doherty et al. (2014b), which include AGB and super-AGB models. We note that quite different abundances characterize the different sets of models, even when sharing the same, or similar, initial mass and metallic-

[4]Equation of state and detailed Rosseland mean opacities are computed with the ÆSOPUS at each time step during the evolution, consistently with the chemical composition.

ity. In particular, as already discussed by these authors, the O-poor and Na-rich extreme of the anti-correlation is not reached by the models, in the framework of their adopted prescriptions. As already mentioned, D'Ercole et al. (2012) suggested that this difficulty may be overcome assuming deep mixing during the RGB phase of the second generation stars forming in a gas with high helium abundance.

On the other hand, our analysis shows that the extreme of the O-Na anti-correlation may, in principle, be reproduced with pure ejecta of AGB stars, without invoking extra-mixing episodes in other phases.

In particular, our calculations demonstrate quantitatively that a sizable reduction (by a factor of 3-5) of the rate of the reaction ^{23}Na(p,α)^{20}Ne is necessary to prevent an excessive sodium destruction when the third dredge-up is not efficient or even absent. We should caution, however, that such a drastic change in the rate is not supported by recent nuclear cross section studies (Cesaratto et al. 2013; Iliadis et al. 2010a). The present lower-limit estimates allow to reduce the recommended rate by a factor of $\sim 1.2-1.3$ at the largest.

We did not attempt to fulfill additional chemical constraints, such as those related to the Mg-Al anti-correlation (Carretta 2015). We have verified that no significant magnesium destruction is predicted in AGB models with the adopted set of nuclear rates. In this respect we note that our reference rate for ^{25}Mg(p,γ)^{26}Al is taken from IL10, while a recent revision with LUNA has increased it by roughly a factor of $\simeq 2$ at the temperatures relevant for HBB (Straniero et al. 2013). We plan to adopt the latter rate and to extend our chemical investigation of the Mg and Al isotopes in a follow-up study.

Also, as shown in Table 5.3, our massive TP-AGB models exhibit a large helium content in their ejecta (mainly determined by the second dredge-up on the E-AGB), which would correspond to an increase of $\Delta Y \simeq 0.1-0.12$ with respect to the assumed initial value, $Y_{\rm p} = 0.2485$. These values are larger than the typical range $\Delta Y_{\rm max} \simeq 0.01-0.05$ reported by Milone et al. (2014) for a group of GGCs, and may represent a severe issue to the AGB star scenario (Bastian et al. 2015). We note, however, that our analysis is focused on the Na-rich, O-poor extreme of the anti-correlation, which is mainly populated by the stars of the cluster NGC 2808. For this cluster the helium spread is large, $\Delta Y_{\rm max} \simeq 0.14$ (Milone et al. 2012), consistent with our predictions.

A deeper scrutiny of all these additional chemical constraints requires a dedicated study on each specific cluster, as well as to extend the analysis to other metallicities, and it is beyond the original aim of the present paper.

5.6 Summary and conclusions

In this theoretical study we analyzed the ejecta of ^{22}Ne and ^{23}Na contributed by intermediate-mass stars during their entire evolution. In particular, we focused on the impact of the new LUNA measurements of the astrophysical S-factor for the reaction ^{22}Ne$(p,\gamma)^{23}$Na. The new experimental set-up and the discovery of three new resonances have led to a significant reduction in the uncertainty of the rate, which drops from factors of $\simeq 100$ down to just a few. At the temperatures most relevant for stellar evolutionary models the new LUNA rate is significantly lower than the previous estimate provided by NACRE, but somewhat larger than that of Iliadis et al. (2010a).

In order to evaluate the current uncertainties that still affect the ejecta of ^{22}Ne and ^{23}Na, and to disentangle those associated to nuclear physics from those related to other evolutionary aspects, we calculated a large grid of stellar evolutionary models with initial masses in the interval from $3\,M_{\odot}$ to $5-6\,M_{\odot}$, for three values of the initial composition. For each stellar model, the entire evolution, from the pre-main sequence to ejection of the complete envelope, was computed varying a few key model prescriptions, namely the rate of ^{22}Ne$(p,\gamma)^{23}$Na, the rate of mass-loss on the AGB, the efficiency of the third dredge-up, and the mixing-length parameter used in our adopted theory of convection.

In the light of the results obtained with the new LUNA rate for ^{22}Ne$(p,\gamma)^{23}$Na, we provide below a recapitulation of the most relevant processes that affect the ejecta of ^{22}Ne and ^{23}Na from intermediate-mass stars, the main uncertainty sources, and the implications we derived in relation to the Na-rich, O-poor extreme of the O-Na anti-correlation in GGCs.

- The second dredge-up on the early-AGB causes a significant increase of the surface abundance of ^{23}Na, up to a factor of $\simeq 10$ in stars with high mass and low metallicity. Correspondingly, the surface concentration of ^{22}Ne is diminished by $\approx 30\%$. These elemental changes hardly depend on the adopted rate for ^{22}Ne$(p,\gamma)^{23}$Na, while are controlled by other physical parameters, e.g. the efficiency of mixing and the extension of convective overshoot applied to the inner border of the convective envelope. During the subsequent TP-AGB phase significant changes in the surface abundances of ^{22}Ne and ^{23}Na are caused by the occurrence of third dredge-up events and HBB.

- The main effect of the third dredge-up is the injection of fresh ^{22}Ne into the envelope at thermal pulses, which will be later involved in the NeNa cycle during the next inter-pulse period. The process of HBB leads to an initial depletion of ^{23}Na, followed by an increase of its abundance – through the reaction ^{22}Ne$(p,\gamma)^{23}$Na – when ^{23}Na and ^{24}Mg reach the

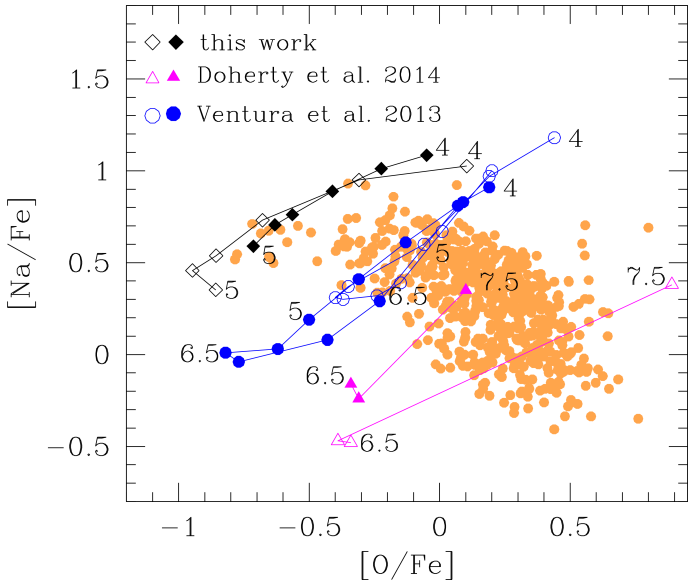

Figure 5.15: Comparison of mean oxygen and sodium abundances in the AGB and super-AGB ejecta computed by various authors. Our best fitting models (*E* and *F*) are shown together with the predictions of Ventura et al. (2013) (initial masses are in the range $4.0-8.0\,M_{\odot}$; filled circles for $Z_{\rm i}=0.0003$; empty circles for $Z_{\rm i}=0.001$) and the prescriptions of Doherty et al. (2014b) (initial masses in the range $6.5-7.5\,M_{\odot}$; filled triangles for $Z_{\rm i}=0.001$; empty triangles for $Z_{\rm i}=0.0001$; mass loss prescription: Blöcker (1995) with $\eta=0.02$). A few selected values of $M_{\rm i}$ are indicated (in $M_{\odot}$) nearby the corresponding models.

nuclear equilibrium. The quantitative details of these general trends critically depend on the rate assumed for ^{22}Ne$(p,\gamma)^{23}$Na.

- Comparing the results for ^{22}Ne and ^{23}Na obtained with our reference set of input prescriptions for the AGB evolution, but varying the rate for ^{22}Ne$(p,\gamma)^{23}$Na, we find that the ^{23}Na ejecta predicted with the LUNA data are quite lower than those derived with NACRE, and somewhat larger than with IL10. The opposite behavior applies to ^{22}Ne.

- Comparing the results for ^{22}Ne and ^{23}Na obtained with the recommended LUNA rate as well as the associated lower and upper limits, we estimated the current uncertainties of the chemical ejecta directly ascribed to the nuclear S-factor. At low metallicity the amplitudes of the largest error bars reach factors of $\simeq 2$ for ^{23}Na and $\simeq 10-30\%$ for ^{22}Ne. These uncertainties are significantly lower than those reported in past studies.

- Other reactions involved in the NeNa cycle may contribute to the nuclear uncertainties of the ^{22}Ne and ^{23}Na ejecta, in particular the destruction rates for sodium, i.e. ^{23}Na$(\mathrm{p},\alpha)^{20}$Ne and ^{23}Na$(\mathrm{p},\gamma)^{24}$Mg. Our present-day knowledge, based on nuclear cross section exper-

iments (Iliadis et al. 2010a; Cesaratto et al. 2013), indicates that destruction of sodium is largely dominated by the ^{23}Na(p,α)^{20}Ne reaction at the temperatures relevant for HBB $0.07\,\mathrm{GK} \lesssim \mathrm{T} \lesssim 1.1\,\mathrm{GK}$. The estimated lower and upper limit uncertainties for this rate are, however, relatively low, not exceeding $20-30\%$.

- The remaining uncertainties of the chemical ejecta for ^{22}Ne and ^{23}Na are mainly dominated by stellar evolutionary aspects, in particular the efficiency of convection, mass loss, and third dredge-up events. While the efficiencies of mass loss and convection mainly control the duration of HBB and the activation of the nuclear cycles, the third dredge-up has a direct effect on the total abundance of the isotopes that enter in the cycles. In fact, the amount of material that is dredged-up to the surface determines the amount of new ^{22}Ne that is added into the envelope and later converted into ^{23}Na by the ^{22}Ne(p,γ)^{23}Na reaction. Our tests indicate only varying the efficiency of the third dredge-up in low-metallicity AGB stars from high values ($\lambda \simeq 1$) to zero ($\lambda = 0$) causes a reduction of the ^{22}Ne ejecta by factors of 10-20, as well a reduction ^{23}Na ejecta by factors of 4-5.

- We examined our results in relation to the hypothesis that the observed O-Na anti-correlation observed in GGCs' stars is due to processed material in the ejecta of low-metallicity AGB stars. The ejecta obtained with the LUNA rate, together with our reference AGB model prescriptions, are able to recover the most Na-enriched stars of the anti-correlation, which are expected to exhibit the chemical composition of pure AGB ejecta. By adopting a simple dilution model, the general morphology of the anti-correlation is also satisfactorily reproduced. At the same time, however, we predict a sizable increase of the CNO content in the AGB ejecta (caused by the efficient third dredge-up assumed in the models), a feature that is at variance with the observations.

  On the other hand, assuming no or weak third dredge-up, hence no or little ^{22}Ne enrichment in the envelope, models are not able to produce the highest [Na/Fe] values on the upper extreme of the anti-correlation. This difficulty holds also under the assumptions of very high mass loss and/or strong HBB, as in both cases the TP-AGB phase is shortened and no significant replenishment of ^{22}Ne is predicted. The contribution from super-AGB stars, not explicitly treated in this work, is likely not to improve the situation since sodium ejecta tend to decrease at increasing stellar mass (Doherty et al. 2014b; D'Ercole et al. 2010).

- Starting from our reference AGB models, we changed various input prescriptions to verify whether the chemical constraints on sodium, oxygen and CNO content can be simultaneously fulfilled. After several tests, we singled out two optimal sets of AGB model assump-

tions under which the Na-rich, O-poor extreme of the anti-correlation is, for the first time, reproduced by pure AGB ejecta (without invoking external processes such as extra-mixing on the RGB).

In the first set of models we allow a moderate third dredge-up, so that the CNO abundance increases by a factor $\lesssim 4-5$. Matching the oxygen and sodium abundances requires an efficient HBB and a significant reduction, by a factor of 5, of the rate for ^{23}Na(p,α)^{20}Ne, in combination with the LUNA rate for ^{22}Ne(p,γ)^{23}Na.

In the second set of models we impose the absence of any third dredge-up event, in order to keep the total CNO abundance constant. In this case the extreme of the anti-correlation is also reached by adopting moderately different prescriptions for the mass loss, HBB, and the sodium destruction rate (with a reduction by a factor of 3).

- Such "calibrated" modifications (by a factor of 3-5) of the nuclear rate for ^{23}Na(p,α)^{20}Ne confirm quantitatively earlier suggestions by independent studies (D'Antona et al. 2016; Renzini et al. 2015; Ventura & D'Antona 2006). At the same time, they appear to be too large if one considers that present lower-limit estimates of the nuclear cross section allow a maximum reduction by a factor of $\simeq 1.3$. At present, this poses a severe problem that undermines the suitability of the AGB star solution in the context of the GGCs anti-correlations. Future nuclear experiments will be of key relevance to quantify more precisely the extent of sodium destruction in the stellar sites where the NeNa cycle operates.

- Other constraints, such as the magnesium depletion and the helium spread of different stellar populations, are not explicitly considered in the chemical calibration. We note that our AGB ejecta at low metallicity, likewise many other sets in the literature, are highly enriched in helium as a consequence of the second dredge-up. In the framework of a simple dilution model, this would likely imply a large helium spread between stars of the first and second generations, and therefore may represent a serious difficulty to the AGB scenario, as discussed by Bastian et al. (2015, but see also Chantereau et al. (2016) for a different approach).

  In conclusion, the AGB star hypothesis still deserves further quantitative analyses, which may be performed through stellar evolution experiments similar to those we have carried out in this study.

Bibliography

Abbott, B. P., Abbott, R., Abbott, T. D., et al. 2016, ApJ, 818, L22

Abbott, D. C. 1982, apj, 259, 282

Abbott, D. C., Bieging, J. H., Churchwell, E., & Bignell, C. 1982, in baas, Vol. 14, Bulletin of the American Astronomical Society, 914

Alongi, M., Bertelli, G., Bressan, A., & Chiosi, C. 1991, A&A, 244, 95

Anders, E. & Grevesse, N. 1989, Geochim. Cosmochim. Acta, 53, 197

Angulo, C., Arnould, M., Rayet, M., et al. 1999a, Nuclear Physics A, 656, 3

Angulo, C., Delbar, T., Graulich, J.-S., & Leleux, P. 1999b, in American Institute of Physics Conference Series, Vol. 495, American Institute of Physics Conference Series, 381–384

Arcavi, I., Gal-Yam, A., Kasliwal, M. M., et al. 2010, ApJ, 721, 777

Arnett, W. D. 1972, ApJ, 176, 699

Asplund, M., Grevesse, N., Sauval, A. J., Allende Prieto, C., & Kiselman, D. 2004, A&A, 417, 751

Asplund, M., Grevesse, N., Sauval, A. J., & Scott, P. 2009, ARA&A, 47, 481

Aubert, O., Prantzos, N., & Baraffe, I. 1996, A&A, 312, 845

Barlow, M. J. & Hummer, D. G. 1982, in IAU Symposium, Vol. 99, Wolf-Rayet Stars: Observations, Physics, Evolution, ed. C. W. H. De Loore & A. J. Willis, 387–392

Bastian, N., Cabrera-Ziri, I., & Salaris, M. 2015, MNRAS, 449, 3333

Bedijn, P. J. 1988, A&A, 205, 105

Beers, T. C. 1999, Ap&SS, 265, 105

Beers, T. C., Preston, G. W., & Shectman, S. A. 1992, AJ, 103, 1987

Bennett, M. E., Hirschi, R., Pignatari, M., et al. 2012, MNRAS, 420, 3047

Bethe, H. A., Brown, G. E., Applegate, J., & Lattimer, J. M. 1979, Nuclear Physics A, 324, 487

Bisnovatyi-Kogan, G. S. & Kazhdan, Y. M. 1967, Soviet Ast., 10, 604

Blöcker, T. 1995, A&A, 297, 727

Böhm-Vitense, E. 1958a, ZAp, 46, 108

Böhm-Vitense, E. 1958b, ZAp, 46, 108

Bond, J. R., Arnett, W. D., & Carr, B. J. 1982, in NATO Advanced Science Institutes (ASI) Series C, Vol. 90, NATO Advanced Science Institutes (ASI) Series C, ed. M. J. Rees & R. J. Stoneham, 303–311

Bond, J. R., Arnett, W. D., & Carr, B. J. 1984, ApJ, 280, 825

Boothroyd, A. I. & Sackmann, I.-J. 1988a, ApJ, 328, 632

Boothroyd, A. I. & Sackmann, I.-J. 1988b, ApJ, 328, 653

Boothroyd, A. I., Sackmann, I.-J., & Wasserburg, G. J. 1995, ApJ, 442, L21

Bossini, D., Miglio, A., Salaris, M., et al. 2015, in European Physical Journal Web of Conferences, Vol. 101, European Physical Journal Web of Conferences, 06012

Botticella, M. T., Riello, M., Cappellaro, E., et al. 2008, A&A, 479, 49

Bressan, A., Fagotto, F., Bertelli, G., & Chiosi, C. 1993, A&AS, 100, 647

Bressan, A., Marigo, P., Girardi, L., et al. 2012, MNRAS, 427, 127

Bressan, A. G., Chiosi, C., & Bertelli, G. 1981, A&A, 102, 25

Broggini, C., Bemmerer, D., Guglielmetti, A., & Menegazzo, R. 2010, Annual Review of Nuclear and Particle Science, 60, 53

Bromm, V. 2005, in IAU Symposium, Vol. 228, From Lithium to Uranium: Elemental Tracers of Early Cosmic Evolution, ed. V. Hill, P. Francois, & F. Primas, 121–128

Bruenn, S. W., Mezzacappa, A., Hix, W. R., et al. 2009, Journal of Physics Conference Series, 180, 012018

Bruenn, S. W., Mezzacappa, A., Hix, W. R., et al. 2013, ApJ, 767, L6

Buchmann, L. 1996, ApJ, 468, L127

Caffau, E. & Ludwig, H.-G. 2007, A&A, 467, L11

Caffau, E., Ludwig, H.-G., Bonifacio, P., et al. 2010, A&A, 514, A92

Caffau, E., Ludwig, H.-G., Steffen, M., et al. 2008a, A&A, 488, 1031

Caffau, E., Ludwig, H.-G., Steffen, M., Freytag, B., & Bonifacio, P. 2011, Sol. Phys., 268, 255

Caffau, E., Maiorca, E., Bonifacio, P., et al. 2009, A&A, 498, 877

Caffau, E., Sbordone, L., Ludwig, H.-G., et al. 2008b, A&A, 483, 591

Caffau, E., Steffen, M., Sbordone, L., Ludwig, H.-G., & Bonifacio, P. 2007, A&A, 473, L9

Cappellaro, E., Riello, M., Altavilla, G., et al. 2005, A&A, 430, 83

Carretta, E. 2015, ApJ, 810, 148

Carretta, E., Bragaglia, A., Gratton, R., & Lucatello, S. 2009, A&A, 505, 139

Carretta, E., Gratton, R. G., Lucatello, S., Bragaglia, A., & Bonifacio, P. 2005, A&A, 433, 597

Castor, J. I., Abbott, D. C., & Klein, R. I. 1975, apj, 195, 157

Caughlan, G. R. & Fowler, W. A. 1988, Atomic Data and Nuclear Data Tables, 40, 283

Cavanna, F., Depalo, R., Aliotta, M., et al. 2015a, Physical Review Letters, 115, 252501

Cavanna, F., Depalo, R., Aliotta, M., et al. 2015b, Physical Review Letters, 115, 252501

Cavanna, F., Depalo, R., Menzel, M.-L., et al. 2014, European Physical Journal A, 50, 179

Cayrel, R., Depagne, E., Spite, M., et al. 2004, A&A, 416, 1117

Cesaratto, J. M., Champagne, A. E., Buckner, M. Q., et al. 2013, Phys. Rev. C, 88, 065806

Chafa, A., Tatischeff, V., Aguer, P., et al. 2007, Phys. Rev. C, 75, 035810

Chantereau, W., Charbonnel, C., & Meynet, G. 2016, A&A, 592, A111

Charbonnel, C., Meynet, G., Maeder, A., & Schaerer, D. 1996, A&AS, 115, 339

Charbonnel, C., Meynet, G., Maeder, A., Schaller, G., & Schaerer, D. 1993, A&AS, 101, 415

Chen, Y., Bressan, A., Girardi, L., et al. 2015, MNRAS, 452, 1068

Chieffi, A. & Limongi, M. 2004, ApJ, 608, 405

Chieffi, A. & Limongi, M. 2013, ApJ, 764, 21

Chiosi, C., Bertelli, G., & Bressan, A. 1992, ARA&A, 30, 235

Chiosi, C. & Maeder, A. 1986, ARA&A, 24, 329

Christlieb, N., Gustafsson, B., Korn, A. J., et al. 2004, ApJ, 603, 708

Clark, J. S., Goodwin, S. P., Crowther, P. A., et al. 2002, A&A, 392, 909

Colgate, S. A., Herant, M., & Benz, W. 1993, Phys. Rep., 227, 157

Conroy, C. 2012, ApJ, 758, 21

Conroy, C. & Spergel, D. N. 2011, ApJ, 726, 36

Conti, P. S. 2000, PASP, 112, 1413

Costantini, H., Formicola, A., Imbriani, G., et al. 2009, Reports on Progress in Physics, 72, 086301

Cottrell, P. L. & Da Costa, G. S. 1981, ApJ, 245, L79

Couch, S. M. 2013, ApJ, 775, 35

Cristallo, S., Piersanti, L., Straniero, O., et al. 2011, ApJS, 197, 17

Cristallo, S., Straniero, O., Gallino, R., et al. 2009, ApJ, 696, 797

Cristallo, S., Straniero, O., Piersanti, L., & Gobrecht, D. 2015, ApJS, 219, 40

Crowther, P. A. 2001, in Astrophysics and Space Science Library, Vol. 264, The Influence of Binaries on Stellar Population Studies, ed. D. Vanbeveren, 215

Crowther, P. A. 2008, in IAU Symposium, Vol. 250, Massive Stars as Cosmic Engines, ed. F. Bresolin, P. A. Crowther, & J. Puls, 47–62

Crowther, P. A., De Marco, O., & Barlow, M. J. 1998, MNRAS, 296, 367

Crowther, P. A., Schnurr, O., Hirschi, R., et al. 2010, MNRAS, 408, 731

Cyburt, R. H., Amthor, A. M., Ferguson, R., et al. 2010, ApJS, 189, 240

Dababneh, S., Heil, M., Käppeler, F., et al. 2003, Phys. Rev. C, 68, 025801

Dalcanton, J. J., Williams, B. F., Seth, A. C., et al. 2009, ApJS, 183, 67

D'Antona, F., Vesperini, E., D'Ercole, A., et al. 2016, MNRAS, 458, 2122

Davidson, K. 1999, in Astronomical Society of the Pacific Conference Series, Vol. 179, Eta Carinae at The Millennium, ed. J. A. Morse, R. M. Humphreys, & A. Damineli, 6

de Jager, C., Nieuwenhuijzen, H., & van der Hucht, K. A. 1988, A&AS, 72, 259

de Mink, S. E., Pols, O. R., Langer, N., & Izzard, R. G. 2009, A&A, 507, L1

Decressin, T., Meynet, G., Charbonnel, C., Prantzos, N., & Ekström, S. 2007, A&A, 464, 1029

Deheuvels, S. & Michel, E. 2010, Astronomische Nachrichten, 331, 929

Denissenkov, P. A. & Hartwick, F. D. A. 2014, MNRAS, 437, L21

Denissenkov, P. A. & Herwig, F. 2003, ApJ, 590, L99

Depalo, R., Cavanna, F., Ferraro, F., et al. 2015, Phys. Rev. C, 92, 045807

D'Ercole, A., D'Antona, F., Carini, R., Vesperini, E., & Ventura, P. 2012, MNRAS, 423, 1521

D'Ercole, A., D'Antona, F., Ventura, P., Vesperini, E., & McMillan, S. L. W. 2010, MNRAS, 407, 854

Descouvemont, P., Adahchour, A., Angulo, C., Coc, A., & Vangioni-Flam, E. 2004, Atomic Data and Nuclear Data Tables, 88, 203

Dessart, L., Burrows, A., Ott, C. D., et al. 2006, ApJ, 644, 1063

Dessart, L., Hillier, D. J., Livne, E., et al. 2011, MNRAS, 414, 2985

Dewitt, H. E., Graboske, H. C., & Cooper, M. S. 1973, ApJ, 181, 439

Doherty, C. L., Gil-Pons, P., Lau, H. H. B., Lattanzio, J. C., & Siess, L. 2014a, MNRAS, 437, 195

Doherty, C. L., Gil-Pons, P., Lau, H. H. B., et al. 2014b, MNRAS, 441, 582

Dolence, J. C., Burrows, A., Murphy, J. W., & Nordhaus, J. 2013, ApJ, 765, 110

D'Orazi, V., Campbell, S. W., Lugaro, M., et al. 2013, MNRAS, 433, 366

Eggenberger, P., Meynet, G., Maeder, A., et al. 2008a, Ap&SS, 316, 43

Eggenberger, P., Meynet, G., Maeder, A., et al. 2008b, Ap&SS, 316, 43

El Eid, M. F. & Langer, N. 1986, A&A, 167, 274

Eldridge, J. J., Fraser, M., Smartt, S. J., Maund, J. R., & Crockett, R. M. 2013, MNRAS, 436, 774

Eldridge, J. J. & Tout, C. A. 2004a, MNRAS, 353, 87

Eldridge, J. J. & Tout, C. A. 2004b, MNRAS, 353, 87

Ertl, T., Janka, H.-T., Woosley, S. E., Sukhbold, T., & Ugliano, M. 2016, ApJ, 818, 124

Fagotto, F., Bressan, A., Bertelli, G., & Chiosi, C. 1994, A&AS, 105

Fenner, Y., Campbell, S., Karakas, A. I., Lattanzio, J. C., & Gibson, B. K. 2004, MNRAS, 353, 789

Ferguson, J. W., Alexander, D. R., Allard, F., et al. 2005, ApJ, 623, 585

Forestini, M. & Charbonnel, C. 1997, A&AS, 123

Fowler, W. A. & Hoyle, F. 1964, ApJS, 9, 201

Fraley, G. S. 1968, Ap&SS, 2, 96

Frayer, D. K. & Taylor, M. 2012, in Proc. SPIE, Vol. 8487, Novel Optical Systems Design and Optimization XV, 848702

Frost, C. A. & Lattanzio, J. C. 1996, ApJ, 473, 383

Fryer, C. L. 1999, ApJ, 522, 413

Fryer, C. L. & Kalogera, V. 2001, ApJ, 554, 548

Fryer, C. L., Young, P. A., & Hungerford, A. L. 2006, ApJ, 650, 1028

Fynbo, H. O. U., Diget, C. A., Bergmann, U. C., et al. 2005, Nature, 433, 136

Gal-Yam, A., Mazzali, P. A., Manulis, I., & Bishop, D. 2013, PASP, 125, 749

García-Hernández, D. A., García-Lario, P., Plez, B., et al. 2006, Science, 314, 1751

García-Hernández, D. A., Manchado, A., Lambert, D. L., et al. 2009, ApJ, 705, L31

Girardi, L., Rubele, S., & Kerber, L. 2009, MNRAS, 394, L74

Girardi, L., Williams, B. F., Gilbert, K. M., et al. 2010, ApJ, 724, 1030

Goriely, S. & Siess, L. 2004, A&A, 421, L25

Görres, J., Arlandini, C., Giesen, U., et al. 2000, Phys. Rev. C, 62, 055801

Görres, J., Becker, H. W., Buchmann, L., et al. 1983, Nuclear Physics A, 408, 372

Goswami, A. & Prantzos, N. 2000, A&A, 359, 191

Graboske, H. C., Dewitt, H. E., Grossman, A. S., & Cooper, M. S. 1973, ApJ, 181, 457

Gräfener, G. 2008, in Clumping in Hot-Star Winds, ed. W.-R. Hamann, A. Feldmeier, & L. M. Oskinova, 103

Grevesse, N. & Noels, A. 1993, in Perfectionnement de l'Association Vaudoise des Chercheurs en Physique, ed. B. Hauck, S. Paltani, & D. Raboud, 205–257

Grevesse, N. & Sauval, A. J. 1998, Space Sci. Rev., 85, 161

Haft, M., Raffelt, G., & Weiss, A. 1994, ApJ, 425, 222

Hale, S. E., Champagne, A. E., Iliadis, C., et al. 2002, Phys. Rev. C, 65, 015801

Hale, S. E., Champagne, A. E., Iliadis, C., et al. 2004, Phys. Rev. C, 70, 045802

Hamuy, M. 2003, ApJ, 582, 905

Hannaford, P., Lowe, R. M., Grevesse, N., & Noels, A. 1992, A&A, 259, 301

Haubois, X., Perrin, G., Lacour, S., et al. 2009, A&A, 508, 923

Heger, A., Fryer, C. L., Woosley, S. E., Langer, N., & Hartmann, D. H. 2003, ApJ, 591, 288

Heger, A., Langer, N., & Woosley, S. E. 2000a, ApJ, 528, 368

Heger, A., Langer, N., & Woosley, S. E. 2000b, ApJ, 528, 368

Heger, A. & Woosley, S. E. 2002, ApJ, 567, 532

Herwig, F. 2004, ApJ, 605, 425

Hirschi, R., Chiappini, C., Meynet, G., Ekström, S., & Maeder, A. 2007, in American Institute of Physics Conference Series, Vol. 948, Unsolved Problems in Stellar Physics: A Conference in Honor of Douglas Gough, ed. R. J. Stancliffe, G. Houdek, R. G. Martin, & C. A. Tout, 397–404

Hirschi, R. & et al. 2006, in Reviews in Modern Astronomy, Vol. 19, Reviews in Modern Astronomy, ed. S. Roeser, 101

Hirschi, R., Meynet, G., & Maeder, A. 2004, A&A, 425, 649

Hirschi, R., Meynet, G., & Maeder, A. 2005a, in Astronomical Society of the Pacific Conference Series, Vol. 342, 1604-2004: Supernovae as Cosmological Lighthouses, ed. M. Turatto, S. Benetti, L. Zampieri, & W. Shea, 131

Hirschi, R., Meynet, G., & Maeder, A. 2005b, A&A, 433, 1013

Hoffman, R. D., Woosley, S. E., & Weaver, T. A. 2001, ApJ, 549, 1085

Humphreys, R. M. & Davidson, K. 1979, ApJ, 232, 409

Humphreys, R. M. & Davidson, K. 1994, PASP, 106, 1025

Hurley, J. R., Pols, O. R., & Tout, C. A. 2000, MNRAS, 315, 543

Iglesias, C. A. & Rogers, F. J. 1993, ApJ, 412, 752

Iglesias, C. A. & Rogers, F. J. 1996, ApJ, 464, 943

Iliadis, C. 2010, in American Institute of Physics Conference Series, Vol. 1238, American Institute of Physics Conference Series, ed. H. Susa, M. Arnould, S. Gales, T. Motobayashi, C. Scheidenberger, & H. Utsunomiya, 36–43

Iliadis, C., D'Auria, J. M., Starrfield, S., Thompson, W. J., & Wiescher, M. 2001, ApJS, 134, 151

Iliadis, C., Longland, R., Champagne, A. E., & Coc, A. 2010b, Nuclear Physics A, 841, 251

Iliadis, C., Longland, R., Champagne, A. E., Coc, A., & Fitzgerald, R. 2010a, Nuclear Physics A, 841, 31

Imbriani, G., Costantini, H., Formicola, A., et al. 2005, European Physical Journal A, 25, 455

Itoh, N. & Kohyama, Y. 1983, ApJ, 275, 858

Itoh, N., Uchida, S., Sakamoto, Y., Kohyama, Y., & Nozawa, S. 2008, ApJ, 677, 495

Ivans, I. I., Sneden, C., Kraft, R. P., et al. 1999, AJ, 118, 1273

Izzard, R. G., Lugaro, M., Karakas, A. I., Iliadis, C., & van Raai, M. 2007, A&A, 466, 641

Jaeger, M., Kunz, R., Mayer, A., et al. 2001, Physical Review Letters, 87, 202501

Janka, H.-T. 2001, A&A, 368, 527

Janka, H.-T. 2012, Annual Review of Nuclear and Particle Science, 62, 407

Janka, H.-T., Langanke, K., Marek, A., Martínez-Pinedo, G., & Müller, B. 2007, Phys. Rep., 442, 38

Jenkins, D. G., Bouhelal, M., Courtin, S., et al. 2013, Phys. Rev. C, 87, 064301

José, J. 2012, Bulletin of the Astronomical Society of India, 40, 443

José, J., Coc, A., & Hernanz, M. 1999, ApJ, 520, 347

Kaeppeler, F., Wiescher, M., Giesen, U., et al. 1994, ApJ, 437, 396

Kalirai, J. S., Marigo, P., & Tremblay, P.-E. 2014, ApJ, 782, 17

Kamath, S. G. 2010, in American Institute of Physics Conference Series, Vol. 1246, American Institute of Physics Conference Series, 174–177

Karakas, A. & Lattanzio, J. C. 2007, PASA, 24, 103

Karakas, A. I. 2010, MNRAS, 403, 1413

Karakas, A. I., Fenner, Y., Sills, A., Campbell, S. W., & Lattanzio, J. C. 2006, ApJ, 652, 1240

Karakas, A. I. & Lattanzio, J. C. 2003, PASA, 20, 393

Karakas, A. I. & Lattanzio, J. C. 2014, PASA, 31, e030

Karakas, A. I., Lattanzio, J. C., & Pols, O. R. 2002, PASA, 19, 515

Kippenhahn, R., Weigert, A., & Weiss, A. 2012, Stellar Structure and Evolution

Kitaura, F. S., Janka, H.-T., & Hillebrandt, W. 2006, A&A, 450, 345

Kozyreva, A., Blinnikov, S., Langer, N., & Yoon, S.-C. 2014a, A&A, 565, A70

Kozyreva, A., Yoon, S.-C., & Langer, N. 2014b, A&A, 566, A146

Kozyreva, A., Yoon, S.-C., & Langer, N. 2014c, A&A, 566, A146

Krause, M., Charbonnel, C., Decressin, T., Meynet, G., & Prantzos, N. 2013, A&A, 552, A121

Kroupa, P. 2001, MNRAS, 322, 231

Kroupa, P. 2008, in Astronomical Society of the Pacific Conference Series, Vol. 390, Pathways Through an Eclectic Universe, ed. J. H. Knapen, T. J. Mahoney, & A. Vazdekis, 3

Kudritzki, R. P. 2002, apj, 577, 389

Kudritzki, R. P., Pauldrach, A., & Puls, J. 1988, NASA Special Publication, 497, 173

Kudritzki, R. P., Pauldrach, A., Puls, J., & Abbott, D. C. 1989, A&A, 219, 205

Kudritzki, R.-P. & Puls, J. 2000, araa, 38, 613

Kunz, R., Fey, M., Jaeger, M., et al. 2002, ApJ, 567, 643

Kuroda, T., Kotake, K., & Takiwaki, T. 2012, ApJ, 755, 11

Kurucz, R. 1994, Solar abundance model atmospheres for 0,1,2,4,8 km/s. Kurucz CD-ROM No. 19. Cambridge, Mass.: Smithsonian Astrophysical Observatory, 1994., 19

Lamers, H. J. G. L. M. 1999, Zenit, 26, 368

Lamers, H. J. G. L. M. & Cassinelli, J. P. 1999, Introduction to Stellar Winds, 452

Langer, N. 1989, A&A, 220, 135

Langer, N. 2012, ARA&A, 50, 107

Langer, N., El Eid, M. F., & Fricke, K. J. 1985, A&A, 145, 179

Langer, N., Norman, C. A., de Koter, A., et al. 2007, A&A, 475, L19

Lattimer, J. M. & Prakash, M. 2007, Phys. Rep., 442, 109

Leitherer, C., Robert, C., & Drissen, L. 1992, apj, 401, 596

Li, W., Chornock, R., Leaman, J., et al. 2011, MNRAS, 412, 1473

Limongi, M. & Chieffi, A. 2003, ApJ, 592, 404

Limongi, M. & Chieffi, A. 2006, ApJ, 647, 483

Limongi, M., Straniero, O., & Chieffi, A. 2000, ApJS, 129, 625

Lucy, L. B. & Solomon, P. M. 1970, apj, 159, 879

Mackey, J., Bromm, V., & Hernquist, L. 2003, ApJ, 586, 1

Maeder, A. & Conti, P. S. 1994, ARA&A, 32, 227

Maeder, A. & Meynet, G. 1987, A&A, 182, 243

Maeder, A. & Meynet, G. 2000, A&A, 361, 159

Maeder, A. & Meynet, G. 2001, A&A, 373, 555

Mannucci, F., Della Valle, M., & Panagia, N. 2007, MNRAS, 377, 1229

Mapelli, M., Zampieri, L., Ripamonti, E., & Bressan, A. 2013, MNRAS, 429, 2298

Marek, A. & Janka, H.-T. 2009, ApJ, 694, 664

Marigo, P. 2001a, A&A, 370, 194

Marigo, P. 2001b, A&A, 370, 194

Marigo, P. 2015, in Astronomical Society of the Pacific Conference Series, Vol. 497, Why Galaxies Care about AGB Stars III: A Closer Look in Space and Time, ed. F. Kerschbaum, R. F. Wing, & J. Hron, 229

Marigo, P. & Aringer, B. 2009, A&A, 508, 1539

Marigo, P., Bernard-Salas, J., Pottasch, S. R., Tielens, A. G. G. M., & Wesselius, P. R. 2003a, A&A, 409, 619

Marigo, P., Bressan, A., Girardi, L., et al. 2011, in Astronomical Society of the Pacific Conference Series, Vol. 445, Why Galaxies Care about AGB Stars II: Shining Examples and Common Inhabitants, ed. F. Kerschbaum, T. Lebzelter, & R. F. Wing, 431

Marigo, P., Bressan, A., Nanni, A., Girardi, L., & Pumo, M. L. 2013, MNRAS, 434, 488

Marigo, P. & Girardi, L. 2007, A&A, 469, 239

Marigo, P., Girardi, L., Bressan, A., et al. 2010, in IAU Symposium, Vol. 262, Stellar Populations - Planning for the Next Decade, ed. G. R. Bruzual & S. Charlot, 36–43

Marigo, P., Girardi, L., Bressan, A., et al. 2008, A&A, 482, 883

Marigo, P., Girardi, L., & Chiosi, C. 2003b, A&A, 403, 225

Marigo, P., Ripamonti, E., Nanni, A., Bressan, A., & Girardi, L. 2016, MNRAS, 456, 23

Marion, J. B. & Fowler, W. A. 1957, ApJ, 125, 221

Martins, F., Hillier, D. J., Paumard, T., et al. 2008, A&A, 478, 219

Mattila, S., Dahlen, T., Efstathiou, A., et al. 2012, ApJ, 756, 111

Mauron, N. & Josselin, E. 2011, A&A, 526, A156

Meynet, G. & Arnould, M. 1993, in Nuclei in the Cosmos 2, ed. F. Kaeppeler & K. Wisshak, 503–508

Meynet, G. & Arnould, M. 2000, A&A, 355, 176

Meynet, G., Arnould, M., Prantzos, N., & Paulus, G. 1997, A&A, 320, 460

Meynet, G., Chomienne, V., Ekström, S., et al. 2015, A&A, 575, A60

Meynet, G., Maeder, A., Schaller, G., Schaerer, D., & Charbonnel, C. 1994, A&AS, 103

Milone, A. P., Marino, A. F., Dotter, A., et al. 2014, ApJ, 785, 21

Milone, A. P., Piotto, G., Bedin, L. R., et al. 2012, A&A, 537, A77

Mokiem, M. R., de Koter, A., Vink, J. S., et al. 2007, A&A, 473, 603

Mowlavi, N. 1999a, A&A, 344, 617

Mowlavi, N. 1999b, A&A, 350, 73

Mucciarelli, A., Caffau, E., Freytag, B., Ludwig, H.-G., & Bonifacio, P. 2008, A&A, 484, 841

Müller, B. & Janka, H.-T. 2015, MNRAS, 448, 2141

Müller, B., Janka, H.-T., & Heger, A. 2012, ApJ, 761, 72

Munakata, H., Kohyama, Y., & Itoh, N. 1985, ApJ, 296, 197

Nomoto, K. 1984, ApJ, 277, 791

Nomoto, K., Kobayashi, C., & Tominaga, N. 2013, ARA&A, 51, 457

Nomoto, K., Tominaga, N., Umeda, H., Kobayashi, C., & Maeda, K. 2006, Nuclear Physics A, 777, 424

Nugis, T. & Lamers, H. J. G. L. M. 2000, A&A, 360, 227

Ober, W. W., El Eid, M. F., & Fricke, K. J. 1983, A&A, 119, 61

O'Connor, E. & Ott, C. D. 2011, ApJ, 730, 70

Oppenheimer, J. R. & Volkoff, G. M. 1939, Physical Review, 55, 374

Paxton, B., Bildsten, L., Dotter, A., et al. 2011, ApJS, 192, 3

Pejcha, O. & Thompson, T. A. 2012, ApJ, 746, 106

Pejcha, O. & Thompson, T. A. 2015, ApJ, 801, 90

Perego, A., Rosswog, S., Cabezón, R. M., et al. 2014, MNRAS, 443, 3134

Pignatari, M., Gallino, R., Heil, M., et al. 2010, ApJ, 710, 1557

Pignatari, M., Herwig, F., Hirschi, R., et al. 2016, ApJS, 225, 24

Portinari, L., Chiosi, C., & Bressan, A. 1998, A&A, 334, 505

Powers, J. R., Fortune, H. T., Middleton, R., & Hansen, O. 1971, Phys. Rev. C, 4, 2030

Prantzos, N. 2000, New A Rev., 44, 303

Prantzos, N. 2011, ArXiv e-prints

Prantzos, N. & Charbonnel, C. 2006, A&A, 458, 135

Prantzos, N., Charbonnel, C., & Iliadis, C. 2007, A&A, 470, 179

Prantzos, N., Hashimoto, M., & Nomoto, K. 1990, A&A, 234, 211

Puls, J., Springmann, U., & Lennon, M. 2000, A&AS, 141, 23

Rakavy, G. & Shaviv, G. 1967a, ApJ, 148, 803

Rakavy, G. & Shaviv, G. 1967b, ApJ, 148, 803

Ratnatunga, K. U. & van den Bergh, S. 1989, ApJ, 343, 713

Rauscher, T. & Thielemann, F.-K. 2000, Atomic Data and Nuclear Data Tables, 75, 1

Renzini, A. 2008, MNRAS, 391, 354

Renzini, A., D'Antona, F., Cassisi, S., et al. 2015, MNRAS, 454, 4197

Rolfs, C. E. & Rodney, W. S. 1988, Cauldrons in the Cosmos (Chicago 60637: The University of Chicago Press)

Rolfs, C. E. & Rodney, W. S. 1988, Cauldrons in the cosmos: Nuclear astrophysics

Rosenfield, P., Marigo, P., Girardi, L., et al. 2014, ApJ, 790, 22

Rosenfield, P., Marigo, P., Girardi, L., et al. 2016, ArXiv e-prints

Rowland, C., Iliadis, C., Champagne, A. E., et al. 2004, ApJ, 615, L37

Sallaska, A. L., Iliadis, C., Champange, A. E., et al. 2013, ApJS, 207, 18

Schaerer, D., Charbonnel, C., Meynet, G., Maeder, A., & Schaller, G. 1993a, A&AS, 102, 339

Schaerer, D., Meynet, G., Maeder, A., & Schaller, G. 1993b, A&AS, 98, 523

Schaller, G., Schaerer, D., Meynet, G., & Maeder, A. 1992, A&AS, 96, 269

Schneider, F. 2014, PhD thesis, University of Bonn

Schnurr, O., Casoli, J., Chené, A.-N., Moffat, A. F. J., & St-Louis, N. 2008, MNRAS, 389, L38

Schröder, K.-P. & Cuntz, M. 2005, ApJ, 630, L73

Schwarzschild, M. 1958, Structure and evolution of the stars.

Shingles, L. J., Karakas, A. I., Hirschi, R., et al. 2014, ApJ, 795, 34

Siess, L. 2006, A&A, 448, 717

Siess, L. 2007, A&A, 476, 893

Siess, L. 2010, A&A, 512, A10

Slemer, A., Marigo, P., Piatti, D., et al. 2017, MNRAS, 465, 4817

Smartt, S. J. 2009, ARA&A, 47, 63

Smiljanic, R., Gauderon, R., North, P., et al. 2009, A&A, 502, 267

Smith, L. F. & Maeder, A. 1989, A&A, 211, 71

Smith, L. F. & Maeder, A. 1991, A&A, 241, 77

Smith, N. 2014, ARA&A, 52, 487

Smith, N. 2015, in Astrophysics and Space Science Library, Vol. 412, Very Massive Stars in the Local Universe, ed. J. S. Vink, 227

Smith, N., Li, W., Filippenko, A. V., & Chornock, R. 2011, MNRAS, 412, 1522

Spera, M., Mapelli, M., & Bressan, A. 2015, MNRAS, 451, 4086

Spite, M., Cayrel, R., Plez, B., et al. 2005, A&A, 430, 655

Stahl, O., Jankovics, I., Kovács, J., et al. 2001, A&A, 375, 54

Straniero, O., Cristallo, S., & Piersanti, L. 2014, ApJ, 785, 77

Straniero, O., Imbriani, G., Strieder, F., et al. 2013, ApJ, 763, 100

Sukhbold, T. & Woosley, S. E. 2014, ApJ, 783, 10

Tang, J., Bressan, A., Rosenfield, P., et al. 2014, MNRAS, 445, 4287

Tang, J., Bressan, A., Slemer, A., et al. 2016, MNRAS, 455, 3393

The, L.-S., El Eid, M. F., & Meyer, B. S. 2000, ApJ, 533, 998

The, L.-S., El Eid, M. F., & Meyer, B. S. 2007, ApJ, 655, 1058

Thielemann, F. K. & Arnett, W. D. 1985, ApJ, 295, 604

Thielemann, F.-K., Hirschi, R., Liebendörfer, M., & Diehl, R. 2011, in Lecture Notes in Physics, Berlin Springer Verlag, Vol. 812, Lecture Notes in Physics, Berlin Springer Verlag, ed. R. Diehl, D. H. Hartmann, & N. Prantzos, 153–232

Timmes, F. X., Woosley, S. E., & Weaver, T. A. 1995, ApJS, 98, 617

Timmes, F. X., Woosley, S. E., & Weaver, T. A. 1996, ApJ, 457, 834

Tominaga, N., Umeda, H., & Nomoto, K. 2007, ApJ, 660, 516

Torres, G., Vaz, L. P. R., Sandberg Lacy, C. H., & Claret, A. 2014, AJ, 147, 36

Ugliano, M., Janka, H.-T., Marek, A., & Arcones, A. 2012, ApJ, 757, 69

Umeda, H. & Nomoto, K. 2002, ApJ, 565, 385

Umeda, H. & Nomoto, K. 2008, ApJ, 673, 1014

Utrobin, V. P. & Chugai, N. N. 2009, A&A, 506, 829

Utrobin, V. P. & Chugai, N. N. 2013, A&A, 555, A145

Utrobin, V. P., Chugai, N. N., & Botticella, M. T. 2010, ApJ, 723, L89

Vassiliadis, E. & Wood, P. R. 1993, ApJ, 413, 641

Ventura, P. & D'Antona, F. 2005a, A&A, 431, 279

Ventura, P. & D'Antona, F. 2005b, A&A, 439, 1075

Ventura, P. & D'Antona, F. 2005c, ApJ, 635, L149

Ventura, P. & D'Antona, F. 2006, A&A, 457, 995

Ventura, P. & D'Antona, F. 2008, A&A, 479, 805

Ventura, P. & D'Antona, F. 2009, A&A, 499, 835

Ventura, P., D'Antona, F., Mazzitelli, I., & Gratton, R. 2001, ApJ, 550, L65

Ventura, P., Di Criscienzo, M., Carini, R., & D'Antona, F. 2013, MNRAS, 431, 3642

Ventura, P., García-Hernández, D. A., Dell'Agli, F., et al. 2016, ApJ, 831, L17

Ventura, P. & Marigo, P. 2010, MNRAS, 408, 2476

Vink, J. S. 2000, PhD thesis, Universiteit Utrecht <EMAIL>jvink@phys.uu.nl</EMAIL>

Vink, J. S. & de Koter, A. 2002, A&A, 393, 543

Vink, J. S., de Koter, A., & Lamers, H. J. G. L. M. 2000, A&A, 362, 295

Vink, J. S., de Koter, A., & Lamers, H. J. G. L. M. 2001, A&A, 369, 574

Vink, J. S. & Gräfener, G. 2012, ApJ, 751, L34

Vink, J. S., Muijres, L. E., Anthonisse, B., et al. 2011, A&A, 531, A132

Wallerstein, G., Iben, Jr., I., Parker, P., et al. 1997, Reviews of Modern Physics, 69, 995

Walter, G., Beer, H., Kaeppeler, F., & Penzhorn, R.-D. 1986a, A&A, 155, 247

Walter, G., Beer, H., Kaeppeler, F., Reffo, G., & Fabbri, F. 1986b, A&A, 167, 186

Wanajo, S., Tamamura, M., Itoh, N., et al. 2003, ApJ, 593, 968

Ward, R. A. & Newman, M. J. 1978, ApJ, 219, 195

Weisberg, J. M. & Taylor, J. H. 2005, in Astronomical Society of the Pacific Conference Series, Vol. 328, Binary Radio Pulsars, ed. F. A. Rasio & I. H. Stairs, 25

Wilmes, S., Wilmes, V., Staudt, G., Mohr, P., & Hammer, J. W. 2002, Phys. Rev. C, 66, 065802

Woosley, S. E. 1986, in Saas-Fee Advanced Course 16: Nucleosynthesis and Chemical Evolution, ed. J. Audouze, C. Chiosi, & S. E. Woosley, 1

Woosley, S. E. 2016

Woosley, S. E., Arnett, W. D., & Clayton, D. D. 1972, ApJ, 175, 731

Woosley, S. E., Arnett, W. D., & Clayton, D. D. 1973, ApJS, 26, 231

Woosley, S. E. & Heger, A. 2015, in Astrophysics and Space Science Library, Vol. 412, Very Massive Stars in the Local Universe, ed. J. S. Vink, 199

Woosley, S. E., Heger, A., & Weaver, T. A. 2002, Reviews of Modern Physics, 74, 1015

Woosley, S. E. & Weaver, T. A. 1995, ApJS, 101, 181

Yong, D., Grundahl, F., D'Antona, F., et al. 2009, ApJ, 695, L62

Yong, D., Grundahl, F., & Norris, J. E. 2015, MNRAS, 446, 3319

Yoon, S.-C., Dierks, A., & Langer, N. 2012, A&A, 542, A113

Yoon, S.-C. & Langer, N. 2005, A&A, 443, 643

Young, D. R., Smartt, S. J., Mattila, S., et al. 2008, A&A, 489, 359

Zamora, O., García-Hernández, D. A., Plez, B., & Manchado, A. 2014, A&A, 564, L4

Zel'dovich, Y. B. & Novikov, I. D. 1971, Theory of gravitation and the evolution of stars.

Acknowledgments

First of all, I would like to thank my supervisor, prof. Paola Marigo, and co-supervisor prof. Alessandro Bressan, for the energy and time spent working with me and for the helpful discussions.

I thank also the examiners, prof. Nikos Prantzos and prof. Laura Portinari, for the very useful suggestions and food for thought to improve my PhD thesis.

A special gratitude goes to dott. Mario Spera, for the help with computational problems, the very helpful discussions and for believing in me, and all other professors and researchers that help me in my research.

A also would thank my parents and my brother, who help me and support me during the whole years at the university.

The very special thanks goes to my climbing-friends, for the all time and all experience we spent together, I would be different today If I have not known you.

Finally, I thank Davide, who support me and believed in me all the time, especially during the last year.